III-Nitride Semiconductor Photonic Nanocavities on Silicon

THÈSE N^O 8823 (2018)

ÉCOLE POLYTECHNIQUE FÉDÉRALE DE LAUSANNE

POUR L'OBTENTION DU GRADE DE DOCTEUR ÈS SCIENCES

PAR

Ian Michael ROUSSEAU

EPFL

ÉCOLE POLYTECHNIQUE
FÉDÉRALE DE LAUSANNE

Suisse
2018

*Each new land brings to light the possibility that
there may be continents as yet unknown.*
—Louis de Broglie

To my friends...
To my family...

Acknowledgements

Abstract

Optical nanocavities enhance light-matter interaction due to their high quality factors (Q) and small modal volumes (V). The control of light-matter interaction lies at the heart of potential applications for integrated optical circuits, including optical communication, quantum computation, biophotonics, and optical projection. Many of these applications could benefit from wide band gap III-nitride semiconductor material, which already forms the basis of industrial lighting technology based on blue light-emitting diodes.

Cleanroom fabrication and optical spectroscopy comprise the laboratory work in this thesis. Air-suspended III-nitride nanocavities are fabricated using electron beam lithography, reactive ion etching, and vapor phase etching from thin (< 300 nm) III-nitride epilayers grown on silicon (111) substrates by metal-organic vapor phase epitaxy. An embedded single InGaN/GaN quantum well serves as an internal light source during micro-photoluminescence experiments. Strain and heating effects are analyzed by micro-Raman spectroscopy. A dedicated quantum optics laboratory is constructed in order to study nanocavities and quantum emitters in III-nitrides at short wavelengths ($\lambda < 500$ nm).

Photonic crystal nanocavities exhibit the highest figure-of-merit for light-matter interaction enhancement, Q/V. However, in contrast to silicon and gallium arsenide nanocavities working at telecommunication wavelengths, III-nitride based nanocavities underperform theoretical Q estimates by nearly three orders of magnitude at short wavelengths ($\lambda = 430-500$ nm). This thesis accounts for this discrepancy by combined experimental and theoretical studies of photonic crystal nanobeam cavity fabrication statistics. Surface state absorption is found to be the primary factor limiting Q at short wavelengths.

Surface effects are studied in the microdisk resonator geometry. UV photoinduced desorption of oxygen gas from the III-nitride surface redshifts and broadens whispering gallery mode resonances over minute timescales. Oxygen desorption incurs additional optical absorption losses up to 100 cm^{-1}. The redshift and broadening is nearly reversible upon the introduction of oxygen into the measurement environment, implicating oxygen in passivation of the III-nitride surface. Finally, optimized surface passivation techniques using rapid thermal processing and conformal chemical vapor deposition more than double state-of-the-art Q of GaN-based microdisk resonators to beyond $Q = 10,000$ in the blue spectral range.

The results demonstrate the capabilities and limitations of III-nitride materials for optical nanocavities and photonic integrated circuits at short wavelengths.

Résumé

Les cavités optiques permettent d'augmenter l'interaction lumière-matière du fait de leur haut facteur de qualité (Q) et de leur petit volume modal (V). Le contrôle de cette interaction est au cœur des applications potentielles des circuits optiques intégrés, notamment en ce qui concerne les communications optiques, les ordinateurs quantiques, la biophotonique et la projection optique. Plusieurs de ces applications pourraient bénéficier de la large bande interdite des semiconducteurs à base de nitrures d'éléments III qui constituent le fondement de la technologie d'éclairage reposant sur les diodes électroluminescentes bleues.

La fabrication de cavités en salle blanche et leur caractérisation à l'aide de techniques de spectroscopie optique constituent le travail principal de cette thèse. Les nanocavités à base de nitrures d'éléments III ont été réalisées en combinant la lithographie par faisceau d'électrons, la gravure ionique réactive et la gravure en phase vapeur de couches minces de nitrures d'éléments III (< 300 nm) crues sur silicium (111) par épitaxie en phase vapeur de composés organométalliques. Un seul puits quantique InGaN/GaN sert de source de lumière interne pendant les expériences de micro-photoluminescence. Les effets de la contrainte et de dissipation thermique ont été analysés par spectroscopie micro-Raman. Un laboratoire d'optique quantique a été construit pour étudier les propriétés des nanocavités et celles d'émetteurs quantiques à base de nitrures d'éléments III dans la gamme des courtes longueurs d'onde ($\lambda < 500$ nm).

Les nanocavités diélectriques conçues sur la base de cristaux photoniques constituent la plateforme présentant le plus haut rapport Q/V, c'est-à-dire le facteur de mérite principal, permettant d'exacerber l'interaction lumière-matière. Contrairement aux nanocavités à base de silicium ou d'arséniure de gallium fonctionnant aux longueurs d'onde de télécommunication, le facteur de qualité des nanocavités à base de nitrures d'éléments III est près de trois ordres de grandeur plus faible que les estimations théoriques aux courtes longueurs d'onde ($\lambda = 430 - 500$ nm). Cette thèse s'attache à expliquer la discordance entre les valeurs de Q théoriques et expérimentales de nanocavités unidimensionnelles à cristaux photoniques à base de nitrures d'éléments III opérant à courtes longueurs d'onde en combinant des études expérimentales et théoriques reposant sur l'analyse statistique de la fabrication de ces échantillons. Cette analyse démontre ainsi que l'absorption optique par les états de surface est le principal facteur limitant le facteur de qualité aux courtes longueurs d'onde.

L'absorption par les états du surface est étudiée en adoptant la géométrie dite de résonateurs de type microdisque. La désorption d'oxygène à la surface est provoquée par illumination avec de la lumière UV. En réponse, les résonances optiques des microdisques présentent

Acknowledgements

un décalage vers le rouge et un élargissement spectral à l'échelle de quelques minutes. La désorption d'oxygène entraîne des pertes additionnelles par absorption optique pouvant atteindre jusqu'à 100 cm^{-1}. Le décalage spectral et l'élargissement des modes de résonance sont presque entièrement réversibles lors de l'introduction d'oxygène dans la chambre de mesure, indiquant une passivation des états de surface des nitrures d'éléments III par l'oxygène. Finalement, des procédés de passivation de la surface reposant sur le recuit rapide et le dépôt chimique en phase vapeur conforme permettent le doublement du facteur de qualité des microdisques à des valeurs records dépassant 10'000 dans le bleu.

Les résultats obtenus soulignent le potentiel et les limites des nitrures d'éléments III pour la réalisation de nanocavités et de circuits intégrés photoniques opérant à courtes longueurs d'onde.

Zusammenfassung

Optische Nanokavitäten verstärken die Licht-Materie-Wechselwirkung aufgrund ihrer hohen Gütefaktoren (Q) und kleinen Modenvolumen (V). Die Kontrolle dieser Licht-Materie-Wechselwirkung steht im Zentrum potentieller Anwendungen für integrierte optische Schaltungen im Rahmen von optischer Kommunikation, Quantenberechnungen, Biophotonik und optischer Projektion. Viele dieser Anwendungen könnten von der Verwendung von III-Nitridhalbleitern mit weiter Bandlücke profitieren, welche bereits die Grundlage der Beleuchtungsindustrie auf Basis der blauen Leuchtdioden bilden.

Die Laborarbeiten für diese Dissertation umfassen Reinraumfertigung als auch optische Spektroskopie. Freistehende III-Nitridnanokavitäten wurden unter Verwendung von Elektronenstrahllithographie, reaktivem Ionenätzen und Dampfphasenätzen aus dünnen (< 300 nm), epitaktischen III-Nitridschichten realisiert, welche auf Silizium-(111)-Substraten durch metallorganische Gasphasenepitaxie gewachsen wurden. Ein einzelner, eingebetteter InGaN / GaN-Quantengraben dient als interne Lichtquelle für Mikrophotolumineszenzexperimente. Verspannungs- und Erwärmungseffekte werden mittels Mikro-Raman-Spektroskopie analysiert. Ein dediziertes Quantenoptiklabor wurde aufgebaut, um Nanokavitäten und Quantenemitter auf Basis von III-Nitriden bei kurzen Wellenlängen ($\lambda < 500$ nm) zu untersuchen.

Photonische Kristallnanokavitäten weisen die höchste Gütezahl Q/V für die Licht-Materie-Wechselwirkung auf. Im Gegensatz zu Silizium- und Galliumarsenid-Nanokavitäten, die im Bereich der Telekomwellenlängen arbeiten, unterschreiten jedoch die experimentellen Q Werte von III-nitridbasierten Nanokavitäten die theoretischen Vorhersagen um nahezu drei Größenordnungen im Bereich kurzer Wellenlängen ($\lambda = 430 - 500$ nm). Die vorliegende Dissertation geht dieser Diskrepanz im kurzwelligen Spektralbereich mittels eindimensionaler, photonischer Kristalle (sogenannte Nanobeams) aus III-Nitriden auf den Grund. Hierzu werden experimentelle und theoretische Studien zur Nanobeam-Fabrikationsstatistik kombiniert. Als Hauptursache wird eine durch Oberflächenzustände bedingte Absorption gefunden, welche die experimentellen Q Werte bei kurzen Wellenlängen begrenzt.

Solche Oberflächeneffekte werden mittels Mikrodiskresonatoren untersucht. Die photoinduzierte Desorption von Sauerstoff von der III-Nitridoberfläche führt zu einer Rotverschiebungen und zu einer Verbreiterung der „whispering gallery" Moden auf einer Zeitskala von Minuten. Die Sauerstoffdesorption verursacht zusätzliche, optische Absorptionsverluste mit bis zu 100 cm^{-1}. Die Rotverschiebung und Verbreiterung der Moden ist durch das Einbringen von Sauerstoff in die Messumgebung nahezu reversibel, was darauf hinweist, dass Sauerstoff die III-Nitridoberfläche passiviert. Schließlich wurden optimierte Oberflächenpassivierungs-

techniken auf Basis von Tempern und Gasphasenepitaxie entwickelt, die zu mehr als einer Verdopplung bisheriger Q Werte von GaN-basierten Mikroscheibenresonatoren auf über $Q = 10.000$ im blauen Spektralbereich führten.

Die Ergebnisse zeigen das Potential, als auch die gegenwärtigen Beschränkungen für die Anwendung von III-Nitridmaterialien für optische Nanokavitäten und optische, integrierte Schaltungen für kurze Wellenlängen.

Contents

Contents

1 Introduction

Optoelectronics, the science and technology of the direct conversion between electrical and optical energy, pervades modern life. We encounter optoelectronic devices on a daily basis, from the laser scanners at the supermarket to the optical fibers carrying our communications to the mobile phone displays in our pockets to the solar cells on our roofs to the white light-emitting diodes (LEDs) illuminating our homes. Crystalline semiconductor materials provide a platform with which energy-efficient optoelectronic devices with operational lifetimes exceeding 100,000 hours may be mass-produced at low cost. Specifically, the III-nitride (III: Al,Ga,In) semiconductor family has powered a lighting revolution during the past 20 years. The nearly 20-fold efficiency improvement realized upon the replacement of existing incandescent lighting by III-nitride-based LED lighting is projected to save humanity 261 TWh of electricity by 2030 [1], approximately the electricity production of Australia in 2016 [2]. III-nitride materials' success in the LED lighting application can be attributed to their ability to emit blue light efficiently.

This thesis explores the suitability of efficient blue light emission in III-nitride semiconductors for new applications: nanolasers and the generation of quantum states of light. Nanolasers, miniaturized versions of laser diodes, are envisioned for future compact, energy-efficient, high-speed optical communication within computer chips [3]. Quantum states of light, on the other hand, are unlike other forms of electromagnetic radiation which we commonly experience, namely laser light and thermal radiation or sunlight. Light has both a wave and discrete character, meaning that it can be caused to interfere like a wave but is detected in discrete chunks called photons. Typically, laser light and thermal radiation are bright or intense light sources, comprised of nearly billions of billions of photons being emitted per square centimeter per second.[1] A quantum light source, on the other hand, controllably emits one or two photons within the measurement time window ($\sim 10^{-8}$ s) of an experimental measurement apparatus. Quantum light sources and detectors have already enabled demonstrations of optical communication encrypted by the laws of quantum physics [4], "ghost" imaging of a non-local object [5], optical microscopy with spatial resolution exceeding the diffraction limit

---

[1]$\mathcal{O}(10^{17})$ photons-s^{-1}-cm^{-2} for sunlight on the Earth's surface.

[6], and the most robust experimental tests of quantum entanglement to-date [7]. However, the widespread commercialization of such quantum technologies is hampered by the lack of availability of turnkey, electrically-driven, bright quantum light sources operating close to room temperature.

III-nitride materials offer unique opportunities and challenges for the realization of miniaturized light sources based on semiconducting materials. Semiconductor light sources are comprised of a light emitting medium and one or more optical elements designed to extract emitted photons in a desired direction. Miniaturized light sources employ optical nanocavities, which are canonically comprised of two closely spaced ($\sim 1\ \mu$m) "mirrors." In the quantum light generation application, III-nitrides' chief advantage is their ability to exhibit quantum light emission up to room temperature [8]. However, high temperature operation comes at the price of having to work with high energy blue photons, which poses problems for the optical nanocavity. Since blue light's wavelength is approximately one-fourth that of the infrared light used in telecommunications, blue nanocavities exhibit increased sensitivity to any small imperfections in the nanocavity mirrors or their alignment.

In the blue and UV spectral ranges, optical nanocavities fabricated from III-nitride materials incorporating a light-emitting active medium exhibit figures-of-merit three orders of magnitude below the values predicted by theoretical simulations [9–15]. This discrepancy stands in stark contrast to the analogous passive cavities made from silicon or gallium arsenide working at telecommunication wavelengths, whose performance approaches the values calculated by theoretical simulations [16, 17]. The main goal of this thesis is to identify, quantify, and minimize the physical mechanisms responsible for the difference between theory and experiment in optical nanocavities made from III-nitride semiconductors in the visible range. Together with parallel and complementary work on the development of III-nitride quantum dot single light emitters in LASPE, the answers culled from this thesis will be called upon to determine the suitability of III-nitride materials for nanolasers and quantum light generation.

This thesis aims to document the development of III-nitride based quantum photonics technologies at LASPE. In writing the thesis, the author chooses to emphasize the original results obtained during the doctoral studies. Of course, a certain amount of background information must be conveyed, both to set the stage for the presentation of the original results as well as to provide the interested reader with additional references for in-depth study of particular sub-topics. With this in mind, the organization of the thesis is as follows:

- **Chapter 2: Background Information** - Provides background information on III-nitride solid-state quantum photonics. First, application-driven figures-of-merit for nanophotonic cavities are defined. Then, the relevant properties of III-nitride semiconductor physics are presented: electronic structure, optical response, mechanical deformation, quantum heterostructures, and surfaces.

- **Chapter 3: Experimental Techniques** - Discusses the experimental techniques utilized during the doctoral research. Although cleanroom techniques were employed exten-

sively, these technologies are well-established; information is therefore restricted to specialties of III-nitride cleanroom processing for nanophotonics applications. The fabricated devices were primarily characterized by optical techniques, especially micro-photoluminescence (μPL) spectroscopy. One major accomplishment of this doctoral thesis was the construction of a new quantum optics laboratory, so substantial space is dedicated to documentation of the design, construction, and performance capabilities of the new setup.

- **Chapter 4: Nanobeam Photonic Crystal Cavities** - Explores the development and experimental limitations of one particular optical nanocavity configuration. The design and simulation of such cavities are discussed. Correspondence between simulated and experimental optical properties is established on the basis of spatially-resolved μPL and cathodoluminescence spectroscopy. The influence of mechanical deformation on optical response is studied by Raman spectroscopy. A novel scheme for increasing the optical collection efficiency is presented and investigated experimentally. Finally, a combined experimental and simulated statistical study is conducted in order to quantify the loss mechanisms responsible for the discrepancy between simulated and experimental figures-of-merit for this cavity design.

- **Chapter 5: Surface Effects** - Investigates surface losses in a simpler optical microdisk geometry, selected for the ability to measure the broadband material response in a single measurement. The importance of optically active surface states is revealed by the reversible adsorption and desorption of oxygen from the microdisk surface. Various surface treatments and passivation techniques are explored to minimize optical absorption losses by surface states. The findings are then applied to tune cavity resonances in the nanobeam geometry.

- **Chapter 6 Conclusions** Summarizes the results and poses ideas for future research.

2 Background Information

This chapter supplies the relevant background information in order to provide context for and understand the thesis results in subsequent chapters. First, the two main application areas for the thesis topic, nanolasers and quantum photonics, are presented. Figures-of-merit for optical nanocavities are defined for the envisioned applications. Next, the III-nitride semiconductor family is introduced, starting from the basic material properties. Then, we delve into specificities of the III-nitride semiconductor family compared to other materials to understand the opportunities and challenges for the development of nanoscale light sources from these materials.

2.1 Light-matter interaction

This thesis is devoted to engineering of light-matter interaction in III-nitride crystalline semiconductors. Direct band gap crystalline semiconductors, especially the mass-manufactured III-arsenide and III-nitride material families,[1] may emit light efficiently from *quantum heterostructures* in which a material with a lower band gap is embedded within a higher band gap host material. If one or more dimensions of the lower band gap material approach(es) the de Broglie wavelength of electron and hole charge carriers,

$$\lambda_d = \frac{2\pi\hbar}{\sqrt{m^* k_B T}},$$

(2.1)

where $\hbar$ is the reduced Planck's constant, m^* is the carrier's effective mass (e.g. $1.2 \cdot m_0$, where m_0 is the electron rest mass), k_B is the Boltzmann constant, and T is the temperature, then the charge carriers experience quantum confinement in that dimension. This leads to the creation of a quantum well (see Section 2.4.4), quantum wire, or quantum dot for confinement occurring in one, two, or three dimensions, respectively [18].

---

[1] III symbolizes an element from Group III of the periodic table, particularly aluminum, gallium, or indium.

Chapter 2. Background Information

Light may also be confined in one, two, or three dimensions in an optical cavity. Theoretically, one could imagine forming an optical cavity by placing the semiconductor between mirrors spaced an integer number of half-wavelengths apart from one another. However, in practice, such a scheme is impractical due to parasitic absorption by the metal mirrors at optical frequencies. Instead, light is confined by embedding a higher refractive index (n_1) dielectric material, such as a semiconductor, inside a lower refractive index material, such as air or fused silica. In analogy to the electronic band gap for semiconductors, the dielectric permittivity ($\propto n_1^2$, where n_1 is the real part of the refractive index) plays the role of the confinement potential in photonic materials [19]. When one or more cavity dimensions approach(es) the nanoscale wavelengths of light in the material, λ/n_1 (roughly 100 nm for this thesis), then light becomes increasingly spatially and energetically confined.

Even with quantum heterostructures and photonic nanocavities, light and matter still interact weakly in most cases.[2] Therefore, Fermi's Golden Rule can be used to calculate the spontaneous emission rate (R_m) for an electron-hole pair (each with wavevector k) into a single mode (m) of the electromagnetic field semiclassically

$$R_m = \frac{\pi}{\hbar} \left| \langle \Psi_{e,k} | q\hat{\mathbf{r}} \cdot \mathbf{E}_m(\mathbf{r}) | \Psi_{h,k'} \rangle \right|^2 \delta(\hbar\omega = E_{e,k} - E_{h,k'}), \tag{2.2}$$

where q is the fundamental charge, $\hat{\mathbf{r}}$ is the position operator, Ψ_e and Ψ_h are the electron (e) and hole (h) wavefunctions, respectively, $\mathbf{E}_m(\mathbf{r})$ is the vacuum electric field of the electromagnetic mode under consideration, and the δ-Dirac function ensures that the photon conserves the electronic transition energy [18]. The transition is assumed to conserve linear momentum ($k = k'$) due to the negligible photon momentum relative to carriers. The overall spontaneous emission rate is the sum of Eq. 2.2 over all available electromagnetic modes. For the case of a randomly oriented emitter in a homogeneous, isotropic medium, the average radiative decay rate is

$$R(\omega) = \sum_m R_m = \frac{1}{3} R_m \rho_\gamma(\omega), \tag{2.3}$$

where $\rho_\gamma(\omega)$ is the photonic density of states and the factor 1/3 is due to the random dipole orientation. In this case, the overall decay rate for a single electron-hole pair is simply 1/3 times the rate of decay into a single electromagnetic mode times the number of available modes, e.g. the decay probability is equally likely into all electromagnetic modes with energy $\hbar\omega$.

Equations 2.2-2.3 encapsulate a substantial quantity of physics. For instance, optical transitions can only occur between wavefunctions of opposite parity due to the odd parity of the electric dipole operator in a bulk semiconductor [20]. In addition, the vacuum electric field intensity is normalized semi-classically by equating the time-averaged energy in the

---

[2]See Section 2.2.2 for an exception.

electromagnetic field to the zero-point energy of the electromagnetic field

$$2 \int_{V_0} \frac{1}{2} \varepsilon_0 |\mathbf{E}_m|^2 dV = \frac{1}{2} \hbar \omega,$$
$$|\mathbf{E}_m| = \left(\frac{\hbar \omega}{2 \varepsilon_0 V_0} \right)^{1/2}. \tag{2.4}$$

In Eq. 2.4, V_0 is the volume in which the electromagnetic field is confined and ε_0 is the dielectric vacuum permittivity.

The photonic density of states, $\rho_\gamma(\omega)$, plays a critical role in determining the strength of light-matter interaction. For free space, which corresponds to a homogeneous, isotropic dielectric environment, $\rho_\gamma(\omega) = \omega^2 V_0 / \pi^2 c^3$. Therefore, the mode volume V_0 cancels out when computing the overall spontaneous emission rate (Eq. 2.3). On the other hand, if $\mathbf{E}_m$ describes an optical cavity mode, then the homogeneous, isotropic environment approximation breaks down; in this case, one can associate an "effective" photonic density of states associated with the cavity mode,

$$\rho_\gamma(\omega_0) = \frac{2Q}{\pi \omega_0} \tag{2.5}$$

at the resonance angular frequency ω_0, where Q is the cavity mode quality factor,

$$Q = \omega_0 / \Delta \omega. \tag{2.6}$$

The broadening, $\Delta \omega$, is the angular frequency corresponding to the rate at which the photonic cavity dissipates the stored optical energy. All experimental optical cavities exhibit such losses due to parasitic absorption or scattering of light. Combining with Eq. 2.4, the rate of spontaneous emission into the cavity mode is seen to be proportional to Q/V_0 [21].

Eq. 2.2 presents several opportunities for engineering of light-matter interaction. The overlap integral between the electron and hole wavefunctions, which are typically delocalized (e.g. k is a good quantum number in one or more spatial dimensions), and the localized position operator justifies the prior statement that spatial electronic localization via quantum confinement in heterostructures leads to enhanced light-matter interaction. Additionally, if an optical cavity modifies the energetic density and coupling to electromagnetic modes, the electric field intensity of one or more desirable electromagnetic modes may be maximized at the spatial position of the quantum confined charge carriers. If and only if the quantum heterostructure's light emission is sufficiently narrow band and couples predominantly to the cavity mode, then the overall spontaneous emission rate may be enhanced relative to the free space case. Spontaneous emission rate enhancement is frequently called the Purcell effect [21, 22]. Alternatively, one may engineer the optical system such that fewer electromagnetic

modes exist over the quantum heterostructure's emission bandwidth. In this case, the overall spontaneous emission rate may be suppressed relative to the free space case [23, 24].

2.2 Applications

Writing broadly, we can orient ourselves in the landscape of potential applications by categorization on the basis of the dimensionalities of the electronic and optical confinement. The strength of light-matter interaction increases as we move down and/or to the right in Fig. 2.1. Commercial applications are written in red and research topics in blue. This thesis

Photonic confinement ⟶				
	None	1D	2D	3D
1D: quantum well	LED	VCSEL Polaritons	Laser diode Polaritons	Nanolasers
3D: quantum dot	Lumophores SPS	OPSL SPS	SPS	Nanolasers SPS QIP

Figure 2.1: Commercial (red) and research (blue) application areas for semiconductor optoelectronic devices based on the dimensionality of electronic and photonic confinement. II-VI colloidal semiconductor quantum dot lumophores have been used for improved color rendering in televisions [25, 26]. Other applications include the vertical cavity surface-emitting laser (VCSEL), optically pumped semiconductor laser (OPSL), single photon source (SPS), and quantum information processing (QIP). Here, "polaritons" refers to the exciton-polaritons formed by hybridization of bosonic quantum well excitons and photons. This should not be confused with exciton-polaritons formed in the strong coupling regime for cavity quantum electrodynamics and QIP, in which a fermionic quantum dot exciton is hybridized with photons.

treats three-dimensional photonic confinement, so the following sections apply the aforementioned physics in order to define figures-of-merit for three-dimensional photonic cavities in the nanolaser, single photon source (SPS), and quantum information processing (QIP) applications.

2.2.1 Nanolasers

Nanolasers promise not only reduced energy consumption for short-range optical communication within computer chips [3] but also remain objects of scientific interest due to their "thresholdless" lasing behavior [27], special photon statistics [28, 29], and proposed generation of squeezed light [30].

First, we consider the optical communication application. Here, the modulation bandwidth is limited by the slowest between the nonradiative decay rate of the active medium, spontaneous emission rate, the cavity decay rate ($\propto 1/Q$), and the stimulated emission rate, which depends

on the material properties and whether the laser is being driven above or below threshold [31]. Compared to normal semiconductor diode lasers, nanolasers exhibit a reduced lasing threshold for two reasons. First, as the cavity volume is reduced, the amount of gain material that is inside the cavity that needs to be pumped above threshold is reduced. This is a purely geometrical effect. Second, as the cavity volume approaches $(\lambda/n)^3$, the fraction of spontaneous emission that couples to the lasing mode (β) ideally approaches one [30]. For the sake of comparison, $\beta = 10^{-5} - 10^{-4}$ in a normal semiconductor diode laser [32]. In the limit of negligible nonradiative recombination in the gain medium, the lasing threshold (I_{th}) in the small cavity limit is proportional to [31]

$$I_{th} \propto \frac{1}{\beta Q}. \tag{2.7}$$

If β scales inversely with the cavity mode volume V_0, then the relevant figure-of-merit for nanolaser threshold is Q/V_0.

As $\beta \to 1$, the abrupt increase in light emission at threshold smoothens and the laser input-output curve takes on a linear, "thresholdless" shape [31]. This is because each spontaneously emitted photon goes into the cavity mode in the limit $\beta = 1$. This does not mean that the laser no longer exhibits a threshold for stimulated emission; rather, one can no longer extract the threshold from the input-output curve and must instead rely upon power-dependent measurements of the first- and second-order photon correlation statistics to find the threshold [33]. Although a thresholdless input-output characteristic would reduce the modulation depth for optical communication, such behavior can be engineered out of the system by decreasing β or increasing the nonradiative recombination rate of the active medium, albeit at the cost of increased lasing threshold [31]. Optical modulation bandwidths up to several hundred GHz have been measured on nanolasers, but this result could be attributed to fast surface recombination [34].

2.2.2 Solid-state quantum photonics

The idea of quantum computation has captivated the world since pioneering theoretical work in the early 1980s [35, 36]. Quantum computers promise to be able to solve certain kinds of problems, such as prime number factorization and quantum many-body simulation of physical systems, faster than classical computers by using "qubits" that are quantum superpositions of the classical 0 and 1 bits. As of the writing of this thesis, the most promising, scalable quantum computers have been built using qubits realized from superconducting Cooper pair boxes due to their long coherence times [37], up to 85 μs in 2016 [38]. The qubits are linked together on a microwave transmission line [39] and cooled to millikelvin temperatures in a dilution fridge.

Solid-state quantum photonic systems pose an alternative paradigm that is more amenable to higher temperature operation and optical networking over long distances using conventional

optical fiber. In a solid-state quantum photonic device based on semiconducting material, an "artificial atom" formed by two energy levels within a semiconductor quantum dot or deep defect state may serve as the 0 and 1 in a qubit. The two level system is embedded in a photonic cavity [40]. Within this hardware instantiation [36, 41], qubits are encoded on the polarization of single photons. Quantum logic gates are implemented in strongly coupled artificial atom-cavity systems, in which the light-matter interaction is strong enough that a single control photon can cause a switching or phase shift in the passage of the second signal photon. Therefore, to implement such a scheme, single photon sources and quantum logic gates are needed.

Quantum logic gates can be realized if the light-matter interaction exhibits vacuum Rabi splitting in the strong coupling regime [42]. If a photon can be spontaneously emitted by this two-level system into a cavity mode (Eq. 2.2) faster than the rate at which photons are lost from the cavity ($\gamma = \omega_0/Q$),[3] then a photon may be reabsorbed by the two-level system before exiting the cavity. Thus, spontaneous emission becomes a reversible process; the two-level system and cavity photons hybridize to form a Jaynes-Cummings ladder of exciton-polariton energy states in the strong coupling regime, which opens the possibility for scalable quantum information processing based on single photon phase gates [36, 41, 44].

As we have seen that the spontaneous emission rate depends on the dielectric environment, we can define a dimensionless, environment-independent figure-of-merit for the emitter called the oscillator strength [18]

$$f_{\mathrm{osc}} = \frac{2m_0\omega}{\hbar}\left|\langle\Psi_{e,k}|\hat{\mathbf{r}}\cdot\hat{\mathbf{e}}|\Psi_{h,k'}\rangle\right|^2, \tag{2.8}$$

where $\hat{\mathbf{e}}$ is the electric field's polarization vector. The condition $\gamma \ll R_m$ leads to the following figure-of-merit for the transition between the strong and weak coupling regime

$$\frac{Q}{V_0^{1/2}} \gg \frac{4\pi n_1}{q\lambda}\left(\frac{m_0}{\mu_0 f_{\mathrm{osc}}}\right)^{1/2}, \tag{2.9}$$

where n_1 is the bulk refractive index of the semiconductor and μ_0 is the vacuum permeability [43]. Again, the figure-of-merit is proportional to cavity Q and small modal volumes remain favorable. Assuming a realistic radiative lifetime of 1 ns in a III-nitride quantum dot embedded in a GaN matrix [8, 45] and $V_0 = (\lambda/n_1)^3$, Eq. 2.9 would require $Q \gg 6500$ to achieve strong coupling at $\hbar\omega = 2.76$ eV.

Single photon sources can be realized by an artificial atom-cavity system in the weak coupling regime, e.g. where Eq. 2.9 is not satisfied. Working in the weak coupling regime is beneficial for maximizing the source brightness for two reasons. First, the spontaneous emission coupling

---

[3]Assuming the emitter linewidth κ is less than γ, as is typically the case. κ is the overall linewidth, including contributions from homogeneous (radiative lifetime) and inhomogeneous (nonradiative) broadening [43].

rate β scales inversely with V_0, so more spontaneously emitted photons are collected by the desired electromagnetic modes [46, 47].[4] Second, the brightness can be enhanced by the Purcell effect if the emitter linewidth (κ) remains narrower than the cavity linewidth. In this case, the spontaneous emission rate can be enhanced relative to the free space rate up to a factor F_p by the cavity [21, 48]

$$F_P = \frac{3Q(\lambda/n_1)^3}{4\pi^2 V_0}.$$
(2.10)

In this case, the cavity figure-of-merit is again proportional to Q/V_0. Purcell factors between $5 - 15$ have been observed experimentally in quantum nanophotonic systems based on semiconductor quantum dots, far less than the factors of several hundred predicted by simple application of Eq. 2.10 due to random spectral and position fluctuations of fabricated quantum dots relative to the electromagnetic mode [40, 48–50].

In this section, we learned about the basic physics of light-matter interaction in semiconductors and the possible application domains. For each application, the figure-of-merit of the optical cavity proved to be proportional to the cavity quality factor Q and inversely proportional to the (square root of the) modal volume V_0. Therefore, the optical cavity figure-of-merit for the thesis is defined as Q/V_0.

2.3   State-of-the-art

Direct bandgap semiconductors, based on III-arsenide, III-nitride, and III-phosphide materials, remain promising as scalable, manufacturable optoelectronic devices for nanolasers and QIP. Their direct bandgap offers strong light-matter interaction, extrinsic doping allows realization of electrically driven devices, and quantum engineering by heteroepitaxial crystal growth creates the possibility for precise control of emission energies over large ranges. Competing platforms, such as diamond-based systems, cannot be electrically-driven due to the absence of quantum heterostructures and the lack of reliable n-type doping [51]. Although colloidal II-VI CdSe/ZnSe quantum dots exhibit single photon emission at room temperature [52], creation of integrated optical circuits and formation of electrical contacts on a single nanocrystal would require laborious dot placement schemes [53].

III-nitride semiconductors' greatest advantage resides in efficient, high temperature operation. For QIP, III-arsenide semiconductors are restricted to low temperature operation (< 40 K) due to coupling of quantum dot emitters to longitudinal acoustic phonons [40, 54]. In contrast, III-nitride quantum dots have demonstrated single photon emission up to 300 K, albeit at an emission energy of 4 eV / 310 nm and poor photon statistics relative to III-arsenide dots [8]. On the other hand, in the nanolaser application, the "poor" wall plug efficiency of InAs-InGaAsP based quantum wells at telecommunication wavelengths and room temperature ($< 15\%$ [3])

---

[4]If the emitter couples to one polarization mode, $\beta \to 1$. If it couples to both polarizations, $\beta \to 1/2$.

may outweigh integrated optical waveguide losses of shorter wavelength devices for short distance, intrachip optical communication. In contrast, blue laser diodes can achieve up to 40% wall plug efficiency at 450 nm [55].

Many possible optical nanocavity designs have been explored for solid-state nanophotonics. Strong coupling between an artificial atom and a photonic mode has been achieved in GaAs-based microdisks [56, 57], Bragg micropillars [58], as well as 1D [59] and 2D photonic crystals [60] in addition to diamond-based 1D photonic crystals [61].[5] In the literature, photonic crystal optical nanocavities have been shown to experimentally exhibit the strongest light-matter coupling (Eq. 2.2) due to their high Q and small modal volumes V_0 [40]. Therefore, this thesis focuses primarily on photonic crystal cavities.
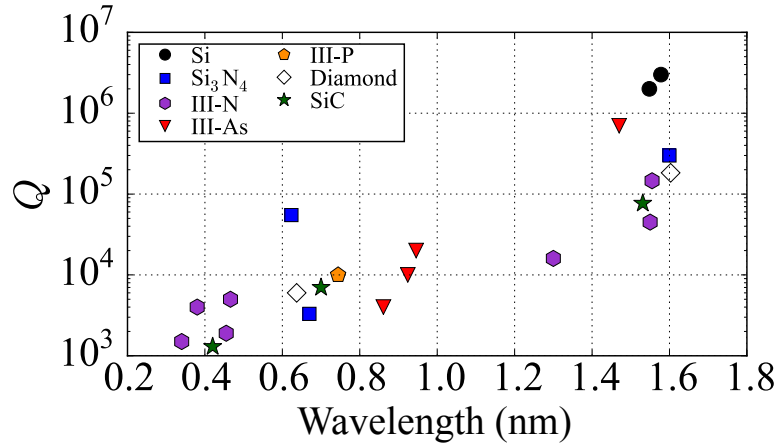
Figure 2.2: Literature review of the highest reported 1D and 2D photonic crystal cavity Q as a function of wavelength for Si [16, 62], SiN [63–65], III-N [10, 12, 66–68], III-As [59, 69, 70], III-P [71], diamond [61, 72], and SiC [73–75]. Reproduced from [14] with permission from APS.

Figure 2.2 presents the highest Q values recorded in the literature for both 1D and 2D photonic crystal cavity designs in a variety of materials. The empirical exponential decrease in Q with decreasing wavelength is perhaps most discouraging for researchers working in the visible and UV with wide band gap materials such as diamond, SiC, GaN, and AlN. Only silicon and gallium arsenide based cavities operating at telecom wavelengths ($\lambda = 1.55\ \mu$m) exhibit Q values approaching theoretical design limits between 10^6 and 10^7. For both materials, surface passivation proved to be critical for attaining such high values [17, 76–78]. Other materials have not been investigated as systematically, especially at short wavelengths. A primary aim of this thesis is to identify and quantify the origins of the decreased Q in III-nitride photonic crystals operating at short wavelengths.

---

[5]For an introduction to Bragg and photonic crystal cavities, see Section 4.1. For an introduction to microdisks, see Section 5.1.

2.4 III-nitride semiconductors

This section explains the basic properties of III-nitride semiconductors, which currently provide the basis for mass-manufactured optoelectronic devices such as blue to green LEDs and laser diodes. Growth on silicon is motivated by the low substrate cost, potential for CMOS integration, and ease of air gap creation. Particular attention is paid to peculiarities of these materials, such as spontaneous polarization and the quantum-confined Stark effect. Finally, a brief review of III-nitride surface science is provided in preparation for Ch. 5.

2.4.1 Essentials

III-nitride binary semiconductors are comprised of wurtzite (2H) phase alloys of aluminum, gallium, or indium and nitrogen.[6] Fig. 2.3 shows the ideal wurtzite unit cell, which is formed
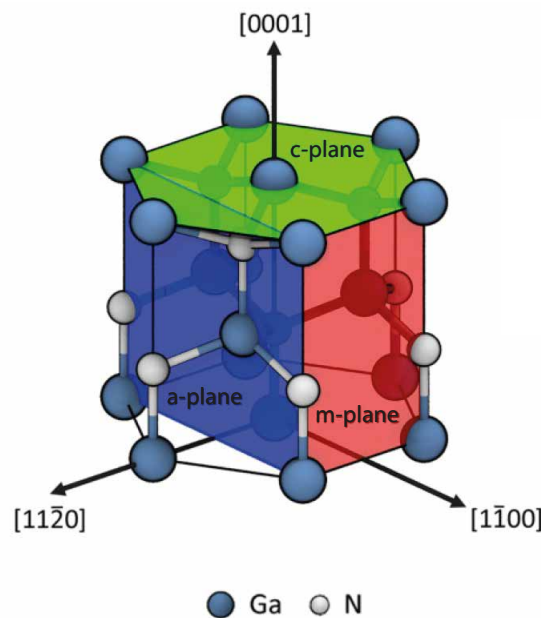
Figure 2.3: Crystal structure of wurtzite GaN showing two interpenetrating hexagonal closed packed lattices of nitrogen and metal atoms. Major crystal planes are highlighted in different colors. Adapted from [80]. Reproduced with permission from APS.

by two interspersed hexagonal lattices, one of metal atoms and the other of nitrogen atoms. Ideally, the ratio of the unit cell height c to the hexagon side length a is $c/a = \sqrt{8/3}$ and the vertical offset between the two sub-lattices is $u = 3c/8$. Basic parameters of the binary alloys can be found in Table 2.1.

The lack of inversion symmetry results in piezoelectricity, while the offset of the negatively charged nitrogen and positively charged metal charge centers creates a permanent spontaneous polarization dipole in the unit cell parallel to the polar c-axis, dubbed pyroelectricity for

---

[6]The zincblende cubic phase (3C) can also be grown, but is generally metastable with wurtzite inclusions [79].

13

Material	u	a (Å)	c/a	$\frac{1}{a}\frac{\partial a}{\partial T}$ (10^{-6} K^{-1})	E_g (eV)	α_V (meV/K)	β_V (K)
GaN	0.377	3.189	1.634	5.59	3.42	0.909	830
AlN	0.382	3.110	1.606	2.9	6.03	1.799	1462
InN	0.379	3.538	1.618	3.70	0.7	0.414	454

Table 2.1: Basic material properties of wurtzite AlN, GaN, and InN [81]. $1/a \cdot \partial a/\partial T$ is the thermal expansion coefficient. E_g is taken at room temperature. α and β are parameters for the band gap's temperature dependence in the Varshni model (Eq. 2.14).

its temperature sensitivity. The spontaneous polarization plays an important role in III-nitride quantum heterostructures (Section 2.4.4). III-nitrides are primarily grown parallel to the metal-polar $+c$-plane (0001), although it is also possible to grow along the N-polar $-c$-plane (000$\bar{1}$), nonpolar m-plane (10$\bar{1}$0), and semipolar a-planes (1$\bar{2}$10) to cite the most common examples.

The electronic band structure for GaN is shown in Fig. 2.4. GaN is a direct band gap semicon-
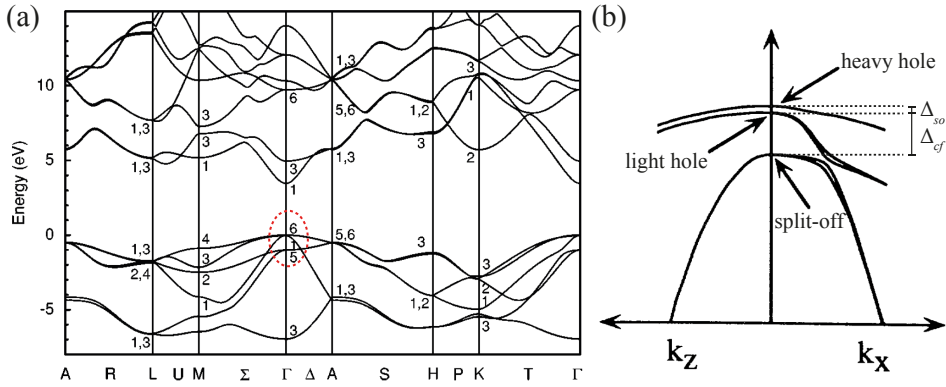
Figure 2.4: (a) Band structure of wurtzite GaN calculated by an empirical pseudopotential approach. Adapted from [82] and reproduced with permission from APS. The circle highlights the valence band maximum, which is shown schematically on a higher resolution energy scale in (b). Heavy hole and light hole band degeneracy are lifted by the spin-orbit interaction (Δ_{so}), whereas the split-off band is shifted by the much larger crystal field interaction (Δ_{cf}). Adapted from [83] and reproduced with permission from APS.

ductor with conduction band minimum and valence band maximum at the Γ-point, $\mathbf{k} = 0$. At the Γ-point, the corresponding conduction band wavefunctions have s-like symmetry and are two-fold spin degenerate. Meanwhile, the situation for the valence band is more complex. Near the valence band maximum, the corresponding wavefunctions have p-like symmetry, leading to effective mass anisotropy. Each of the three valence bands is two-fold spin degenerate. The heavy-hole band contains the valence band maximum. The crystal field (Δ_{cf}) moves the split-off band 22 meV below the heavy and light hole bands, while the spin-orbit interaction (Δ_{so}) breaks the degeneracy between the light and heavy hole bands, shifting the light hole band 8 meV below the valence band maximum at the Γ-point [81, 83].

Since III-nitride layers are grown by heteroepitaxy on foreign substrates (Section 2.4.2), strain may affect the band structure. Generally, hydrostatic tensile strain has a tendency to decrease the wavefunction overlap between adjacent atoms in the crystal lattice, leading to a decreased band gap [84].

Using ternary alloys, the band gap of III-nitride semiconductors can be tuned from the deep ultraviolet to the infrared, as shown in Fig. 2.5. Properties of the ternary alloys can generally
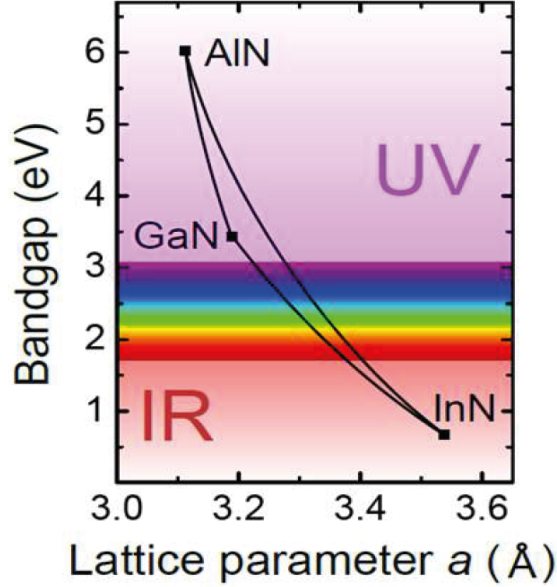
Figure 2.5: Band gap of III-nitride ternary alloys from the UV through the infrared. Reused from [85].

be linearly interpolated following Vegard's law [81]. However, others, such as the band gap for ternary alloys, require bowing parameters which may depend on strain and material quality. Such a modified Vegard's law for the band gap of a ternary alloy is,

$$E_g(A_x B_{1-x} N) = x E_g(AN) + (1 - x) E_g(BN) + x(1 - x) b_{A,B}. \tag{2.11}$$

Unlike the nearly lattice-matched GaAs and AlAs, only GaN and the ternary alloy $Al_{0.82}In_{0.18}N$ are lattice-matched [86], which has important consequences for growth. For bowing parameters of the band gap of ternary alloys, see Table 2.4.

The anisotropy of the wurtzite crystal structure is imprinted on III-nitrides' optical response. Fig. 2.6 shows the complex refractive index for bulk GaN and AlN. In this thesis, the frequency-dependent refractive index, the relative permittivity, and the absorption coefficient are used interchangeably. The refractive index is related to the materials' complex relative permittivity by

$$\tilde{\varepsilon}(\omega) = \varepsilon_1(\omega) + i\varepsilon_2(\omega) = \left(n_1(\omega) + in_2(\omega)\right)^2, \tag{2.12}$$

15

and the absorption coefficient ($\alpha(\omega)$) to the imaginary part of the refractive index ($n_2(\omega)$) by

$$\alpha(\omega) = \frac{2\omega n_2(\omega)}{c}. \tag{2.13}$$

As a well-behaved response function, the real ($\varepsilon_1(\omega)$) and imaginary ($\varepsilon_2(\omega)$) relative permittivities are linked by the Kramers-Krönig relations [87].

III-nitride materials are birefringent, meaning that the refractive index depends on the relative orientation of the propagating electric field (**E**) to the c-axis. If $\mathbf{E} \perp c$, then the electric field is said to be aligned along the crystal's ordinary axis (subscript o). If $\mathbf{E} \parallel c$, then the electric field is propagating along the crystal's extraordinary (subscript e) axis. At the design target energy of 2.76 eV / 450 nm in this thesis, the difference between n_e and n_o is on the order of 2% and is ignored for the rest of the thesis.

In Fig. 2.6, the absorptive, imaginary part of refractive index increases abruptly from zero at the
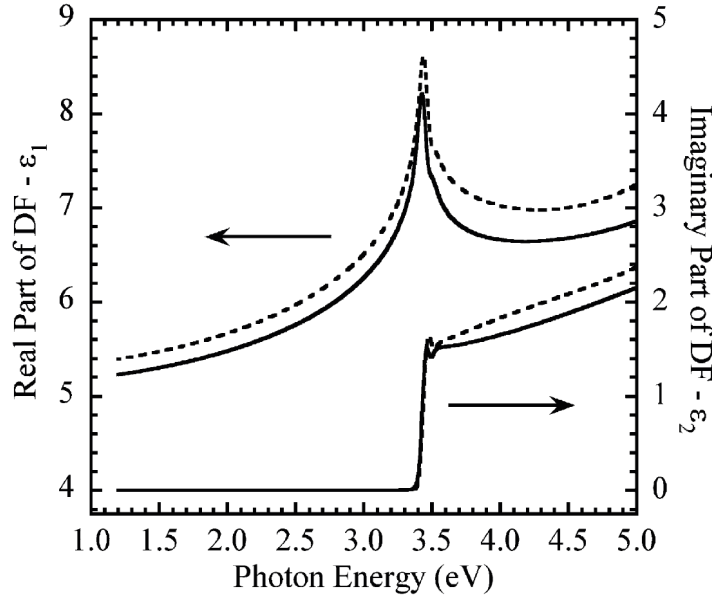
Figure 2.6: Anisotropic complex relative permittivity of wurtzite GaN in the visible and UV measured by spectroscopic ellipsometry. Reproduced with permission from [88].

bandgap energy, as expected for band-to-band transitions in a direct band gap semiconductor. The slight peak in the imaginary part of the refractive index above the band gap energy is related to excitonic (two-particle) effects. The temperature dependence of the fundamental band gap follows an empirical Varshni relation [89]

$$E_g(T) = E_g(0) - \frac{\alpha T^2}{T + \beta}, \tag{2.14}$$

which has zero slope near $T = 0$ K. Varshni model parameters for the binary alloys can be found in Table 2.1.

At telecommunication wavelengths, GaN's refractive index of 2.3 is less than silicon and GaAs ($n \approx 3.5$) due to the Kramers-Krönig relations and the larger band gap.[7] As a consequence, the ultimate modal volumes of GaN optical nanocavities are a factor 3.5 larger than their GaAs or silicon counterparts in units of cubic wavelengths, *ceteris paribus*. GaN is ordinarily dispersive ($dn/d\omega > 0$) around a hypothetical operation wavelength for optical communication, 405 nm / 3.06 eV, based on widely available lasers for Blu-ray[TM] optical discs. This poses a trade-off between the bandwidth (BW) and propagation distance (D) in GaN waveguides [92],

$$D = \frac{1}{2\,\text{BW}\,\text{GVD}\,\text{FSR}}. \tag{2.15}$$

We find $D = 800$ cm when plugging in a bandwidth of $2\pi \cdot 10$ GHz, group velocity dispersion (GVD) of 2.6×10^{24} m^{-1}-s^2 for GaN at optical frequencies,

$$\text{GVD} = \frac{d}{d\omega}\left(\frac{d\omega}{dk}\right)^{-1},$$

and free spectral range (FSR) of $2\pi \cdot 600$ GHz for a 100 μm long Fabry-Perot laser resonator made of GaN [18]. This value is sufficient for intra-chip optical communication. However, waveguide losses, which are determined by experimental factors and power consumption, currently pose a stricter limit on D. The lowest material losses presented this thesis are $\alpha = 15$ cm^{-1} at 2.6 eV (Ch. 5). Thus, a -3 dB loss would correspond to a hypothetical integrated GaN waveguide length of $D = 460$ μm, more than four orders of magnitude below the dispersion limit, a distance likely insufficient for power-efficient intrachip optical communication.

2.4.2 Growth

Historically, III-nitrides have been grown epitaxially on foreign substrates (Table 2.2). All foreign substrates are lattice-mismatched with the III-nitrides, so the epilayer quality depends critically on the selected substrate. Depending on the growth technique and parameters, the resulting strain is relaxed through the formation of surface roughness, point defects that serve as non-radiative recombination centers, dislocations, and, in extreme cases, macroscopic crack formation. Even if the strain is relaxed at the growth temperature, upon cooling the differing thermal expansion coefficients of the III-nitrides and foreign substrates impose additional stress at the substrate-epilayer interface, which may lead to additional strain, crack formation, substrate bowing, and/or epilayer delamination. Despite the large lattice mismatch, c-plane sapphire (α-Al$_2$O$_3$) remains the substrate of choice for the LED industry, while thermally conductive silicon (111) is the substrate of choice for the power electronics industry, both due to their low cost. Recently, free-standing GaN and AlN substrates have

---

[7]Empirically, the semiconductor band gap and the refractive index are related by $n_1 \propto E_g^{-4}$ [90, 91].

Substrate	Mismatch (%)	$\frac{1}{a}\frac{\partial a}{\partial T}$ $(10^{-6}\,\mathbf{K}^{-1})$	κ (W/cm·K)	$\varnothing$ (mm)	Cost (CHF)
Al_2O_3 (0001)	13	7.5	0.3	200	40
Si (111)	-17	2.6	1.5	300	15
6H-SiC	-3.4	4.2	4.9	150	>1000
2H-GaN	0	5.59	2.3	50	>1000
2H-AlN	2.48	4.2	3.2	25	4000

Table 2.2: Mismatch, thermal expansion coefficient, thermal conductivity (κ), maximum diameter ($\varnothing$), and cost of 50 mm diameter substrate material for III-nitride epitaxy. Mismatch is for GaN epilayers, $(a_{\text{sub}} - a_{\text{GaN}})/a_{\text{sub}}$. Physical parameters are taken from [81]. Prices for research quantities and maximum diameters are issued from internal group records.

become available. Growth on free-standing substrates substantially reduces defect densities, albeit at a price that can only be justified in research environments and for laser diodes. Free-standing substrate cost is expected to decrease in the future.

Silicon (111) is the substrate of choice in this thesis for several reasons. First, the photonic nanocavities produced in this thesis must be suspended in air to achieve the smallest modal volumes (Section 4.1). Due to the maturity of silicon semiconductor fabrication, many techniques exist to selectively remove the silicon substrate without damaging the III-nitride epilayers (Section 3.1.4). No processes exist that would selectively etch sapphire or free-standing III-nitride substrates without damaging the overlying epilayers. Alternatively, researchers have developed selective photoelectrochemical etching of heavily doped GaN [93], InGaN [94], or AlInN [95] interlayers. However, such methods may leave behind a rough undersurface of the nanostructures or leave "whiskers" sticking out of a nanostructure corresponding to dislocations [96], which lead to increased optical losses due to scattering.

Second, if nanolaser research is predicated on the eventual application of intrachip optical communication, then growth on silicon offers a scalable pathway for eventual optical and electronic integration. Although this thesis grows on a silicon crystal orientation that differs from the industry-standard (100) orientation, researchers have shown that it is possible to grow III-nitrides on suitably prepared silicon (100) substrates [97]. For more information on growth of GaN on silicon (111), consult [98].

III-nitrides are epitaxially grown by one of three techniques:

- **Molecular beam epitaxy (MBE):** MBE growth occurs using the raw elements as precursors in a ultrahigh vacuum ($< 1 \times 10^{-10}$ mbar) environment. The metals are placed in heated crucibles aimed at the sample surface, which is heated to the growth temperature. Active nitrogen is supplied either by a nitrogen plasma or by thermal decomposition of ammonia on the wafer surface. As MBE utilizes elemental precursors, it is expected to produce crystals with the lowest impurity levels. The high vacuum environment creates the opportunity for use of *in situ*, surface-sensitive metrology techniques, such

as reflection high energy electron diffraction (RHEED).

- **Metal-organic vapor phase epitaxy (MOVPE):** Instead of pure elemental sources, MOVPE growth occurs via thermal cracking of metal-(trimethyl/triethyl)organic precursors carried by H_2 or N_2 gases with ammonia gas on the heated substrate surface. In contrast to MBE, MOVPE growth remains closer to thermal equilibrium. Higher growth rates than MBE are possible (1-10 μm per hour), which makes it the tool of choice for the optoelectronics industry. All epilayers utilized in this thesis are grown by MOVPE.

- **Hydride vapor phase epitaxy (HVPE):** HVPE is the oldest of the three growth techniques, and uses metal hydrides and ammonia as the sources for III-nitride material. Due to the high growth rate (up to 500 μm per hour), HVPE is the method of choice for growing bulk, free-standing GaN substrates or thick, relaxed epilayers to serve as templates for subsequent growth by other methods.

2.4.3 Mechanical properties

As the III-nitrides exhibit piezoelectricity, both strain (ϵ) and DC electric fields (F) may induce stress (σ). For the wurtzite crystal symmetry, the electromechanical coupling in stress-charge form is [99]

$$
\begin{pmatrix} \sigma_{xx} \\ \sigma_{yy} \\ \sigma_{zz} \\ \sigma_{yz} \\ \sigma_{xz} \\ \sigma_{xy} \end{pmatrix} = \begin{pmatrix} C_{11} & C_{12} & C_{13} & 0 & 0 & 0 \\ C_{12} & C_{11} & C_{13} & 0 & 0 & 0 \\ C_{13} & C_{13} & C_{33} & 0 & 0 & 0 \\ 0 & 0 & 0 & C_{44} & 0 & 0 \\ 0 & 0 & 0 & 0 & C_{44} & 0 \\ 0 & 0 & 0 & 0 & 0 & \frac{C_{11}-C_{12}}{2} \end{pmatrix} \begin{pmatrix} \epsilon_{xx} \\ \epsilon_{yy} \\ \epsilon_{zz} \\ 2\epsilon_{yz} \\ 2\epsilon_{xz} \\ 2\epsilon_{xy} \end{pmatrix} - \begin{pmatrix} 0 & 0 & e_{31} \\ 0 & 0 & e_{31} \\ 0 & 0 & e_{33} \\ 0 & e_{15} & 0 \\ e_{15} & 0 & 0 \\ 0 & 0 & 0 \end{pmatrix} \begin{pmatrix} F_x \\ F_y \\ F_z \end{pmatrix} . \quad (2.16)
$$

The first term represents the elastic stiffness matrix in Hooke's law, while the second represents the piezoelectric contribution. In the Voigt notation, axis $3/z$ is aligned with the $+c$ crystal axis. The overall electrostatic displacement field in the III-nitride material is

$$
\begin{pmatrix} D_x \\ D_y \\ D_z \end{pmatrix} = \begin{pmatrix} 0 \\ 0 \\ P_{sp} \end{pmatrix} + \begin{pmatrix} 0 & 0 & 0 & 0 & e_{15} & 0 \\ 0 & 0 & 0 & e_{15} & 0 & 0 \\ e_{13} & e_{13} & e_{33} & 0 & 0 & 0 \end{pmatrix} \begin{pmatrix} \epsilon_{xx} \\ \epsilon_{yy} \\ \epsilon_{zz} \\ 2\epsilon_{yz} \\ 2\epsilon_{xz} \\ 2\epsilon_{xy} \end{pmatrix} + \varepsilon_0 \begin{pmatrix} \varepsilon_{11} & 0 & 0 \\ 0 & \varepsilon_{11} & 0 \\ 0 & 0 & \varepsilon_{33} \end{pmatrix} \begin{pmatrix} F_x \\ F_y \\ F_z \end{pmatrix} , \quad (2.17)
$$

where the first term accounts for the spontaneous polarization, the second for the converse piezoelectric effect, and the third for the normal static electric polarizability. ε_0 is the vacuum permittivity. Table 2.3 lists the corresponding material parameters for GaN and AlN. In this thesis, as-grown films are normally biaxially strained. However, we will also work with uniaxial

Material	C_{11}	C_{12}	C_{13}	C_{33}	C_{44}	e_{31}	e_{33}	e_{15}	ε_{11}	ε_{13}	P_{sp}
GaN	390	145	106	398	105	-0.34	0.67	-0.30	9.5	10.28	-0.034
AlN	396	137	108	373	116	-0.53	1.5	-0.48	9.0	10.31	0.090
InN	223	115	92	224	48	-0.41	0.69	-0.32	15.3	14.61	-0.042

Table 2.3: Elastic stiffness constants, piezoelectric, relative permittivity, and spontaneous polarization coefficients for GaN and AlN. C_{ij}, e_{ij}, and P_{sp} units are GPa, C-m^2, and C/m^2, respectively [81].

and unstrained III-nitride layers in nanostructures. Ignoring the piezoelectric contribution,[8] Hooke's law in Eq. 2.16 for the case of biaxial strain,

$$\vec{\sigma} = \left(\begin{array}{cccccc} \sigma_{xx} & \sigma_{xx} & 0 & 0 & 0 & 0 \end{array} \right)^T,$$

leads to

$$
\begin{aligned}
\epsilon_{yy} &= \epsilon_{xx}, \\
\epsilon_{zz} &= -2\frac{C_{13}}{C_{33}}\epsilon_{xx}, \\
\sigma_{xx} &= (C_{11} + C_{12} - 2\frac{C_{13}^2}{C_{33}})\epsilon_{xx}.
\end{aligned}
\tag{2.18}
$$

While the condition for uniaxial strain,

$$\vec{\sigma} = \left(\begin{array}{cccccc} \sigma_{xx} & 0 & 0 & 0 & 0 & 0 \end{array} \right)^T,$$

results in

$$
\begin{aligned}
C_0 &= \frac{C_{12} - \frac{C_{13}^2}{C_{33}}}{C_{11} - \frac{C_{13}^2}{C_{33}}}, \tag{2.19} \\
\epsilon_{yy} &= -C_0 \epsilon_{xx}, \\
\epsilon_{zz} &= \frac{C_{13}}{C_{33}}(C_0 - 1)\epsilon_{xx}, \\
\sigma_{xx} &= [C_{11} - C_0 C_{12} + \frac{C_{13}^2}{C_{33}}(C_0 - 1)]\epsilon_{xx}. \tag{2.20}
\end{aligned}
$$

For completeness, the bowing parameters for several alloy parameters are given in Table 2.4.

---

[8]Normally, the piezoelectric contribution to the stress is on the order of 2%, so the second term in Eq. 2.16 is ignored [99].

Material	$E_g^{A,B}$ (eV)	$P_{sp}^{A,B}$ (C/m^2)
InGaN	-1.43	0.0709
InAlN	-3.1	0.0378
AlGaN	-1.0	0.0191

Table 2.4: Bowing parameters for band gap and spontaneous polarization in modified Vegard's law (Eq. 2.11) in III-nitride ternary alloys [81]. In this thesis, a linear interpolation without bowing is used for the elastic moduli and piezoelectric constants, e_{ij} [81].

2.4.4 InGaN/GaN quantum wells

As mentioned in Section 2.1, sandwiching a lower band gap semiconductor within a wider band gap semiconductor can lead to type-I electronic confinement, e.g. confinement of both electron and holes along the growth axis, if one or more dimensions of the inclusion approach(es) the de Broglie wavelength (Eq. 2.1), which is about 5 nm for GaN at 300 K. Not only does the spatial confinement increase the strength of light-matter interaction by improved electron-hole wavefunction overlap (Eq. 2.2), but the crystal grower can tune the light emission energy by changing the size of heterostructure as well as the material composition. In this Section, we treat single InGaN/GaN quantum well gain media, which serve as an internal light source for all experiments in this thesis. For future quantum nanophotonics experiments, GaN/AlN-based quantum dots may be substituted as the active medium. For the interested reader, additional references provide an overview of the properties of these quantum dots [8, 45, 100–102].

The energy levels (E_l) and envelope wavefunctions (ψ_l^e) for electrons in a quantum well are found by solving Schrödinger's time-independent wave equation for the quickly varying crystal potential ($V_c(x, y, z)$) and the slowly-varying confinement potential ($V_e(z)$), where z is the material growth axis and l is an integer,

$$-\frac{\hbar^2}{2m_0}\nabla^2\psi_l^e(x, y, z) + V_c(x, y, z) + V_e(z)\psi_l^e(x, y, z) = E_l^e\psi_l^e(x, y, z). \tag{2.21}$$

Assuming we are working near the conduction band Γ-point in the band structure, the parabolic band effective mass approximation can be used. Due to the translational symmetry in the xy plane, a separable wavefunction is a reasonable ansatz $\psi_l(x, y, z) = e^{ik_x x + ik_y y}\phi_l(z)$. Plugging this into Eq. 2.21 leads to a one-dimensional wave equation in z and $\phi_m(z)$,

$$-\frac{\hbar^2}{2}\frac{d}{dz}\frac{1}{m_e^*}\frac{d}{dz}\phi_l^e(z) + V_e(z)\phi_l^e(z) = (E_m^e + E_k^e)\phi_l^e(z), \tag{2.22}$$

where $E_k^e = \hbar^2 k_\parallel^2 / 2m_e^*$ and $k_\parallel^2 = k_x^2 + k_y^2$.

The simplest case, which is applicable to III-arsenide quantum wells, involves a rectangular

well

$$V_e = \begin{cases} -\Delta E_c & |x| < d/2 \\ 0 & |x| \geq d/2 \end{cases} \tag{2.23}$$

where d is the well width and ΔE_c is the conduction band offset, typically assumed to be 70% of the overall band gap offset in such a type-I quantum well following the common anion rule [18]. Due to the symmetry of the potential, the eigenfunctions must have positive $\big(\phi(z) = \phi(-z)\big)$ or negative $\big(\phi(z) = -\phi(z)\big)$ parity. In the well, the wavefunctions follow a $\sin(k_z z)$ or $\cos(k_z z)$ dependence, which couple to decaying exponential functions in the barriers. Solving for the continuity of the wavefunction and the current continuity at $\pm d/2$ leads to a singular equation for the eigenenergies, E_l, where l is an integer. In the limit $\Delta E_c \to \infty$, the energy sublevels follow a simple m^2 spacing

$$E_l^e = l^2 \frac{\hbar^2 \pi^2}{2m_e^* d^2}.$$

An analogous treatment occurs for holes, leading to eigenenergies E_l^p. However, due to the energetic proximity of the six valence bands,[9] a full $k \cdot p$ model is often used to accurately compute the hole wavefunctions and eigenenergies, which can be mixed by the confinement potential [85]. Optical transitions again have selection rules. Generally, near the Γ-point, the electron and hole envelope wavefunctions must have the same parity. The selection rules regarding bands further depend on the photon polarization and valence band mixing [18].

The quantum confined Stark effect governs III-nitride quantum well operation for the majority of samples, which are grown along the c-axis. Instead of rectangular potentials, $V(z)$ resembles a triangular potential in InGaN/GaN quantum wells due to spontaneous polarization mismatch and piezoelectric effect. Recalling Section 2.4.3, the displacement field contains contributions from the spontaneous, piezoelectric, and electric field polarizability. In an inhomogeneous dielectric material, Poisson's equation, $\nabla \cdot \vec{D} = 0$, is fulfilled. This implies that D_z, in the case of biaxial strain [99],

$$D_z = P_{sp} + 2\epsilon_{xx}(e_{13} - e_{33}C_{13}/C_{33}) + \varepsilon_0 \varepsilon_{33} F_3 \tag{2.24}$$

is the same in the quantum well barrier (subscript b) and the quantum well (subscript w) material. If we make the further assumption that the electric field in the barrier material is zero, then we can solve for the electric field inside the quantum well material, $F_{3,w}$,

$$F_{3,w} = \frac{P_{sp,b} - P_{sp,w}}{\varepsilon_0 \varepsilon_{33,w}} + \frac{P_{pz,b} - P_{pz,w}}{\varepsilon_0 \varepsilon_{33,w}}. \tag{2.25}$$

Therefore, the change in spontaneous polarization at the InGaN/GaN interfaces produces two oppositely charged sheet charges on either side of the quantum well, which, in combination

---

[9] Each of the three valence bands is spin degenerate.

with the piezoelectric field due to the strained InGaN material, gives rise to a strong built-in electric field within the quantum well.

Evaluation of Eq. 2.25 for a pseudomorphically grown, biaxially strained $In_{0.15}Ga_{0.85}N/GaN$ single quantum wells employed in this thesis leads to a built-in field of 1.5 MV/cm pointed toward the $+c$ axis [99]. 2/3 of the contribution originates from the piezoelectric effect and 1/3 from the spontaneous polarization effect. An electric field of this magnitude corresponds to a potential drop of 0.45 eV over a 3 nm thick quantum well. Roughly speaking, the quantum confined Stark effect redshifts optical transitions of the rectangular well by $eF_z d_w$, where d_w is the quantum well thickness. More precisely speaking, such a large quantum confined Stark effect is too large to be included perturbatively in the solutions for a rectangular potential well, so Schrödinger's equation must be solved numerically. Experimentally, at high excitation intensities, the emission blue shifts due to screening of $F_{3,w}$ and a Schrödinger-Poisson model is required to compute the energy levels.

The quantum confined Stark effect dramatically affects III-nitride optoelectronic device operation. The strong built-in field has a tendency to push electron and hole envelope wavefunctions to opposite sides of the quantum well (Fig. 2.7(a)). The spatial overlap between electron and hole envelope wavefunctions is reduced exponentially in the electric field or quantum well width. This leads to an exponential decrease in the oscillator strength in addition to a redshift. Absorption primarily occurs by excited quantum well states with higher wavefunction overlap, so it is blue (Stokes) shifted relative to the quantum well photoluminescence (Fig. 2.7(b)).

Appendix A presents the detailed experimental optical properties of the InGaN/GaN single quantum wells employed as light sources in this thesis. In contrast to III-arsenides, III-nitride materials exhibit exciton binding energies (E_B) exceeding $k_B T$ at room temperature For instance, E_B is 26 meV in GaN [81] and may be enhanced up to 4× in a quantum well [18]. At low excitation densities, this means that excitations in a quantum well must be described by two-particle composite, bosonic excitons rather than the typical fermionic picture. At high excitation densities approaching the transparency threshold for optical gain ($\sim 10^{12}$ cm^{-2}), the Mott transition from excitons to single-particle, fermionic electron-hole plasma occurs [85]. All experiments in this thesis are performed in the low excitation (excitonic) regime unless otherwise noted.

Real-world InGaN/GaN quantum wells further depart from the simple models employed here (see Appendix A for an in-depth discussion). Two unexpected real-world observations surprised the semiconductor optoelectronics community, who had not observed similar behavior in III-arsenide based optoelectronic devices. First, despite the large number of defects in III-nitride quantum heterostructures grown on foreign substrates, the radiative efficiency of InGaN/GaN quantum wells is unexpectedly high. The internal quantum efficiency (IQE) can be over 90% (Appendix A). Second, the LED radiative efficiency is known to "droop" at high current densities [105]. The current working hypothesis is that that quantum well thickness and indium alloy fluctuations produce a potential landscape in the lateral (xy) dimensions.
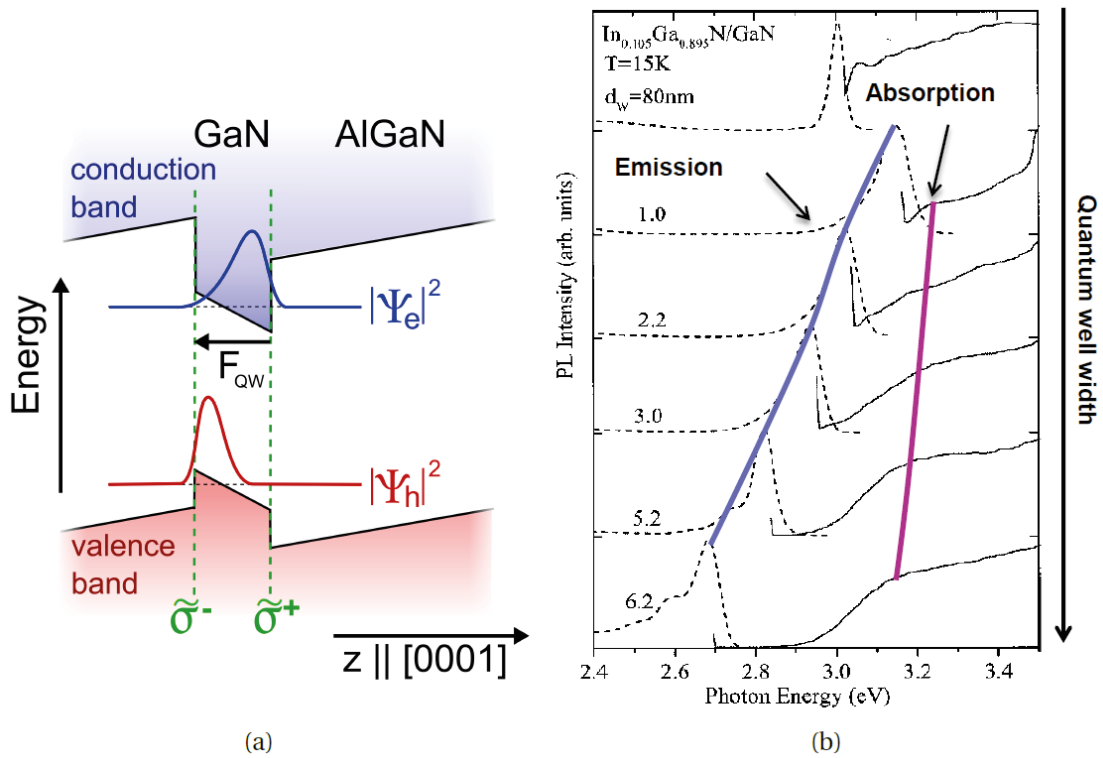
Figure 2.7: (a) Schematic of electron and hole envelope wavefunctions in a triangular potential well caused by the quantum confined Stark effect, which (b) leads to a redshift of the quantum well photoluminescence relative to the quantum absorption with increasing InGaN thickness. Taken from [103] (left) and [104] (right). Reproduced with permission from APS.

Excitons settle into local potential minima, preventing them from reaching nonradiative re-combination centers like threading dislocations. Provided the distance between localization centers remains less than the threading dislocation density, the resulting hybrid quantum well-quantum dot gain medium emits light efficiently due to three-dimensional electronic confinement [106, 107]. The increased emission efficiency is paid at the price of augmented nonradiative Auger recombination at high intensities due to the increased likelihood of three-particle processes in localized potential minima [108]. This issue is likely to continue to be debated.

2.4.5 Surfaces

In this subsection, we examine the role of *surface states* in semiconductor devices, first from a broad, material-independent perspective and then shift focus to the specificities of III-nitrides. The semiconductor band structure from Fig. 2.4 remains valid only within the bulk material volume. All experimental semiconductor devices have finite spatial extent and are connected to the external environment by one or more interfaces. The termination of the infinite crystal lattice at such an interface may result in the formation of *intrinsic* surface states, which are spatially localized at the interface. Surface states may exist with energy eigenvalues within the bulk material band gap. Additional *extrinsic* surface states may exist due to the presence of structural defects or chemical impurities [109].

Surface passivation describes a family of techniques which modify the semiconductor surface in a favorable manner for device operation. Typically, surface passivation treatments decrease the density of surface states, whose charging and discharging may impede transistor device switching [109] or supply mid-gap states that facilitate nonradiative recombination at the semiconductor surface and laser facets [110]. Historically, the success of silicon-based microelectronics can be largely attributed to silicon's ability to thermally grow a low interface state density oxide layer [111].
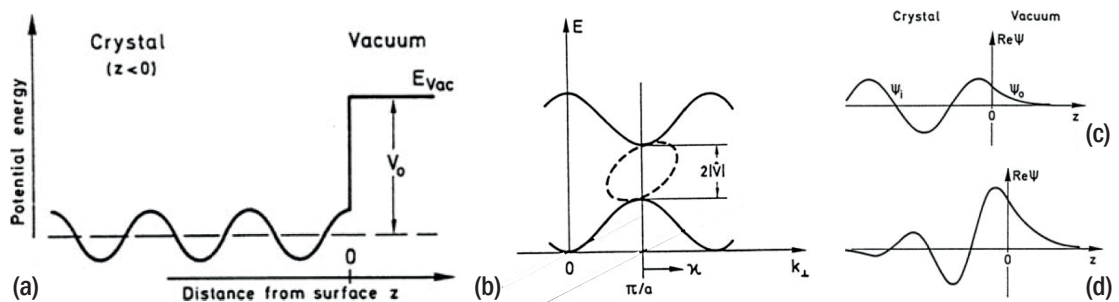
Figure 2.8: (a) Potential $V(z)$ in the nearly-free electron model with a surface. (b) Energy dispersion relation of bulk states (solid lines) and surface states (dashed lines) in the gap near $k = \pi/a$. (c) Delocalized bulk wavefunction decaying into interface and (d) localized surface state wavefunction with energy eigenvalue lying in the gap. Adapted from [112].

A simple one-dimensional quantum mechanical model explains intrinsic surface state forma-

tion. Fig. 2.8(a) sketches the system under consideration, which is an addition to the nearly free electron model. A weak periodic potential, $V(z)$, with period a extending to $z \to -\infty$ is terminated by a surface at $z = 0$, with the vacuum level offset by ΔE_{vac} above the periodic potential. Far away from the boundary, one recovers the normal behavior of the nearly free electron model that is in most solid-state physics textbooks. However, the ansatz wavefunction for real κ_{z-},

$$\psi(z) = \begin{cases} Ge^{\kappa_{z-}z \mp i\phi}\left(e^{i(\frac{\pi}{a}z\pm\phi)} \mp e^{-i(\frac{\pi}{a}z\pm\phi)}\right) & z < 0 \\ He^{-\kappa_{z+}z} & z \geq 0 \end{cases}, \tag{2.26}$$

also solves the one-dimensional Schrödinger equation. In Eq. 2.26,

$$\begin{aligned} \kappa_{z+} &= \sqrt{\frac{2m_0}{\hbar^2}\left(\Delta E_{vac} - E(q)\right)}, \\ \phi(q) &= \frac{1}{2}\arcsin\left(\frac{\hbar^2\pi^2\kappa_{z-}^2}{m_0|V_{\pi/a}|}\right), \\ E(\kappa_{z-}) &= \frac{\hbar^2}{2m_0}\left[\left(\frac{\pi}{a}\right)^2 - (\kappa_{z-})^2\right] \pm |V_{\pi/a}|\sqrt{1 - \left(\frac{\hbar^2\pi\kappa_{z-}}{ma|V_{\pi/a}|}\right)^2}, \end{aligned} \tag{2.27}$$

where $E(\kappa_{z-})$ is the energy eigenvalue, $|V_{\pi/a}|$ is the Fourier transform amplitude of the periodic potential, and κ_{z-} is restricted to keep the energy real-valued. Physically, the wavefunction in Eq. 2.26 comprises a decaying standing wave in the crystal matched to a decaying exponential wave on the barrier. Matching the wavefunction and its first derivative[10] at $z = 0^-$ and $z = 0^+$ results in a system of two equations in three unknowns, $E(\kappa_z^-)$, G, and H.

The determinantal solution to the resulting two-by-two system of equations yields the ratio G/H and the energy dispersion for surface states. Fig. 2.8(c) shows that the introduction of the surface at $z = 0$ leads to possible solutions localized at the crystal surface with energy eigenvalues within the bulk gap. Such intrinsic surface states involving nearly free electrons derived from the conduction band are called *Shockley states*. They can only exist within the energy gap because this produces the exponential wavefunction decay into the semiconductor crystal [112].

In a real, three-dimensional crystal, a two-dimensional dispersion diagram for surface states can be constructed. Multiple terms label surface states in scientific literature; it is worth repeating textbook definitions [112] for the uninitiated reader. Although they are physically equivalent to Shockley states, the *Tamm state* model describes surface state formation via linear combinations of atomic eigenstates: surface atoms have fewer neighbors and therefore experience less hybridization (mode splitting and shifting) than their bulk neighbors. Theoretically, every unbonded molecular orbital creates an intrinsic surface state. If the chemical

---

[10]The probability current is zero at $z = 0$ for the ansatz wavefunction.

bonding is sufficiently strong in the compound (covalent compounds such as Si or Ge), the absence of neighboring atoms at the surface may distort the other molecular orbitals of that surface atom, forming a *dangling bond state*. Dangling bond states are more energetically separated from bulk states due to the larger relative impact of the surface. Finally, *back bond states* may result from the surface modifying the bonding between sub-surface atoms. Energetically, such states are less displaced from the bulk than dangling bond states because the modifications more delocalized in real space. In summary, surface states are classified by their surface wavevector, energetic separation from the bulk bands, and their spatial location within the lattice.

Surface states energetically located near the conduction band can accept charge and are negative when filled (acceptor-like), whereas surface states energetically located near the valence band can donate a charge and remain positively charged when empty [112]. Note that this terminology is the opposite of the standard extrinsic chemical doping of bulk semiconductors [84]. Additionally, chemical adsorbates, crystal damage, and/or non-crystal plane terminations can result in the formation of additional extrinsic surface defect states [109]. Therefore, when reading experimental surface science literature, one must distinguish between ideal surfaces, which are created by cleaving crystals in ultrahigh vacuum, and real world surfaces, which result from exposure to atmosphere and/or cleanroom processing. Even ideal surfaces may undergo reconstruction to minimize their surface energy [112]; when reading theory papers, one must ensure that the theoretical geometry corresponds to a realistic experimental surface configuration.

III-nitride surfaces again depart from past community experience with other semiconductors. In III-arsenides and II-VI semiconductors, intrinsic surface states do not exist in the bulk material band gap for surfaces cleaved on major crystal planes due to surface reconstruction following cleaving. In group-IV semiconductors, such as silicon, intrinsic surface states exist in the bulk material band gap due to the covalent nature of the bonds [109]. In contrast, calculations and measurements of both c- and m-plane GaN surfaces indicate a high density of acceptor-like intrinsic surface states located approximately 1.0 and 0.6 eV below the conduction band minimum, respectively [80, 113]. Sub-gap optical absorption by surface states is energetically allowed between surface state bands as well as between surface state and bulk semiconductor bands. Surface photovoltage [109] measurements of c-plane GaN exhibit a continuum of optical surface transitions for photon energies between 1.3 eV and the bulk band gap, 3.4 eV [114]. Furthermore, oxygen adsorption is known to modify the surface states of pristine facets, resulting in (de)increased band bending for $(m)c$-plane surfaces [115–117]. Finally, oxygen can be desorbed from the GaN surface by UV illumination under vacuum [115]. Surface passivation of III-nitride surfaces remains a topic of ongoing research.

2.5 Summary

This chapter presented background information for the thesis. The goals of the presentation were twofold: first, in order to place this work in a larger context, the possible applications of the thesis research were discussed. Application-grounded, quantitative figures-of-merit were defined for experimental evaluation in subsequent chapters. Second, the relevant physics and materials science of III-nitride semiconductors were presented. Emphasis was paid to differences between III-nitrides and other semiconductor families, such as III-arsenide compound semiconductors and silicon.

3 Experimental Methods

In this chapter, we examine the experimental methods used to create and characterize III-nitride materials and optical nanocavities resonant in the blue and near-ultraviolet portions of the electromagnetic spectrum. Thus, the chapter is broken into two subsections, one focusing on fabrication and the other on characterization. The short operation wavelength imposes strict conditions on the dimensions and tolerances of the final optical nanocavity structure. First, the epitaxial films must be thin ($\sim \lambda/n$), free of pits and cracks, and smooth while exhibiting both low residual absorption and minimal strain. Second, the operation wavelength dictates the lateral feature size which, in the case of photonic crystal cavities, is on the order of $\lambda/2n$ or 120 nm for operation in the blue. At such short length scales, pattern transfer and subsequent high-aspect ratio etching occur at the edge of the process window, which may result in compromises for other parameters such as surface roughness. Next, the absorptive silicon substrate must be removed to create an air-suspended cavity by the most gentle, chemically-selective means available. Finally, the samples must be cleaned and passivated to maximize performance without collapsing the air-suspended structures. Such peculiarities specific to III-nitride optical nanocavities are discussed in the first part of this chapter.

The second part of the chapter focuses on characterization techniques. The samples are primarily studied by all-optical, contact-free techniques, such as microphotoluminescence (μPL) spectroscopy. Conventionally, photoluminescence spectroscopy of semiconductors examines the light emitted by a semiconductor under non-resonant optical excitation, e.g. with a pump laser whose photon energy exceed the semiconductor's bulk band gap. The construction of a new laboratory for optical spectroscopy was an objective of the thesis. The goal of the related subsection is to document the setup's capabilities for future users. The laboratory is configured in a modular design to enable a variety of measurements, including:

- μPL spectroscopy

- Micro-Raman (μRaman) spectroscopy

- Hakki-Paoli technique for laser gain measurement

- Time-correlated single photon counting (TCSPC) spectroscopy

- Time-resolved photoluminescence (TRPL) spectroscopy

The nanoscale objects studied in the laboratory, including quantum dots and optical nanocavities, demand sub-micron mechanical stability and positioning precision. As such nanoscale light-emitters do not emit much light,[1] the setup is configured to maximize the collection and detection efficiency. Furthermore, as Chapter 5 evidences, nanoscale objects may exhibit extreme sensitivity to the measurement environment, requiring additional apparatus modifications. The constraint of short wavelength operation[2] restricts the availability of suitable optical components and imposes free space operation due to high dispersion and losses in optical fibers in the ultraviolet and blue spectral ranges. Finally, custom LabView measurement software in conjunction with a scanning stage, motorized filter wheel, motorized $\lambda/2$-waveplate, and electromechanical shutter automates measurements such as time- power- and polarization-dependencies, photon statistics, and spatial mappings of μPL.

3.1 Fabrication

This section describes the equipment utilized during the fabrication of III-nitride optical nanocavities. The process flow (Fig. 3.1) outlines each high-level step in the fabrication procedure. One subsection is devoted to each substep: epilayer growth, pattern writing, pattern transfer by dry etching, silicon substrate removal, and sample cleaning. The goal is not to be an exhaustive, self-contained reference for each technique but rather to explain critical process parameters for III-nitride optical nanocavities and to provide the interested reader with references for further reading.

3.1.1 Epitaxial growth

All samples in this thesis were grown on silicon (111) wafers by Dr. Jean-François Carlin using metal-organic vapor phase epitaxy (MOVPE) in an Aixtron 200/4 RF-S low pressure horizontal reactor. Although the growth took place on the (111) silicon surface due to its three-fold symmetry, in principle III-nitrides can be grown on suitably prepared (100) surfaces, opening the possibility for CMOS integration [118]. However, III-nitride growth on Si (100) has not been widely explored. In this thesis, however, the growth on silicon was motivated by the ease of removal of the substrate material to create air-suspended optical nanocavities.

The recipe was co-developed by Dr. Carlin and my predecessor, Dr. Noelia Vico-Triviño, during her doctoral thesis [103] and remained unchanged in this work. A 40-50 nm aluminum nitride

---

[1]The III-nitride quantum dots' shortest recorded lifetime is 1 ns [45], of which the fraction $1/2(1 - \sqrt{1 - NA^2}) = 0.06$ for NA= 0.5 is emitted into a microscope objective's cone, giving a maximum available photon count rate of 6×10^7 s^{-1} not taking collection and detection efficiency into account.

[2]The shortest wavelength pump laser is 244 nm.

(a)

Thickness (nm):   Material:
90 — GaN
3 — InGaN
110 — GaN
45 — AlN
Substrate — Si (111)

(b)
70   120
90 — HSQ

(c)   (d)   (e)
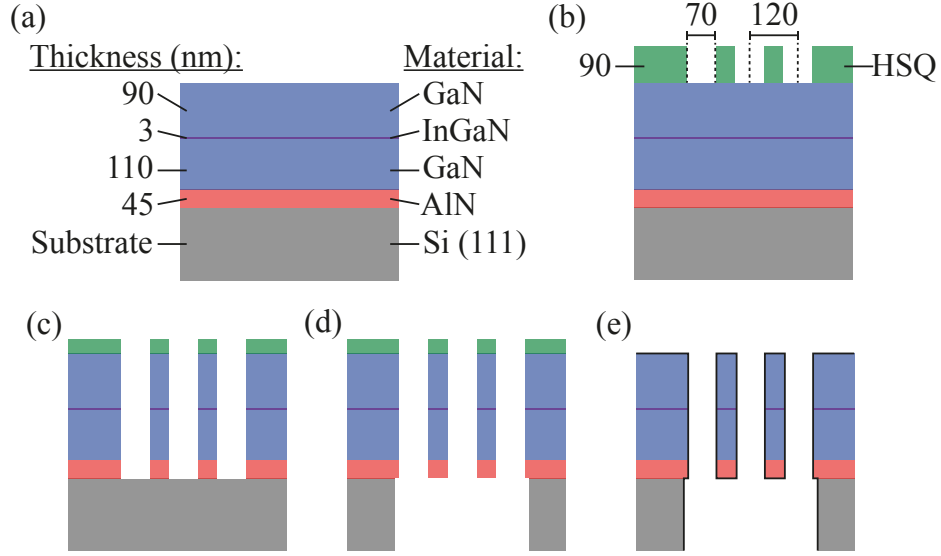
Figure 3.1: Process flow for creation of III-nitride photonic crystal cavities resonant in the blue. (a) Epitaxial growth by metal-organic vapor phase epitaxy. (b) Electron beam lithography of hydrogen silsesquioxane (HSQ) hard mask. (c) Pattern transfer by dry etching. (d) ~ 750 nm air gap creation by XeF_2 vapor phase etching. (e) Resist strip, cleaning, and passivation (black layer). All dimensions (nm) are to scale.

buffer layer (Fig. 3.1(a)) must be grown on the substrate because gallium nitride reacts with the silicon substrate, leading to melt-back etching [97, 119]. The optimum growth conditions for the smoothest surface without pits or cracks necessitate an overall epilayer thickness of 300 nm, thicker than the ideal $\lambda/(2n_{eff}) \approx 100$ nm required for single electromagnetic mode operation of photonic crystals in the blue spectral region (Section 4.1.2). A single $In_{0.15}Ga_{0.85}$/GaN quantum well placed 10 nm above the geometric center of the epilayer stack maximizes coupling of the internal light source to the fundamental electromagnetic mode due to the lower refractive index of AlN (Section 4.1). For more information on growth of III-nitride epilayers on silicon (111) using MOVPE, see [98, 103].

3.1.2   Pattern writing

Optical nanocavity patterns must be written by electron beam lithography due to the small feature size ($l_{\text{crit}} \sim 70$ nm) of photonic crystal patterns. This follows from the diffraction limited resolution ($l_{\text{min},\gamma}$) of an ideal optical imaging system,

$$l_{\text{min},\gamma} = \frac{\lambda}{2\,\text{NA}},$$

(3.1)

where λ is the illumination wavelength and NA ≤ 1 is the imaging system's numerical aperture. The available photolithography equipment at EPFL employs mercury arc lamps ($\lambda \sim 400$ nm),

so $l_{\min,\gamma} \gg l_{\mathrm{crit}}$ and the photolithography system cannot be used for processing blue photonic crystals.

By using electrons instead of photons for patterning, $l_{\min}$ can be shrunk by several orders of magnitude. One can turn to the de Broglie wavelength of an electron as a back-of-the-envelope estimate of an upper-bound on the resolution of patterning by electron beam lithography,

$$l_{\min,\mathrm{e}} = \frac{hc}{pc}, \tag{3.2}$$

where h is Planck's constant and p is the electron momentum. The relativistic relationship between momentum, kinetic energy, and rest mass for a massive particle is

$$pc = \sqrt{\mathrm{KE}^2 + 2\mathrm{KE}\, m_0 c^2}, \tag{3.3}$$

where KE is the kinetic energy and m_0 is the electron rest mass (511 keV). For a realistic maximum electron kinetic energy of 100 keV, $l_{\min,\mathrm{e}}$ is on the order of 0.04 Å, far below l_{crit}.

Although the theoretical resolution limits of electron beam lithography remain at subatomic length scales, practical systems are limited to resolutions of a few nanometers. The first patterning by electron beam lithography was demonstrated in 1969 by IBM Research [120], and the first practical electron beam lithography system was demonstrated in 1975 by Bell Labs [121]. Modern, commercial electron beam lithography systems are primarily utilized for writing the master photomasks for photolithography [122]. The principal components of such systems include (Fig. 3.2) a thermal or cold cathode emission gun to source electrons, coils to focus and deflect the beam, a beam blanker or shutter, and a sample coated with an electron-sensitive resist mounted on a stage controlled by a laser-interferometer.

The practical resolution is limited by several factors. First, as the beam current increases, electrostatic electron-electron repulsion in the focus increases the spot size. Second, the spot position does not immediately settle after opening the beam blanker. Finally, electrons are backscattered by the underlying substrate, raising the background dose of electrons within a ~ 30 μm radius. This necessitates a pattern-density dependent exposure correction, called proximity effect correction, which is calibrated using well-established procedures [123] and the Layout BEAMER software at EPFL.

The best lithography exposures require careful optimization and knowledge of how the patterns are written. EPFL's 100 kV Vistec (now owned by Raith) EBPG5000 system writes patterns by breaking the patterns up into $200 \times 200 \ \mu\mathrm{m}^2$ write fields whose size is limited by the range of the deflection coils. Between write fields, the sample stage moves and may introduce stitching errors into the patterns. Therefore, nanostructures must be grouped into blocks inside a single write field while keeping the overall pattern density low enough such that proximity correction effects do not play a major role. The "fracturing" of the pattern, the algorithm controlling how
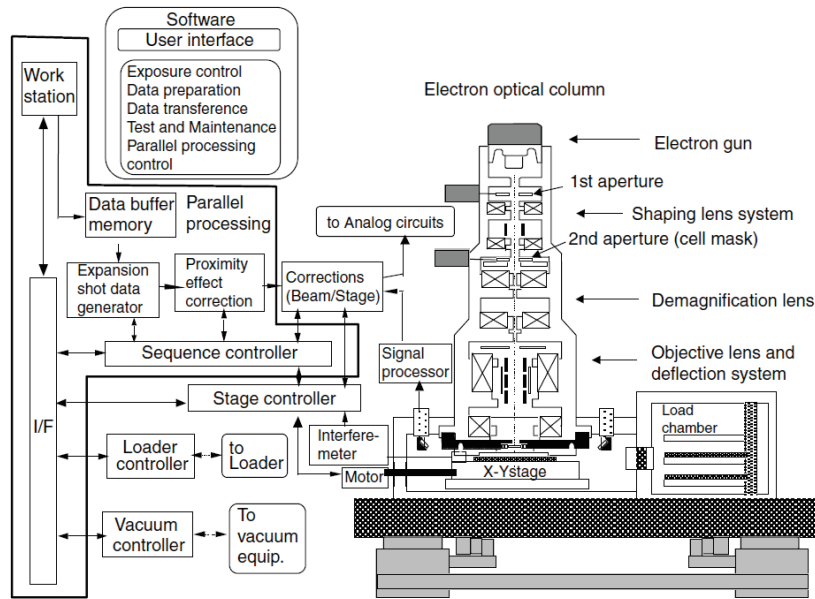
Figure 3.2: A schematic example of the building blocks of an electron beam lithography system. Reproduced from [122].

the shapes are broken into primitive polygons, is of paramount importance; the beam shutter blanks in between polygons, introducing a few nanometer settling error. The smoothest, roundest structures can be realized when the inside and outside perimeters are patterned without blanking the beam (Fig. 3.3).
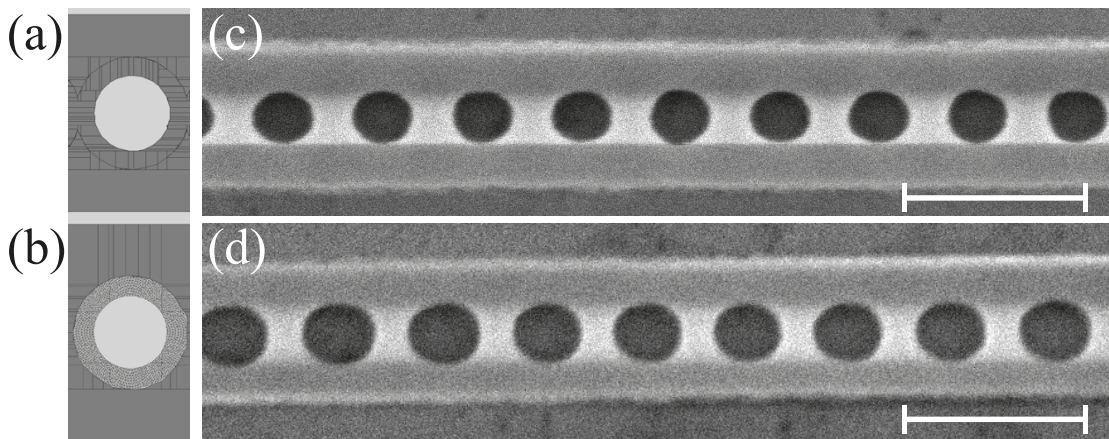
Figure 3.3: BEAMER previews for (a) conventional polygon and (c) sequence fractures. SEM images of corresponding lithography in 90 nm of 6% HSQ developed in TMAH 25% for (b) conventional polygon and (d) sequence fractures. Note the improved hole homogeneity. Scale bars are 200 nm.

With such an optimized exposure, the minimum hole diameter that can be reliably written in the negative tone resist hydrogen silsesquioxane (HSQ) developed in high contrast 25% tetramethylammonium hydroxide (TMAH) developer is around 60 nm, which gives a 1:5 aspect ratio for a resist thickness of 90 nm. Although the EBPG5000 could write smaller holes if the resist were thinner, the use of HSQ as a hard mask for dry etching precludes thinning due to the 300 nm epilayer thickness, etch process selectivity, and aspect-ratio dependent etch rate, which are discussed in the next subsection.

3.1.3   Dry etching

The optimized lithographic exposure must be transferred to the underlying III-nitride epilayers with maximum fidelity. Due to the high density of dislocations in the III-nitride epilayers grown on Si(111) and small, high aspect ratio (height/width ~ 5) of the desired features, wet etch techniques remain generally unsuitable. Etching using plasmas containing halogen gases Cl_2 and BCl_3 mixed with Ar, or N_2 are known to etch nitrides at a rate of several hundred nanometers per minute in reactive ion etchers (RIE). The inert gases stabilize the plasma and contribute to physical etching or ion milling [124, 125].

In RIE, the sample is clamped to a DC-isolated electrode of a parallel plate capacitor which is fed several hundred watts of power at radio frequencies of ~ 13 MHz. In the resulting plasma, the light, mobile electrons strike the sample and a charge builds up on the surface due to the DC isolation of this electrode. This charge generates a DC bias of several hundred volts between the positively charged plasma and negatively charged sample which promotes the physical bombardment of the wafer surface with chemically and non-chemically reactive ions. By adding a second RF coil to generate the plasma, inductively coupled plasma reactive ion etching (ICP-RIE) improves upon the RIE technique by allowing independent control of the plasma density and kinetic energy of ions striking the surface. ICP-RIE etching utilizing Cl_2 and BCl_3-based plasmas yield the highest etch rates and best anisotropic etch profiles in III-nitride materials [126].

A Cl_2/N_2 plasma in EPFL's Sentech ICP-RIE SI 500 etcher was used to etch all optical nanocavities in this thesis. This etcher's unique design feature is a planar triple spiral antenna for the ICP plasma generation, which supposedly results in a low average and narrow ion energy distribution ideal for etching nanostructures [127]. The recipe employed in this thesis yields an etch rate of 75-80 nm/min and etch selectivity better than 8 of GaN over HSQ. However, the quoted etch rate is for an isolated, external dimension.

A small, internal dimension like a sub-100 nm diameter hole etches slower and exhibits a different sidewall profile due to the aspect ratio dependent etching phenomenon: as the feature size decreases and/or aspect ratio increases, the etch rate slows because of transport of reactive ions to the etched surface and neutral byproducts away from the etched surface can be hindered by gas-phase collisions, surface scattering, and surface charging [128]. Fig. 3.4 shows the etch rates of slits and holes normalized by the etch rate of 78 nm/min. One sees that
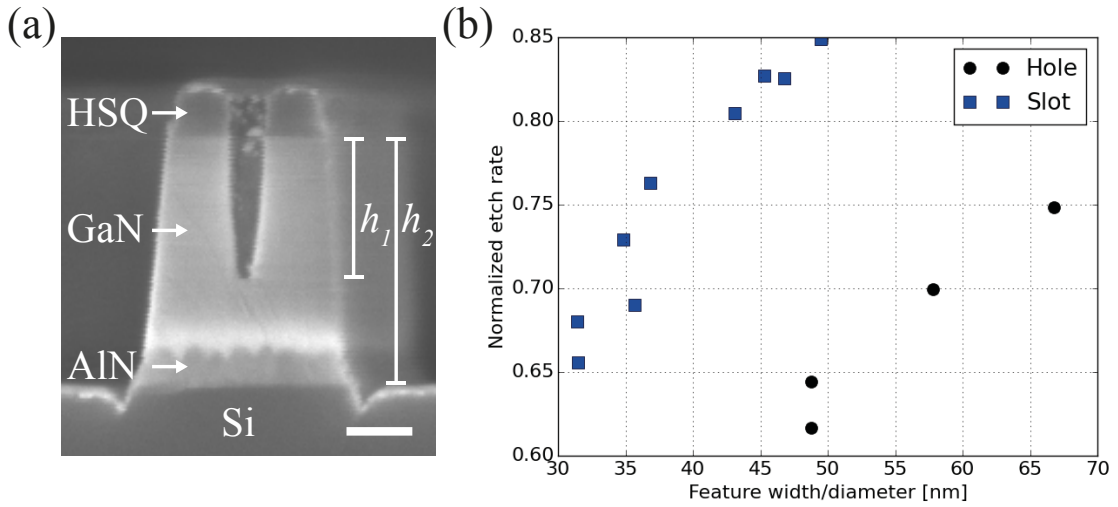
(a)

(b)

Figure 3.4: Normalized aspect-ratio dependent etch rates (h_1/h_2) for sub-100 nm width slots and holes during ICP-RIE etching. (a) SEM cross-section of cleaved etch test structure coated with 5 nm of gold to improve conductivity. Scale bar is 100 nm (b) Normalized etch rate for slot and hole etch test structures as a function of width.

as the dimensionality and the width of the feature decrease, the relative etch rate decreases. The solution to this dilemma is to increase the etch time such that the holes are etched fully through the III-nitride epilayers. Consequently, the external dimensions are overetched into the silicon substrate and a thicker resist/hard mask is required.

3.1.4 Air gap creation

After pattern transfer, the optical nanocavity is suspended in air in order to eliminate the parasitic coupling losses between the resonating optical mode and the absorptive silicon substrate. Ideally, such an etch would be entirely chemical in nature, eliminating additional etch damage from ion bombardment during dry etching while promoting a nearly infinite selectivity of silicon to III-nitrides. The XeF$_2$ vapor phase etch meets these criteria. In such a pulsed process, evaporation of XeF$_2$ crystals generates fluorine gas [129], which attacks silicon but leaves III-nitrides untouched. Nitrogen purges between cycles clear reaction byproducts.

XeF$_2$ vapor phase etching has several advantages over silicon removal in a fluorine-based ICP(-RIE) process. First, the etch is more isotropic, leading to shorter process times required to remove all material beneath a nanostructure. Fig. 3.5 reveals the anisotropic nature of selective SF$_6$-based plasma etching of silicon in the Oxford ICP etcher in EPFL's III-V cleanroom. The silicon posts retain the square nature of the GaN pattern and the ratio of the vertical to horizontal etch rate is roughly four. More importantly, the ICP plasma damages the III-nitride nanobeam photonic crystal, resulting in sidewall waviness (Fig. 3.5(b)).

On the XeF$_2$ etcher at EPFL, the user controls the gas pressures, soak times, and number of

(a)

(b)
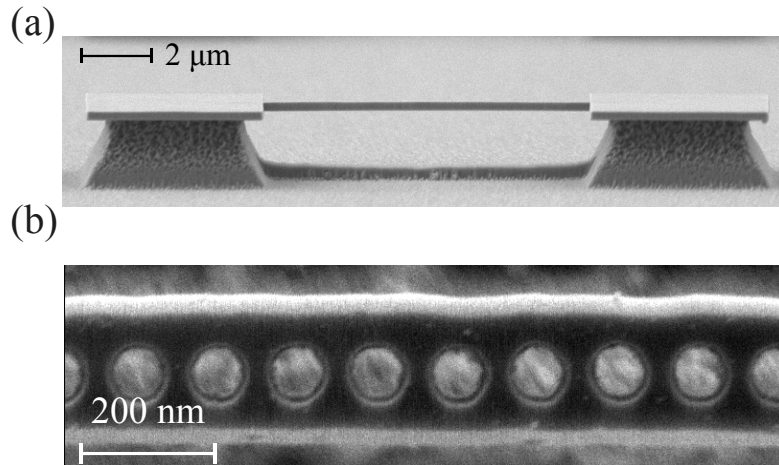
Figure 3.5: SEM images of nanobeams fabricated using ICP etching of silicon in a SF_6 plasma. (a) Side view revealing partially anisotropic nature of etch. (b) Top view showing sidewall damage of finished structure.

cycles to tune the process. As shown in Fig. 3.6(a), this process exhibits high selectivity of silicon over III-nitrides. Note how the membrane bends upward toward the edges due to the release of tensile strain created by lattice mismatch during epilayer growth. For an XeF_2 pressure of 2500 mTorr and soak time of 18 s, the ratio of the vertical to lateral etch rate is roughly one. The rough silicon surface results from the anisotropic etch rate of silicon in XeF_2 for different crystal orientations. By proper sizing of bowtie-like anchor pads (Fig. 3.6(b)), the desired air gap can be created beneath the nanocavity to isolate the optical mode. Two silicon posts beneath two $5 \times 5 \ \mu m^2$ support pads mechanically support the membrane and maintain uniaxial tensile strain (Fig. 3.6(b)).

3.1.5 Cleaning and passivation

To complete the structures, the residual HSQ resist is stripped in 49% BHF acid and the surface is then cleaned and passivated. For instance, BHF etching leaves behind fluorine ions adsorbed on the nitride surface [130]. Additionally, the ICP-RIE etching may damage and embed ions in the III-nitride material [131, 132]. A variety of techniques were used in this thesis to clean and manipulate the nanocavity surface. Please see Section 5.5 for more details.

3.2 Characterization

This section details the techniques utilized to characterize the photonic nanocavities. Atomic force microscopy (AFM) and scanning electron microscopy (SEM) reveal the surface roughness and geometry of the finished structures, while spectroscopic ellipsometry measures the thicknesses and refractive indices of the various epilayers. As we are primarily interested in the optical properties of III-nitride optical nanocavities, the primary characterization methods
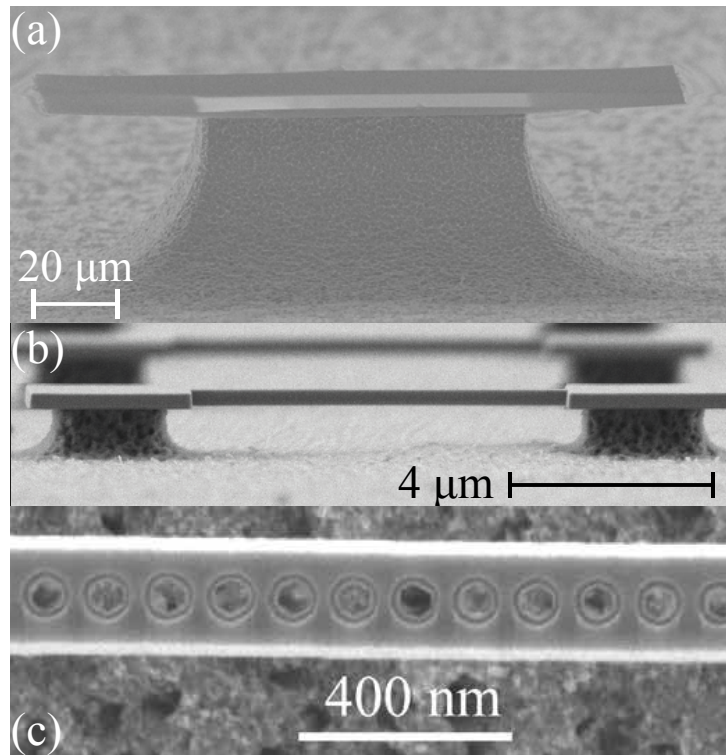
Figure 3.6: SEM images of air-suspended III-nitride structures created by XeF$_2$ vapor phase etching. (a) Air-suspended epilayer membrane created by 35 μm of lateral silicon under etch without affecting the epilayers. (b) Nanobeam photonic crystal with air gap. (c) Top view showing straight, undamaged sidewalls. The remaining silicon surface is rough due to etch rate anisotropy on different crystal orientations but this roughness does not affect optical performance because the air gap is more than 800 nm.

are comprised of optical techniques. One of the main tasks of this thesis was to construct a new optical laboratory for characterization of nanocavities and single photon emitters. Thus, extra space is allocated to document the design and capabilities of the setup.

3.2.1 Scanning electron microscopy

Due to the optical diffraction limit (Eq. 3.1), nanocavities with sub-100 nm dimensions cannot be visualized by conventional optical microscopy. Again, the use of electron-based techniques allows an increase in the optical resolution to a few nanometers. A scanning electron microscope resembles the electron beam lithography system depicted in Fig. 3.2, with a few important differences. First, the specimen-dependent acceleration voltage is much lower to increase sensitivity to the surface. Second, the laser interferometer stage is not necessary, as samples are examined with the stage locked in position. Third, the beam blanker is eliminated and the beam is continuously scanned in a raster pattern. The incident electrons may be scattered, generate secondary ionized and/or Auger electrons, or create X-rays as a function of the position. Different information can be extracted from different particles at various detection angles [133].

SEM images of III-nitride-based nanostructures depicted in this thesis were acquired using a Zeiss Merlin SEM [134]. The Gemini II column was operated in high resolution mode with an accelerating voltage of 3 kV. Unless otherwise noted, the in-lens secondary electron detector was used to maximize the system's spatial resolution and sensitivity to the sample surface. Fig. 3.7 shows a side-by-side comparison of the same sample imaged with the Merlin and a Jeol
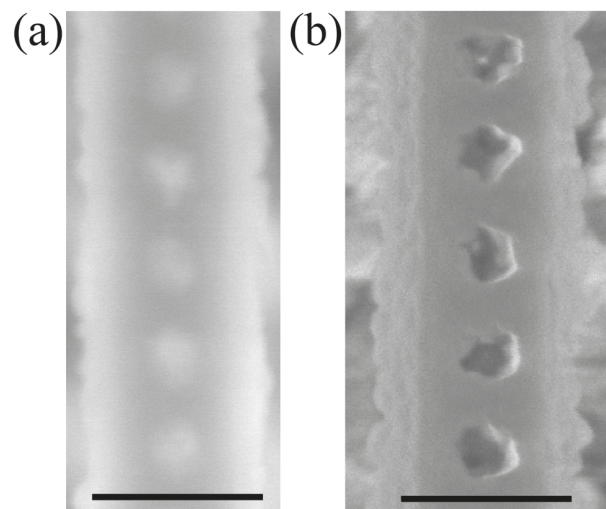
Figure 3.7: The same nanobeam photonic crystal imaged with (a) Jeol JSM-6701 and (b) Zeiss Merlin SEMs at 3 kV with in-lens detection in both cases. Scale bars are 200 nm. The nanobeam photonic crystals have been exposed to O_2 at 850 °C for more than 60 minutes.

JSM-6701F SEM at 3 kV with in-lens detection. The Merlin images exhibit higher contrast and surface sensitivity under similar conditions, likely due to the reconfigurability of the electron

optics in the Gemini II column.

3.2.2 Cathodoluminescence

Excitation by electron beams in a SEM may also generate luminescence from the sample under study. As a primary electron whizzes by the sample with several keV of kinetic energy, the Fourier transform of the transient electric field seen by the sample contains frequency components up to several tens of eV. Therefore, an electron beam may act as a broadband illumination source, perfect for the study of wide band gap semiconductors for which no above gap laser source may be available. Additionally, the size of the excitation spot remains far below the optical diffraction limit. By raster scanning the electron beam and dispersing the cathodoluminescence signal from each point in a spectrometer, so-called hyperspectral images can be created where each pixel in an image contains an entire spectrum. In this thesis, cathodoluminescence mappings were used to measure the profile of optical nanocavity modes with resolution exceeding the diffraction limit using a prototype cathodoluminescence system (Attolight SA). Beyond such rapid measurements, this technique's utility is limited in this thesis due to rapid degradation of the optical modes caused by charging and deposition from the electron beam. For more details on the cathodoluminescence setup, please see [135]. All cathodoluminescence measurements in this thesis were conducted by Dr. Gwénolé Jacopin.

3.2.3 Atomic force microscopy

AFM is used to map the spatial topography of a sample with atomic resolution. The AFM technique, invented in 1986 by IBM researchers [136], relies upon a raster scanning a piezoelectrically-driven vibrating cantilever with an atomically sharp tip across the sample surface. The beam deflection is measured by a laser beam reflected off the back surface of the cantilever and centered on a four-quadrant photodetector. At tip-sample distances between 1-10 nm, the tip-sample force is attractive due to Van der Waals interactions. At shorter distances, the force is repulsive due to physical contact between the two surfaces.

AFM images in this thesis are measured using a Bruker FastScan AFM head and Bruker FastScan A cantilevers operating in the manufacturer's proprietary PeakForce® tapping mode. In the conventional tapping mode, the most common AFM operating mode, the vibrating tip is driven slightly off-resonance and lowered until it is in periodic contact with the surface under investigation [137]. A feedback loop changes the cantilever vertical position to maintain the same oscillation amplitude. Topographical information can be extracted from the cantilever vertical position and relative phase between the piezoelectric driving and photodetector signals. PeakForce® mode is a variation on tapping mode where the maximum force value is the feedback loop control parameter. According to the manufacturer, maintaining forces below 10 pN with an active feedback loop increases tip life and image fidelity while minimizing damage to the sample surface [138].

3.2.4 Spectroscopic ellipsometry

Spectroscopic ellipsometry is an optical technique used to measure the thicknesses and optical properties of thin film stacks. The measurement apparatus is straightforward: a beam of circularly or elliptically polarized light is specularly reflected from the sample surface. A second, optional waveplate and rotating polarizer measures the rotation of the polarization ellipse by the sample. The result is a measurement of the ratio of the complex reflectivity for p- and s-polarized light from the sample surface,

$$\frac{r_p}{r_s} = \tan(\Psi)e^{i\Delta} \qquad (3.4)$$

where $\tan\Psi$ is the amplitude ratio and Δ is the phase difference between the s and p reflection coefficients. Spectroscopic ellipsometers measure Ψ and Δ as a function of illumination wavelength, either using monochromatic illumination and point-by-point measurement or using white light illumination and dispersing the reflected light in a spectrometer. The difficult part of the technique is fitting the measured data to a physical model of the thin film stack for layer thicknesses and refractive indices [139].

The epilayer stack (Fig. 3.1) is modeled using a look-up table for the silicon substrate [140] and empirical Cauchy dispersion models for each of the aluminum nitride and gallium nitride layers at energies less than 3.1 eV, e.g. below both the GaN and AlN bandgaps where no absorption is expected,

$$n(\lambda) = C_1 + C_2/\lambda^2 + C_3/\lambda^4. \qquad (3.5)$$

Material	C_1	C_2 (μm^2)	C_3 (μm^4)
GaN	2.267	2.13×10^{-2}	3.85×10^{-3}
AlN	2.19	2.72×10^{-3}	–

Table 3.1: Cauchy model parameters deduced for III-nitride epilayers grown on silicon (111) from fitting between 3.0 and 1.4 eV to spectroscopic ellipsometry data. GaN's ~ 2% relative birefringence in the blue spectral range [88] is ignored in all subsequent modeling efforts.

The thicknesses of the materials are determined to within a few nanometers by SEM cross-section of cleaved samples, leaving only the constants C_1, C_2, and C_3 to be determined for each of gallium nitride and aluminum nitride (Fig. 3.8 & Table 3.1). Compared to the literature [141], the MOVPE-grown AlN films used in this thesis have higher refractive index. This is likely due to the differing growth techniques as well as the proximity to the silicon substrate for the MOVPE-grown films, which results in diffusion of Si into the AlN layer (Fig. 5.9).
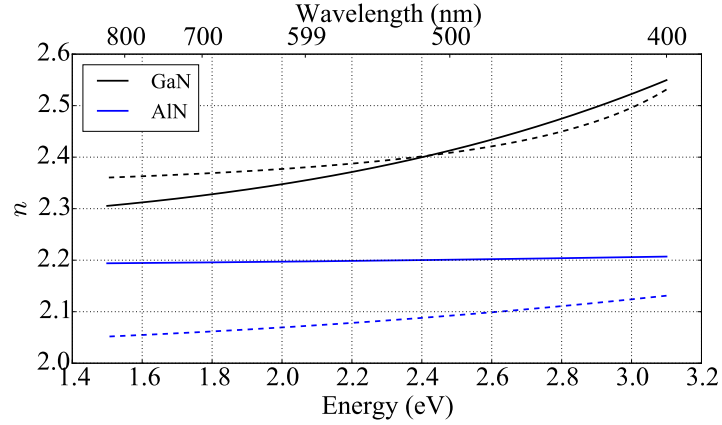
Figure 3.8: Dispersion of the refractive index of the thin III-nitride epilayers grown on silicon following the Cauchy model (solid lines) compared to the literature (dashed lines) for strain-free epilayers grown on a buffer on silicon by molecular beam epitaxy [141]. The wafer-to-wafer reproducibility for the films utilized in this thesis is < 1%.

3.2.5 Raman spectroscopy

In the Raman spectroscopy of semiconductors, light is inelastically scattered by optical phonons. Due to energy conservation, the laser photons are shifted in energy, giving rise to a unique spectral fingerprint of the sample [142]. In semiconductors, Brillouin zone center optical phonons are probed by first-order Raman processes. When a phonon is added to the sample, the scattered light is redshifted relative to the excitation line (Stokes scattering). When a phonon is absorbed from the sample, the scattered light is blueshifted relative to the excitation line (anti-Stokes scattering). We work with Stokes scattered light, whose intensity is higher than the anti-Stokes lines because of the negligible population of optical phonons in III-nitrides (92 meV) at room temperature (26 meV). The crystal symmetry and experimental geometry determine allowed Raman optical transitions [20].

First-order Raman transitions are weak processes. They are described by third-order time-dependent perturbation theory in Schrödinger's equation and the process is therefore proportional to the sixth power of the interaction Hamiltonian, or the third power of the excitation intensity [142]. Therefore, modern Raman spectrometers use filtered monochromatic laser illumination to achieve appreciable signal. The Institute of Physics at EPFL owns a commercial confocal Raman microscope with 800, 532, 488, and 405 nm laser sources and a spectral resolution of around 1 cm^{-1} [143]. Accordingly, in this thesis, we work in the backscattering geometry ($Z(x,x)\bar{Z}$ or $Z(x,y)\bar{Z}$), where either the co-(x,x) or cross-polarized (x,y) incident and scattered radiation are detected along the same optical axis (Z).

For III-nitrides, subtle peak shifts provide information about the composition, local strain, lattice quality, temperature, and coupling to free carrier plasmons. In the backscattering experimental geometry, only the E_2 and $A_1(LO)$ modes are allowed [144, 145]. Fig. 3.9 shows a confocal Raman spectrum of the thin biaxially strained III-nitride epilayers grown on silicon

Material	Mode	$\tilde{v}_0$ (cm^{-1})	a_λ (cm^{-1})	b_λ (cm^{-1})	c_λ (cm^{-1})
GaN	E_2^L	144	208(36)	-199(33)	--
GaN	E_2^H	567.6	-911(54)	-852(76)	--
GaN	$A_1(LO)$	734	-860(85)	-1042(111)	--
AlN	E_2^H	657.4	-1092(91)	-965(101)	--

Table 3.2: Characteristic phonon modes and deformation potentials for III-nitride Raman-active phonons visible in the $Z\bar{Z}$ experimental configuration [145–147]. Parentheses contain ± error bars.

(111) in the $Z\bar{Z}$ geometry. A 10 μm air gap underneath the structure combined with the
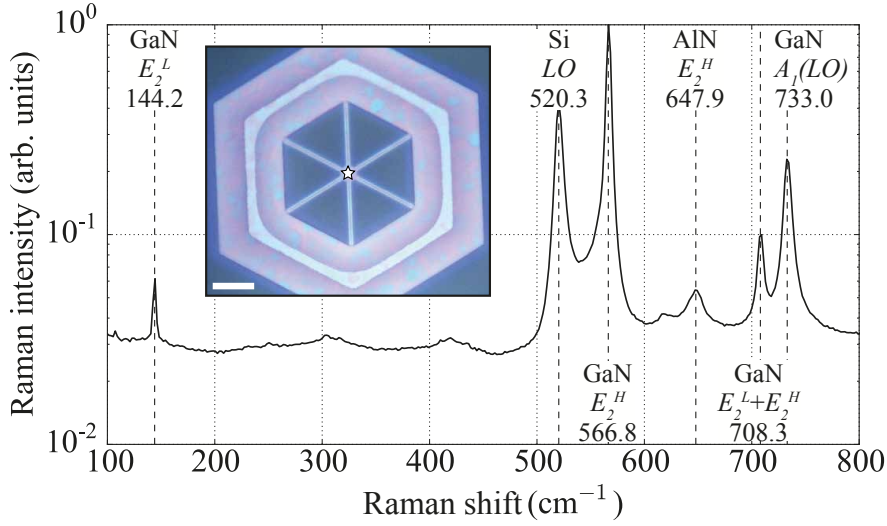
Figure 3.9: Confocal Raman spectrum of a biaxially strained GaN membrane (inset) with a 10 μm air gap recorded with a 532 nm laser and a 0.95 NA, 100× objective. Star shows the laser spot location during the measurement. Scale bar is 10 μm. Error bars on the peak locations are ±0.5 cm^{-1}.

confocal detection results in the relative attenuation of the silicon substrate's LO phonon mode, which is normally stronger in intensity than the III-nitride modes. Furthermore, the large air gap and high numerical aperture of the microscope objective drop the background signal low enough such that the peaks from the 45 nm thick AlN film become visible. The origin of the mode at 708 cm^{-1} is presently unknown; its energy is consistent with the GaN harmonic, $E_2^H + E_L^2$ and this mode is observed only in nanostructures with a large air gap beneath.

The Raman shifts ($\Delta\tilde{v} = \tilde{v} - \tilde{v}_0$) from the equilibrium mode positions can be converted to stress (σ) using the deformation potentials (a_λ, b_λ, c_λ) (Table 3.2), Eqs. 3.6-3.7 [146, 147]

$$\Delta\tilde{v}\big(A_1(LO)\big) = a_\lambda(A_1)\big(\epsilon_{xx} + \epsilon_{yy}\big) + b_\lambda(A_1)\epsilon_{zz}, \tag{3.6}$$

$$\Delta \tilde{v}(E_2) \quad = \quad a_\lambda(E_2)\big(\epsilon_{xx} + \epsilon_{yy}\big) + b_\lambda(E_2)\epsilon_{zz} + c_\lambda(E_2)\sqrt{\big(\epsilon_{xx} - \epsilon_{yy}\big) + 4\epsilon_{xy}^2}. \tag{3.7}$$

and a conversion of the stress (ϵ) to strain using Hooke's law under the appropriate boundary conditions (see Section 2.4.3). As some deformation potential coefficients for III-nitrides have not yet been measured, we use the E_2 value for wurtzite CdS, $c_\lambda(E_2) = 107$ cm^{-1}[148], when treating uniaxial strain in Section 4.3. Both the E_2^H and $A_1(LO)$ modes serve as effective strain sensors because their deformation potentials are strong. The combination of Eqs. 2.18-2.20 with 3.6-3.7 leads to the following expressions for the linear dependence of the shift rate with strain

$$\Delta \tilde{v}^u\big(A_1(LO)\big) \quad = \left[(1 - C_0)a_\lambda\big(A_1(LO)\big) - b_\lambda\big(A_1(LO)\big)\frac{C_{13}}{C_{33}} \right] \epsilon_{xx}^u, \tag{3.8}$$

$$\Delta \tilde{v}^u\big(E_2^H\big) \quad = \left\{ (1 - C_0)\left[a_\lambda(E_2^H) - b_\lambda(E_2^H)\frac{C_{13}}{C_{33}} \right] + c_\lambda(E_2^H)(A + 1) \right\} \epsilon_{xx}^u, \tag{3.9}$$

$$\Delta \tilde{v}^b\big(A_1(LO)\big) \quad = 2\left[a_\lambda\big(A_1(LO)\big) - b_\lambda\big(A_1(LO)\big)\frac{C_{13}}{C_{33}} \right] \epsilon_{xx}^b, \tag{3.10}$$

$$\Delta \tilde{v}^b\big(E_2^H\big) \quad = 2\left[a_\lambda\big(E_2^H\big) - b_\lambda\big(E_2^H\big)\frac{C_{13}}{C_{33}} \right] \epsilon_{xx}^b, \tag{3.11}$$

where the subscripts u and b stand for uniaxial and biaxial strain, respectively. As a reminder, C_0 is related to the elasticity constants by Eq. 2.19 The shift to lower wavenumbers is indicative of the tensile strain expected for growth on silicon (Section 2.4.2). Further quantitative analysis of Fig. 3.9 is deferred until Section 4.3, which compares the strain state of as-grown epilayers with uniaxially strained, biaxially strained, and free-standing microstructures.

3.2.6 Optical laboratory construction

A new laboratory was built for optical characterization of III-nitride nanoscale light emitters. The application requires operation wavelengths from the shortest available pump laser (244 nm) to the blue-green luminescence of InGaN/GaN quantum wells (500 nm), positioning precision and reproducibility less than 1 μm, maximum possible light collection efficiency, spectral resolution down to 100 μeV, temperature control down to 4 K, controllable measurement atmosphere capable of high vacuum ($< 10^{-6}$ mbar), time-correlated single photon counting with maximum possible detection efficiency and temporal resolution, and automated measurement routines for drift-compensation, polarization-, power-, and time-dependent series. The purpose of this section is to document the setup's design, capabilities, and limitations for future users.

The heart of the setup is a Cryostation C2 from Montana Instruments, Inc., a closed cycle helium cryostat capable of cooling from room temperature to 4 K in around three hours. Inside the sample chamber (Fig. 3.10) is a three-axis piezoelectric positioning stack (2 × ANPx101/RES, 1 × ANPz101/RES from Attocube GmbH) with resistive encoders from Attocube
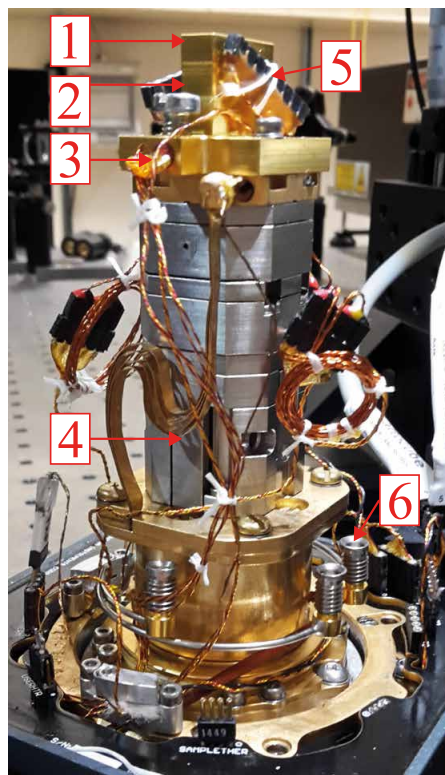
Figure 3.10: Sample holder and piezoelectric stack of the Cryostation C2 from Montana Instruments with custom modifications. (1) Removeable copper bar for gluing sample. (2) Custom sample holder. (3) Sample heater up to 3 W. (4) Attocube ANPz101/RES positioner. (5) 16 DC electrical feedthroughs going to banana connector box. (6) 4 RF feedthroughs leading to SMA connectors.

Systems AG for rough sample positioning with 5 mm overall travel in each axis. Because the thermal conductivity of the titanium piezoelectric stack is poor at low temperature, Montana Instruments engineered a thermal link to transfer heat from the sample to the cold finger. We re-engineered the sample holder, the top portion of the stack, to be more flexible for our needs. The new sample holder is machined out of copper and electroplated with 5 microns of nickel and 20 microns of gold (Collini GmbH). We also added a custom cartridge heater inside a transverse hole within the sample mount for faster temperature sweeps above 70 K. Samples can be mounted in one of three ways: a 4.8×3.2 mm^2 sample can either be glued in a ceramic DIP package and clamped for electrical contacting via sixteen DC electrical feedthroughs or all-optical characterization can be carried out on a maximum 8×8 mm^2 piece by gluing the sample to a copper bar and then fastening the bar to the sample holder. The final option would be to bond the chip to a printed circuit board with the correct hole spacing for high-frequency electrical characterization via four RF feedthroughs.

The vacuum system of the stock Cryostation was modified to enhance the system's performance. After cryo-gettering on the sample surface was observed , a turbomolecular pump (Pfeiffer Vacuum GmbH) was added through a window port to complement the built-in cryopumping. The cold cathode vacuum gauge, mounted adjacent to the sample chamber, registers pressures as low as 2.5×10^{-7} mbar at 5 K. Therefore, the chamber pressure must be lower than this value due to cryopumping. At room temperature, a continuous gas flow can be set up in the chamber by manually regulating a needle valve for the gas input and a butterfly valve between the vacuum gauge and turbomolecular pump (Fig. 3.11, V). This configuration solves the deposition problem, enabling long integration time measurements such as time-correlated single photon counting.

A custom UV photoluminescence microscope was built on a breadboard (Fig. 3.11). The pump lasers (Table 3.3) are in-coupled by a rail, periscope, and beamsplitter B1 (50:50 broadband or dichroic 325 and 355 nm mirrors). Two beamsplitters (B2 & B3) mounted in a beam offset compensating geometry can be flipped into the beam line in order to visualize the laser position on the sample. Beamsplitter B2's arm contains a lamp illumination in the Köhler configuration and beamsplitter B3's arm contains a tube lens and CCD camera. All light is reflected downward on mirror M1 toward the low working distance viewport on the Montana Cryostation. A $20\times$ NA= 0.4 UV focusing objective (Thorlabs Inc.) is mounted on a PI xy piezo scanning stage with 100 μm travel and sub-micron positioning repeatability, which in turn is mounted on a vertical translation stage. The sample photoluminescence is collected in the backscattering geometry, and propagated back toward the beamsplitter B1, where it is sent to one of two detection arms by the selection of a flip mirror (M2).

Microphotoluminescence (μPL) spectroscopy

The first detection arm is comprised of a Horiba Jobin-Yvon FHR 640 spectrometer and Symphony II liquid-N$_2$ cooled CCD. This 640 mm focal length single-pass spectrometer is equipped with 150, 1800, and 3600 lp/mm gratings and has a resolution limit of 9 pm or 80
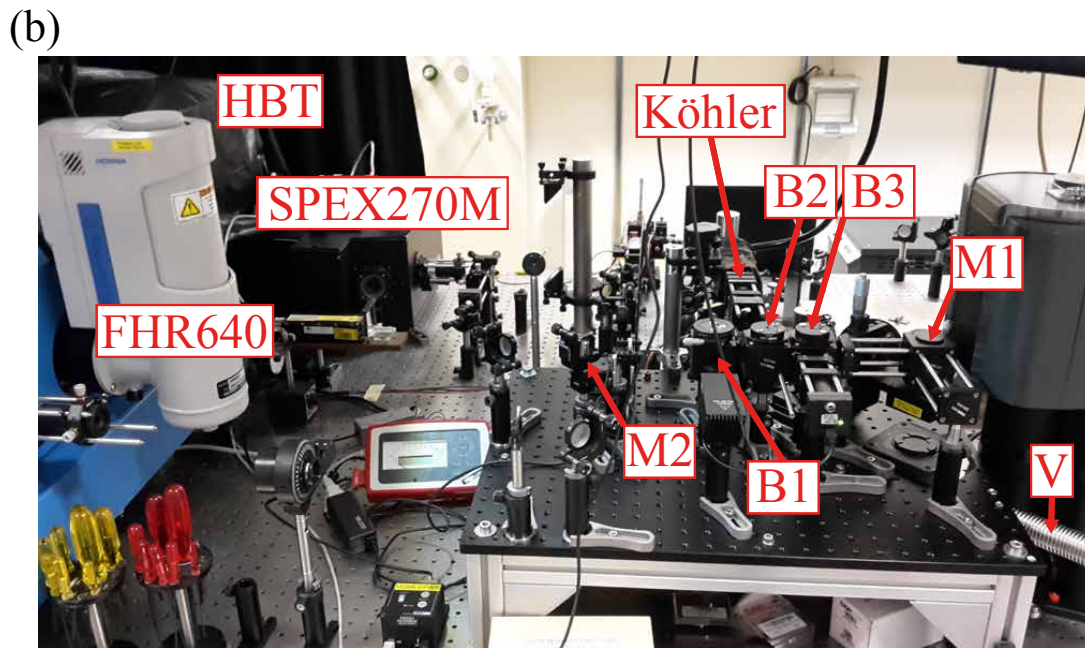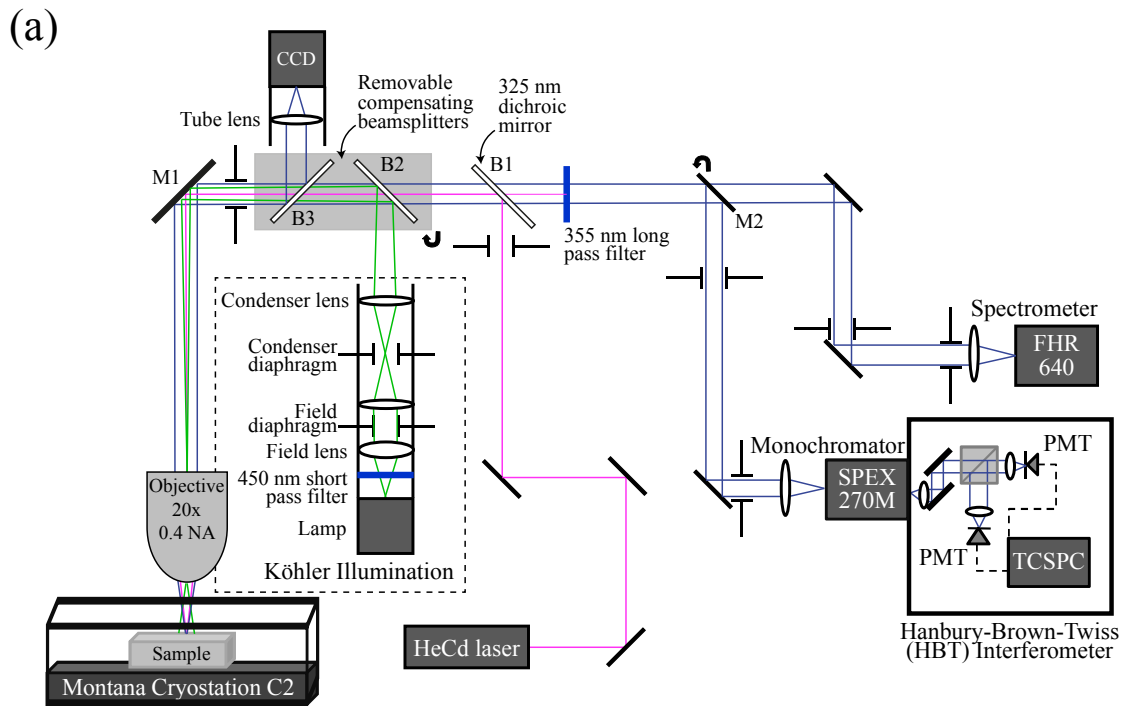
Figure 3.11: (a) Schematic and (b) image of custom UV fluorescence microscope. See text for description.

Output λ (nm)	Manufacturer	Model	Power (mW)	Technology
244	Spectra-Physics	Wavetrain	70	2× 488 nm
266	CryLas	FQCW266	100	4× 1064 nm Nd:YAG
325	Kimmon	IK3101R-D	7	HeCd gas
355	Cobolt	Zouk	20	3× Nd:YAG
375	Spectra-Physics	Excelsior	70	laser diode
405	Coherent	Radius	50	laser diode
488	Coherent	Genesis CX	2000	optically pumped semiconductor

Table 3.3: List of lasers available for cw optical pumping.

μeV Hg line of 435.83 nm / 2.845 eV (Fig. 3.12) for the 3600 lp/mm grating in first-order. The
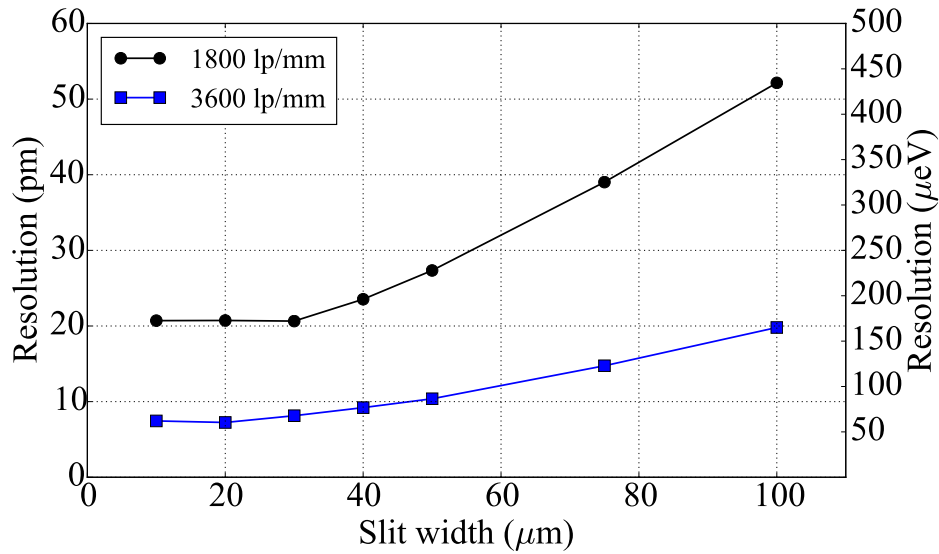
Figure 3.12: Spectral resolution of the Hg(I) line at $\lambda = 435.83$ nm as a function of slit width for the 1800 and 3600 lp/mm gratings in the FHR 640 spectrometer. linewidths extracted from Gaussian line shape fits.

optimum resolution is achieved by correctly choosing the in-coupling lens focal length (f_2) such that the grating is fully illuminated. Since we are working with an infinite conjugate ratio objective, the back aperture of the microscope objective has $d = 8$ mm diameter, and the input aperture of the FHR 640 is $F/\# = 5.5$, then the optimum focal length of the in-coupling lens is $dF/\# = 44$ mm. The closest available UV fused silica commercial lens is a 25 mm diameter, $f_2 = 50$ mm lens. The magnification of the system is given by the ratio of the focal length of the in-coupling to the effective focal length of the objective lens, $M = f_2/f_1 \sim 5$ for the selected parameters. Finally, the resolution with the 3600 lp/mm grating in first-order or the 1800 lp/mm grating in second-order is adequate for Hakki-Paoli measurements of gain in III-nitride laser diodes.

By programming the synchronous operation of the PI scanning stage and Symphony CCD in LabView, hyperspectral mapscans can be performed. In this context, hyperspectral means that each pixel in a raster scan contains a μPL spectrum, creating a three-dimensional data set (x, y, energy/wavelength). For samples with a short minority carrier diffusion length such as III-nitrides on silicon [149], the spatial resolution of the microscope[3] is dictated by the size of the focused pump spot on the sample. Ideally, the minimum spot size should be given by the diffraction limit, $\lambda/(2\,\text{NA})$ or about 400 nm for the available pump lasers. However, real world non-idealities, such as dust on optics, the objective's geometrical aberrations, and nonideal laser beam profiles ($M^2 > 1$) increase the spot size. Fig. 3.13(a) shows the integrated
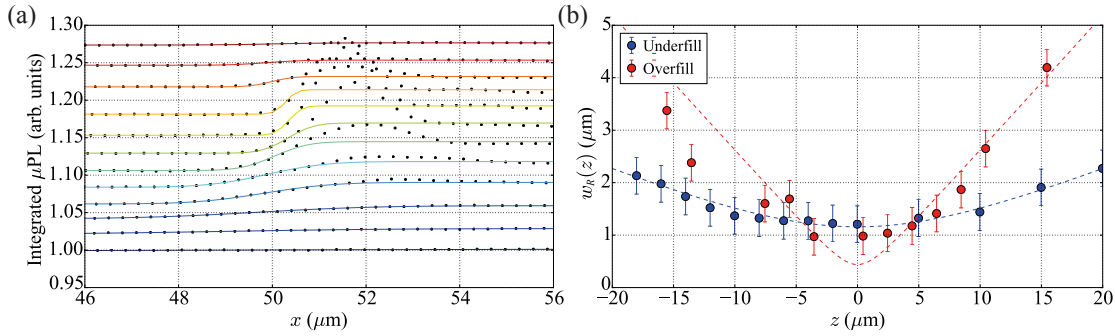
Figure 3.13: (a) Integrated InGaN/GaN quantum well μPL dispersed with a 150 lp/mm grating as the 355 nm laser (black) is scanned across a lithographic step edge. Colored lines show the fits to an error function. The peak for the in-focus data can be attributed to a thin film interference effect. (b) Extracted waist as a function of sample vertical position for (blue) underfilling and (red) overfilling the microscope objective's back aperture. Dashed lines are fits to Eq. 3.13.

μPL intensity as the 355 nm pump laser ($M^2 < 1.1$ [150]) is scanned over a lithographically patterned edge. Lines are fits to an error function. In Gaussian beam propagation, the FWHM is related to the beam waist (w_R) by

$$w_R = \frac{\text{FWHM}}{\sqrt{2\ln 2}}. \tag{3.12}$$

The extracted beam waists are then are plotted in Fig. 3.13(b) as a function of sample height (z) for cases where the 355 nm pump laser underfills (blue) and is beam expanded to overfill (red) the objective's back aperture. The dashed lines are fits assuming Gaussian beam propagation,

$$w_R(z) = w_0\sqrt{1 + \left(\frac{z}{z_R}\right)^2}, \tag{3.13}$$

where $z_R = \pi w_0^2/\lambda$ is the Rayleigh range [151]. We extract for $w_0 = 1.16\ \mu$m and 440 nm for the overfilled and underfilled case, respectively. As expected, w_0 is larger for the underfilled

---

[3]A spatial filter could be added to the detection line for confocal operation at the cost of attenuated μPL signal.

case due to the decrease in the effective numerical aperture of the objective. Using a Gaussian approximation to the Airy function and the Rayleigh criterion, $w_0 = 440$ nm corresponds to a resolution of 640 nm, which is commensurate with the diffraction limit for the objective, $1.22\lambda/(2\,\mathrm{NA}) = 540$ nm. Therefore, we conclude that the setup's spatial resolution is nearly diffraction limited.

Micro-Raman (μRaman) spectroscopy

Although the Institute of Physics at EPFL owns a commercial confocal Raman microscope (Section 3.2.5), use of the UV lasers in the μPL setup at LASPE for Raman spectroscopy is advantageous due to resonant enhancement of the signal for above band gap illumination.

The μPL setup can be quickly converted for μRaman measurements by inserting steep edge long pass filters in the detection line behind beamsplitter B1 (RAZOREDGE® from Semrock, Inc). Lasers for Raman scattering must be single mode so that the scattered light exhibits a well-defined Raman shift from a single laser line. Therefore, diode lasers are generally not appropriate unless special precautions (i.e. external cavity or distributed feedback grating) are taken to ensure single mode operation. Gas lasers' output must be spectrally filtered to eliminate any additional spectral lines in the measurement window. Filters are currently available for the 244, 266, 325, and 488 nm lasers. The 355 nm laser would be suitable as well with the purchase of an additional filter. Next, the Raman laser must be chosen in a spectral window where the sample exhibits little μPL. Otherwise, the Raman signal may be swamped by the μPL signal. Finally, if the selected laser's photon energy exceeds the band gap of the material under study, power-dependent measurements should be undertaken for two reasons: Raman lines may shift due to heating and the generation of free carriers [145, 152].

Time-correlated single photon counting (TCSPC) spectroscopy

The second detection arm contains a SPEX 270M monochromator with 2400 and 600 lp/mm gratings coupled to a Hanbury-Brown-Twiss (HBT) intensity interferometer (Fig. 3.14(a)). The resolution[4] versus slit width is given in Fig. 3.14(b) at 435.83 nm for an in-coupling lens focal length of $f_3 = 50$ mm, chosen using the same criteria as for the FHR 640. The ultimate resolution with the 2400 lp/mm grating is 100 pm or 280 μeV. The HBT intensity interferometer is comprised of a UV fused silica 50:50 polka dot beamsplitter (ThorLabs Inc.), chosen for its polarization-independent response, two UV-sensitive PMA 175 photomultiplier tube (PMT) single photon detectors, and a Picoharp 300 time correlator (Picoquant GmbH). When a single photon strikes the first PMT, a cascade amplification in the PMTs' dynodes sends a 10 nanosecond pulse of current down RF cables to the time correlator, which records the pulse's arrival time. This arrival event starts an internal stopwatch within the time correlator, which is stopped by the arrival of an electrical pulse from PMT 2. The time correlator then builds up a histogram of the delay in arrival times between the two PMTs. The measured histogram,

---

[4]Two identical Gaussian peaks become distinguishable when separated by a distance of one standard deviation.
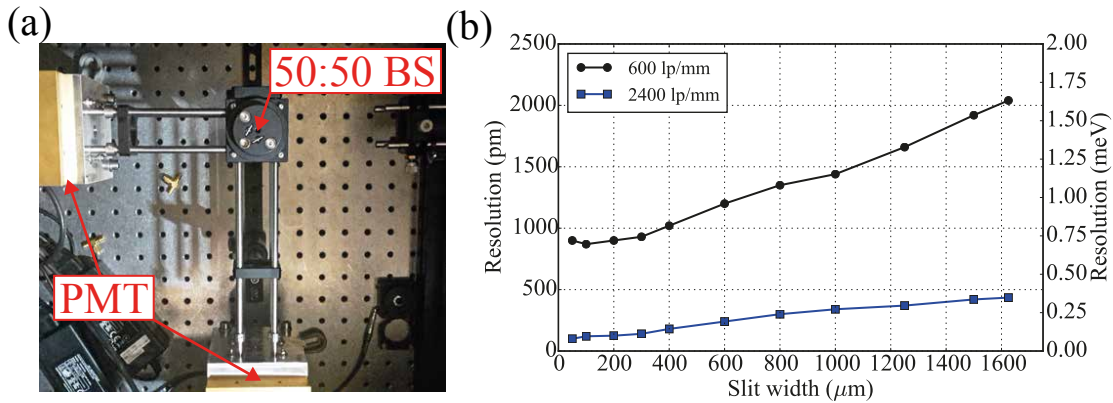
(a)

(b)

Figure 3.14: (a) The dark box (Fig. 3.11(a), top left)contains the Hanbury-Brown-Twiss interferometer, which is comprised of an outcoupling lens, polka dot 50:50 beamsplitter, and two photomultiplier tubes. (b) Spectral resolution of the Hg(I) line at λ = 435.83 nm as a function of slit width for the 600 and 2400 lp/mm gratings in the SPEX 270M monochromator as measured and analyzed by Dr. Gordon Callsen.

dubbed the intensity autocorrelation function or $g^{(2)}(\tau)$, where τ is the time delay, yields important information about the photon statistics of the emitting object [153].

The measured photon statistics are a convolution of the instrument response function (IRF) with the bare experimental $g^{(2)}(\tau)$. Thus, due to the Nyquist sampling theorem, photon statistics on timescales below the IRF are not recorded. Furthermore, the convolution with the IRF has the tendency to decrease the magnitude of any peaks or dips in $g^{(2)}(\tau)$ [154]. Because a single photon emitting light source exhibits $g^{(2)}(0) \leq 0.5$, $g^{(2)}(0)$ values reported in literature are frequently given for both the raw and deconvolved data, possibly including modeling of the effects of a broad μPL background, which further improves the fit $g^{(2)}(0)$ values. Therefore, the reader should appreciate that the deconvolution and modeling procedure is not standardized and therefore opens up the possibility for data manipulation to minimize the coveted $g^{(2)}(0)$ in publications.

Second, the time correlator exhibits a characteristic dead time < 95 nanoseconds following a photon arrival event. Therefore, it is important to maintain count rates far below the 200 ns width of the typical measurement time window, about 5×10^6 s^{-1} in order to avoid so-called pile-up effects where missed photons during detector downtime distort photon arrival time statistics [154]. Furthermore, count rates higher than 5×10^6 s^{-1} may destroy the PMTs [155].[5] Typically, for $g^{(2)}(\tau)$ measurements, the count rates of nanoscale light-emitters are in the 10^3-10^4 s^{-1} range, safely below this threshold. However, when working at higher count rates, one should attenuate the signal with a neutral density filter and verify that the measured $g^{(2)}(\tau)$ does not appreciably change. Pile-up effects are more important in time-resolved photoluminescence (TRPL) spectroscopy, where the object under study may be larger and

---

[5]Automatic closing of the PMT interlocks at high count rates has been implemented in the setup's LabView software combined with the LINX library and an Arduino microcontroller.

brighter than a quantum dot or photonic crystal cavity.

cw TCSPC measurements pose strict requirements on the coherence time of the pump laser. The ideal relationship between Lorentzian-broadened linewidth (ν_l) and $g^{(2)}(\tau)$ is [153]

$$g^{(2)}(\tau) = 1 + |g^{(1)}(\tau)|^2 = 1 + e^{-2\nu_l \tau}. \tag{3.14}$$

It is desirable to use lasers approaching the theoretical ideal $g^{(2)}(\tau) = 1$ because, if the studied emitter's decay time is shorter than the width of the cw laser bunching peak, its photon statistics may follow those of the pump laser. From the $\tau_0 = 250$ ps temporal resolution of the detection, $\nu_l \ll 2/\tau_0 = 9$ GHz to remain below the detection limit. Therefore, $g^{(2)}(\tau)$ was measured for the pump lasers available at LASPE (Fig. 3.15). One sees that only the 244, 355,
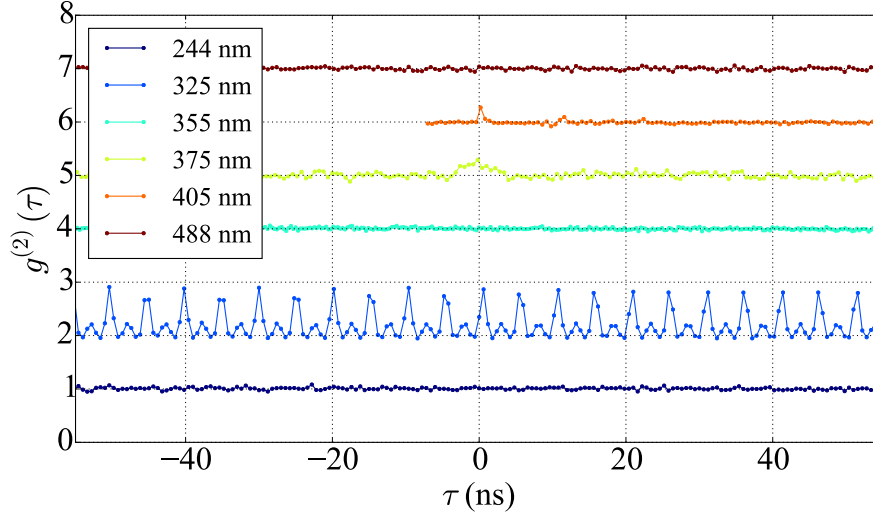
Figure 3.15: Photon statistics of the cw pump lasers available at LASPE (Table 3.3). $g^{(2)}$ functions are shifted for clarity and are not deconvoluted. The period of the oscillations in the 325 nm data corresponds to the optical cavity length.

and 488 nm lasers are suitable for optical pumping during $g^{(2)}$ measurements due to their ideal laser characteristic $g^{(2)}(\tau) = 1$.

Finally, as the $g^{(2)}(\tau)$ measurement time scales with the inverse count rate squared, overnight or multi-day measurement times may be required to generate high quality data. Such long integration times exacerbate real-world experimental issues. First, both the piezoelectric stages and laser position may drift. Automated repositioning routines have been implemented in LabView to tackle this problem. Second, the emission line under study may change in intensity, emission energy, or width due to deposition on the surface, charging, or photobleaching of the emitter [156]. Although the vacuum system greatly improves this situation, such effects remain sample and measurement condition dependent. Such effects are empirically observed to be worse for emitters close to the surface under high pump illumination intensities ($\sim$kW/cm^2) at short wavelengths (244 & 266 nm).

Time-resolved photoluminescence (TRPL) spectroscopy

The HBT apparatus can be converted into a single-color TRPL setup by a few simple modifications. First, one switches from cw to pulsed laser illumination. In LASPE, 266 and 355 nm pulsed lasers are available at 8 kHz repetition rates (Teem Photonics SA). In the TRPL configuration, instead of using PMT 1 to start and PMT 2 to stop the time correlator, PMT 1 is disconnected. In its place, a silicon photodiode (PHD-400-UV from Becker & Hickl GmbH) which is illuminated by a beam pickoff from the pump laser, starts the time correlator. The removal of the beamsplitter in the HBT box ensures that all TRPL photons are captured by the remaining PMT. In this configuration, an IRF response time (≤ 250 ps) can be measured (Fig. 3.16). The time correlator discriminators were set at -50 mV. The thin GaN epilayers on silicon
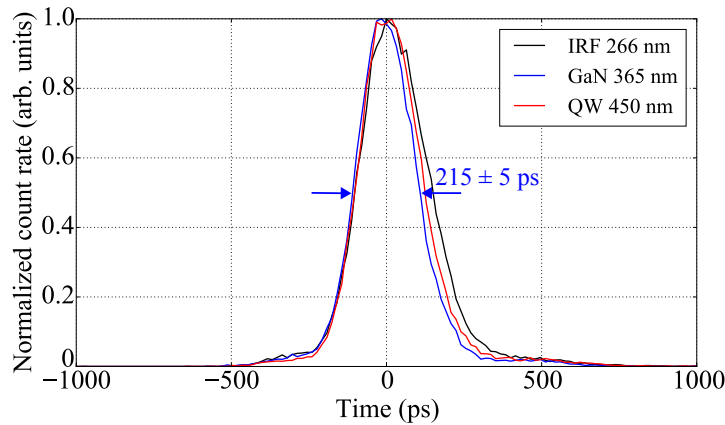
Figure 3.16: Spectral dependence of the IRF The measured response FWHM ranges from 215 ± 5 ($\lambda = 365$ nm) to 250 ± 5 ps ($\lambda = 266$ nm).

incorporating a single InGaN/GaN quantum well were illuminated at room temperature to find the spectral dependence, as these are known to have decay time constants ≤ 50 ps at room temperature (Section 5.4.2). Note that 250 ps is an upper bound on the time resolution of the PMT and time correlator electronics because the finite laser pulse width (450 ps) and photodetector rise time (≤ 200 ps) contribute to the overall, measured time response in the test configuration. Combined with the PMT's transit time spread of ≤ 180 ps and electrical resolution of ≤ 12 ps, the measured resolution of ≤ 250 ps are in reasonable agreement with the manufacturer's specifications.

Due to the relatively low repetition rate, high fluences are required to generate appreciable signal. Typical time-averaged powers should remain below 10 μW range in order to avoid heating and optical damage from the spatially and temporally focused pump laser. The modified HBT setup was not used for TRPL measurements in this thesis due to fast (~ 10 ps) nonradiative recombination in the thin III-nitride epilayers on silicon, even at cryogenic temperatures (Appendix A).

For time constants faster than the 200 ps time resolution of the HBT setup, a dedicated setup

in another lab is available which generates a polychromatic time-resolved measurement in a single shot. However, the cryostat in this setup vibrates and only coarse micropositioners are available. Therefore, this setup is only suitable for measurements on large features (> 50 μm). In this setup, the sample is excited by a few picosecond pulsed laser oscillator (Spectra-Physics) frequency tripled to 280 nm (GWU tripler) using a $80\times$, NA$= 0.55$ UV objective (Mitutoyo). The base frequency of 80.5 MHz can be lowered by use of a pulse picker. The TRPL is dispersed in a Jobin-Yvon iHR 320 spectrometer with 320 mm focal length and 300 lp/mm grating for a resolution better than 3 meV. A Hamamatsu C5680 streak camera synchronized to the laser oscillator detects the light for an overall temporal resolution of around 10 ps. For more details on this setup, see [135]. All streak camera measurements in this thesis were conducted by Dr. Gwénolé Jacopin.

3.2.7 Variable stripe length method

The variable stripe length technique is an all-optical gain measurement technique for unprocessed epilayers. In the variable stripe length method, the amplified spontaneous emission (ASE) from a cleaved facet is measured under intense, pulsed laser excitation. Two measurements are taken, one with a narrow strip of material of length L illuminated and the other with $2L$ illuminated, giving rise to two measured spectra $I_L(\lambda)$ and $I_{2L}(\lambda)$. The net modal gain, $G(\lambda)$, is then [157],

$$G(\lambda) = f_g g(\lambda) - \alpha(\lambda) = \frac{1}{L} \ln\left(\frac{I_{2L}(\lambda)}{I_L(\lambda)} - 1 \right), \tag{3.15}$$

where f_g is the fraction of the electromagnetic eigenmodes' electric field intensity that overlaps the gain region [32], $g(\lambda)$ is the material gain, and $\alpha(\lambda)$, is the internal loss.

Figure 3.17 describes the variable stripe length measurement apparatus. The 355 nm third harmonic of a < 200 ps pulse width, 8.1 kHz repetition rate Q-switched Nd:YAG laser (Teem Photonics SA) is $10\times$ expanded to produce a large, Gaussian excitation spot which overfills the cylindrical lens. An aperture blocks the edge of the beam, ensuring that the focused stripe has a homogeneous intensity along its typical excitation length of a millimeter. The waveguided PL within the sample epilayers is collected from a cleaved facet and coupled into an optical fiber for dispersion in a Jobin-Yvon iHR 320 mm focal length spectrometer. The sample and collection optics are mounted on a stage with a micropositioner in order to vary the stripe length without adjusting any optics.

A few aspects of the variable stripe length method require closer attention. First, diffraction from the aperture may result in inhomogeneous illumination, so the aperture needs to be mounted as close as possible to the sample. Second, although the choice of illumination spot size with length L and $2L$ leads to a simple analytical solution for the gain (Eq. 3.15), the two data points are sufficiently far apart such that gain saturation may occur [158]. Furthermore, if L is too small, then edge effects from the cleaved facet may be present. Therefore, it is
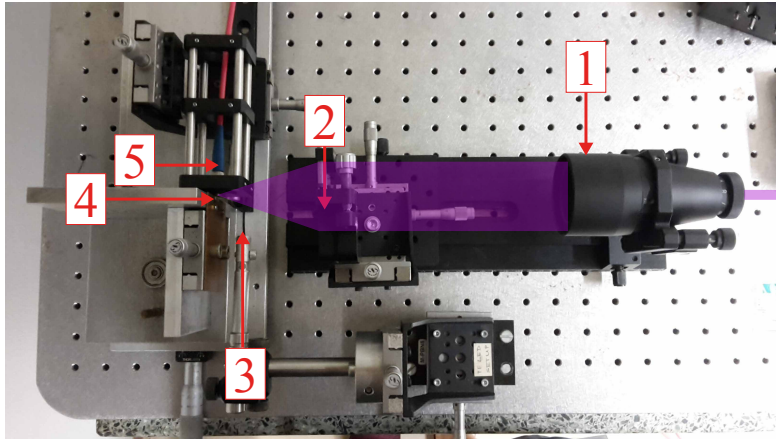
Figure 3.17: Picture of the variable stripe length measurement apparatus. A picosecond pulsed UV pump laser (shaded purple region) enters a beam expander (1) before being focused into a stripe by a (2) cylindrical lens and spatially filtered through a (3) slit. Waveguided photoluminescence from the (4) cleaved sample is collected from the side facet by an (5) optical fiber.

important to explore different L values, or to adopt illumination of stripe lengths L and xL, where $2 > x > 1$ and repeat the analysis to achieve consistent results [158].

3.2.8 "Old" μPL apparatus

Many of the measurements in Chapter 4 were completed before construction of the afore-mentioned optical laboratory. In this second, older μPL setup, the $\lambda = 351$ nm line of a cw Spectra-Physics argon ion laser was used for optical pumping. A Mitutoyo NUV 100×, NA=0.5 objective was used to focus the laser light to a spot FWHM of 1.8 μm and collect the μPL, which was sent through a 50:50 beamsplitter and 375 nm long pass dielectric filter (Edmund Optics, Inc.) before dispersion in a Jobin-Yvon $f = 550$ mm focal length spectrometer with a 2400 lp/mm grating and 50 μm slit width, yielding a spectral resolution of 33 pm (260 μeV) for the Hg(I) line at $\lambda = 435.83$ nm. Spectra were recorded by a Symphony II liquid-N$_2$ CCD in high sensitivity mode. The sample was mounted in an Oxford MicrostatHires cryostat maintained under vacuum levels better than 1×10^{-3} mbar during operation. Further details on the setup can be found in Ref. [159]. Any measurements in Chapter 4 reported using the now decommissioned 351 nm argon ion laser were by default done in the "old" setup, whereas all other measurements were done in the "new" laboratory.

3.3 Summary

This chapter described the experimental techniques necessary to grow, fabricate, and characterize quantum photonic devices based on III-nitrides operating in the blue and near-UV regions of the electromagnetic spectrum. Air-suspended optical nanocavities may be fabri-

cated using electron beam lithography and reactive ion etching from 300 nm thick III-nitride epilayers grown on silicon (111) substrates due to the availability of chemically selective etch processes to remove the silicon substrate. The fabricated nanocavities are inspected using atomic force and scanning electron beam microscopy. Their optical properties are primarily studied in a new laboratory constructed as part of this thesis. The quantum optical laboratory is designed for visible and near-UV spectroscopy of quantum dots and nano-optical resonators due to its high spectral resolution, collection efficiency, HBT interferometer, positioning stability, cryogenic operation, and vacuum system.

4 Nanobeam Photonic Crystal Cavities

This chapter focuses on single mode optical nanocavities based on the one-dimensional photonic crystal nanobeam geometry. First, we introduce the photonic crystal concept. Then, we calculate a nanobeam photonic crystal cavity's eigenmodes and eigenenergies using first-principles methods and demonstrate correspondence with experimental data. μRaman spectroscopy and finite element simulations help to examine the influence of strain on nanobeam geometry. Finally, we exploit the relationship between theory and experiments to answer two questions critical to the development of future quantum optical devices based on III-nitride materials: how can light efficiently be extracted from such structures and why is the experimental Q three orders of magnitude below the theoretical prediction? In the last section, we apply the lessons learned to demonstrate high-yield fabrication of photonic crystal nanobeam cavities with Q sufficient to achieve strong coupling in the blue spectral region.

4.1 Dielectric mirrors, waveguides, and cavities

Photonic crystals control the allowed directions and energies of light propagation using periodically patterned dielectric materials in one, two, or three dimensions. Ignoring the fact that photons are massless, neutral bosons while electrons are charged, massive fermions, one can draw parallels from the electronic band structure of crystals, such as band structure in momentum space. Such well-developed tools were readily transposed into the optics domain after the initial photonic crystal proposals by Yablonovitch [23] and John [24] in 1987, at which time it became apparent that evolving nano and microfabrication techniques may be capable of realizing such structures. Examples of photonic crystals abound in the natural world, such as the wings of the morpho butterfly and the peacock's feathers, where structured materials rather than pigments create bright, iridescent displays of light [160].

4.1.1 Bragg mirrors and cavities

The dielectric Bragg mirror is the simplest example of a one-dimensional photonic crystal. Dielectric mirrors are comprised of a $2N$-period repetition of a unit cell of two materials with thicknesses d_i and d_j and refractive indices $n_{1,i}$ and $n_{1,j}$. At each interface, part of the incident plane wave is back-reflected at each interface. The choice of the thicknesses, $n_{1,i}d_1 = n_{1,j}d_2 = \lambda_0/4$ (Fig. 4.1(a)) maximizes the destructive interference of the forward propagating wave (Fig. 4.1(c)), creating a high reflectivity "stop" band or *photonic band gap* of spectral width [19]

$$\Delta E = \frac{4E_0}{\pi} \cdot \sin^{-1}\left(\frac{|n_{1,i} - n_{1,j}|}{n_{1,i} + n_{1,j}}\right), \tag{4.1}$$

at normal incidence, where $E_0 = hc/\lambda_0$ is the photon energy, for large N values [19]. The
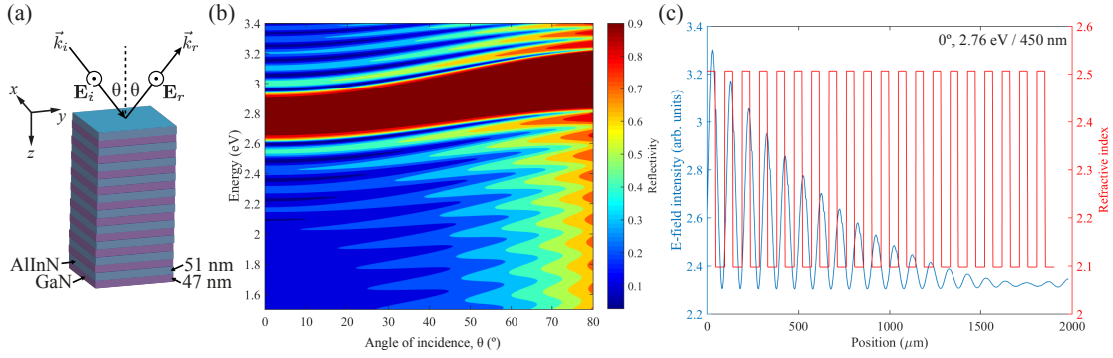
Figure 4.1: (a) 10-pair lattice-matched AlInN/GaN $\lambda_0/4$ Bragg stack [86]. (b) Angular dispersion of the reflectivity for s-polarized (electric field polarization perpendicular to the plane of incidence) radiation in the vicinity of λ_0. (c) Electric field intensity within the stop band as a function of position in the mirror for $\theta = 0$. Calculations performed using a transfer matrix method MATLAB code written by Dr. Marlene Glauser and Dr. Georg Rossbach during their Ph.D. theses [85, 161].

condition for maximum reflectivity is maintained so long as the projection of the incident wavevector along the Bragg mirror axis, $|k_i|\cos\theta = 2\pi/\lambda_0$, remains constant. The electric field intensity exponentially falls off in the mirror in the stop band (Fig. 4.1(c)) Thus, the stop band blue shifts with increasing angle of incidence θ. p-polarized radiation (electric field polarization parallel to the plane of incidence) has a different but qualitatively similar dispersion relation.

Now, imagine the dielectric Bragg mirror is split in two and a half wavelength thick ($d = n_{1,j}\lambda_0/2$) "defect" is sandwiched between the two resulting mirrors (Fig. 4.2(a)) to create a Bragg planar microcavity. A transmission peak appears in the middle of the high reflectivity stop band (Fig. 4.2(b), blue) at energy $E_0 = h\nu_0$. Unlike the case of the dielectric Bragg mirror, the Bragg planar microcavity's electric field intensity peaks in the defect section (Fig. 4.2(c)). Therefore, we can conclude that the introduction of a $\lambda_0/2$ defect in the Bragg mirror creates

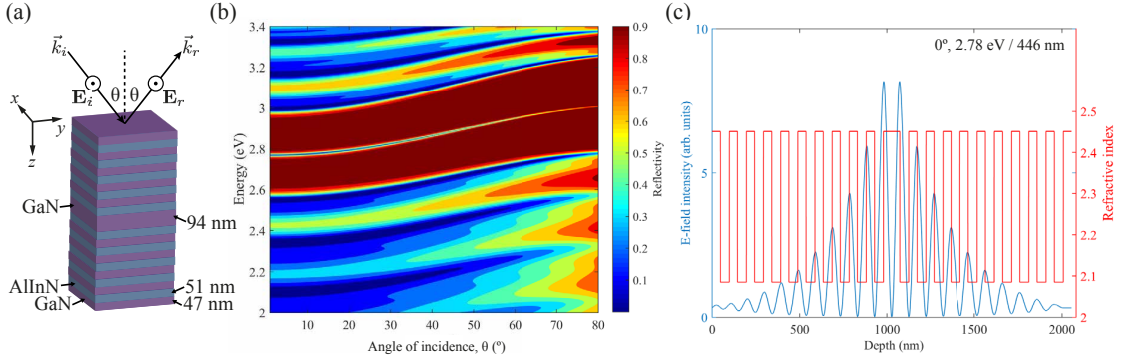Figure 4.2: (a) Schematic of a Bragg planar microcavity. Two 5-pair lattice-matched AlInN/GaN $\lambda_0/4$ Bragg stacks surround a $\lambda/2$ GaN "defect" [86]. (b) Angular dispersion of the reflectivity for s-polarized radiation in the vicinity of λ_0. (c) Electric field intensity of the cavity mode at $\theta = 0°$ as a function of position. Calculations performed using a transfer matrix method MATLAB code written by Dr. Marlene Glauser and Dr. Georg Rossbach during their Ph.D. theses [85, 161].

a spatially localized defect mode with a loss rate $\gamma_p = \omega_0/Q$. Recalling Ch. 2, the cavity loss rate is the crucial parameter for determining the strength of light-matter interaction in cavity quantum electrodynamics.

The microcavity constructed following the above procedure remains unsuitable for single photon cavity quantum nanophotonics. This can be seen in Fig. 4.2(b), where the transmission peak of the resonance shifts with the angle of the incident radiation following a $E_p(\theta) = E_p(0)/\cos\theta$ dependence near $\theta = 0$, such that the projection of the wavevector along the optical axis z remains constant. Because of this dispersion with angle, a single photon emitter may couple to any electromagnetic mode with the matching energy at an arbitrary azimuthal angle ϕ, corresponding to a ring in k-space. Even if perfect resonance is achieved for the single electromagnetic mode at $k = 0$, the spontaneous emission coupling factor β does not approach one in this geometry. Although such cavities are useful for commercial vertical cavity surface emitting lasers and research on exciton-polariton [162] and photon condensation [163], this design does not satisfy the objective to have a cavity with a single electromagnetic mode resonantly interacting with an embedded single quantum emitter. The number of available modes must be restricted by optically confining light in the additional two spatial directions.

4.1.2 Waveguides

A waveguide enables directional propagation of radiation with minimal losses due to optical diffraction. To construct a waveguide, a higher refractive index waveguide core ($n_{1,\mathrm{co}}$) is embedded within a lower refractive index cladding ($n_{1,\mathrm{cl}}$) material. The simplest waveguide consists of the waveguide core layer (thickness $2d$) sandwiched between two cladding layers which extend to infinity (Fig. 4.3(a), inset). If $2d \gg \lambda/n_{1,\mathrm{co}}$, then the ray optics picture of light
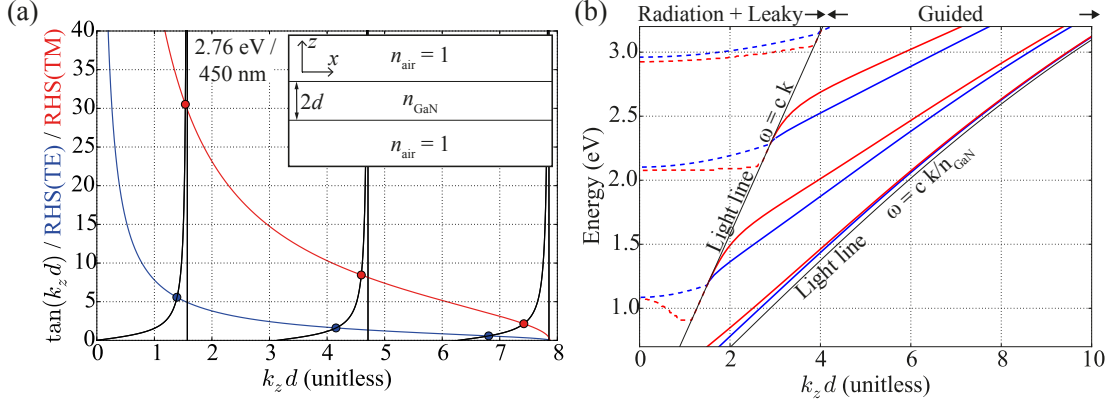
Figure 4.3: (a) Graphical solutions to Eqs. 4.6-4.7 for a $2d = 250$ nm thick GaN slab in air (inset) at 2.76 eV / 450 nm including material dispersion (Fig. 3.8) for TE (blue) and TM (red) modes. RHS means the right-hand side of Eq. 4.6 or 4.7. Black curve corresponds to $\tan(k_z d)$. (b) Dispersion relation for the same GaN slab. Black lines correspond to the light cone in air and in the waveguide core.

is valid; any ray propagating within the core at an angle greater than the critical angle given by Snell's law, $\theta_c = \arcsin\left(n_{1,\text{cl}}/n_{1,\text{co}}\right)$, will propagate within the waveguide due to total internal reflection [164].

When $2d$ approaches the wavelength of light, Maxwell's wave equation must be solved directly. The planar waveguide is one of few geometries which admit an analytic solution, which is instructive for the following discussion. Two families of solutions are possible due to the mirror symmetry of the slab, $n_1(x, y, z) = n_1(x, y, -z)$ [19]. The first solution is symmetric in electric field ($\mathbf{E}(z) = \mathbf{E}(-z)$) and has transverse electric (TE) polarization

$$\mathbf{E}(x, y, z) = \begin{cases} A\cos(k_z z)e^{-ik_x x}\hat{y} & |z| < d \\ Be^{-\kappa_z|z|}e^{-ik_x x}\hat{y} & |z| \geq d \end{cases}, \tag{4.2}$$

while the second is symmetric in magnetic field ($\mathbf{H}(z) = -\mathbf{H}(-z)$) and has transverse magnetic (TM) polarization,

$$\mathbf{H}(x, y, z) = \begin{cases} C\cos(k_z z)e^{-ik_x x}\hat{y} & |z| < d \\ De^{-\kappa_z|z|}e^{-ik_x x}\hat{y} & |z| \geq d \end{cases}. \tag{4.3}$$

Maxwell's wave equation relates k_z, the propagation constant k_x, the attenuation constant κ_z, and the wavevector $k_0 = 2\pi/\lambda = \omega/c$,

$$k_x^2 - \kappa_z^2 = n_{1,\text{cl}}^2 k_0^2, \tag{4.4}$$
$$k_x^2 + k_z^2 = n_{1,\text{co}}^2 k_0^2. \tag{4.5}$$

By solving for the continuity of the transverse (longitudinal) electric (magnetic) field at $z = \pm d$, one finds the determinantal equations for each polarization [92]

$$\tan(k_z d) = \sqrt{\frac{k_0^2(n_{1,\text{co}}^2 - n_{1,\text{cl}}^2)}{k_z^2} - 1} \qquad \text{TE,} \qquad (4.6)$$

$$\tan(k_z d) = \frac{n_{1,\text{co}}^2}{n_{1,\text{cl}}^2}\sqrt{\frac{k_0^2(n_{1,\text{co}}^2 - n_{1,\text{cl}}^2)}{k_z^2} - 1} \qquad \text{TM.} \qquad (4.7)$$

$$(4.8)$$

Fig. 4.3(a) shows the graphical solutions to Eqs. 4.6-4.7 at 2.76 eV or 450 nm for a 250 nm thick GaN slab (dispersion following Eq. 3.5) in air. Eqs. 4.6-4.7 each have at least one solution. Due to the periodicity of $\tan(k_z d)$, multiple solutions may occur if d is large enough. Physically, this translates to an absence of a cutoff for the fundamental TE and TM modes, while higher order modes exhibit a finite cutoff energy. Due the factor of $(n_{1,\text{co}}/n_{1,\text{cl}})^2$ on the right-hand side of Eq. 4.7, TM modes lie above TE modes in the dispersion relation.

By iteratively solving the determinantal equations for various energies, the dispersion relation for the 250 nm thick GaN slab in air is constructed (Fig. 4.3(b)). There are four families of solutions: guided, leaky, radiation, and evanescent modes. If k_x is purely real, the mode is guided and the modes fall between the light cone in air, $\omega < ck_x$, and the light cone in the core material $\omega > ck_x/n_{1,\text{co}}$. Both leaky and radiation modes reside above the light cone in air [164]. Physically, leaky modes can be thought of as guided modes below cutoff; they are spatially localized in the waveguide but eventually propagate away because k_x and α_z are both complex numbers (Eq. 4.4). The imaginary part of k_x gives the attenuation rate. Radiation modes form a continuum within the light cone, but, in contrast to leaky modes, are spatially localized far from the waveguide. The last family of solutions, evanescent modes, are highly localized in space (complex k_z) and are required to construct the near-field radiation distribution of a radiation source. They do not enter into this analysis because they cannot propagate into the far-field. The slab waveguide is one of few geometries for which (semi)analytic solutions exist [164]. For realistic geometries such as those explored in this thesis, Maxwell's equations must be solved numerically to obtain the eigenfrequencies and their corresponding eigenvectors or electromagnetic field profiles.

By reducing the extent of the waveguide in y to 200 nm, a rectangular waveguide is built. Figure 4.4 shows the dispersion relation for a rectangular waveguide with realistic dimensions made from the III-nitride epilayers detailed in Chapter 3. The simulation was conducted using Lumerical's MODE Solutions finite element solver [165]. Only guided modes below the light line (black) are shown. Branches are drawn in different colors depending on the branch's polarization: primarily transverse electric (TE, $\mathbf{E}||x$) modes are blue and primarily transverse magnetic (TM, $\mathbf{E}||y$) modes are red. Higher-order mixed polarization modes (black) exist in this geometry due to the presence of the 40 nm thick AlN layer, which breaks the
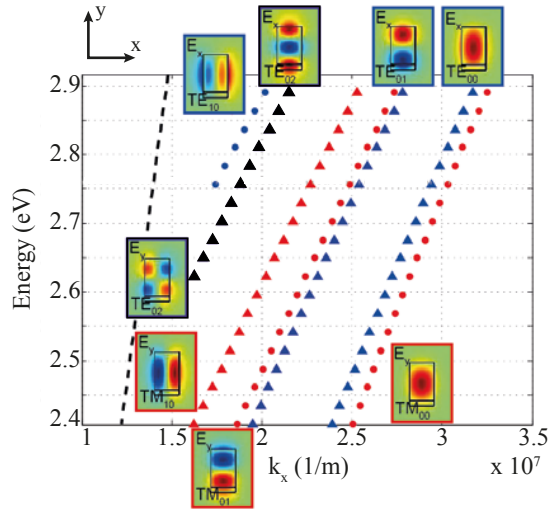
Figure 4.4: FEM simulated mode dispersion for a 200 nm wide beam of 270 nm of GaN on 40 nm AlN. Corresponding TE-like (blue) and TM-like (red) mode profiles are shown for each branch. $|E_x|^2$ and $|E_y|^2$ are shown for TE- and TM-like modes, respectively. Mixed polarization modes are black.

inversion symmetry about the y-axis. Each branch contains a picture of the corresponding electric field intensity in the dominant field component. The subscripts label the number of nodes in the horizontal and vertical directions. One sees that, at a fixed wavevector, the number of nodes in both x and y increases with energy. Most importantly, the presence of such (anti-)nodes allows the epilayer stack thicknesses to be engineered; coupling to TM modes, which is difficult to control in a photonic crystal, can be minimized by placing the InGaN/GaN quantum well light source at the center of the lowest-order TM mode where $|\mathbf{E}_x| = 0$, about 10 nm above the geometric center of the epilayer stack. The combination of two-dimensional (xy) confinement by total internal reflection in an optical waveguide with the one-dimensional diffractive confinement in the Bragg mirror microcavity leads to the desired three-dimensional confinement of a single optical mode, as shown in the next section.

4.1.3 Photonic crystal nanobeam cavities

A photonic crystal nanobeam (Fig. 4.5(a), inset) confines light in three dimensions. Waveguiding is exploited in two dimensions and diffractive confinement in the third. To build a photonic crystal nanobeam cavity, one could visualize an optical waveguide with periodic holes drilled along the longitudinal (z) axis or wire cross-section from a Bragg microcavity. Fig. 4.5(a) shows the dispersion diagram in the reduced zone representation for a waveguide with the same external dimensions as in Fig. 4.4 simulated by a commercial finite-difference time-domain (FDTD) software package, except that $d_b = 70$ nm diameter holes are drilled at a periodicity of $a_b = 118$ nm to create a "Bragg-like" mirror. When comparing the two figures, the splitting at $k_x = \pi/a$ for the fundamental TE (2.7 to 3.1 eV) and TM branches (2.7
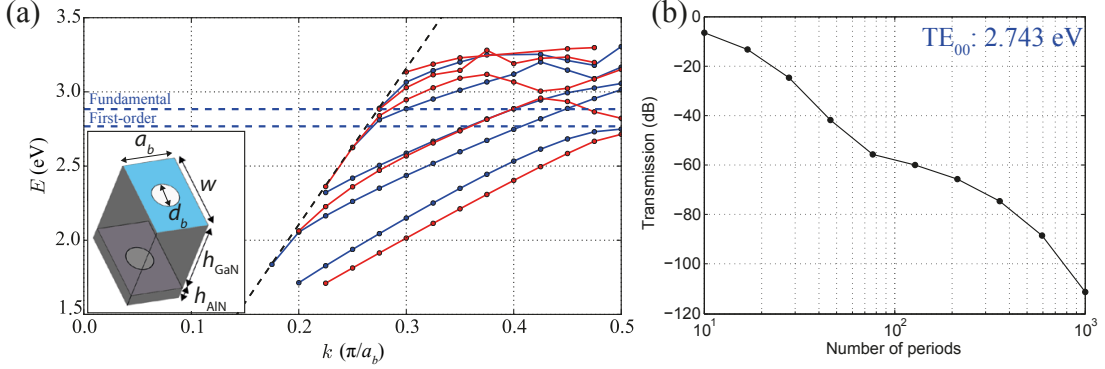
Figure 4.5: (a) 3D-FDTD simulated mode dispersion for an infinite lattice of unit cells comprised of a $w = 200$ nm wide beam with periodicity $a_b = 118$ nm and hole diameter $d_b = 70$ nm of $h_{GaN} = 270$ nm of GaN on $h_{AlN} = 40$ nm of AlN. Corresponding TE-like (blue) and TM-like (red) mode profiles are shown for each branch. Dashed blue lines show mode energies when a cavity is incorporated. Dashed black line is the light cone in air. (b) Transmission of the fundamental TE_{00} mode as a function of the number of photonic crystal periods calculated by the eigenmode expansion method.

to 2.8 eV) becomes readily apparent. The photonic band gap is not complete because there is no energy gap for higher order modes in the energy range from 2.7 to 3.1 eV. Since TM modes' electric field vector is parallel to the holes' cylindrical axis, the TM-like fundamental gap remains smaller than the TE-like gap. The transmission of the fundamental TE_{00} mode of the unperforated waveguide (Fig. 4.4), as calculated by the eigenmode expansion method in MODE Solutions, exhibits a power law ($\approx N^{-6}$ for $N < 100$) dependence as a function of the number of photonic crystal periods (Fig. 4.5(b)).

In analogy with the Bragg microcavity, a small number of electromagnetic modes can be localized spatially and spectrally in the defect region by inserting a well-designed "defect" in the middle of a photonic crystal mirror (dashed blue lines in Fig. 4.5(a)). Instead of simply removing a hole, the maximum theoretical Q factors can be achieved by tapering hole sizes and spacings gradually between the mirror and cavity center because the hole taper improves the impedance matching between the mirror and cavity sections [166]. Fig. 4.6 shows the geometry for a published design procedure [167] using a 18-hole quadratic taper from each 18-hole photonic crystal mirror to larger holes in the cavity center. The FDTD method was used to find the eigenmode energies, Q, and electric field intensity profiles in the xy- and yz-planes. Care was taken to ensure convergence in the spatial mesh resolution, simulation length, and distance to perfectly-matched layer absorbing boundary conditions. The simulated geometry was $a_b = a_c = 119$ nm, $d_b = 70$ nm, and $d_c = 84$ nm, where a_c and d_c are the lattice constant and hole diameter in the cavity center, respectively. The TE mode has electric field polarization $\mathbf{E} \parallel y$ and the subscripts indicate the number of nodes in the electric field intensity along the x and z directions. Therefore, the fundamental TE mode is labeled by the subscript "00" and the fundamental TM mode by the subscript "01."
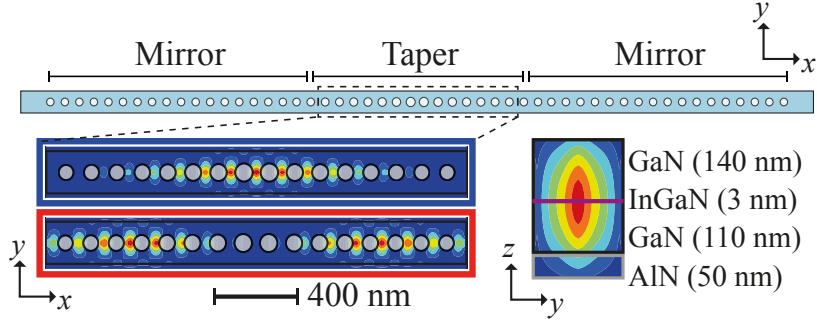
Figure 4.6: (a) Photonic crystal cavity geometry (dimensions to scale) and simulated TE-like cavity mode electric field intensity profiles in the InGaN/GaN quantum well (xy) plane (lower left) for the fundamental (blue) and first-order (red) cavity modes. The TE-like fundamental mode electric field intensity exhibits an antinode at the cavity center, with a similar yz profile as the TE_{00} mode in the ridge waveguide (Fig. 4.4). Reproduced from [14] with permission from APS.

The fundamental and first-order Q exceeded 1×10^5, while the energies were 2.731 eV (454 nm) and 2.678 eV (463 nm), respectively. Contrary to naïve physical intuition, the fundamental mode, without a node along x, is at higher energy because of its localization in the cavity center, where the average refractive index is lowest due to the larger hole size. The volumes of the fundamental and first-order modes are 1.4 and 2.6 $(\lambda/n)^3$, respectively, following the conventional definition from Painter *et al.* [168],

$$V_0 = \frac{\int_\Omega \varepsilon(\mathbf{r})|\mathbf{E}(\mathbf{r})|^2 d^3\mathbf{r}}{\max[\varepsilon(\mathbf{r})|\mathbf{E}(\mathbf{r})|^2]} \tag{4.9}$$

4.2 Correspondence between simulations and experiments

Figure 4.7(a) shows a typical μPL spectrum for a nanobeam photonic crystal cavity under 1.6 kW/cm^2 cw pumping at room temperature with the 351 nm line of an Ar-ion laser. The energy splitting is roughly in agreement with the simulated values. μPL mappings at the two energies reveal that the fundamental mode is more localized about the cavity center (Fig. 4.7(a), insets). The spatial resolution can be further improved by cathodoluminescence mappings, in which the node in the first-order mode is readily apparent (Fig. 4.7(b)). Note that nanobeams with different dimensions ($a_b = a_c$, d_b, d_c) were investigated in each of Fig. 4.6, Fig. 4.7(a), and Fig. 4.7(b). Although the peak positions shift, the mode profiles, order, and splittings are in agreement with simulation.

Both modes exhibit Q_{exp} values on the order of several thousand, far below the theoretically predicted values in Section 4.1.3. To account for the discrepancy, an empirical formula is used to scale the theoretical Q factors due to several real-world non-idealities that are not taken
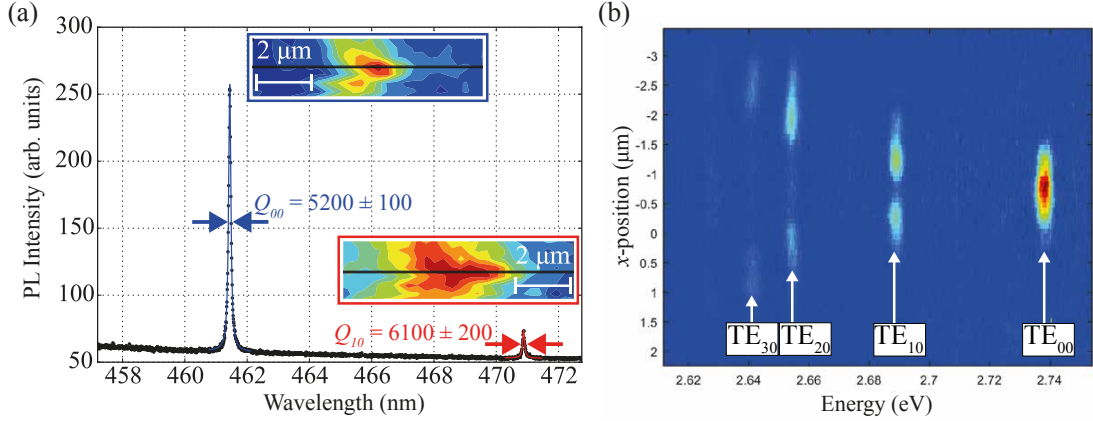
Figure 4.7: (a) Typical μPL spectrum at room temperature showing the fundamental (λ_{00},Q_{00}) and first-order (λ_{10},Q_{10}) cavity modes. Insets are μPL mappings. Reproduced from [14] with permission from AIP. (b) Cathodoluminescence line scan along nanobeam performed by Dr. G. Jacopin.

into account by the FDTD simulation,

$$Q_{exp}^{-1} = Q_{th}^{-1} + Q_{abs}^{-1} + Q_{sr}^{-1} + Q_{fab}^{-1}, \tag{4.10}$$

where Q_{exp} is the experimental Q value, Q_{th} is the FDTD-calculated Q value, Q_{abs} accounts for dissipative losses due to bulk and surface absorption, Q_{fab} accounts for scattering losses due to hole size and position fluctuations from fabrication disorder, and Q_{sr} denotes scattering losses due to nanoscale surface roughness and waviness. This formula assumes that the individual loss contributions add incoherently, which should be the case so long as the scattering loss contributions are due to random geometric fluctuations [77].

The linear polarization dependence of the two modes agrees well with the simulated dependence so long as fabrication disorder (Section 4.5.4) is taken into account. In such measurements, a rotatable $\lambda/2$ waveplate and a fixed wire grid polarizer are inserted in the detection line. The normalized peak height as a function of polarization angle is plotted in Fig. 4.8. Both modes are co-linearly experimentally polarized perpendicular to the nanobeam. The dashed lines represent the fits to simulations without hole shape and position disorder, while the solid lines show best fits to a single disorder realization (Section 4.5.4). The most dramatic effect of fabrication disorder is to break the symmetry that results in the quadrupole polarization distribution of the first-order mode (λ_{10}), mixing it with the fundamental mode (λ_{00}) to create a dipole distribution in the far-field. As a result of the correspondence between experiments and simulations, we can make use of simulations to understand and improve III-nitride nanobeam photonic crystal cavities for quantum photonics applications.
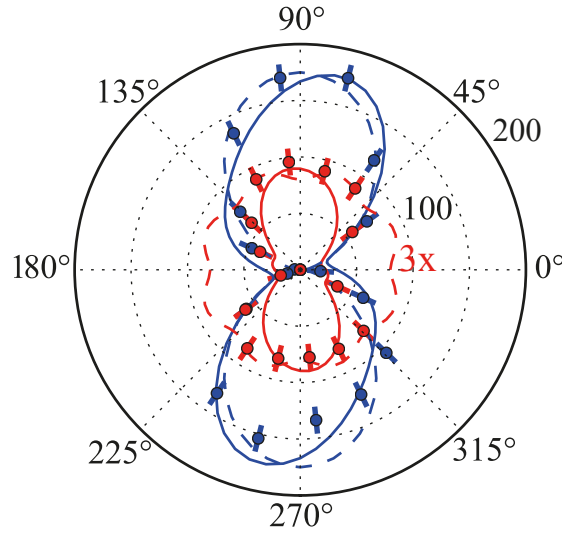
Figure 4.8: Polarization dependence of the fundamental (blue) and first-order (red) μPL peak amplitudes. Dashed and solid lines show simulated dependences with and without hole size and position disorder.

4.3 Mechanical deformation

In this section, we explore the consequences arising from fabrication of air-suspended nanostructures from epilayers with tensile strain. In Chapter 2, we learned that growth of III-nitrides on silicon (111) results in tensile strain in the epilayers due to the -17% lattice mismatch between AlN and silicon (111). Removal of the substrate beneath the epilayers results in partial release of the associated biaxial strain, which in turn may lead to a mechanical deformation of the associated nanostructure. The effects of mechanical deformation on the photonic crystal cavity and InGaN/GaN quantum well are explored using confocal Raman spectroscopy and simulation.

Figure 4.9 presents normalized confocal Raman spectra of as-grown epilayers (blue), an air-suspended, biaxially-strained membrane (black), and a uniaxially strained nanobeam without holes (red) measured using 532 nm illumination in the Renishaw inVia system. The creation of a 10 μm air gap beneath the epilayer membrane suppresses the Raman signal from the silicon LO peak at 523 cm^{-1} and the broad background. As a result, the GaN and AlN peak visibility increases dramatically due to elimination of out-of-focus background signal in the confocal geometry.

Table 4.1 lists the stress and strain extracted from Fig. 4.9 and processed using Eqs. 3.8-3.11. When moving from the biaxially strained epilayer to the biaxially strained membrane, the stress and strain in the GaN layer slightly decrease to within experimental error, likely due to relaxation due to a slight mechanical deformation. This stands in stark contrast to the uniaxially strained nanobeam with 800 nm width, where the stress and strain markedly increase.
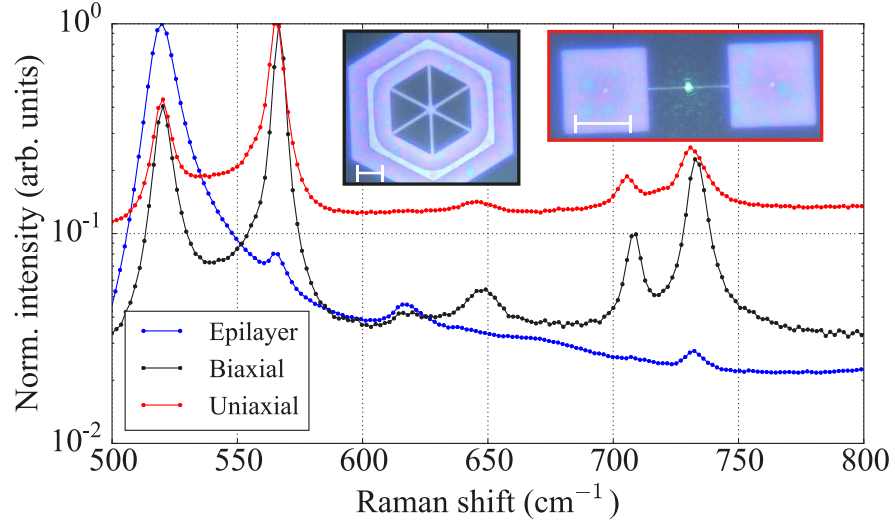
Figure 4.9: Comparison of confocal μRaman spectra between unprocessed epilayers with biaxially (inset, black) and uniaxially strained (inset, red) nanostructures. Measurements were taken in the center of each nanostructure. Scale bar represents 10 μm. Dots are used to show the finite CCD resolution.

Structure	Material	Mode	$-\Delta\tilde{\nu}$ (cm^{-1})	$-\varepsilon_{xx}$ (%)	$-\sigma_{xx}$ (MPa)
Unprocessed	GaN	E_2^H	1.5(0.5)	0.040	190
Unprocessed	GaN	$A_1(LO)$	1.6(0.5)	0.040	190
Biaxial	GaN	E_2^H	1.2(0.5)	0.029	140
Biaxial	GaN	$A_1(LO)$	1.0(0.5)	0.027	130
Biaxial	AlN	E_2^H	9.9(0.5)	0.23	1100
Uniaxial	GaN	E_2^H	2.2(0.5)	0.32	1000
Uniaxial	GaN	$A_1(LO)$	3.0(0.5)	0.39	1300
Uniaxial	AlN	E_2^H	12.2(0.5)	1.5	4800

Table 4.1: Strain and stress of III-nitride epilayers and processed nanostructures.

In order to understand the difference between the uniaxially and biaxially strained structures, COMSOL finite element modeling was performed [169] by summer intern, Aurélien Pélissier. A 6 μm long, 200 nm wide nanobeam was perforated with holes with 70 nm diameter and 119 nm periodicity. The AlN and GaN layer thicknesses were 50 and 250 nm, respectively. Two $5 \times 5 \ \mu m^2$ silicon support pads with 750 nm of both air gap and material removed around the support pad perimeter were assumed. The elastic stiffness parameters from Table 2.3 were used. All vertical surfaces were assumed to be free, and the strain on the support pads was assumed to follow the epilayer values in Table 3.2.
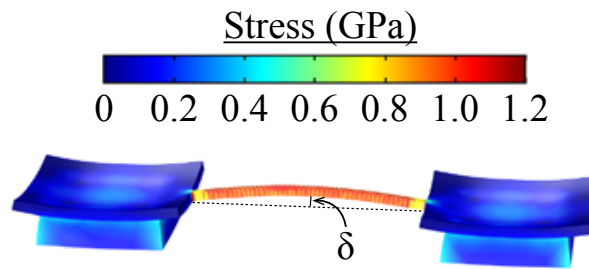
Figure 4.10: Finite element simulation of stress distribution and mechanical deformation (magnified 50×) of a nanobeam photonic crystal cavity with realistic dimensions. δ is the maximum vertical displacement in the nanobeam center. Simulation performed by Aurélien Pélissier.

Fig. 4.10 shows the simulation results. The computed stress, which is superposed on the structure exterior, is in excellent quantitative agreement with the Raman results to within experimental uncertainty. The stress of a few hundred MPa at the anchoring support increases to around 1 GPa at the nanobeam center. Beyond confirming the experimental results, the simulations also predict the mechanical deformation associated with such a stress distribution.

Figure 4.10 displays the mechanical deformation of the simulated structure exaggerated by a factor of 50× in order to be made visible. The unfixed edges of the support pad and the nanobeam bend upwards due to the inhomogeneous strain profile in the epilayers. According to COMSOL, the upward bending should amount to $\delta = 5$ nm upward deflection in the nanobeam center, a value that is too small to be observed at the requisite magnification in the SEM. This simulated result poses two questions: can the bending be observed experimentally and does such a bending deformation affect the photonic crystal cavity modes?

The upward bending can be observed experimentally on similar nanostructures. A 12 μm long, 200 nm wide cantilever (Fig. 4.11(a)) exhibits an upward deflection $\delta = 150$ nm over the entire length. Fig. 4.11(b) demonstrates a more dramatic upward deflection of a doubly clamped photonic crystal nanobeam cavity. In this sample, the AlN epilayer is partially removed by chemically selective etching of the N-polar surface in 25% TMAH. The absence of the highly strained AlN layer removes a constraining force that would otherwise prevent such bowing.

FDTD electromagnetic simulations were performed on deformed nanobeam photonic crystal
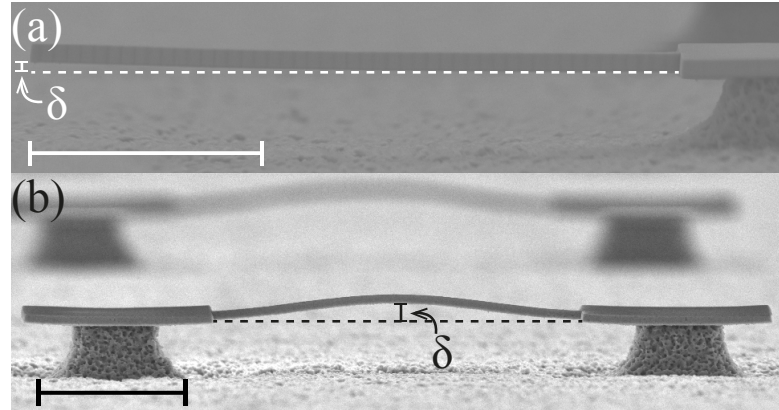
Figure 4.11: SEM images of upward bowing in fabricated nanostructures. (a) $\delta = 150$ nm in a cantilever. (b) $\delta = 450$ nm in a nanobeam where part of the AlN layer is removed by selective chemical etching. Scale bars represent 4 μm.

cavities. A cantilever geometry was simulated due to the larger possible mechanical deformation. Fig. 4.12 shows the computed change in fundamental mode resonance wavelength for a
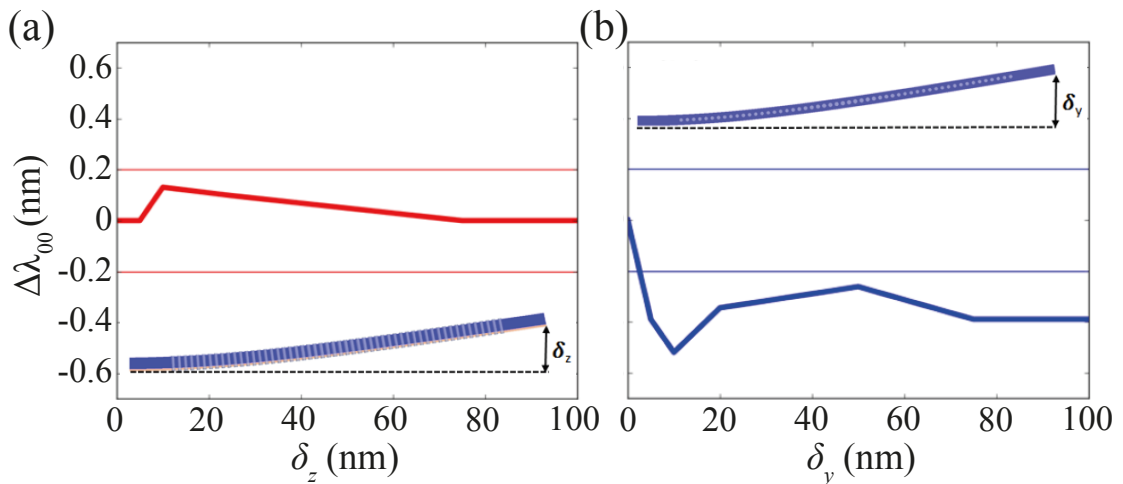
Figure 4.12: FDTD calculations of fundamental TE mode shifts ($\Delta\lambda_{00}$) in a nanobeam photonic crystal cavity cantilever caused by (a) vertical (δ_z) and (b) in-plane (δ_y) tip deflections. Horizontal lines are the "error bars," which correspond to the repeatability upon small perturbations of input parameters. Simulations performed by Aurélien Pélissier.

design similar to the one explored in Section 4.2. For vertical bending as in Fig. 4.11(a), no change in resonance wavelength to within the simulation error bars is found. The nanobeam geometry is known to be stable against such deformations because the mirror symmetry about the nanobeam's longitudinal axis remains unbroken, preserving the separation of TE- and TM-like modes. However, when the mirror symmetry along the longitudinal axis (y) is broken, as in Fig. 4.12(b), just 10 nm of deflection is sufficient to shift the mode by 0.5 nm. This shift corresponds to five linewidths of a $Q = 5000$ cavity at $\lambda_{00} = 460$ nm. Such a scheme could

be feasible by fabricating a piezoelectric actuator at the tip of a nanobeam photonic crystal cavity utilizing a cantilever instead of the doubly clamped structure pursued in this thesis, as in [170].

To summarize, optical nanocavities fabricated from thin III-nitride epilayers on silicon may deform due to the large amount of tensile strain in the as-grown epilayers. Confocal μRaman spectroscopy is a useful tool to characterize the stress in fabricated nanostructures and the results agree well with finite element calculations using input parameters from the literature. Depending on the cavity geometry and deformation of the nanostructure, mechanical deformations may modify optical resonances. The small vertical bowing in the doubly clamped photonic crystal cavities explored in this thesis is not expected to influence optical resonances. In the future, however, in-plane bending by piezoelectric actuators fabricated at the tip of a nanobeam photonic crystal cantilever may be utilized for *in situ* electric tuning of photonic crystal cavity resonances.

4.4   Light extraction

The light inside the photonic crystal nanocavity must be coupled efficiently into the measurement apparatus. By definition, a high Q cavity ideally leaks little light to the external environment. Because $g^{(2)}(\tau)$ measurements depend on the number of coincidence counts, the total integration time for a given number of counts scales inversely with the count rate squared. Therefore, the engineering of light outcoupling into the microscope objective's light cone would minimize experimental integration times. This section explores an outcoupling scheme based on sub-harmonic nanobeam width modulation.

Design principle

The sub-harmonic sidewall modulation works using a band folding concept. Band folding has already been demonstrated in photonic crystals using hole size modulation [171, 172] but the physics is the same for width modulation. If the photonic crystal has period a, sub-harmonic width modulation introduces a sinusoidal undulation of the nanobeam width with period $2a$. In real-space (Fig. 4.13(a)), such a modulation produces no perceptible changes in the near-field electric field intensity profile of the cavity mode at a plane located 15 nm above the nanobeam top surface. The 2D Fourier transforms of these spatial profiles (Fig. 4.13(b), left) reveal that the cavity mode is highly localized at $k_x = \pm\pi/a$ for the nanobeam without the sidewall modulation. The 12 nm peak-to-peak sidewall modulation shifts a small amount of cavity emission by the subharmonic modulation wavevector, $k_x = \pi/2a$, back to the Brillouin zone center at $k_x = 0$. When propagated to the far-field using a standard transform [174] (Fig. 4.13 (b), right), the subharmonic sidewall modulation greatly increases the far-field emission inside the light cone of a NA = 0.5 objective.

In Figure 4.13(c), far-field emission profiles (i.e. Fig. 4.13(b), right) are integrated over the
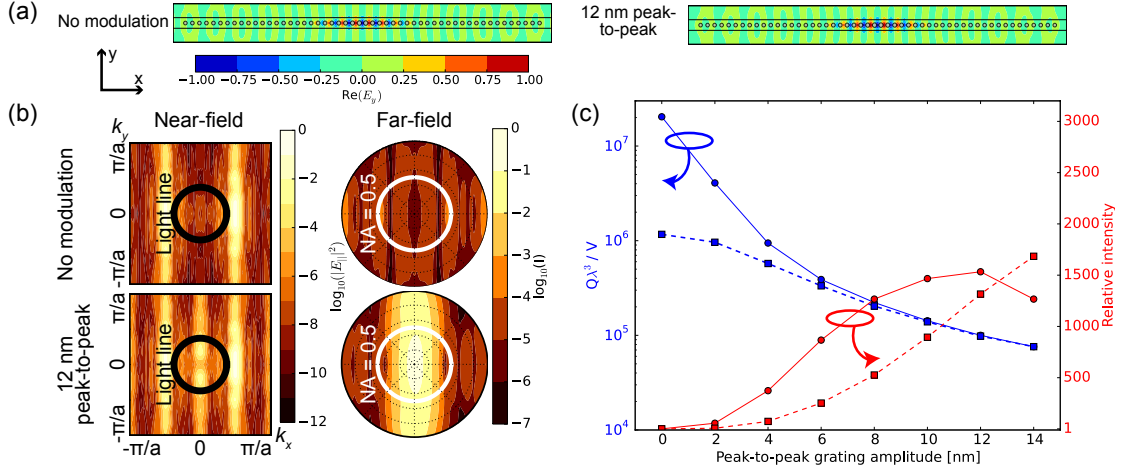
Figure 4.13: (a) Real space electric field intensity profiles in the xy plane 15 nm above the top of the nanobeam with and without sidewall modulation. (b) Corresponding near-field and far-field radiation patterns. (c) Figure-of-merit $Q\lambda^3/V$ and integrated far-field intensity for a NA= 0.5 objective of the fundamental mode with increasing sidewall grating amplitude. Solid lines are for vertical sidewalls and dashed lines are for 2° sloped sidewalls. Reproduced with modification from [173] and permission from AIP.

NA = 0.5 light cone as a function of peak-to-peak sidewall grating amplitude and compared with the change in Q value. The collected emission is predicted to increase by a factor of 1500×, while the theoretical Q factor only decreases by a factor of 270×; this suggests that the sub-harmonic sidewall modulation reshapes the far-field emission pattern more than increasing the total amount of light scattering from the cavity.

In principle, the same sub-harmonic grating outcoupler should work for the first-order mode, whose Fourier transform is also peaked at $k_x = \pm\pi/2a$. However, as the first-order mode represents an "antibonding" state as opposed to the fundamental mode's "bonding" character, we would expect the relative phase of the two lobes at $k_x = \pm\pi/2a$ to be offset by 180° for the first-order mode. Therefore, to get constructive interference of the first-order mode in the far-field at $\mathbf{k} = 0$, it may be necessary to translate the grating coupler relative to the photonic crystal to produce the necessary phase matching. This is left for future work.

Overall, the outcoupler is expected to increase the fraction of far-field emission captured by the microscope. However, since we know that experimental Q factors ($\approx 5 \times 10^3$) remain far below the theoretical Q factors depicted in Fig. 4.13(c), we should expect the increase in experimental far-field emission to be much lower. Furthermore, experimental non-idealities such as 2° sloped hole sidewalls (dashed lines) impact the theoretical results, so such simulation results should only be interpreted as a qualitative confirmation of the design principle rather than a quantitative prediction. Of course, the simulation predictions must be confirmed by experiment.

71

Experimental realization

Nanobeam photonic crystal cavities were fabricated using the techniques described in Ch. 3. Groups of 12 nominally identical nanobeams with sidewall-peak-to-peak grating amplitudes ranging from 0 to 14 nm were fabricated side-by-side in order to control for random fabrication imperfections. The same base design of a 200 nm wide beam with an 18-hole mirror with a 119 nm lattice constant and 70 nm hole diameter adjoining an 18-hole quadratic taper to a hole diameter of 84 nm was used for each group. Fig. 4.14(a) shows a SEM image of a fabricated nanobeam with sub-harmonic sidewall modulation.
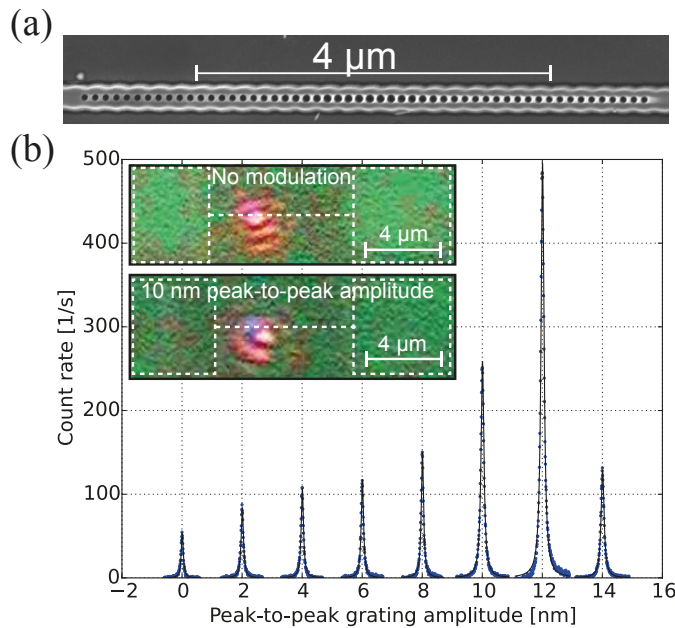
Figure 4.14: (a) SEM image of nanobeam photonic crystal cavity incorporating sub-harmonic sidewall modulation outcoupler. (b) Representative μPL peak of the fundamental nanobeam photonic crystal cavity mode shifted to the corresponding peak-to-peak grating outcoupler amplitude under 1.6 kW/cm^2 cw 351 nm excitation at room temperature. Reproduced from [173] with permission from AIP.

Figure 4.14(b) shows representative fundamental mode μPL spectra, where each peak has been re-zeroed and shifted by the peak-to-peak grating amplitude. The sub-harmonic width modulation increases the amount of light collected up to a peak-to-peak grating amplitude of 12 nm. The insets show images captured by the microscope camera for the case without sidewall modulation (top) and with sidewall modulation (bottom). The red pump laser spot is accompanied by blue μPL for the case with the sidewall modulation, while only the pump laser is visible for the nanobeam cavity without sidewall modulation. Such images confirm the increase in μPL intensity due to the sidewall modulation. Within each group, random fabrication imperfections produce some variance in the μPL intensity. Therefore, statistics were collected over 12 nominally identical nanoobeams for each value of peak-to-peak sidewall modulation.
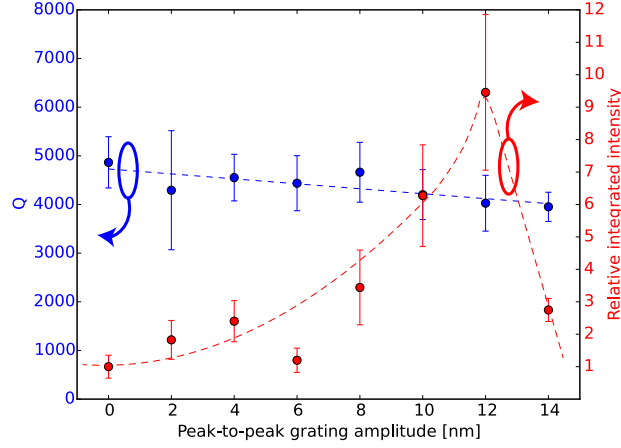
Figure 4.15: *Q* and intensity statistics of sub-harmonic grating outcoupler measured over 12 nominally identical nanobeam photonic crystal cavities. Error bars represent one standard deviation. Dashed lines are guides for the eye.

The influence of fabrication fluctuations on both *Q* and *μ*PL intensity is shown in Figure 4.15. The *Q* values were extracted from Lorentzian lineshape fits with linear background subtraction. Each data point is the mean over 12 nominally identical nanobeam cavities and the error bars represent one standard deviation. The sidewall modulation increases the *μ*PL intensity by nearly an order of magnitude while producing a slight decrease in *Q* which is negligible within experimental error due to fabrication fluctuations. A quick quantitative analysis of these numbers will allow us to close the loop and compare simulation with experiment.

The simulation predicts a decrease in theoretical *Q* from $Q_{\mathrm{th}}(0) = 1 \times 10^6$ to $Q_{\mathrm{th}}(14\ \mathrm{nm}) = 8 \times 10^4$ upon introducing the sidewall modulation with 14 nm amplitude. Assuming loss rates add incoherently, the theoretical loss $Q_{\mathrm{th,oc}}$ introduced by the output coupler is $Q_{\mathrm{th,oc}}^{-1} = Q_{\mathrm{th}}(14\ \mathrm{nm})^{-1} - Q_{\mathrm{th}}(0)^{-1} = \left(8.7 \times 10^4\right)^{-1}$. If we then subtract this value from the experimental $Q_{\mathrm{exp}}(0) = 4800$, then we would expect $Q_{\mathrm{exp}}(14\ \mathrm{nm})^{-1} = Q_{\mathrm{exp}}(0)^{-1} - Q_{\mathrm{th,oc}}^{-1} = 4300^{-1}$, which is consistent with the experimental results within error due to fabrication fluctuations.

A second calculation provides an upper bound on the fraction of scattering losses into the light cone compared to total losses. From the theoretical simulations, the sidewall modulation is known to increase far-field emission in the microscope's light cone by both reshaping the far-field emission and decreasing *Q*, with the far-field reshaping effect being dominant. In order to find an upper bound on the fraction of scattering losses into the microscope cone, let us assume that the effect of the sidewall modulation is solely to decrease *Q*. Losses are partitioned into two contributions, an unknown intrinsic broadening mechanism (Q_{i}) and losses outcoupled into the microscope light cone (Q_{oc}). Therefore,

$$Q_{\mathrm{exp}}^{-1}(0) = Q_{\mathrm{i}}^{-1} + Q_{\mathrm{oc}}^{-1}(0), \tag{4.11}$$

$$Q_{\mathrm{exp}}^{-1}(12\ \mathrm{nm}) = Q_{\mathrm{i}}^{-1} + Q_{\mathrm{oc}}^{-1}(0) + Q_{\mathrm{oc}}^{-1}(12\ \mathrm{nm}). \tag{4.12}$$

Eqs. 4.11-4.12 represent two equations in three unknowns, Q_i, $Q_{oc}(0)$, $Q_{oc}(12\,\mathrm{nm})$.

If we further assume that the experimental μPL intensity is proportional to the scattering loss rates (Q_{oc}^{-1}), then the system of equations can be solved. Plugging in the Q and the experimental μPL intensity ratio $(Q_{oc}^{-1}(0) + Q_{oc}^{-1}(12\,\mathrm{nm}))/Q_{oc}(0)^{-1} = 9$, a quantitative upper bound on scattering losses into the microscope light cone as a fraction of the overall loss rate can be established for the case without any grating outcoupler,

$$\frac{Q_i}{Q_{oc}(0)} < 0.6\%. \tag{4.13}$$

Therefore, the collection efficiency remains far below that predicted by FDTD simulations (Fig. 4.13(c), inset) and the primary experimental loss mechanism must be either scattering outside the microscope objective's light cone or dissipative absorption. This will be investigated in greater detail in the next section.

4.5 Experimental Q quantification

As shown in Fig. 2.2, the discrepancy between simulated and experimental Q values is not unique to III-nitride materials designed at short wavelengths. The purpose of this section is to find the origin of this discrepancy. Since $Q_{th} \gg Q_{exp}$, Eq. 4.10 is rewritten to expand the term for absorption to separate bulk GaN (Q_{bk}), quantum well (Q_{qw}), and surface state (Q_{sa}) absorption contributions,

$$Q_{exp}^{-1} = Q_{bk}^{-1} + Q_{qw}^{-1} + Q_{sa}^{-1} + Q_{sr}^{-1} + Q_{fab}^{-1}. \tag{4.14}$$

In this section, we quantify the relative weight of the individual loss mechanisms which decrease Q from the theoretically simulated value of $\sim 10^6$ to experimental values of several thousand.

4.5.1 Bulk absorption

Bulk absorption can be measured on the GaN layers before cleanroom processing using various techniques. Spectroscopic ellipsometry has a noise floor around $\alpha = 100\ \mathrm{cm}^{-1}$, where α is the absorption coefficient and is related to the complex index of refraction $\tilde{n} = n + ik$ by $\alpha = 4\pi k/\lambda$ [139]. Ellipsometry measurements and detailed fitting using a generalized oscillator model were performed at the Universität Otto von Guericke in Magdeburg, Germany by Martin Feneberg and Rüdiger Goldhahn and no absorption below the bulk GaN bandgap was found at this measurement floor. Other techniques with lower noise floors are required to rule out sub-band gap bulk absorption.

Variable stripe length measurements were conducted by Dr. Kanako Shojiki using the 355 nm third harmonic of a 8.1 kHz repetition rate Q-switched Nd:YAG laser as an excitation source.

The beam was shaped by an expander and cylindrical lens. The spectra $I_L(\lambda)$ and $I_{2L}(\lambda)$ (Fig. 4.16(a)) from epilayers with the single quantum well on silicon at 5 mJ/cm^2 fluence (red)
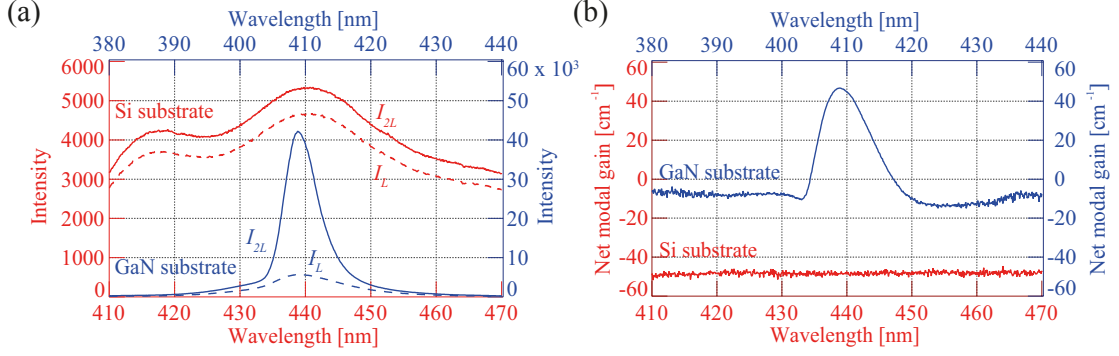
Figure 4.16: (a) Amplified spontaneous emission spectra for laser diode epilayers incorporating InGaN/GaN multiple quantum wells on free-standing GaN substrate (blue) and for thin epilayers incorporating a single 3 nm In$_{0.15}$Ga$_{0.85}$N/GaN quantum well on silicon (red) (b) Calculated net modal gain following Eq. 3.15. Reproduced from [14] with permission from APS.

were compared to a laser diode epilayer reference sample consisting of multiple InGaN/GaN quantum wells grown on a free-standing GaN substrate at 0.7 mJ/cm^2 fluence (blue). A clear change in the shape of the reference sample spectra is observed, whereas the single quantum well on silicon exhibits a broadband increase in intensity.

Evaluation of Eq. 3.15 leads to the result in Fig. 4.16(b). As expected, lower baseline loss and a narrowband net gain are found for the laser diode epilayer reference sample. A flat baseline is observed for the single quantum well on silicon because the maximum available fluence of 5 mJ/cm^2 is not high enough to push the sample into the amplified spontaneous emission regime at room temperature ($f_g g(\lambda) \approx 0$). This is due to losses in the higher refractive index, absorptive silicon substrate, the high defect density of III-nitride epilayers on silicon, and low quantum efficiency at room temperature. Therefore, the flat baseline value of $\alpha(\lambda) = 50$ cm^{-1} provides an upper bound for absorption losses by the III-nitride epilayer bulk material, as it includes absorption by the silicon substrate, whose band gap is at 1.1 eV.

The upper bound of 50 cm^{-1} can be translated into a lower bound on nanobeam photonic crystal Q factors using electromagnetic perturbation theory [175],

$$\Delta\nu = -\frac{\nu_0}{2} \frac{\int_{V,\text{GaN}} \varepsilon^{(1)}(\mathbf{r})|\mathbf{E}(\mathbf{r})|^2 d^3\mathbf{r}}{\int_{\Omega} \varepsilon_r^{(0)}(\mathbf{r})|\mathbf{E}(\mathbf{r})|^2 d^3\mathbf{r}}, \tag{4.15}$$

where $\varepsilon_r^{(0)}(\mathbf{r})$ is the relative permittivity function describing the geometry in the absence of the perturbation, $|\mathbf{E}(\mathbf{r})|^2$ is the electric field intensity. The integral in the numerator goes over the material experiencing the permittivity change ($\varepsilon_r^{(1)}(\mathbf{r})$) and the integral in the denominator goes over the entire computational domain. Taking a complex change in absorption in GaN

only corresponding to $\alpha = 50$ cm^{-1}, the imaginary change in permittivity would be $\varepsilon_i^{(1)} = n_1 \lambda_0 \alpha / 2\pi = 9 \times 10^{-4}$. Evaluation of Eq. 4.15 leads to a $Q_{\text{bk}} = \omega_0 / \Delta\omega > 1.6 \times 10^4$. Moreover, finite element modeling of the geometry indicates that the silicon substrate losses can entirely account for the measured losses of 50 cm^{-1}. Therefore, we conclude that bulk absorption cannot be limiting experimental quality factors in the blue spectral range and neglect it for the remainder of the thesis. Nevertheless, it is worth mentioning that dry etch damage sustained during cleanroom processing may modify the material's optical properties from the unprocessed epilayers measured here.

The pulsed pump laser is a shortcoming of the variable stripe length measurement technique because high fluences could saturate quantum well absorption losses. Hence, other techniques should complement and confirm the variable stripe length technique's findings. Power-dependent μPL of nanocavities under cw optical pumping should in principle differentiate between scattering and dissipative loss mechanisms [176], as the former are non-saturable and the latter saturable with increasing pump power. Ideally, the Q value would be taken at the lasing threshold, as this is the point at which the net gain is zero. Further increases of pump power should result in linewidth narrowing following the modified Schawlow-Townes formula [18].

4.5.2 Quantum well absorption

Under low illumination intensities and/or at room temperature, the quantum well, which serves as an internal light source, absorbs light, broadening the photonic crystal cavity mode. The goal of this section is to optically pump the system hard enough to saturate quantum well absorption losses, e.g. push the quantum well beyond the transparency threshold (i.e. Bernard-Duraffourg condition). The transparency threshold is manifested as a narrowing of the photonic crystal cavity lineshape. Meeting the Bernard-Duraffourg condition is a necessary yet insuffucient condition for lasing; additional pumping is required to raise the quantum well carrier density beyond the transparency threshold such that the quantum well modal gain equals the additional losses of the cavity due to scattering, outcoupling (commonly known as mirror loss), and surface state absorption. Above the lasing threshold, the quantum well carrier density clamps at the threshold value [18, 31].

Photonic crystal nanobeam cavities do not exhibit a sharp, well-defined lasing threshold due to the high fraction of spontaneous emission which is coupled into the cavity mode [31, 33]. Conventional semiconductor diode lasers exhibit a sharp "kink" in the input-output intensity curve concomitant with an abrupt decrease in linewidth, photon bunching statistics, and subsequent linewidth narrowing following a modified Schawlow-Townes law at threshold [18, 177]. In nanolasers, the extended threshold regime results in a slow build-up of coherence over more than an order of magnitude of pump intensities [178]; an ideal $\beta = 1$ nanolaser has a linear, kink-free input-output curve [31]. The linewidth narrows at the transparency density to satisfy the Bernard-Duraffourg condition for lasing but then plateaus before following the

modified Schawlow-Townes relation [178]. The photon statistics simultaneously transition slowly from chaotic ($g^{(2)}(0) = 2$) to coherent ($g^{(2)}(0) = 1$) behavior [27, 33, 177, 178].

The experimental observation of linewidth narrowing in III-nitride photonic crystal nanobeams remains a complex issue for several practical reasons. First, heat produced by hot carrier thermalization and nonradiative recombination must be conducted to the substrate via a narrow, perforated semiconductor strip which does not exhibit high thermal conductivity. Heating will lead to a decrease of the semiconductor band gap and increase of the effective refractive index, redshifting the cavity mode [13]. Additionally, at room temperature, photoinduced oxygen desorption (see Chapter 5) broadens the mode faster than the linewidth may be narrowed above threshold. Combined with the low internal quantum efficiency of thin epilayers on silicon and a strong thermally activated nonradiative recombination mechanism ($E_a \sim 85$ meV, see Appendix A), we have never conclusively observed linewidth narrowing at room temperature in these structures. Nevertheless, power-dependent $g^{(2)}(0)$ measurements indicate that nanobeam photonic crystal cavities fabricated from the epilayers utilized in this thesis do indeed exhibit lasing behavior at room temperature under intense nonresonant optical pumping (~ 10 kW/cm^2 at $\lambda = 325$ nm) [27].

Cooling the sample to cryogenic temperatures improves the quantum efficiency of the sample by between two and four orders of magnitude (Appendix A). Due to the improved quantum efficiency of the material at low temperatures, the transparency threshold shifts to lower intensities. The quantum efficiency at 4 K is high enough such that resonant pumping of the InGaN/GaN quantum well with a 405 nm pump laser can reach the transparency threshold, avoiding possible parasitic effects due to heating of the nanostructure.

Resonant pumping requires a few additions to the μPL apparatus (Section 3.2.6). In order to measure with high spectral precision close to the laser line, the 405 nm pump laser's residual electroluminescence is filtered by a notch filter (Semrock, Inc.), polarized by a Rochon prism and rotated using a half-wave plate to become cross-polarized with the photonic crystal modes' emission (Fig. 4.8). By detecting the nanobeam μPL through a 409 nm long pass filter (Semrock, Inc.) and wire grid polarizer, the laser is sufficiently attenuated so as not to distort the nanostructure's optical spectrum, even at high pump intensities. Power-dependent photonic crystal spectra are recorded with the 1800 lp/mm grating in second order to achieve ~ 100 μeV spectral resolution. Reference spectra on an unprocessed portion of the sample are measured using the 150 lp/mm grating to obtain a sufficiently large spectral window.

Figure 4.17(a) shows the μPL spectrum of unprocessed epilayers containing a thinner, 2 nm thick In$_{0.15}$Ga$_{0.85}$N/GaN quantum well compared to that used in variable stripe length measurements. Photonic crystal cavities are redesigned and fabricated to target operation at the peak PL energy rather than in the low energy tail of the quantum well emission (blue and red dashed lines). The cavity design differs from the rest of this chapter; 24-period mirrors with period $a_b = 119$ nm and hole diameter $d_b = 70$ nm surrounded a 9-hole linear taper to a smaller hole diameter $d_c = 60$ nm and lattice constant $a_c = 102$ nm [179]. These changes
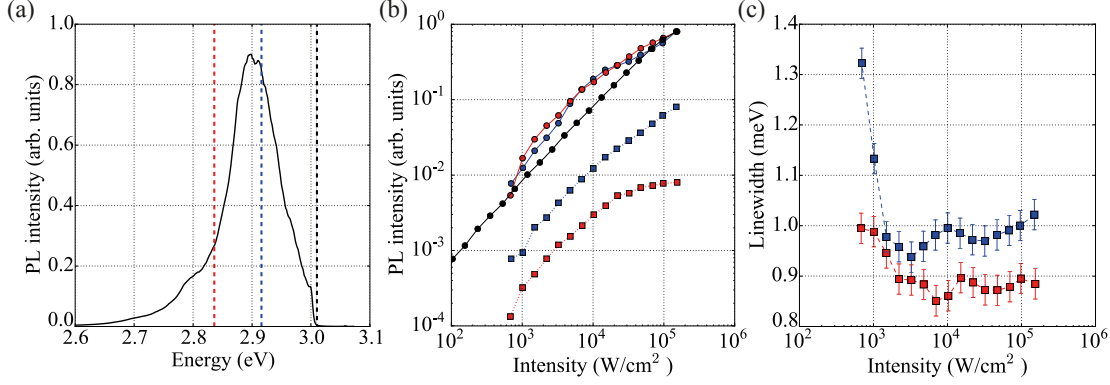
Figure 4.17: Power-dependent μPL with resonant optical pumping ($\lambda = 405$ nm) of a 2 nm In$_{0.15}$Ga$_{0.85}$N/GaN quantum well of unprocessed epilayers (black) and fundamental (blue, $\lambda_{00} = 426$ nm)/first-order (red, $\lambda_{10} = 437$ nm) photonic crystal cavity modes at 4.3 K. (a) Low resolution μPL spectrum of an unprocessed portion of the sample. The dashed colored lines indicate the positions of the photonic crystal cavity resonances. The dashed black line shows the long pass filter cut-on. (b) Power dependence of the integrated μPL intensity of the unprocessed portion (black) and photonic crystal cavity modes (blue/red circles with solid lines). The blue/red squares with dotted lines indicate the μPL background intensity beneath the PhC mode. (c) Photonic crystal cavity mode linewidth narrowing.

accentuate quantum well absorption, allowing a measurement of an upper bound on quantum well absorption losses.

Since the quantum well time response can be described by a simple exponential time dependence (Appendix A), the steady-state photogenerated exciton density (n_{ph}) can be estimated from the related first-order differential equation by

$$n_{\text{ph}} = \frac{R_{\text{ph}}}{\gamma_{\text{exp}}(T)}, \tag{4.16}$$

where R_{ph} is the optical pump rate and γ_{exp} is the experimental decay rate at 4 K. R_{ph} is related to the pump photon intensity (I) by,

$$R_{\text{ph}} = \frac{I \cdot \text{Tr}_{\text{GaN}} \cdot \left(1 - e^{-\alpha d_{\text{qw}}}\right)}{\hbar \omega}. \tag{4.17}$$

where $\text{Tr}_{\text{GaN}} = 0.82$ is the Fresnel transmission of the GaN layers at 405 nm and α is the quantum well absorption coefficient at 405 nm. d_{qw} is the quantum well thickness (2 nm). Taking $\alpha = 1 \times 10^5$ cm^{-1} for bulk GaN absorption above the band edge[1] [180], about 1.8% of the transmitted 405 nm pump is absorbed by the quantum well. Employing an estimated $\gamma_{\text{exp}}^{-1} \sim 5$ ns from Appendix A and $I = 10$ kW/cm^2, $n_{\text{ph}} \sim 6 \times 10^{12}$ cm^{-2}. This compares favorably

---

[1]We assume that 405 nm is sufficient to pump the InGaN alloy in the bulk continuum of states and that the alloy's absorption above its bulk band gap is similar to GaN.

with the transparency threshold for InGaN/GaN quantum well, $n_{tr} \sim 3 \times 10^{12}$ cm^{-2}. Therefore, we conclude that the observation of linewidth narrowing at 4 K is consistent with quantum well densities exceeding the transparency threshold.

Figure 4.17(c) demonstrates clear linewidth narrowing for both cavity modes. The fundamental mode narrows by 300 μeV, whereas the first-order mode narrows by 100 μeV. Since the fundamental mode resides on the high energy side of the quantum well emission, it experiences more absorption due to the Stokes shift imparted by the quantum confined Stark effect (Section 2.4.4). 100 μeV linewidth narrowing constitutes an upper bound on quantum well absorption loss; this corresponds to a $Q_{qw} > 2.9 \times 10^4$ at 437 nm, whereas 300 μeV of narrowing corresponds to a $Q_{qw} > 9.5 \times 10^3$ at 426 nm. Therefore, we conclude that quantum well absorption does not limit nanobeam photonic crystal cavity Q when the photonic crystal cavity mode is on the low energy tail of the quantum well photoluminescence spectrum.

Comparing the power-dependent intensity (Fig. 4.17 (b)) with the linewidth narrowing (Fig. 4.17(c)) enrichens the discussion of nanolaser physics. At around 10 kW/cm^2, a change in the photonic crystal power dependence from approximately linear to sublinear behavior occurs concomitant with a plateau in the linewidth. This input-output curve kink is in the opposite direction of a conventional laser; this could be attributed to the complex nature of the InGaN/GaN quantum well gain medium at cryogenic temperatures [27, 181]. As discussed in Appendix A, under low pumping intensities at temperatures below 120 $\sim$ 160 K, the majority of excitons in the quantum well are localized. At high power approaching the transparency threshold, the Mott transition to an electron-hole plasma in the quantum well is expected [85].

The kink occurs simultaneously with a saturation of the background μPL intensity of the first-order mode (Fig. 4.17(b), red dotted line), which is consistent with clamping of the carrier density in the gain medium at this energy, e.g. lasing in the first-order mode. The fundamental mode, on the other hand, does not exhibit gain medium clamping, which is coherent with the lower relative Q. However, we note that power-dependent $g^{(2)}$ measurements remain the ultimate arbiter of lasing behavior [27, 33]. In addition to such measurements, further setup modifications should allow for higher resonant excitation intensity to see if the linewidth again narrows after the plateau following the modified Schawlow-Townes law for semiconductor lasers [18]. As the focus of this chapter is on nanobeam cavity Q, we leave such measurements to future work.

4.5.3 Surface scattering

In this subsection, the effects of scattering due to surface height fluctuations are examined by experiments and simulations. First, the experimental top and bottom surface roughness are extracted from AFM scans. Then, the experimental surface roughness profiles serve as input for Q_{sr} simulations.

Horizontal surfaces
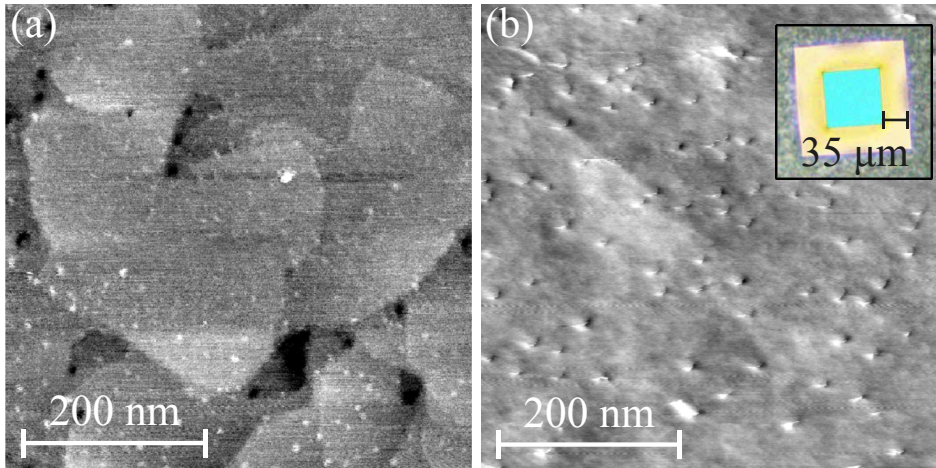
Figure 4.18: 500×500 nm^2 AFM scans of the (a) top and (b) bottom surfaces. Vertical scale is 6 nm. Inset shows an optical microscope image prior to exfoliation to access the nitrogen-polar AlN surface. Reproduced from [14] with permission from APS.

500×500 nm^2 AFM scans of the top GaN and bottom AlN surfaces are shown in Fig. 4.18(a) and (b), respectively. The top surface RMS surface roughness was 1.4 nm. The bottom surface was accessed following an extended underetch of the Si substrate in XeF$_2$ vapor to expose a ~ 35 μm wide edge at the corner of a 200×200 μm^2 lithographically patterned square, as shown in Fig. 3.6(a). Then, the sample chip was flipped upside down onto a piece of double sided adhesive tape stuck to a silicon carrier wafer. After the chip was removed, the free-standing GaN edge remained stuck to the carrier wafer for AFM scanning. For 500×500 nm^2 scans, the back surface RMS roughness was 0.6 nm and the apparent pin pricks are actually dips corresponding to dislocations, whose density is 3-4 $\times 10^{10}$ cm^{-2}, a typical value for AlN on silicon [98]. While such small scans characterize high spatial frequency surface roughness, it is also important to understand lower frequency spatial components from large area scans, which is henceforth called surface *waviness*.

Over a 25×25 μm^2 area (Fig. 4.19(a)), waviness at lower spatial frequencies becomes apparent. The RMS waviness is 4.9 nm. 30 nm peak-to-valley height variations over 5-10 μm length scales become readily visible under sufficient magnification in a standard optical microscope as different colors arising from thin film interference (Fig. 4.19(b)). With the surface roughness and waviness characterized by multi-scale AFM mappings, modeling, and simulations may begin.

First, the surface roughness and waviness must be parameterized. An AFM mapping can be thought of as a 2D matrix of height values, $H(x_i, y_j)$. The 2D autocorrelation function ($\gamma(x, y)$)
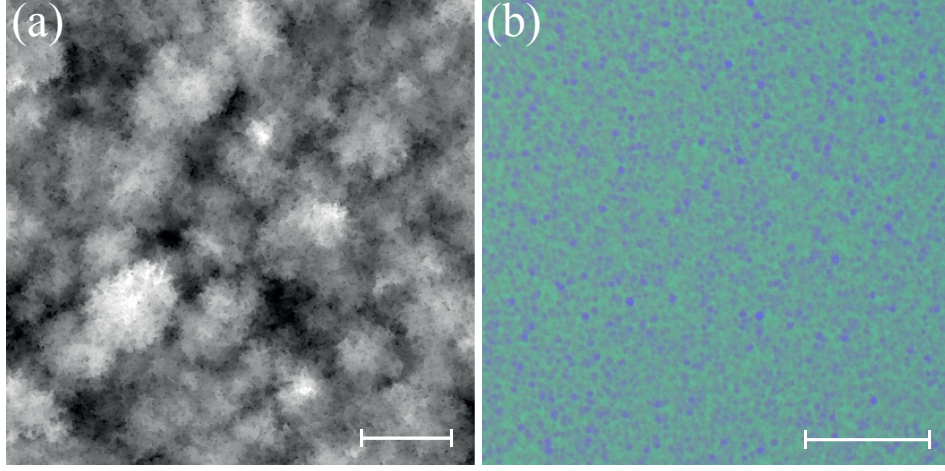
Figure 4.19: (a) 25×25 μm^2 AFM scan of the top epilayer surface. Vertical scale is 30 nm. Scale bar is 5 μm. (b) Corresponding optical microscope image under 20× magnification. Scale bar is 50 μm.

for the mapping is

$$\gamma(x,y) = \lim_{N_x \to \infty} \lim_{N_y \to \infty} \frac{1}{N_x N_y} \sum_{i=0}^{N_x} \sum_{j=0}^{N_y} H(x_i, y_j) H(x_i + x, y_j + y). \tag{4.18}$$

By the Wiener-Khinchin theorem, $\gamma(x,y)$ is the inverse Fourier transform of the power spectral density function, $S(k_x, k_y)$ [153]. Figs. 4.20(a-b) show the power spectral density functions taken along cuts at $\theta = \arctan(k_y/k_x) = 30$, 45, and 60° for the 500×500 nm^2 and 30×30 μm^2 scans of the top surfaces, respectively. The solid lines show fits to parameterizations for surface roughness (Fig. 4.20(a)),

$$S_r(k_x, k_y) \propto A e^{-2|k|^2/L_{r1}^2} + B e^{-2|k|/L_{r2}}, \tag{4.19}$$

where $A/B = 73$. $L_{r1} = 32$ nm and $L_{r2} = 26$ nm are the correlation lengths for surface roughness. For surface waviness (Fig. 4.20(b)),

$$S_w(k_x, k_y) \propto |k|^p, \tag{4.20}$$

where $p = -2.1$ is the exponent for surface waviness. The functions were selected to fit the experimental relationships.

Computationally generated rough and wavy surfaces can now be algorithmically generated using the following recipe [182],

1. Initialize a random k-space matrix using a uniform distribution.
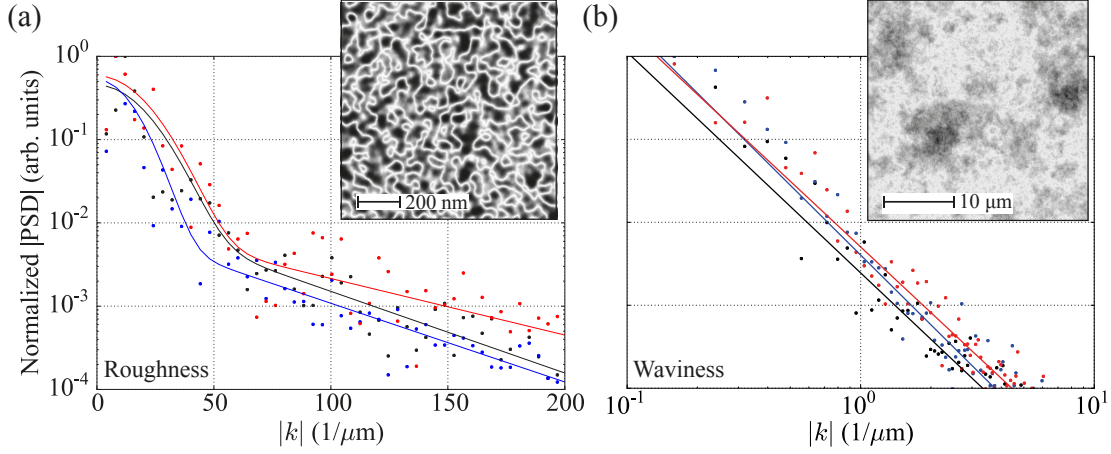
Figure 4.20: Power spectral density (PSD) of surface roughness along different directions in k-space for (a) high (roughness) and (b) low (waviness) spatial frequencies of the AFMs shown in Figs. 4.18-4.19, respectively. Insets show corresponding computationally generated surfaces using the parameterizations and algorithm described in the text.

2. Apodize the random matrix (Eq. 4.19 or Eq. 4.20).

3. Take the square root of the resulting matrix.

4. Apply the 2D inverse Fourier transform to generate a real-space matrix of height fluctuations.

5. Adjust the fluctuation amplitude such that the RMS roughness matches the experimental value.

Now, the parameterized rough surface may serve as an input parameter for electromagnetic computations.

Electromagnetic perturbation theory is well-suited for scattering shifts and losses due to nanoscale roughness and waviness. Let us assume that a photonic crystal described by real-valued relative permittivity $\varepsilon_r(\mathbf{r}) = \varepsilon_r^{(0)}(\mathbf{r}) + \varepsilon_r^{(1)}(\mathbf{r})$, where $\varepsilon_r^{(1)}(\mathbf{r})$ describes a small perturbation due to surface roughness or waviness. The simple formalism presented in Eq. 4.15 must be revised for the case of shifted high refractive index contrast boundaries, such as photonic crystals, due to the continuity of the perpendicular component of the electric displacement field at material interfaces,

$$\Delta \nu = -\frac{\nu_0}{2} \frac{\int_V \left\{ \varepsilon_r^{(1)}(\mathbf{r}) |\mathbf{E}_\parallel(\mathbf{r})|^2 - [\varepsilon_r^{(1)}(\mathbf{r})]^{-1} |\mathbf{D}_\perp(\mathbf{r})|^2 \right\} d^3\mathbf{r}}{\int_\Omega \varepsilon_r^{(0)}(\mathbf{r}) |\mathbf{E}(\mathbf{r})|^2 d^3\mathbf{r}}, \tag{4.21}$$

where $\mathbf{D}_\perp = \varepsilon^{(0)} \mathbf{E}_\perp$ is the component of the displacement field perpendicular to the interface and $[\varepsilon_r^{(1)}(\mathbf{r})]^{-1} = 1/\varepsilon_r^{(1)}(\mathbf{r}) - 1/\varepsilon_r^{(0)}(\mathbf{r})$ [175].
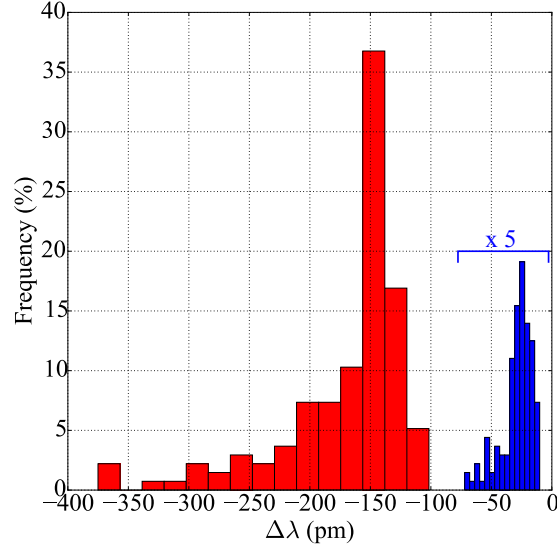
Figure 4.21: Cavity resonance shifts due to a 4.9 nm RMS surface waviness on the nanobeam's top surface in Section 4.1.3. 131 realizations of surface waviness (Eq. 4.20) were simulated to construct the histograms of the fundamental (blue) and first-order (red) modes. The fundamental mode shift has been magnified by five for clarity.

Fig. 4.21 shows the calculated wavelength shifts for the nanobeam photonic crystal geometry from Section 4.1 over 131 random surfaces generated using Eq. 4.20.[2] The two distributions are skewed with long tails to the red. The first-order mode is shifted more than the fundamental mode due to its larger spatial extent, demonstrating how surface roughness may increase the mode splitting. Both shifts, however, will be shown to be minor compared to the fabrication disorder fluctuations (Section 4.5.4). At first glance, the greater relative impact of a small hole shift compared to a 30 nm peak-to-peak height fluctuation may seem counterintuitive. However, this result can be explained by defining surface-to-volume integrals of the 3D-FDTD simulated electric field intensities,

$$
f_S = \Delta x \frac{\int_S \varepsilon_r^{(0)}(\mathbf{r})|\mathbf{E}(\mathbf{r}) \cdot \hat{n}|^2 \, dS}{\int_V \varepsilon^{(0)}(\mathbf{r})|\mathbf{E}(\mathbf{r})|^2 d^3\mathbf{r}}, \tag{4.22}
$$

where Δx is the simulation pixel size. Table 4.2 reflects the values computed for the geometry presented in Section 4.1. The simulated overlap with the top and bottom surfaces (f_H) is a factor of 760× smaller than that of the vertical sidewalls (f_V), justifying the small sensitivity to surface height fluctuations. Since Eq. 4.21 computes only the wavelength shift, another perturbative formalism, the volume current method, is required to compute scattering losses.

Appendix B presents the derivation of the volume current method, discusses the physical insight associated with the scattering equations, and documents the validation of a scattering code for nanobeam photonic crystals written in the context of this thesis. The same 131 wavy

---

[2]The surface roughness fluctuations (Eq. 4.19) are an order of magnitude smaller and are ignored here.

Mode	$\bar{Q}_{\mathrm{sr}}$	$\tilde{Q}_{\mathrm{sr}}$	f_V	f_H	$V_0 \; (\lambda/n_{GaN})^3$
TE$_{00}$	2.8×10^5	2.2×10^5	9.9×10^{-2}	1.3×10^{-4}	1.4
TE$_{10}$	4.1×10^4	3.1×10^4	8.9×10^{-2}	1.5×10^{-4}	2.6

Table 4.2: Computed mean ($\bar{Q}_{\mathrm{sr}}$) and median ($\tilde{Q}_{\mathrm{sr}}$) scattering loss contributions due to 131 realizations of surface waviness for the fundamental (TE$_{00}$) and first-order (TE$_{10}$) nanobeam photonic crystal cavity modes. Surface overlap integrals for the two pixels (~ 12 nm) surrounding the horizontal (f_H) and vertical (f_V) sidewalls (Eq. 4.22) are shown alongside the computed modal volume (Eq. 4.9). The same base geometry was used as in Section 4.1.3.

surfaces (Eq. 4.20) employed for the resonance shift calculations were used as input for the volume current method. The Q_{sr} due to surface roughness (Eq. 4.19) were comparable to Q_{th} because of the smaller RMS roughness and are therefore considered to be negligible for the remainder of the thesis. Fig. 4.22 exhibits the calculated Q_{sr} distributions for the fundamental
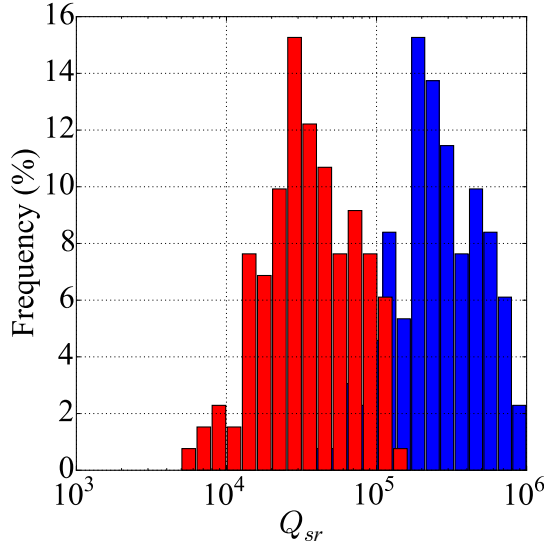
Figure 4.22: Scattering losses due to a 4.9 nm RMS surface waviness computed by the volume current method for the nanobeam geometry from Section 4.1.3. 131 realizations of surface waviness (Eq. 4.20) were simulated to construct the histograms of the fundamental (blue) and first-order (red) modes.

and first-order modes, both of which are skewed with a high Q_{sr} tail (Table 4.2). Q_{sr} is lower for the first-order mode due to its larger spatial extent and lower Q_{th}. However, the computed Q_{sr} of both modes are much greater than the experimentally observed Q. This finding is bolstered by experimental results of photonic crystal and microdisk cavities fabricated from thin ($\lambda/2n$) AlN epilayers on silicon (111) by MBE. Despite the atomically flat surfaces of such epilayers, the experimental Q do not exceed several thousand [11, 15]. Our group has observed similar results in microdisk cavities fabricated from epilayers grown by LASPE Ph.D. student Sebastian Tamariz-Kaufmann using MBE. Therefore, we conclude that scattering due to surface roughness and waviness do not constitute the primary limitation of experimental

Q.

Vertical sidewalls

Sidewall roughness is expected to create additional scattering losses for the TE-like nanobeam photonic crystal cavity modes under study. In contrast to the top surface, sidewall roughness remains relatively inaccessible experimentally, particularly inside the photonic crystal holes. The few publications of sidewall roughness in photonics literature relied upon TEM imaging [77] or AFM of specially designed and cleaved test samples [183]. The sidewall roughness generally is columnar in nature, as it results from line edge roughness of the etch mask and is transferred to the underlying epilayers by dry etching [183]. Furthermore, the edges of dry etched GaAs cavities have been shown to be amorphous due to dry etch damage [77].

The situation in dry etched III-nitrides is unknown. No apparent surface roughness has been observed when looking at cleaved III-nitride surfaces in the Zeiss Merlin SEM, providing an upper bound on the RMS sidewall roughness of ~ 2 nm. Any periodicity of the line edge roughness of the etch mask would be between the step size (1 nm) and spot size (5 nm) in electron beam lithography. The impact of columnar sidewall roughness was simulated using the volume current method (Appendix B) for periods ranging from 1 to 5 nm and RMS roughness up to 3 nm. The resulting Q_{sr} values were on the order of Q_{th} and are considered to be negligible in subsequent discussion. Experimentally, comparison of anisotropic wet etched nanobeams with a control sample processed without wet etching reveals no statistical difference in Q_{exp} (see Section 4.5.5). Therefore, we conclude that sidewall roughness cannot principally limit experimental Q_{exp}.

4.5.4 Fabrication disorder

The theoretical simulations in Section 4.1.3 assume an ideal photonic crystal. In the real world, hole shape and positions fluctuate randomly about their target values due to the finite resolution of electron beam lithography and subsequent pattern transfer. In this section, the magnitude of such critical dimension fluctuations and their impact on nanobeam cavity Q are examined using experiments and simulations.

Experimental critical dimension control

Critical dimension fluctuations after etching are quantified by computational image processing of high resolution SEM images. Images of nominally identical holes were acquired using a Zeiss Merlin SEM operating in immersion mode at 3 kV and secondary electron in-lens detection. The image pixel size corresponded to 0.7 nm at the $90,000\times$ magnification used for critical dimension extraction. The images were processed by a custom algorithm written in Python 2.7 with the OpenCV computational imaging library [184]. In the following, an image can be thought of as a two-dimensional matrix of 8-bit intensity values $I(x, y)$ ranging from 0

(black) to 255 (white). The steps of the algorithm were:

1. Sum the image along the axis perpendicular to the nanobeam, producing a vector $\mathbf{v}_1$.

2. Locate the nanobeam edges by edge detection on $\mathbf{v}_1$.

3. Extract the intensity along a line centered between the nanobeam edges, creating a vector $\mathbf{v}_2$.

4. Estimate each hole's central position by extracting the positions corresponding to local minima of $\mathbf{v}_2$.

5. Break the overall image into a series of sub-images $I_j(x, y)$ of one photonic crystal period each; boundaries were at the nanobeam edges and perpendicular bisectors of the line adjoining adjacent holes.

6. Determine the area belonging to the hole in sub-image $I_j(x, y)$ through application of a binary threshold (I_{th}).

7. Compute the hole radius and position following Eqs. 4.23 and 4.25, respectively.

The radius of the jth hole ($\hat{r}_j$) was estimated from the hole area,

$$\hat{r}_j = \frac{\Delta x}{\pi} \sqrt{\sum_{x,y} \theta\big(I_{th} - I_j(x,y)\big)}, \tag{4.23}$$

where $\theta(x)$ is the Heaviside step function, Δx is the pixel size, and the sum goes over all axes of the sub-image $I_j(x, y)$. The hole centroids ($\hat{x}_j, \hat{y}_j$) were calculated using a weighted sum of the binary thresholded image,

$$\hat{x}_j = \frac{\sum_{x,y} x \cdot \theta\big(I_{th} - I_j(x,y)\big)}{\sum_{x,y} \theta\big(I_{th} - I_j(x,y)\big)}, \tag{4.24}$$

$$\hat{y}_j = \frac{\sum_{x,y} y \cdot \theta\big(I_{th} - I_j(x,y)\big)}{\sum_{x,y} \theta\big(t - I_j(x,y)\big)}. \tag{4.25}$$

Higher order shape errors, such as ellipticity, were not analyzed [185].

In order to check that no artifacts arose from the measurement apparatus, additional tests were performed. First, SEM images with orthogonal raster directions (Fig. 4.23(a-b)) were compared to see if charging affects critical dimension extraction. Little difference is seen between the images. Finally, the SEM images were compared with AFM images of the same nanostructure (Fig. 4.23(c-d)). The image processing algorithm extracted 24.2 ± 0.4 and 24.5 ± 0.6 nm (95% confidence interval) for the hole radii in the SEM and AFM images, respectively. Both techniques detected a slight ellipticity (1-2 nm) along the nanobeam's longitudinal axis.
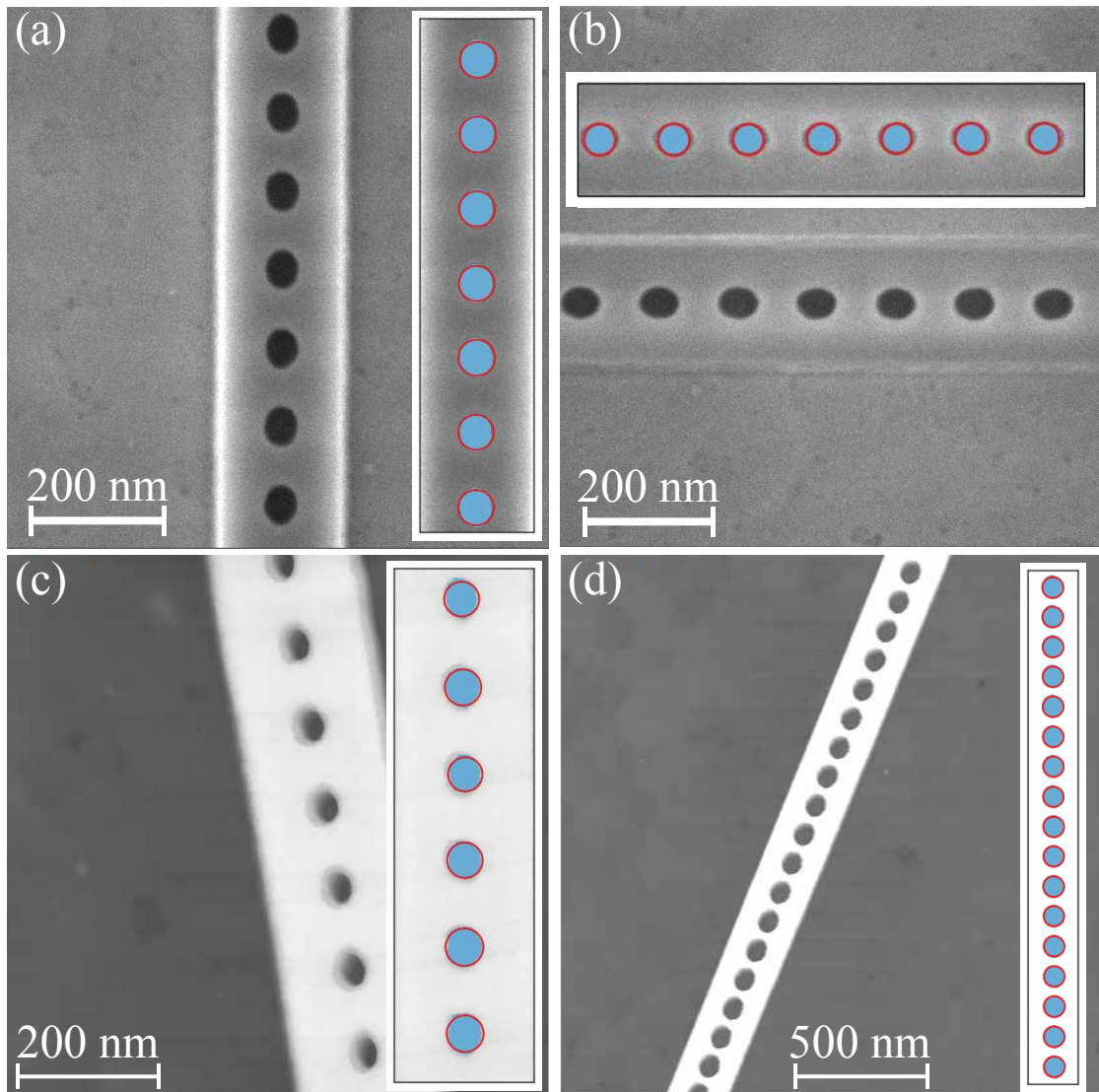
Figure 4.23: (a-b) SEM images of the same HSQ nanobeam on III-nitride epilayers with orthogonal scan directions. Insets show the algorithmically extracted holes (blue) and best fit circle (red). (c-d) AFM images of the same nanostructure at two different length scales. Insets again show the algorithmically processed images for the AFM scans. Reproduced from [14] with permission from APS.

However, the excellent agreement between the techniques affirms the accuracy and precision of the two measurement tools. Although it is non-ideal to work close to the ultimate limits of SEM resolution [186], SEM is one of few techniques capable of delivering hole size statistics at reasonable speed and cost. Therefore, we proceed under the assumption that the SEM images reflect the true underlying material profile.

Figures 4.24(b-c) summarize the statistics of etched hole shape and positioning fluctuations extracted by computational imaging of high magnification SEM images. 85, 128, 158, and 60 holes were analyzed for each of the four target hole diameters, 45, 55, 65, and 75 nm, respectively. The histogram distributions pass statistical tests for normality [187]. As one may naïvely expect, the distribution FWHM broadens as the target hole diameter decreases due to the higher aspect ratio (height/diameter) of the resist pattern and etched hole. Therefore, the minimum nanobeam hole diameter was chosen to be 60 nm for the remainder of this Chapter. For the 65 and 75 nm target hole diameter distributions, the FWHM of the diameter and positioning error was less than or equal to 1.8 nm. This level of precision is on par with estimations of residual disorder in photonic crystal cavities fabricated from silicon at telecom wavelengths [188], proving that it is possible to fabricate with the same level of precision in III-nitride semiconductors.

Figure 4.24(d) documents the other significant deviation from the theoretical ideal, sloped sidewalls. The left-hand side image shows a top-down view of the finished structure, where the rough silicon substrate can be seen through the etched III-nitride holes. The top and bottom surfaces of the nanobeam holes are outlined in red and blue, respectively. Knowing the thickness of the epilayer (h), an effective taper angle of $\arctan(\Delta r / h) = 2.0 \pm 0.3°$ can be deduced. The right-hand side image shows a cross-section of a cleaved slot, which shows that the internal sidewall taper sidewalls are not linearly tapered. Rather, the slope of the sidewall is vertical near the top surface and tapers more rapidly near the silicon substrate. Published theoretical simulations have shown the nanobeam geometry to be resilient to sidewall tapering, as it does not break the symmetry about the nanobeam's longitudinal axis (Fig. 4.6, yz plane), avoiding coupling between gapped TE and ungapped TM modes [189]. For all subsequent simulations, photonic crystal holes are modeled as a quadratic taper with vertical sidewalls at the top surface with an effective taper angle of 2°.

Simulated effect of fabrication disorder

The experimentally determined critical dimension distributions served as input for FDTD simulations of fabrication disorder. Each hole's position and radius was randomly fluctuated about its nominal value by a Gaussian probability distribution with standard deviation 1 nm. Different random number generator seed values were used to generate 100 different realizations of a base nanobeam photonic crystal cavity design, which were then simulated using FDTD. Fig. 4.25 presents histograms of the simulated resonance wavelength and Q_{fab} values for the fundamental (blue) and first-order (red) cavity modes.
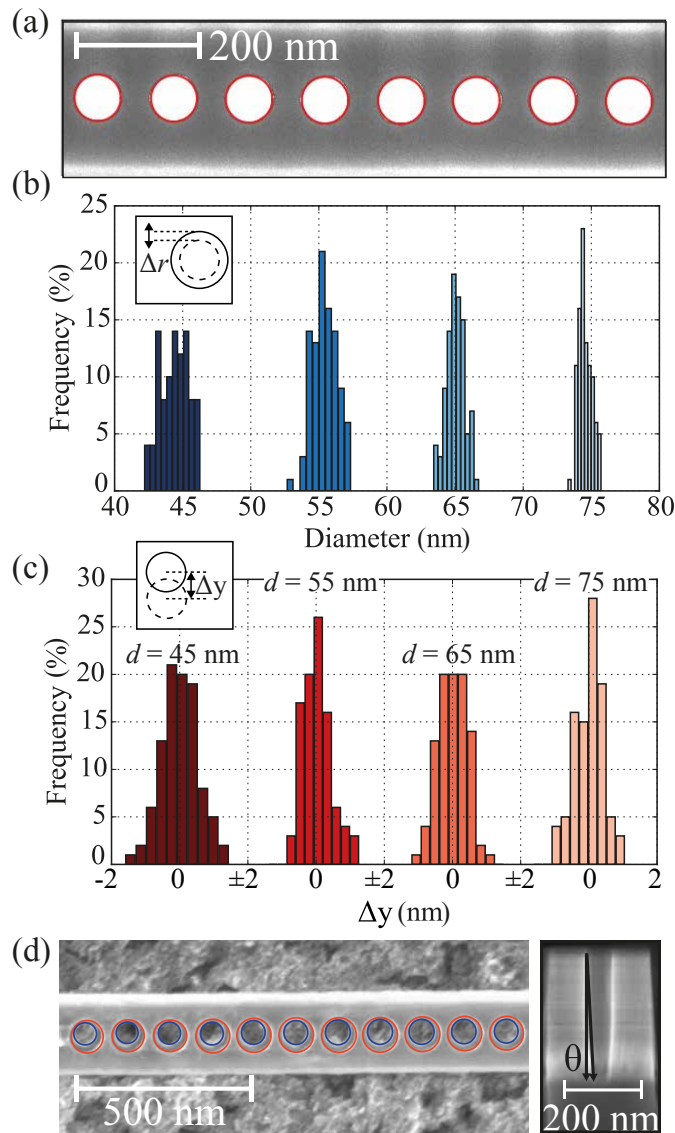
Figure 4.24: Extraction of hole size and positioning errors (critical dimensions or CDs) from SEM images by computational image processing. (a) Processed SEM image showing detected hole area (white) and best fit circles (red). (b) Hole diameter fluctuations for different target hole sizes. $N = 85$, 128, 158, and 60 holes were extracted for the target hole diameters 45, 55, 65, and 75 nm, respectively. (c) Vertical positioning error from best fit centerline for the four target diameters. (d) Parabolic sidewall tapering of $2.0 \pm 0.3°$ measured by SEM of a top view (left) and cross-section view of a test structure (right). Reproduced from [14] with permission from APS.
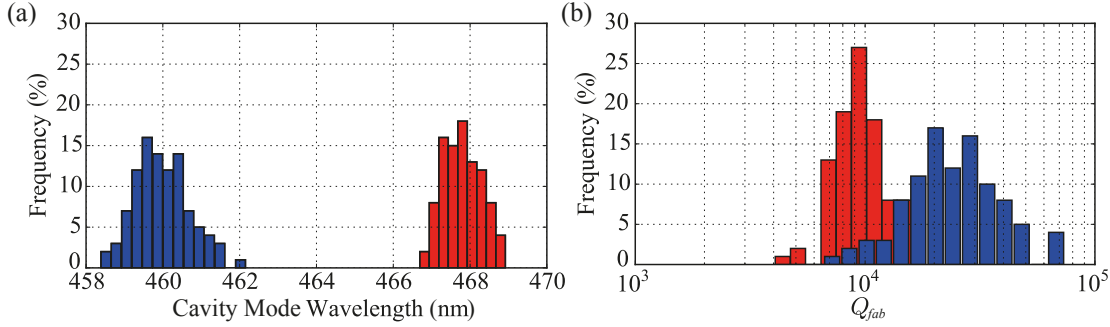
Figure 4.25: 3D-FDTD simulations of 100 realizations of fabrication disorder for hole size and position fluctuations following normal distributions with standard deviation 1 nm. (a) Wavelength histograms for fundamental (blue) and first-order (red) cavity modes. (b) Corresponding Q histograms. Reproduced from [14] with permission from APS.

The wavelengths are normally distributed, but the Q_{fab} are skewed distributions with a tail towards lower values. Such statistics have been previously observed in Gaussian disorder simulations of 2D photonic crystal cavities [190]. The median Q_{fab} values for the fundamental and first-order modes were 2.4×10^4 and 9.6×10^3, respectively, showing that higher order modes are more susceptible to fabrication fluctuations. Narrowing the simulated disorder distributions to 0.5 nm standard deviation resulted in a wavelength distribution narrower than that observed experimentally for nominally identical nanostructures. Broadening the disorder distributions to 2 nm standard deviation resulted in the simulated yield of viable cavities falling far below the experimental yield. Increasing the simulation spatial resolution did not have a significant effect on wavelength and Q distributions. The next section compares disorder simulations with experiment, supporting the claim of single nanometer critical dimension control in the fabricated III-nitride photonic crystal nanobeams.

Comparison with experiment

With the critical dimension statistics known, the influence of nanobeam geometry on Q_{fab} was explored theoretically and experimentally. For each of four base designs (Table 4.3), all

Design #	λ_{00} (nm)	λ_{10} (nm)	a_b (nm)	d (nm)	d_c (nm)
1	451	458	117	70	84
2	457	464	119	70	84
3	461	471	120	60	84
4	471	479	122	60	84

Table 4.3: Four cavity design dimensions without any lithographic hole bias and 3D-FDTD simulated fundamental (λ_{00}) and first-order (λ_{10}) cavity mode wavelengths including material dispersion and hole sidewall taper. There are 18 holes in each Bragg mirror with period a_b and diameter d_b surrounding an 18-hole quadratic taper to a central hole cavity diameter d_c.

hole radii were simultaneously lithographically biased from -3 to +4 nm in single nanometer

steps. Twelve nominally identical nanobeams were fabricated and measured for each hole bias of each base design for a total of 372 nanobeams, of which 361 (97%) exhibited at least one measureable cavity resonance. On the simulation side, twenty disorder realizations of each hole bias were simulated using sidewall tapering and Gaussian-distributed hole radii and position fluctuations.

Figures 4.26(a) and 4.26(b) exhibit the experimental and simulated Q distributions for the fundamental and first-order cavity modes, respectively. Each color represents a different base
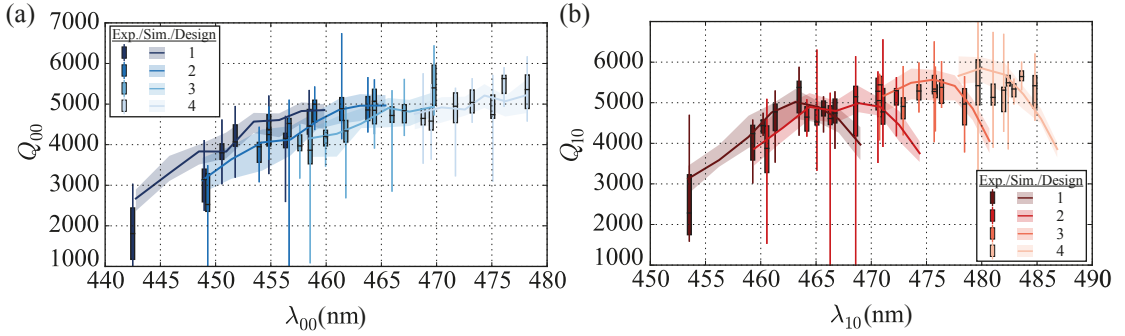
Figure 4.26: Simulated (solid polygons) and experimental (boxes) Q of (a) fundamental and (b) first-order modes for lithographically biased variations of the four base designs (c.f. Table 4.3) from -3 to +4 nm. Each geometry was simulated 20 times and the polygon represents the interquartile range of fit Q values (see text for procedure). Each box-and-whisker point represents the measured interquartile range and extrema over 12 nominally identical nanobeams under 351 nm 1.6 kW/cm^2 cw optical pumping at room temperature. Reproduced with permission from [14] with permission from APS.

design and each data point within each color represents twelve measurements over twelve nominally identical structures. Due to the non-Gaussian Q statistics, a box-and-whiskers format is adopted for experimental data representation, where the box, line within the box, and whiskers represent the first and third quartile, median, and extrema of the measured values. As expected within each data series, larger hole sizes result in the cavity mode blueshift due to more of the electric field being in the lower refractive index material, air. Generally, as the hole diameter is increased within each geometry, experimental Q decreases for the fundamental mode while many first-order modes exhibit a local maximum as a function of the lithographic hole bias.

The geometry dependence of experimental fundamental and first-order cavity mode Q can be explained by fabrication disorder. To fit the FDTD-simulated Q_{fab} to experiment, an offset Q_{off} must be added to account for bulk absorption (Q_{bk}), surface absorption (Q_{sa}), and surface roughness/waviness scattering (Q_{sr}) losses (Eq. 4.10), where

$$Q_{\text{off}}^{-1} = Q_{\text{bk}}^{-1} + Q_{\text{sa}}^{-1} + Q_{\text{sr}}^{-1}. \tag{4.26}$$

The Q_{off} values were fit separately for the fundamental and first-order modes by several meth-

ods, including global and pair-wise least-squares minimization [14]. No matter the method, $Q_{off,00} \approx 6000$ and $Q_{off,10} \approx 8500$ were found. In Fig. 4.26, the offset simulations are represented by the shaded polygons in the background, where the polygon represents the interquartile range and the solid line the simulated median. Even with the simple, dispersionless Q_{off}, the simulations fit the experimental data well; the decreasing Q_{00} with larger hole radius and the local maxima within each design Q_{10} can be accounted for by fabrication disorder. Most importantly, since $Q_{off} < Q_{fab}$, we can conclude that fabrication disorder does not limit experimental Q. However, such modeling does not explain the physical origin of Q_{off}, the principal limiting mechanism for experimental Q_{exp}, so additional experiments are needed to identify the broadening mechanisms and then reduce their impact on Q_{off}.

Clues buried in the statistics of the experimental data suggest that Q_{off} is linked to the surface. Two-sided statistical tests on the experimental Q for two sets of twelve nanobeams with different base designs but whose holes are lithographically biased such that their average resonance wavelengths are statistically equal reveal correlations with cavity design geometry. Statistically speaking, the condition "average resonance wavelengths are statistically equal" was translated as being unable to reject the null hypothesis at $p = 0.05$ in a two-sided unequal variances t-test, which was selected because the average resonance wavelengths should be normally distributed but the variances of the parent populations are unknown and likely unequal. However, as the Q distributions are skewed, one cannot simply use Student's t-test to compare Q population means. Instead, Wilcoxon-Mann-Whitney rank tests with $p = 0.05$ were used for comparing Q values [191, 192]. A look-up table was used instead of the normal approximation because of the $N = 12$ sample size.

The null hypothesis, two geometries draw from the same Q population distribution, was rejected in 5/39 two-sided tests of Q_{00} and for 0/31 tests on Q_{01}, when controlling for average wavelength. In each of the cases where the null hypothesis was rejected, the cavity with the largest central cavity hole diameter (d_c) exhibited lower experimental Q. The fact that the first-order mode's electric field intensity profile exhibits a node in the cavity center (Fig. 4.6) further supports the correlation between central cavity hole diameter and experimental Q. Although correlation does not imply causation, a plausible causal explanation would be that larger central cavity holes increase the interfacial surface area where the electric field intensity is strongest in the cavity center, which maximizes the overlap integral in electromagnetic perturbation theory (Eq. 4.22/Table 4.2).

Despite the satisfactory agreement between simulated and experimental Q values, certain experimental fabrication statistics remain unexplained by the simple model fabrication disorder with normally distributed hole size and position fluctuations. Fig. 4.27 shows the average of the first and fundamental mode wavelengths versus half their average splitting for (a) simulated and (b) experimental data. For each of the 12 nominally identical nanobeams corresponding to a specific hole bias and base design, the average wavelength and splitting were computed individually. Each data point in Fig. 4.27 represents the average and standard deviation over each of the twelve cavities' mean wavelengths and splittings. Simulated
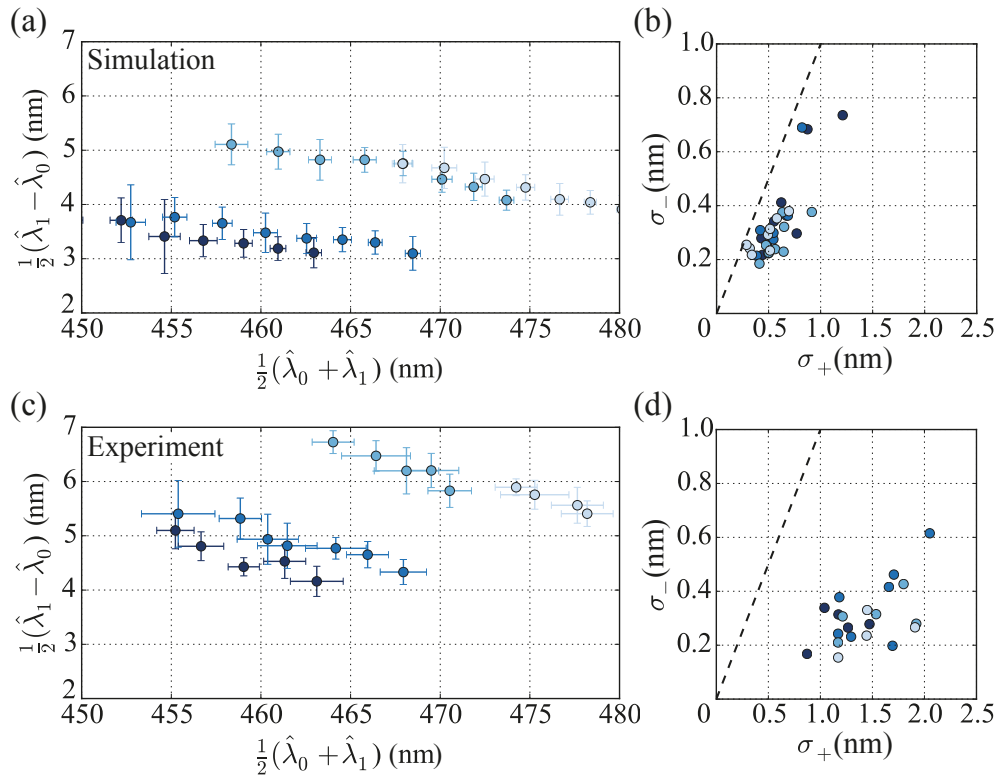
Figure 4.27: Comparison of (a,b) simulated and (c,d) experimental average wavelengths and splittings. (b,d) show the correlations in the standard deviations of the average wavelength and splittings. Reproduced with modification from [14] with permission from APS.

and experimental average wavelengths are in reasonable agreement, but the simulations systematically underestimate the splitting between the two modes.

The insets in Fig. 4.27 show the standard deviations of the average wavelengths (σ_+) and splittings (σ_-). The disorder model's σ_- is approximately the same as experiment, but the experimental fluctuations in the average wavelength (σ_+) are more than a factor of two larger. Despite the single nanometer critical dimension tolerances, $\sigma_+ > \lambda/Q$ poses a barrier to future development and eventual commercialization because it is not possible to deterministically manufacture a cavity to be resonant with an emitter at a specific wavelength; additional metrology & fabrication steps and/or active tuning mechanisms would be required for post-fabrication tuning. In Section 4.5.5 and Chapter 5, photoinduced oxygen desorption is shown to be a possible mechanism to deterministically tune cavity resonances. However, such discrepancies suggest a need for more complex models of fabrication disorder.

4.5.5   Surface absorption

Surface absorption must account for the remaining losses ($Q_{\mathrm{sa}} \approx Q_{\mathrm{off}}$). Many hints at the role of surface absorption are buried in the results of the previous experiments: scattering from both fabrication disorder and surface waviness impacts the first-order mode more than the fundamental mode. On the other hand, we find that $Q_{\mathrm{off,10}} > Q_{\mathrm{off,00}}$ is required to fit experimental disorder data to FDTD simulations of disordered cavities. Therefore, a different mechanism must be at play. This apparent contradiction can be resolved by invoking surface state absorption, which could be due to intrinsic or extrinsic defects. The ratio of the overlap integrals of the electric field with the vertical sidewalls, $f_{v,00}/f_{v,10}$ (Eq. 4.22 / Table 4.2), roughly corresponds to the ratios of the offset $Q_{\mathrm{off,10}}/Q_{\mathrm{off,00}}$.

Recounting Ch. 2, III-nitrides exhibit deep, localized surface states within the bulk material band gap. In n- and uid GaN, the high density of surface states pins the surface Fermi level, resulting in space charge region (SCR) formation and upward band bending at the GaN surface in thermal equilibrium. The surface state density and distribution depend on both the crystal orientation and surface treatment relative to the electric field vector of the photonic crystal mode. Past studies of surface state absorption on GaAs [193] and silicon [194] surfaces indicate that optical absorption by surface states is stronger when the electric field vector is parallel to the surface normal. Although no such studies have been done for III-nitrides, this past result is likely to be further exacerbated by the polar nature of the III-nitride semiconductor material.

In this section, we show that the nanobeam photonic crystal cavities are sensitive to the surface. Surface phenomena are explored in detail in Chapter 5.

Surface sensitivity

Two experiments show that nanobeam photonic crystals are sensitive to the surface. Under 351 nm cw optical pumping in ambient atmosphere, irreversible deposition occurs on the

sample surface. The cavity mode resonances broaden and redshift with time in μPL (Fig. 4.28) and the signal does not return after waiting, even overnight. No such deposition is observed
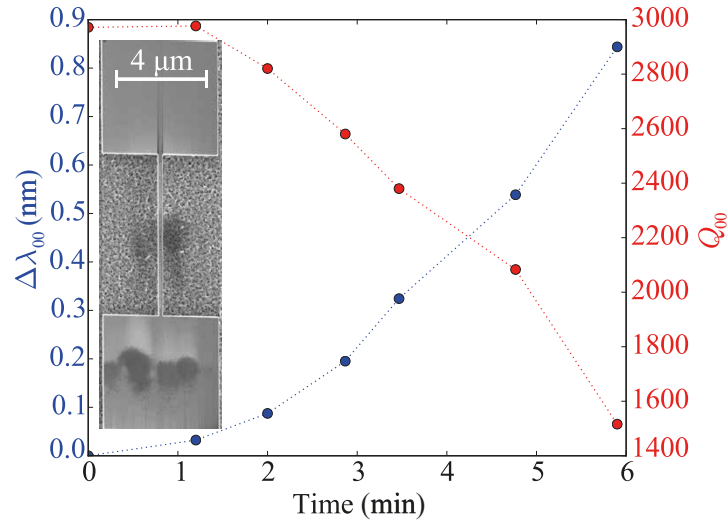
Figure 4.28: Redshift and broadening of fundamental mode observed under cw 351 nm optical pumping in ambient atmosphere. These changes occur concomitantly with a μPL intensity decrease. Inset shows SEM image taken at 3 kV of the same nanobeam photonic crystal cavity following μPL spectroscopy. Reproduced from [14] with permission from APS.

when optical pumping under vacuum. The localized deposition, resembling cigarette burns, is readily visible under low acceleration voltage in the SEM (Fig. 4.28, inset). EDX analysis, although not entirely reliable for light elements [133], suggests that the deposits are carbon-based. The carbon-based deposition is so thin, however, that it does not appear as a surface morphology difference in AFM. Therefore, we conclude that carbon is deposited on the sample surface by cracking of airborne organic molecules or CO_2 under UV laser illumination. Evidently, absorption by a few monolayers of carbon and/or the change in the absorption of surface states is sufficient to completely damp the photonic crystal cavity modes.

In the second experiment, the same set of 12 nanobeams (row 3 in Table 4.3) with lithographic bias is measured before and after conformal coating of 3 nm of high refractive index HfO_2 dielectric by atomic layer deposition (ALD). The refractive index of the as-deposited ALD HfO_2 films was found to be 2.07 in a Cauchy model in spectroscopic ellipsometry, which is close to the refractive index of AlN ($n = 2.1$) and GaN ($n = 2.4$) in this spectral region. Fig. 4.29 shows that, as expected, the fundamental cavity modes redshift due to the addition of dielectric to the structure. Comparing coated and uncoated different lithographic biases at the same resonance wavelength, a decrease in Q_{exp} is observed. However, such an experiment is imperfect because the decrease may be due to scattering from surface roughness at an additional dielectric interface, absorption in the HfO_2, or absorption by modified surface states in the III-nitride. Thus, experiments without coatings are required, which will be explored in Ch. 5.
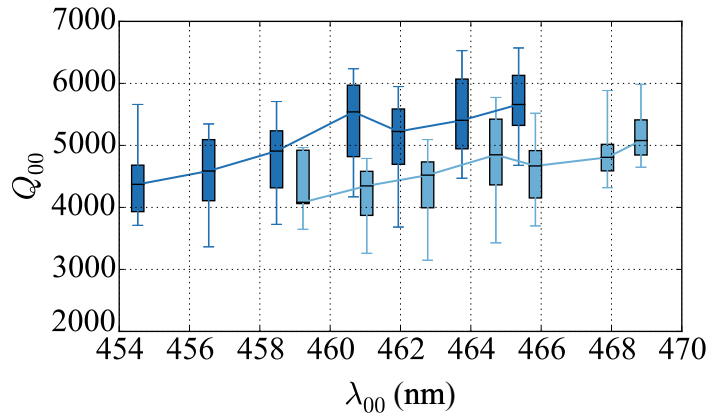
Figure 4.29: Redshift and broadening of fundamental mode for design 2 (Table 4.3) before and after coating with 3 nm ALD HfO$_2$. Twelve nanobeams were measured per point. Reproduced with permission from [14] with permission from APS.

Anisotropic wet etching

Anisotropic wet etching can help remove extrinsic defect states caused by dry etching III-nitride materials [195, 196]. Both TMAH and KOH are known to etch III-nitride materials anisotropically, with the slowest etch rate being on the m-plane [197, 198]. By aligning the nanobeam pattern such that the nanobeam sidewalls are parallel to the m-plane of the crystal, vertical sidewalls aligned with the m-plane can be achieved. The initially round holes become hexagons (Fig. 4.30(a)).

In this thesis, the nanobeams were etched in 3 M KOH solution at 30 °C for 60′. We note that KOH also etches the (100) and (110) planes of the silicon substrate while the (111) silicon plane, which is aligned with the m-plane of GaN, remained nearly untouched. Wet etching should be performed between the dry etch and vapor phase etch steps in order to protect the nitrogen-polar III-nitride surfaces because some bases can vigorously attack the nitrogen-polar AlN surface leading to surface roughness and upward bowing of the nanostructure (e.g. Fig. 4.11(b)). However, 3 M KOH at 30 °C does not appear to attack exposed nitrogen-polar AlN surfaces, which are protected by a nitrided silicon layer at the epilayer-substrate surface. The KOH process was adopted for a comparative study of nanobeam Q with and without wet etching.

A full 2" wafer of 5 nominally identical 9×9 mm^2 nanobeam chips was processed simultaneously. The reference sample and test sample were fabricated from chips at the same radial distance from the wafer center to control for epilayer thickness inhomogeneity across the wafer. The epilayers contained the same 2 nm thick In$_{0.15}$Ga$_{0.85}$N/GaN quantum well used in the quantum well absorption experiments. Both the reference and KOH-etched sample were treated by rapid thermal annealing following the optimized recipe developed in Chapter 5.

The cavity design employed two 24-period mirrors linearly tapering to a pair of holes with
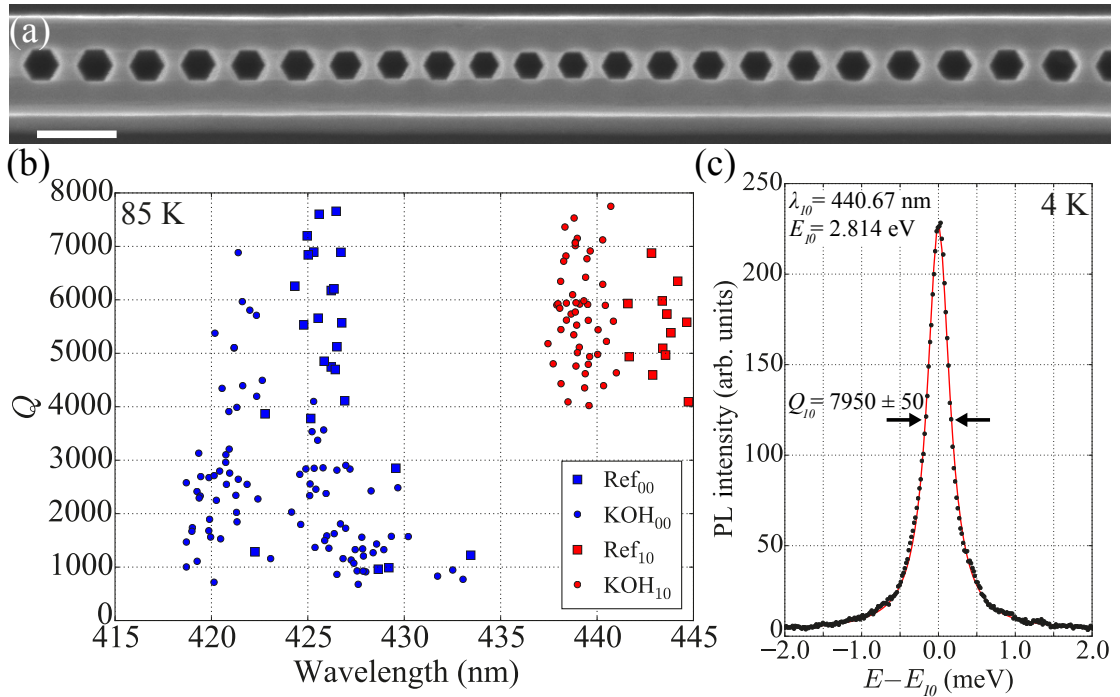
Figure 4.30: (a) Top view of a nanobeam photonic crystal cavity test structure with hexagonal holes created by anisotropic wet etching in 3 M KOH at 30 °C for 60′. The faint circular outline is due to the HSQ mask, which has not yet been stripped. Scale bar is 200 nm. (b) Experimental Q dispersion of 21 nominally identical reference and 69 nominally identical KOH etched nanobeams measured at 10 kW/cm^2 405 nm resonant pumping at 85 K, below the quantum well transparency threshold. Quantum well absorption is subtracted from the linewidth using a two-point linear interpolation based on the values found in Section 4.5.2. Blue is the fundamental and red is the first-order mode of the photonic crystal cavity. (c) High resolution μPL spectrum of the KOH-etched sample with $Q_{10} = 7950 \pm 50$ at 440.67 nm measured using 10 kW/cm^2 resonant pumping at 4 K, above the transparency threshold of the quantum well.

smaller lattice constant and diameter [179]. The parameters written by electron beam lithography were mirror period $a_b = 121$ nm and hole diameter $d_b = 72$ nm surrounding a 9-hole linear taper to a smaller hole diameter $d_c = 61$ nm and lattice constant $a_c = 100$ nm. The effective hole size is enlarged by ~ 2 nm during the KOH etching. The simulated wavelengths and modal volumes of the KOH etched nanobeams with hexagonal holes were $\lambda_{00} = 419/\lambda_{10} = 440$ nm and $V_{00} = 0.3 \cdot (\lambda/n_{\mathrm{GaN}})^3/V_{10} = 0.5 \cdot (\lambda/n_{\mathrm{GaN}})^3$, respectively. The smaller modal volumes are due to the on-axis vertex of the hexagon, which decreases the available volume available for the electromagnetic mode between holes.

μPL spectra were measured at 85 K using 10 kW/cm^2 and $\lambda = 405$ nm resonant pumping to minimize cryo-gettering on the sample surfaces. Although the same amount of linewidth narrowing (Section 4.5.2) was again observed at 4 K in these structures using resonant and non-resonant pumping, no linewidth narrowing was observed at 85 K and 10 kW/cm^2 resonant pumping due to the increased threshold pump intensity caused by thermally activated nonradiative recombination (Appendix A).

Figure 4.30(b) compares the Q of the reference and KOH etched samples. 69 and 21 nominally identical KOH-etched and reference nanobeams were measured, respectively. As expected when enlarging holes, the KOH modes are blueshifted relative to the reference sample. Because the quantum well is being driven below the transparency threshold, the quantum well absorption was subtracted from the linewidth using a two point linear interpolation from the values reported in Section 4.5.2. To check the validity of this procedure, Fig. 4.30(c) shows the maximum $Q_{10} = 7950 \pm 50$ measured using 10 kW/cm^2 405 nm resonant pumping at 4 K, i.e. above the transparency threshold with the 1800 lp/mm grating in second order. This value is in excellent agreement with the highest recorded Q_{10} value for the KOH etched sample.

To test if the KOH treatment improved Q_{10}, a Wilcoxon-Mann-Whitney rank test was performed on the two $\hat{Q}_{10}$. The null hypothesis, that one $\hat{Q}_{10}$ sample is statistically larger than the other, cannot be rejected at $p = 0.05$. Thus, we conclude that it is statistically unlikely that the KOH treatment changes optical performance. This conclusion confirms the prediction of negligble losses by scattering from sidewall roughness and suggests that either intrinsic m-plane defects and/or etch damage at a depth > 2 nm are limiting Q.

Figure 4.31 shows histograms of the etched KOH sample's wavelengths and Q over the 69 measured structures at 85 K and 10 kW/cm^2, $\lambda = 405$ nm resonant optical pumping. The fundamental mode shows a bimodal distribution of wavelengths. We attribute this to the marginal stability of the design with hexagonal holes at 420 nm; despite the epilayer thickness of $3\lambda/2n_{\mathrm{GaN}}$, V_{00} is amazingly $0.3(\lambda/n_{\mathrm{GaN}})^3$ because the fundamental mode is squeezed into a 28 nm wide semiconductor region along the central axis of the nanobeam (Fig. 4.30(a)). This small modal volume is paid at the price of enhanced sensitivity to fabrication fluctuations, which both drop the mean $\bar{Q}_{00}$ and create a bimodal wavelength distribution.

On the other hand, the first-order mode, which exhibits a node at the cavity center (Fig. 4.7(b)), displays no increased sensitivity when moving to hexagonal holes. Both the first-order
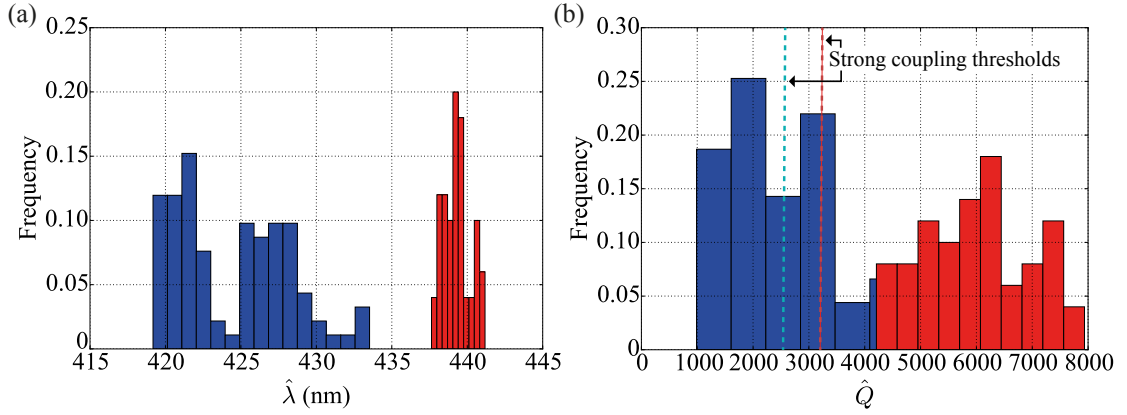
Figure 4.31: Experimental (a) wavelength and (b) *Q* statistics of 69 nominally identical KOH etched nanobeam photonic crystal cavities. Blue is the fundamental mode and red is the first-order mode. Dashed lines show the strong coupling thresholds for an emitter with a spontaneous emission lifetime of 1 ns.

mode wavelength ($\hat{\lambda}_{10}$) and $\hat{Q}_{10}$ (Fig. 4.31, red) follow monomodal distributions which pass statistical tests for normality at $p = 0.05$. The FWHM of $\hat{\lambda}_{10}$ is 2.5 nm, which is consistent with the 3D-FDTD simulated wavelength distributions due to fabrication disorder (Fig. 4.25(a)), again confirming the realization of few nanometer fabrication tolerances. The experimental $\hat{Q}$ distributions can be analzyed to test what fraction of cavities would be suitable for the observation of vacuum Rabi splitting.

The experimental $\hat{Q}$ distributions prove that vacuum Rabi splitting in the strong coupling regime should be possible in these nanobeam photonic crystals, provided a suitable emitter could be found. As a reminder, the strong coupling regime occurs when the light-matter interaction strength exceeds the average of the emitter decoherence rate and optical cavity loss rate (Eq. 2.9). Assuming that the optical cavity loss rate is much faster than the emitter decoherence rate and 1 ns spontaneous emission lifetime of the emitter in bulk GaN, then the strong coupling regime would correspond to $Q_{00} > 2500$ and $Q_{10} > 3300$. Looking at the $\hat{Q}$ histograms, we find that 42% of the fundamental mode and 100% of the first-order mode cavities satisfy the strong coupling criterion.

However, it should be noted that no one has yet demonstrated single photon emission from III-nitride materials at these wavelengths and engineering a 1 ns spontaneous emission lifetime may be challenging due to the quantum confined Stark effect. Nevertheless, localization centers in InGaN/GaN quantum wells (c.f. [96, 199–201] and Appendix A) may serve as candidate emitters provided their emission could be optimized. Currently, the emission energy of localized InGaN centers in these samples is in the absorption continuum of states for the quantum well. Further optimization of the growth parameters and conditions would be required to move these emitters to lower energies and/or to shift the quantum well emission to higher energies. This is left for future work.

4.6 Summary

This chapter:

- Provided the conceptual background to understand one-dimensional optical nanobeam photonic crystal cavities.

- Examined the impact of mechanical deformation of optical nanocavities fabricated from highly strained epilayers on photonic crystal cavity resonances.

- Presented a novel scheme for optimizing the far-field radiation pattern of nanobeam photonic crystal cavities and verified its operation experimentally.

- Demonstrated fabrication of sub-80 nm diameter holes in III-nitride materials to within ~ 1 nm precision in position and size.

- Proved that even process tolerances of ~ 1 nm are not sufficient for the deterministic fabrication of a photonic crystal cavity in resonance with an emitter at a pre-defined energy.

- Quantified the loss mechanisms responsible for the thousandfold discrepancy between simulated and experimental losses of III-nitride nanobeam photonic crystal cavities between $\lambda = 430 - 500$ nm (Fig. 4.32).

- Achieved state-of-the-art Q approaching 8000 at 440 nm and $V = 0.5 \cdot (\lambda / n)^3$, sufficient for observation of vacuum Rabi splitting provided a suitable single photon emitter could be found.

- If absorption losses could be eliminated by surface passivation and removal of the quantum well, then nanobeam photonic crystal cavity modes would be ultimately limited to average $Q \sim 20,000$ in the blue spectral range by the fabrication precision of ~ 1 nm.

As surface state absorption constitutes the dominant mechanism, the next chapter is devoted understanding surface states and improving performance by surface passivation.
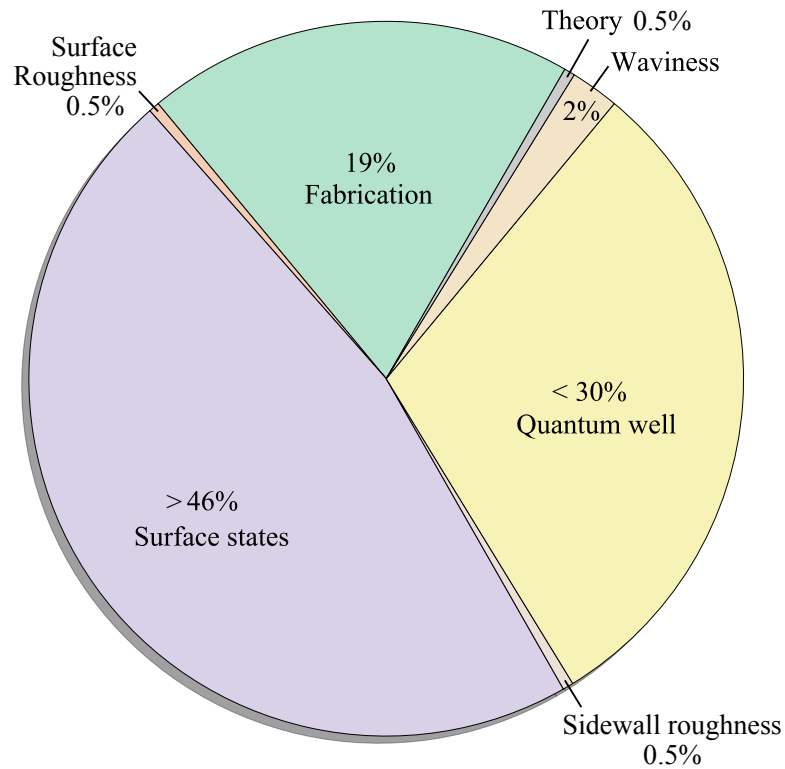
Figure 4.32: Rough estimates of the relative loss contributions discussed in this chapter for a fundamental nanobeam photonic crystal cavity mode at $\lambda_{00} = 425$ nm driven below the transparency threshold of the embedded quantum well. Relative percentages depend on target operation wavelength and specific cavity geometry. Quantum well absorption losses could be reduced by either removing the quantum well or working in the low energy tail of the emission. If quantum well losses were eliminated, surface state absorption would comprise 75% of the optical losses.

5 | Surface Effects

Microdisk optical cavities were chosen for surface absorption studies because, in contrast to nanobeam cavities, they exhibit many regularly spaced resonances. Instead of measuring a plethora of different nanobeams with differing geometries to elucidate the dispersion of losses while being obliged to account for geometry-dependent fabrication disorder (Section 4.5.4), the broadband material response can be measured in a single nanostructure. In this chapter, the theoretical background for understanding microdisk operation is discussed before comparing FDTD simulation results with experiment. Then, the effect of microdisk geometry on repeatability is explored. The bulk of the chapter is devoted to understanding the photoinduced gas (ad)desorption phenomenon. Finally, several surface treatments are examined in an attempt to maximize experimental Q.

5.1   Microdisk cavities

The microdisk optical cavity consists of a thin ($t < \lambda/n_{1,\text{co}}$) high refractive index disk with few micron radius (R), ideally suspended in air or embedded in a low refractive index cladding material ($n_{1,\text{cl}}$). Practically, the microdisk is typically mechanically supported by a thin pedestal. Due to the cylindrical symmetry, we work in cylindrical coordinates, r, θ, and z (Fig. 5.1). In contrast to the photonic crystal nanobeam cavity, which confines light by total internal
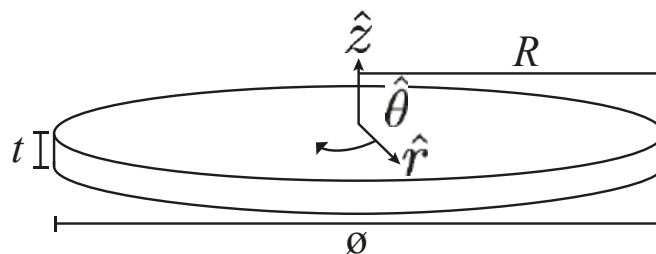
Figure 5.1: Schematic of the microdisk optical cavity geometry.

reflection in two dimensions and diffractive confinement in the third, a microdisk optical

cavity utilizes total internal reflection in all three dimensions.

In the vertical direction (z), light is confined by waveguiding (Section 4.1.2) in the thin disk. If the disk is symmetric ($\varepsilon(z) = \varepsilon(-z)$), then modes are TE- or TM-polarized. If the disk is thinner than $\sim \lambda/2n_{1,\text{co}}$, the lowest order TE- and TM-polarized modes are guided (Section 4.1.2), while if the disk is thinner than $\sim \lambda/4n_{1,\text{co}}$, then the coupling of a quantum well placed in the slab middle to the lowest order TM mode is negligible [202].

Recalling the critical angle from Snell's law, $\theta_{\text{crit}} = \arcsin\left(\frac{n_{1,\text{cl}}}{n_{1,\text{co}}}\right)$, if the angle between an incident, guided ray of light and the surface tangent of the disk edge is larger than θ_{crit}, then the ray is completely reflected. Since the disk edge is curved, rays at such large angles will skim around the edge of the microdisk. As such, these resonances are called whispering gallery modes. Recalling that light is a wave, a resonance requires constructive interference after a single round trip [203],

$$2\pi n_{\text{eff},1} R = m\lambda_m, \tag{5.1}$$

where $n_{\text{eff},1}$ is the mode's effective refractive index ($n_{1,\text{cl}} < n_{\text{eff},1} < n_{1,\text{co}}$) and $m+1$ is the number of azimuthal nodes. For large m, the free spectral range (FSR) is,

$$\text{FSR} = \lambda_m - \lambda_{m+1} \rightarrow \lim_{m \gg 1} \frac{\lambda^2}{2\pi R n_{\text{eff},1}}. \tag{5.2}$$

Going deeper into the wave optics picture, a few details deserve attention. The cylindrical symmetry causes eigenmodes to exhibit an azimuthal $\sim e^{im\theta}$ dependence. Therefore, in the absence of imperfections which break the cylindrical symmetry, each mode is twofold degenerate for $\pm m$. The circular wave propagation creates a repulsive $\sim m^2/R^2$ potential, which in conjunction with the attractive potential due to the dielectric profile, $n_{1,\text{co}} > n_{1,\text{cl}}$, creates a potential minimum which localizes electromagnetic modes near the disk edge [202]. Unlike in the case of the photonic crystal, bending losses are incurred, even in a theoretically ideal microdisk, because the radiation circulates about the disk perimeter. The theoretical Q_{th} from bending losses can be estimated in the WKB tunneling approximation [202]

$$Q_{\text{th}} \propto \exp(2mJ), \tag{5.3}$$

where

$$J = \tanh\left[\sqrt{1 - 1/n_{\text{eff},1}^2}\right] - \sqrt{1 - 1/n_{\text{eff},1}^2}. \tag{5.4}$$

Eqs. 5.1-5.4 describe the fundamental trade-off for microdisks, as a larger microdisk incurs fewer bending losses at the cost of having many modes in the gain bandwidth due to the smaller FSR.

Just as in the case of nanobeams, real world microdisks depart from the aforementioned theoretical ideal. First, the supporting post may be fabricated of a material with a higher refractive index than $n_{1,\mathrm{cl}}$, which could cause leakage of the mode from the disk edges into the post. Therefore, the post diameter must be reduced such that it remains several wavelengths away from the disk edge [202]. Second, roughness losses, in particular sidewall roughness with spatial periodicity sufficient to cause scattering into the light cone, can quickly exceed bending losses [77, 204]. Finally, because the electromagnetic field intensity remains high at the core-cladding interface, the microdisk geometry is also susceptible to surface absorption losses.

5.2 Correspondence between simulations and experiments

Microdisks were fabricated following the process described in Chapter 3. The post diameter was controlled by the length and number of pulses of XeF$_2$ vapor (Figs. 5.2(a) and(b)). A
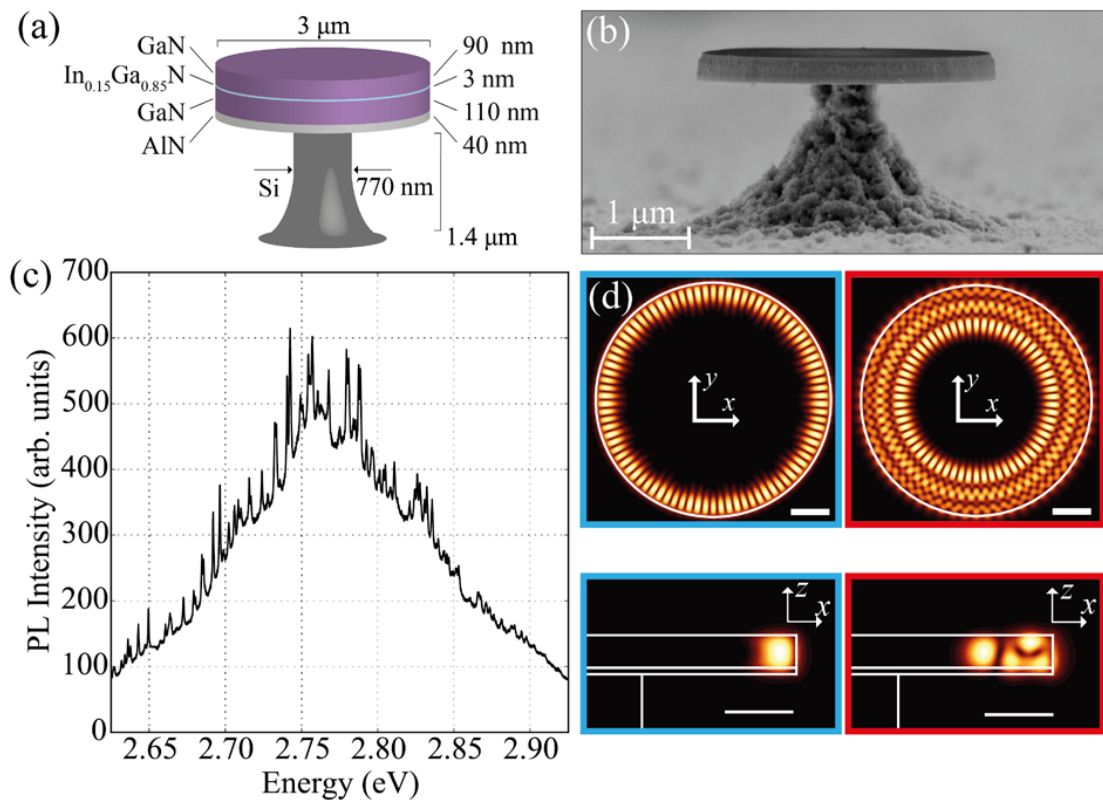
Figure 5.2: (a) Sketch of experimental geometry and (b) corresponding SEM image. (c) A typical μPL spectrum of this microdisk under 1.6 kW/cm^2 cw optical pumping with a 325 nm HeCd laser at 5 K. (d) 3D-FDTD simulations of possible electric field intensity profiles for a $z = 0$ plane bisecting the microdisk center in the $x - y$ planes (top) and a cut through $y = 0$ in the $x - z$ plane. Reproduced from [205] under a Creative Commons license.

typical μPL spectrum of a 3.0 μm diameter microdisk with a 770 nm diameter silicon post is

shown in Fig. 5.2(c). A large number of peaks superposed on the broad quantum well μPL background are seen. Evaluation of Eq. 5.2 for the given geometry yields a FSR of 64 meV (10 nm) at 2.8 eV (440 nm). Experimentally, between 8 and 10 peaks can be identified in a 64 meV window centered at 2.8 eV. In the backscattering μPL geometry, the modes do not exhibit a clear polarization dependence, either linear or circular. Experimental Q factors are on the order of several thousand.

The corresponding microdisk geometry was simulated using 3D-FDTD calculations. A spectral density of 8-10 modes per 64 meV was found and simulated Q values ranged from 10^5 to 10^6. Simulated electric field intensity profiles for two modes separated by 4 meV are shown in Fig. 5.2(d). The mode at 2.762 eV (blue) exhibits a single radial antinode with $m = 91$. The single antinode in the $x - z$ plane indicates that this mode is the fundamental TE-polarized mode. The mode at 2.758 eV (red), on the other hand, with $m = 67$ displays 3 radial antinodes and a rather complex TE-polarized[1] electric field intensity profile. Unlike the ideal microdisks discussed in Section 5.1, the microdisk is much thicker ($\sim 3\lambda/n_{1,\mathrm{co}}$) than the theoretical ideal, $\sim \lambda/2n_{1,\mathrm{co}}$. Recalling the simulations of the ridge waveguide in Section 4.1.2, modes with multiple vertical nodes can be waveguided if the material thickness exceeds half a wavelength. Therefore, we conclude that the high peak density is due to the presence of both TE- and TM-polarized modes with multiple electric field nodes in the xz-plane.

No clear correspondence between the peak position and number of peaks can be established by comparing experiments and simulations. The number and position of peaks exhibits an extreme sensitivity to the simulated geometry, especially the silicon post diameter. The complex refractive index of silicon at 2.76 eV (450 nm) is $\tilde{n}_{\mathrm{Si}} = 5.2 + 0.7i$ [140], much larger than the refractive index of GaN ($n_{1,\mathrm{co}} = 2.42$) at this energy. Therefore, the lowest attractive potential seen by the electromagnetic modes is the silicon post. Therefore, higher order radial modes / lower order azimuthal modes (e.g. red mode at 2.758 eV in Fig. 5.2(e)) which have substantial electric field overlap with the post are sensitive to post diameter. Therefore, the simulated electric field profiles and energies in Fig. 5.2(e) are shown for discussion purposes and should not be assigned to a specific experimental whispering gallery resonance. Unlike in Chapter 4, we conclude that simulations cannot be used for quantification of microdisk performance due to the epilayer thickness and fabrication uncertainty.

5.3 Geometry dependence

Since the lack of correspondence between simulation and experiment precludes the further use of computational tools, the experimental microdisk-to-microdisk reproducibility as a function of geometry should be characterized. Such characterization will reveal the experimental sensitivity to various geometrical parameters. Fig. 5.3 shows μPL spectra recorded for three nominally identical microdisks with $\varnothing = 3$, 4, and 5 μm. SEM cross-sections revealed that the post diameter was equal to the disk diameter minus 1 μm, i.e. that 500 nm over-

---

[1] From examination of the full vectorial **E** field, not shown.
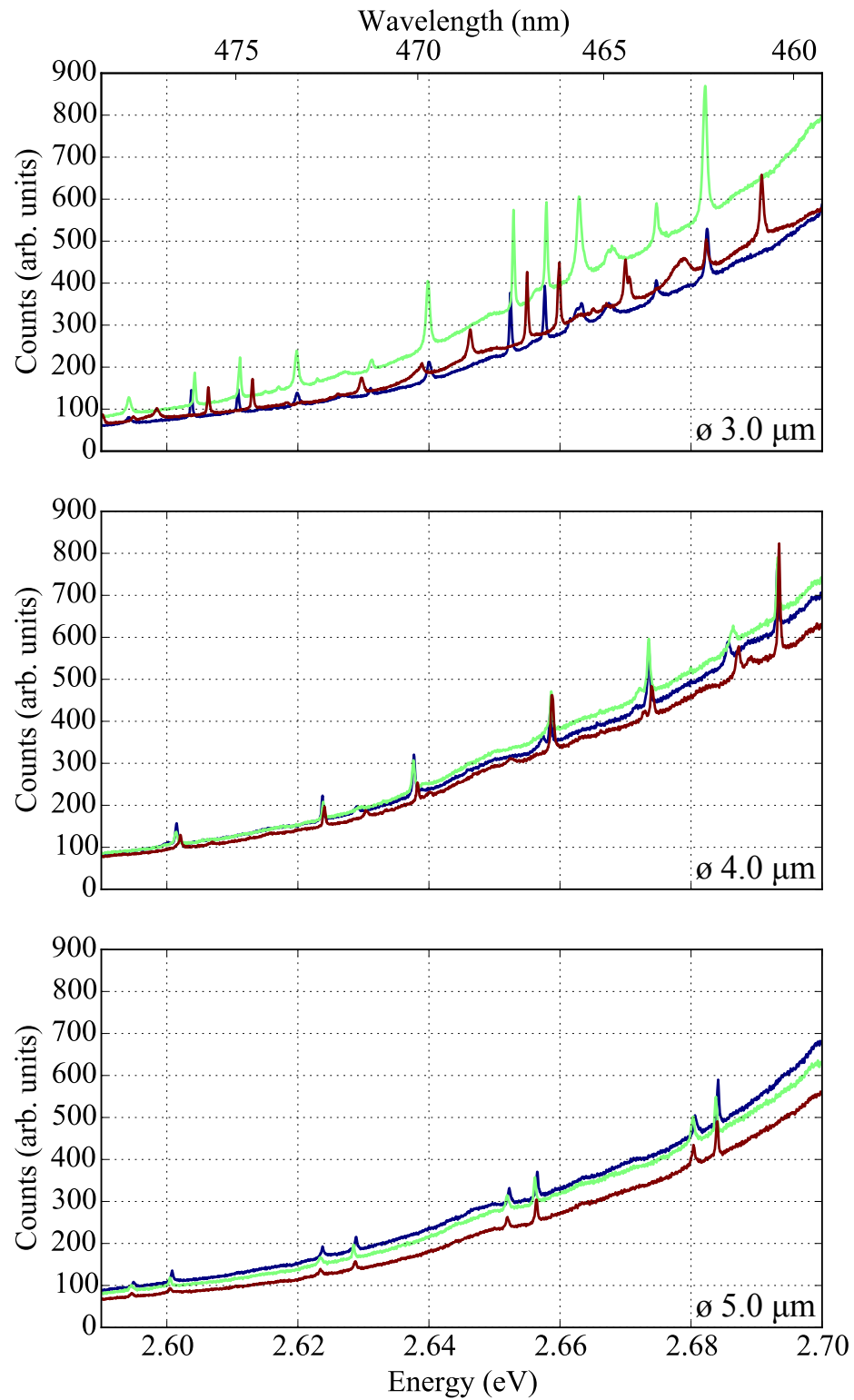
Figure 5.3: μPL spectra under 1.6 kW/cm^2 325 nm cw illumination at 5 K of three nominally identical microdisks for each of (a) $\varnothing = 3$, (b) 4, and (c) 5 μm.

hang remained between the microdisk and silicon post, and an air gap of 1.1 μm beneath the microdisk was established. The spectra are clearly reproducible for 4 and 5 μm but not for 3 μm. Assuming that the two groups of peaks for the 4 and 5 μm diameter microdisks represent the fundamental TE and TM radial modes, the FSR (Eq. 5.2) can be used to back out $n_{\text{eff},1} = 3.2 \pm 0.1$. Therefore, it is likely that some of the mode propagates in the silicon post. However, Fig. 5.3 does not immediately cast light on why the $\varnothing = 3 \, \mu$m disks are not reproducible, so an additional experiment was conducted.

Figure 5.4 shows μPL spectra of three nominally identical $\varnothing = 4 \, \mu$m microdisks with a silicon post of $\varnothing = 1.3 \, \mu$m, smaller than the $\varnothing = 3 \, \mu$m post in Fig. 5.3(b). The peak density has
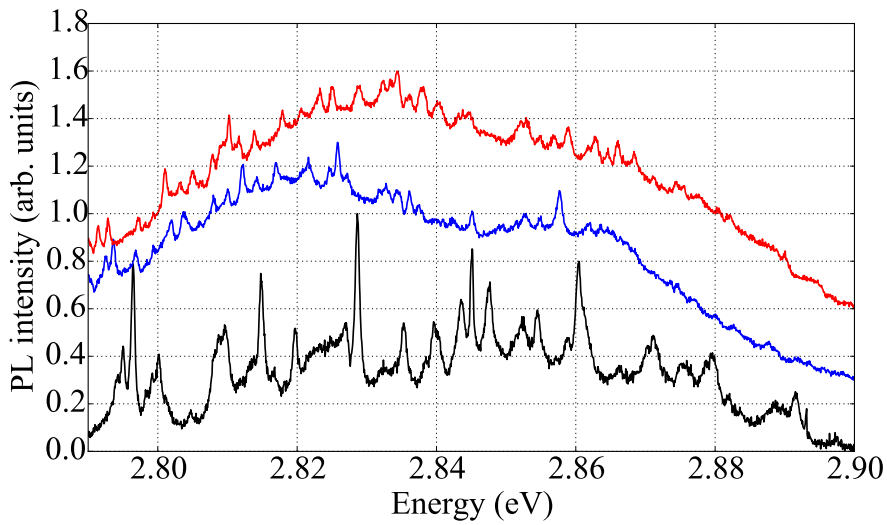
Figure 5.4: μPL spectra under 5 kW/cm^2 325 nm cw illumination at room temperature of three nominally identical $\varnothing = 4 \, \mu$m microdisks with $\varnothing = 1.3 \, \mu$m silicon support posts.

clearly increased as a result of the thinner support post, so the structure now supports the propagation of higher order radial modes. In contrast to Fig. 5.3(b), nominally identical 4.0 μm $\varnothing$ microdisks no longer exhibit reproducible μPL spectra. The reasons for this are twofold. First, as the edge of the disk is unclamped, the tensile strain from the lattice mismatch is released and the microdisk will bend upwards at the edges (Fig. 3.6). Due to epilayer thickness fluctuations (Fig. 4.19), such cupping may not be completely reproducible between microdisks once enough silicon is removed for the post. The cupping should most strongly affect the reproducibility of the lowest order radial modes which are localized at the disk edges. Additionally, the higher-order radial modes, which circulate partially within the silicon post, may not be reproducible due to the silicon post porosity (Fig. 5.2(b)), which is caused by the anisotropic vapor phase etch rates. Therefore, we conclude that microdisk μPL spectra are only reproducible for relatively thick silicon posts compared to the microdisk diameter

The lack of correspondence between simulations and experiments limits the quantifiable information that may be extracted from experiments on the microdisk geometry. Furthermore, the fact that spectra are reproducible only for relatively thick posts, where a significant fraction

of the mode propagates within the lossy silicon material, is at odds with the stated motivation of understanding the broadband response of the III-nitride material under various surface treatments. Therefore, we proceed in the following manner: no attempt is made to identify the azimuthal and radial mode numbers for experimental peaks or apply computational tools for quantitative analysis as in Ch. 4. When analyzing Q factors under various surface treatments, silicon post size is minimized and the maximum Q values within a spectral interval are retained. We implicitly assume that the maximum Q values correspond to the lowest order radial modes, which have both the highest theoretical Q values (Section 5.1) and the lowest overlap with the absorptive silicon post. Any comparative, quantitative analysis is done on a relative basis between the same or similar samples.

5.4 Photoinduced gas desorption

Section 2.4.5 introduced prior work on the phenomenon of photoinduced gas desorption from GaN surfaces. As a brief reminder, photogenerated holes may trigger desorption of adsorbed gas from both m- and c-plane GaN surfaces [114, 115, 117]. The gas desorption unpins the Fermi level on the surface, which changes the surface charge and the width of the accompanying space charge region. Poisson's equation equates the change in charge to a change in upward band bending at the semiconductor surface. Experimentally, the change in band bending can be measured directly by the Kelvin probe method upon desorption and re-adsorption of various gas species [115]. Indirectly, the change in band bending is known to change the PL intensity of the yellow defect luminescence band [115] or of nanowires [116]. In this section, oxygen desorption is shown to strongly enhance optical attenuation by surface state absorption.

Fig. 5.5(a, left panel) demonstrates how whispering gallery resonances redshift and broaden due to UV-induced photodesorption at room temperature. The redshift rate has been found to be proportional to UV pump power. Spectra were recorded every ten seconds over the entire experiment. At $t = 30'$, the laser was blocked and the needle valve was opened to allow oxygen into the chamber. The butterfly valve controlling the pump was slightly closed to reduce the vacuum system conduction. Between $t = 30'$ and $t = 35'$, a steady state pressure of 100 mbar was achieved with the turbomolecular pump still running at full speed. The sample was re-illuminated and spectra were recorded every 10 seconds starting at $t = 35'$

It is worth mentioning some additional observations. If left in high vacuum ($< 1 \times 10^{-4}$ mbar), the photonic crystal cavity modes do not recover overnight. They do however, recover after a cryogenic cooling cycle, likely due to the sample acting as a cryocooler for residual gas in the chamber. For a 325 nm pump laser, UV-induced photodesorption does not occur below 200 K for a pump intensity of 1.5 kW/cm^2, whereas for a 244 nm pump laser, photodesorption was observed even at 5 K at intensities of several kW/cm^2. Figure 5.5(a, right panel) shows the reversibility of the optical changes under exposure to oxygen atmosphere at 100 mbar at $t = 30'$.
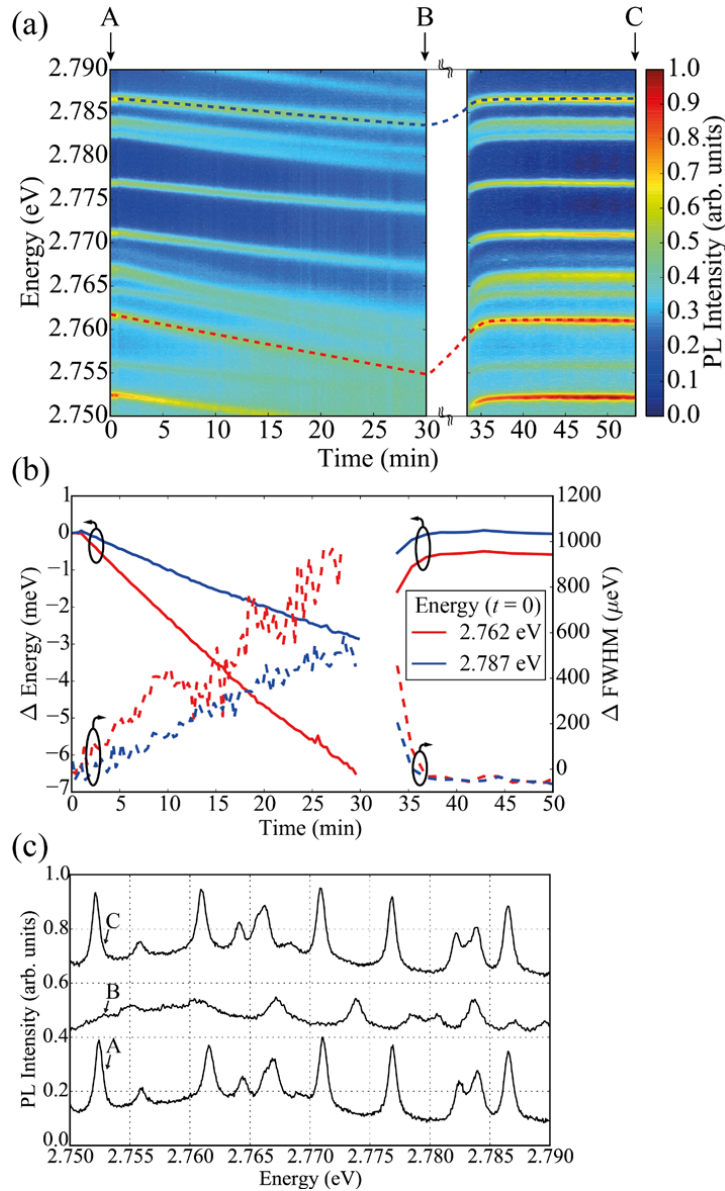
Figure 5.5: (a) Time-dependent μPL of a $\varnothing = 3.0\ \mu$m microdisk with $\varnothing = 770$ nm silicon post under 4.6 kW/cm^2 cw 325 nm illumination at room temperature. In the left-hand panel, the vacuum level is $< 10^{-3}$ mbar. In the right-hand panel, oxygen is injected starting at $t = 30'$ to a pressure of 100 mbar. (b) Time-dependent peak position and FWHM of the two selected whispering gallery resonances at 2.762 (red) and 2.787 (blue) eV. (c) μPL spectra at $t = 0$ (A), $t = 30'$ (B), and $t = 54'$ (C) showing near complete reversibility of the spectral changes following oxygen exposure. Reproduced from [205] under a Creative Commons license.

As the only variable being changed in the system is the vacuum pressure, the optical changes must originate at the semiconductor surface. In vacuum, modes shift and broaden at different rates due to the differing electric field intensity at the surface (Fig. 5.2(d)). The maximum red-shift of 6.5 meV and broadening of 1.0 meV upon oxygen desorption can be related to changes in the refractive index ($\Delta n_{\text{eff,1}}$) using Eq. 5.1 and to changes in the absorption coefficient $\Delta \alpha$ following [206]

$$\Delta \alpha = \frac{2\pi n_{\text{eff,1}}}{hc} \Delta \text{FWHM}. \tag{5.5}$$

Assuming a conservative $n_{\text{eff,1}} = 2.1$, $\Delta n_{\text{eff,2}} = 5 \times 10^{-3}$ and $\Delta \alpha = 100 \text{ cm}^{-1}$. Since the spectral changes are assumed to be uniformly distributed over the entire (bulk) volume of the electromagnetic mode, these estimates serve as lower bounds, evidencing the considerable optical oscillator strength of surface states.

5.4.1 Exclusion of heating

In order to strengthen the conclusion that photoinduced oxygen desorption is responsible for the spectral changes in Fig. 5.5, we combine finite element modeling with power-dependent μRaman measurements using the HeCd pump laser in order to rule out thermal heating as the cause for oxygen desorption. In the backscattering geometry, two zone center GaN Raman modes can be observed, the E_2^{H} transverse optical mode at 568 cm^{-1} and the A_1(LO) longitudinal optical (LO) mode at 734 cm^{-1} [145]. At room temperature, the A_1(LO) mode exhibits the larger shift rate with temperature, -39 K/cm^{-1} [152], meaning that it is better suited for use as a thermometer than E_2^{H}.

However, LO phonons may couple to plasmons (free carrier charge oscillations) in n-doped GaN [145], which would complicate analysis when the photogenerated free carrier concentration becomes substantial at high HeCd pump powers. Comparison of unprocessed areas of intentionally n^+-doped (3×10^{18} cm^{-3}) with the unintentionally doped (uid) epilayers used for the μRaman thermometry revealed no change in A_1(LO) position or shape. This indicates that there is no coupling between LO phonons and plasmons because the plasmon mode is overdamped. Overdamping is an indication of poor electrical mobility (< 100 cm^2·V^{-1}·s^{-1} [207]), which is logical given the high density of dislocations and defects inherent to growth of thin III-nitride epilayers on silicon. Independent attempts at measuring electrical mobility using Hall effect or other techniques during this thesis ended in failure, confirming the poor conductivity of the layers. Therefore, we may proceed with the μRaman thermometry using the A_1(LO) mode confident that any shifts in the peak position are attributable solely to heating and not to free carrier generation.

By using the same HeCd pump laser as in μPL for μRaman spectroscopy and measuring the shift of the A_1(LO) mode with increasing pump power, we determine the average temperature of GaN in the microdisk. A defocused spot FWHM of 2.7 ± 0.3 μm was roughly matched to

the $\varnothing = 3.0\ \mu$m disks. Spectra were calibrated using a neon lamp and the spectrometer was not moved between successive HeCd powers. Fig. 5.6(a) shows microdisk μRaman spectra
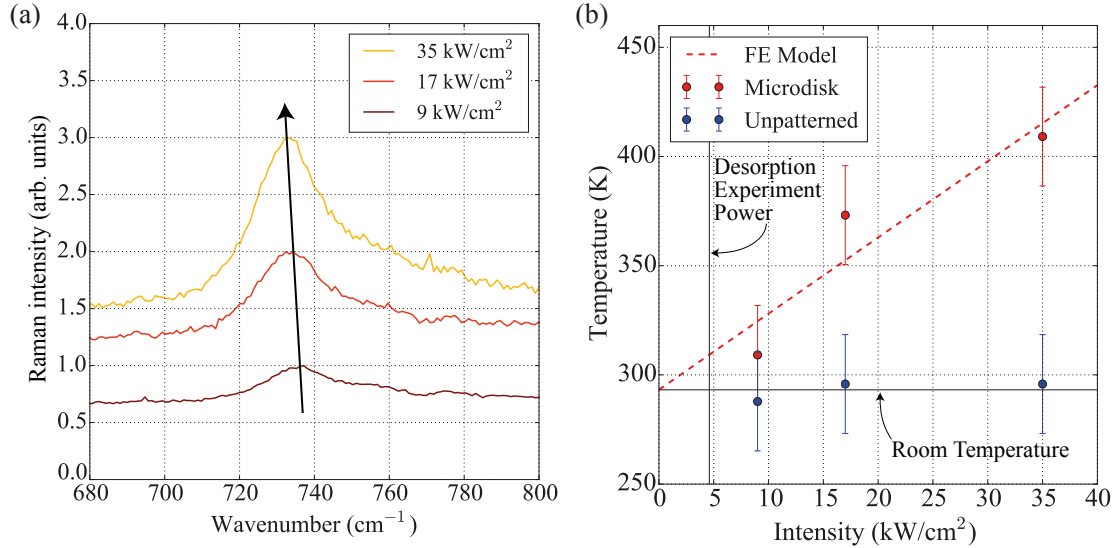
Figure 5.6: (a) Position of Raman A_1(LO) mode of GaN as a function of 325 nm laser intensity on a $\varnothing = 3.0\ \mu$m uid microdisk with silicon post $\varnothing = 1.1\ \mu$m. (b) Peak shifts converted to temperature shifts for μRaman measurements on the microdisk (red) and unprocessed area (blue). The dashed red line is the fit to a finite element model (see text). Reproduced from [205] under a Creative Commons license.

near the A_1(LO) mode at three HeCd illumination intensities. As expected for heating, the peak shifts to lower wavenumbers. The A_1(LO) peak shifts from the unstrained position at 734 cm^{-1} are converted to temperature shifts above ambient in Fig. 5.6(b, red) using the -39 K/cm^{-1} linear shift rate.[2] Control measurements on an unprocessed portion of the sample (e.g. in thermal contact with the silicon substrate) show no heating with increasing pump power, confirming that limited heat transport through the thin silicon post results in heating of the III-nitride epilayers.

The disk temperature during the photodesorption experiment at 4.6 kW/cm^2 can be extrapolated by fitting a finite element model of the heat transport to the experimental data. The azimuthal symmetry of the problem allowed reduction to two dimensions in a commercial finite element software package [169]. The geometric dimensions (Table 5.1) were extracted from an SEM cross-section image of the measured $\varnothing = 3.0\ \mu$m uid microdisks. To simplify the model, it was assumed that the laser spot uniformly generates heat in the GaN volume. The output parameter was the average temperature integrated over the entire volume of GaN. Constant temperature (293 K) boundary conditions were placed in the silicon far away (several μm) from the base of the microdisk such that this parameter did not affect the extracted disk temperature. Table 5.2 details additional material parameters needed to complete the model and their references.

---

[2]Normally a correction would be required for tensile strain, but the microdisk edges are free.

Parameters	Length (nm)
Microdisk diameter	3000
GaN thickness	235
AlN thickness	45
Si post diameter, top	1200
Si post diameter, bottom	2800
Si post height	1400
Si substrate thickness	2000
Si substrate diameter	4000

Table 5.1: Parameters for the simulated geometry found from SEM cross-section images of the microdisks used in the photoinduced desorption experiments. The silicon post is assumed to taper quadratically from the top to the bottom diameter with perpendicular sidewalls at the post-AlN interface.

Material	Density (g·cm^{-3})	Thermal Cond. (W·m^{-1}·K^{-1})	Heat capacity (J·kg^{-1}·K^{-1})
GaN	6.15 [208]	130 [209]	420 [208]
AlN	3.26 [210]	250 [81]	610 [211]
Si	2.33 [208]	156 [208]	700 [208]

Table 5.2: Material properties used for finite element modeling of heat transport in a microdisk.

The dashed red line in Fig. 5.6(b) shows the finite element model result fit to the experimental data using a single proportionality factor. The average simulated GaN temperature increases linearly with pump intensity. The temperature distribution over the simulation volume can be seen in Fig. 5.7. The model predicts 30 °C heating above room temperature for the 4.6 kW/cm^2
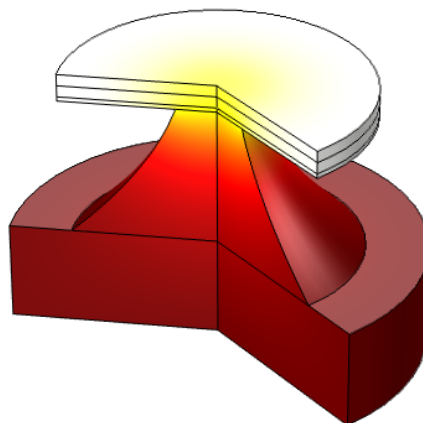
Figure 5.7: Simulated temperature distribution inside a microdisk resonator when considering uniform heat generation throughout the GaN volume. Hot areas are white.

pump intensity utilized for the μPL photoinduced desorption experiments. In any case, 30 °C remains far below the temperature at which previous studies have shown that oxygen

desorbs from GaN surfaces (950°C)[130] or that at which water vapor may be converted to an "oxide-like" surface layer (300°C)[212, 213]. Therefore, we attribute oxygen desorption during μPL in vacuum to a photoinduced rather than thermal effect.

5.4.2 Band bending

Figure 5.8 shows a schematic of the Fermi level pinning in n-GaN in the dark. In order to
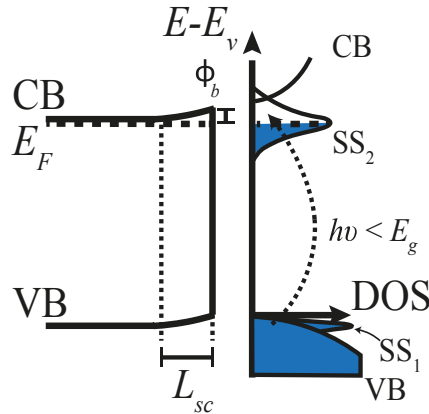
Figure 5.8: For a clean, ideal m-plane surface, one band of surface states lies below the valence band (VB) maximum (SS_1) and a second below the conduction band (CB) minimum (SS_2), within the band gap of bulk GaN [80, 113]. The Fermi level is pinned by the high density of surface states within SS_2 ($\sim 10^{14}$ cm^{-2}). In thermal equilibrium in the dark, the bands bend upward to maintain a flat Fermi level (E_F), resulting in a surface potential (ϕ_b). A depleted space charge region of width (L_{sc}) forms adjacent to the semiconductor-vacuum interface to maintain charge neutrality. Reproduced from [205] under a Creative Commons license.

determine if the cw excitation power density of 4.6 kW/cm^2 for oxygen desorption corresponds to bent (Fig. 5.8) or flattened bands, we need to estimate the photogenerated carrier density. If the photogenerated carrier density remains below the extrinsic carrier density, then we would expect the bent band picture in the dark to remain valid. If the photogenerated carrier concentration exceeds the extrinsic carrier density, then we would expect that the increased positive surface charge decreases the band bending.

We can combine Eq. 4.16 with the measurement of the quantum well lifetime at room temperature from Appendix A to estimate the carrier density in GaN. We note that, since the carriers must be transferred from the GaN barriers to the quantum well, the quantum well lifetime is an upper bound on the GaN lifetime. If the decay time in GaN were slower, then the GaN would serve as a carrier reservoir for transfer to the quantum well at longer time scales. Also, the time-resolved PL measurements were performed for a 3 nm InGaN/GaN quantum well instead of the 2 nm InGaN/GaN quantum well used in this section. Nevertheless, as nonradiative recombination dominates the time-dependence of the 3 nm quantum well and both samples exhibit a strong temperature dependent PL intensity (Appendix A), we expect

the PL lifetime of 50 ps to be a valid estimate for the 2 nm thick quantum well in the microdisk. Finally, in order to arrive at an estimate of the volumetric carrier density in GaN, we divide by the GaN thickness (235 nm).

Substituting $\gamma_{\mathrm{exp}}^{-1}(300\ \mathrm{K}) = 50$ ps, $\mathrm{Tr_{GaN}} = 0.56$ at the pump laser wavelength ($\lambda = 325$ nm), $d = 235$ nm for the GaN layer thickness, and $\alpha \sim 1 \times 10^5$ cm^{-1} for the optical attenuation coefficient [180], we find

$$n_{\mathrm{ph}} < 8 \times 10^{15} \ \ \mathrm{cm}^{-3}. \tag{5.6}$$

The ionized extrinsic carrier density was unable to be determined by Hall effect measurements due to the poor carrier mobility of the sample. Therefore, secondary ion mass spectroscopy measurements were carried out by an external contractor, EAG Laboratories, on the unprocessed epilayers. Fig. 5.9 shows the density profiles of the residual shallow donor impurities in
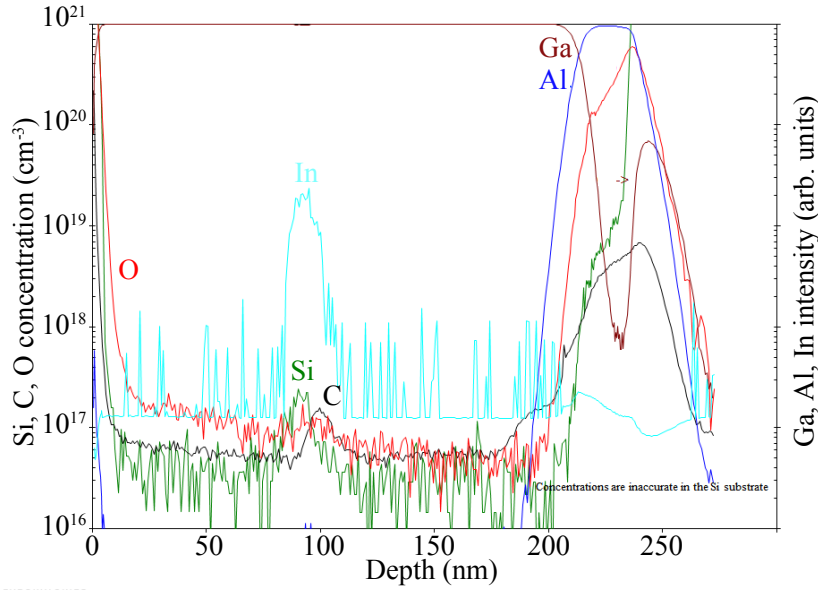
Figure 5.9: Secondary ion mass spectroscopy profile of the unprocessed epilayers used to fabricate the microdisks. $x = 0$ corresponds to the top GaN surface. The quantum well can be seen as the spike in indium concentration. The detection limits are given in Table 5.3.

GaN and AlN. n_{ph} in the GaN remain less than the residual shallow donor concentrations of 8×10^{16} cm^{-3} for carbon, 1×10^{17} cm^{-3} for oxygen, and 7×10^{16} cm^{-3} for silicon, which are higher than the detection limitations of the SIMS technique (Table 5.3). Therefore, we expect the picture of the surface band bending in the dark to remain valid under cw optical pumping with the HeCd pump laser at 4.6 kW/cm^2.

Element	AlN	GaN
C	5×10^{16}	5×10^{15}
O	5×10^{16}	1×10^{16}
Si	1×10^{17}	3×10^{16}

Table 5.3: Detection limits for secondary ion mass spectrometry depth profiling in the AlN and GaN layers as given by EAG Laboratories [214]. All concentrations are in cm^{-3}.

5.4.3 Doping dependence

With the physical picture of band bending at the surface established (Fig. 5.8), the question of whether the optical changes originate at the surface or in the space charge region arises. Experimental work on m-plane GaN suggests that the surface band bending changes from 0.2 to 0.6-1.0 eV upon oxygen desorption [117, 215]. The space charge region width ($L_{\rm sc}$) is expected to scale with the surface potential (ϕ_b) in the abrupt junction approximation following [216],

$$L_{\rm sc} = \sqrt{\frac{2\varepsilon_0\varepsilon_r}{q^2 N_d}\phi_b},$$

(5.7)

where ε_0 is the vacuum permittivity, ε_r is the static dielectric permittivity, q is the fundamental charge, and N_d is the extrinsic carrier density. Evaluation of Eq. 5.7 for the uid ($N_d \approx 3 \times 10^{16}$ cm^{-3}) GaN epilayers leads to $L_{\rm sc} = 140$ nm for $\phi_b = 0.6$ eV, which is on the same order of the internode distance, $L_{\rm em} = \lambda/2n_{\rm eff,1} \approx 100$ nm of the whispering gallery mode. Therefore, substantial overlap between the whispering gallery mode and the space charge region is expected, which would maximize the overlap integral in electromagnetic perturbation theory (Eq. 4.15) for any optical changes that may occur due to the changing width and electric field within the space charge region, by the Franz-Keldysh effect for example [18].

To test this hypothesis, two additional microdisk samples were fabricated side-by-side to minimize differences arising from the fabrication process. The first sample was fabricated from uid epilayers, and the second from heavily Si-doped ($n^+ = 3 \times 10^{18}$ cm^{-3}) epilayers. For the n^+ epilayers, $L_{\rm sc,n^+} = 8$ and 18 nm for $\phi_b = 0.2$ and 1.0 eV, respectively. $L_{\rm sc,n^+}$ remains much less than $L_{\rm em}$ even in the most dramatic scenario for the change in band bending upon oxygen desorption. Therefore, if the space charge region were to contribute substantially to the observed redshift and broadening upon oxygen desorption, then differences in the spectral changes should hypothetically be expected between the two samples.

Figures 5.10(a) and 5.10(b) demonstrate no substantial differences in the redshift magnitude or rate for uid and n^+ microdisks upon oxygen desorption under 4.6 kW/cm^2 cw illumination and high vacuum ($< 1 \times 10^{-3}$ mbar) at room temperature. Due to the lack of day-to-day reproducibility of the XeF$_2$ etcher, $\varnothing = 4.0$ μm microdisks with smaller relative $\varnothing = 1.2$ μm silicon posts were selected for these experiments (Fig. 5.10(d)). Both samples were subjected
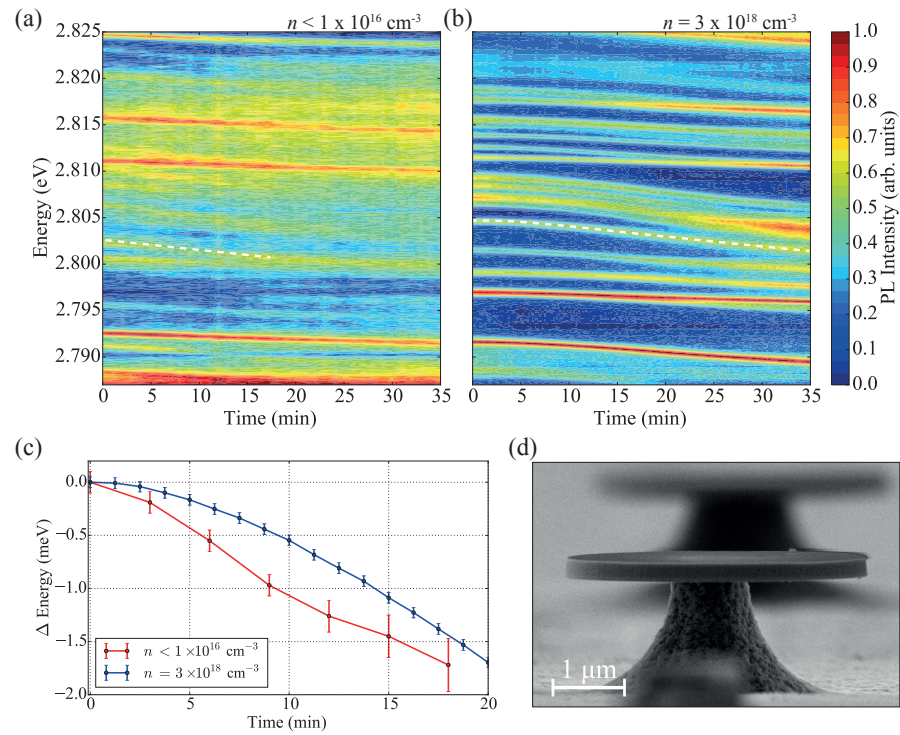
Figure 5.10: Photoinduced oxygen desorption using 4.6 kW/cm^2 illumination for (a) *uid* and (b) n^+ $\varnothing = 4.0$ μm microdisks at room temperature and $< 1 \times 10^{-3}$ mbar. (c) Extracted redshift rate comparison for the two fastest shifting modes. (d) SEM cross-section of studied microdisk geometry. Reproduced from [205] under a Creative Commons license.

to a post-processing anneal in ammonia and then oxygen at 750 °C. The HeCd pump spot was further defocused to fully illuminate the microdisks. Both the overall magnitude and rate of change for the fastest-shifting modes is the same in both cases (Fig. 5.10(c)), suggesting that the space charge region does not play a role in the redshift and broadening observed upon oxygen desorption and that such changes are linked to the semiconductor surface.

Interestingly, in Fig. 5.10, the uid mode redshifts linearly with time whereas the n^+ mode exhibits a slower initial redshift rate that asymptotically approaches the same redshift rate as the uid mode. This difference can be attributed to poor transport of photogenerated holes in the thin, high defect density epilayers. Outside the space charge region in the quasi-neutral material, the minority carrier (hole) diffusion length ($L_{d,h}$) is extrapolated to be on the order of 20 nm [149]. Inside the space charge region, drift occurs and the characteristic transport length is not known; recent work suggests that transport near the surface occurs by hopping through discrete defect states [217]. Therefore, in the uid epilayers, only holes photogenerated within or near the space charge region contribute to photoinduced oxygen desorption. Therefore, the initial dynamics of the n^+ μPL are attributed to an increase in L_{sc,n^+} from a value below to a value exceeding this characteristic transport length in the space charge region such that the overall number of photogenerated holes contributing to oxygen desorption becomes the same in both cases.

5.5   Surface passivation

The previous section proved the important role of surface states for determination of III-nitride optical nanocavity performance in the blue spectral range. This section examines the effect of different surface passivation techniques. This is an entirely experimental, trial-and-error process borrowing various ideas from past scientific literature. Different surface passivations are sequentially performed on the same sample. Then, μPL spectroscopy is performed on the same microdisks under the same experimental conditions (spot size, temperature, illumination wavelength, spectrometer settings). Q factors are extracted from Lorentzian lineshape fittings on several nominally identical microdisks. Because higher order radial modes with low Q factors are persistent in the data set, only the top 15% of Q factors in each 0.2 eV spectral window are maintained. Linear regressions through the resulting data plots serve as guides for the eye.

The passivation strategies can be categorized into two groups, surface treatments and thin film coatings. Surface treatments do not add a foreign material to the surface. They include wet chemistry and annealing. On the other hand, thin film coatings attempt to conformally cover the sample surface with a new dielectric material. Surface treatments may precede or follow thin film coatings. When treatments and coatings are combined in this manner, it is mentioned explicitly in the text.

The following cleaning and passivation techniques were explored in this thesis:

- Supercritical CO_2 drying following BHF

- Rapid thermal annealing (RTA) up to 850 °C (forming gas - 92% N_2 / 8% H_2, N_2, O_2, NH_3)

- $(NH_4)_2S$ 20% aqueous solution

- Atomic layer deposition (ALD) of Al_2O_3 and HfO_2

- Plasma-enhanced chemical vapor deposition (PE-CVD) of Si_3N_4 and SiO_2

- Anisotropic wet etch, TMAH 25% at 40 °C

- Anisotropic wet etch, KOH 3 M at 30 °C

For the sake of completeness and the avoidance of future repetition, negative results are reported here. RTA in forming gas etched dislocation pits in the sample. RTA in O_2 at temperatures above 800 °C for extended periods of time ($> 10'$) resulted in surface roughening (Fig. 3.7) and changes to the InGaN/GaN quantum well with this indium composition. ALD thin films and PE-CVD Si_3N_4 exhibited decreased optical performance likely due to absorption losses in the coating, also after subsequent RTA processing. Supercritical CO_2 and $(NH_4)_2S$ produced no change in optical performance to within experimental error.

5.5.1 Surface treatments

Prior work on cleaning of GaN surfaces suggests that the BHF acid used to remove the residual HSQ (Fig. 3.1(e)) deposits fluorine atoms on the surface and removes any residual oxides [130, 218]. Multiple reports in the surface science literature suggest ammonia at > 500 °C for cleaning GaN surfaces, including fluorine [130, 219, 220]. Fig. 5.11 shows the top 15% of Q measured using μPL spectroscopy at 5 K over the same 7 nominally identical $\varnothing = 3.0$ μm microdisks from Fig. 5.2.

The ammonia and oxygen surface treatment results in a broadband performance enhancement to state-of-the-art values beyond $Q = 1 \times 10^4$. The previous highest reported Q values were 5500 for GaN microdisks around 450 nm / 2.76 eV [221] and 7300 at 413 nm / 3.0 eV for AlN microdisks [9]. Interestingly, a high energy cutoff appears, which is shifted from 2.87 to 2.92 eV by the optimized annealing treatment (Fig. 5.11(a)). Although quantum well absorption may play a role at higher energies, the 750 °C annealing temperature remains below the 880 °C threshold known to modify InGaN/GaN quantum wells [222]. Interestingly, a peak in the joint density of optically active surface states at 2.9 eV was predicted by theorists for m-plane GaN [80, 117] and Fermi level pinning at 2.9 eV above the valence band maximum was found by experimentalists working on GaN nanowires [223]. Therefore, the shift of the cutoff may possibly be attributable to a modification in the joint density of surface states by the RTA treatment.

The RTA surface treatment also improves the Q of nanobeam photonic crystal cavities, as shown in Fig. 5.12. For these experiments, the same nanobeam cavities were measured after

(a)

(b)
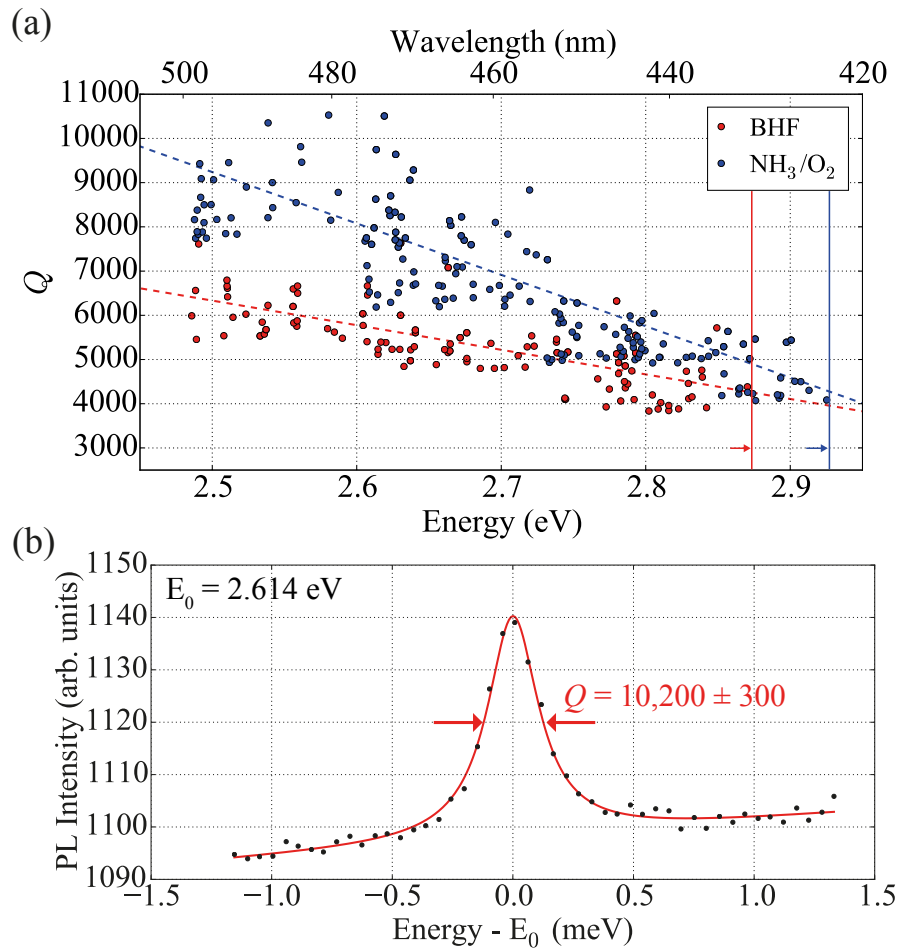
Figure 5.11: (a) Comparison of the same whispering gallery resonances for the standard 49% BHF treatment and then after 5′ in ammonia and oxygen at 750 °C each. Measurements were performed at 5 K under 1.6 kW/cm^2 cw optical pumping with the HeCd laser. Dashed lines are linear regressions through the top 15% of measured Q values reported here. The solid lines are high energy cut-offs. (b) Q value exceeds 1×10^4 at 2.6 eV. The spectrometer resolution corresponded to a $Q = 1.4 \times 10^4$ and no deconvolution was performed. Reproduced from [205] under a Creative Commons license.
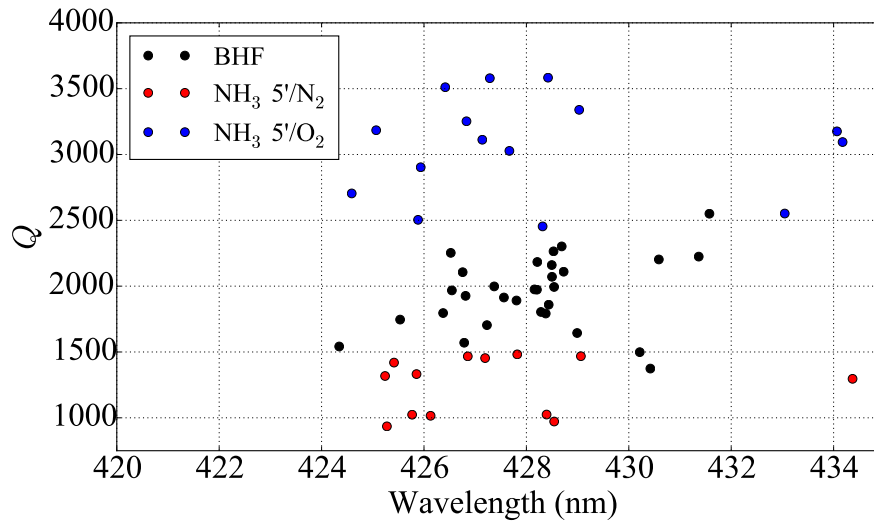
Figure 5.12: Extracted Q from μPL of the same nanobeam photonic crystal cavities under 1.6 kW/cm^2 cw optical pumping with the HeCd laser following sequential surface treatments.

stripping HSQ in BHF, after annealing in ammonia and nitrogen at 750 °C for 5′ each, and then after annealing in ammonia and oxygen at 750 °C for 5′ each. The samples used in these experiments had a different geometry than that explored in Chapter 4. A design with smaller holes in the taper was used [179]. 170 nm width was selected and 24-period $d_b = 70$ and $a_b = 119$ Bragg mirrors surrounded an 18-period linear taper to $d_c = 60$ and $a_c = 102$ nm central holes. Surprisingly, the ammonia and nitrogen surface RTA treatment resulted in worse performance than the BHF reference, whereas the ammonia and oxygen RTA treatment improved Q factors above the BHF reference. Such findings reinforce the importance of oxygen to passivate the surface of optical devices.

5.5.2 Thin film coatings

The ideal thin film coating would encapsulate the entire photonic nanostructure, improving heat dissipation and protecting the nanostructure from the surrounding environment without increasing optical losses due to absorption or scattering. The complicated geometry of optical nanocavities necessitates use of a conformal coating technique capable of coating the interior of holes and the undersides of air-suspended structures. Although ALD is frequently praised for its conformality, the deposition from organometallic precursors at low temperatures results in substantial carbon incorporation into the thin films [224]. Several depositions were attempted with 3 nm thick ALD HfO$_2$ ($n_1 = 2.1$ at 450 nm measured by spectroscopic ellipsometry) and Al$_2$O$_3$ ($n_1 = 1.78$ at 450 nm measured by spectroscopic ellipsometry) layers deposited on surfaces treated with the optimized RTA annealing process. Significant Q degradation was always observed, even after annealing the ALD-coated nanostructures in ammonia and oxygen at 750 °C. The additional losses are attributed to absorption by impurities of the ALD-deposited layers or a change in the GaN surface upon ALD deposition.

With ALD eliminated, plasma-enhanced chemical vapor deposition (PE-CVD) of SiO_2 ($n_1 = 1.5$ at 450 nm) was adopted. SiO_2 was deposited from a silane and nitrous oxide plasma with the sample heated to 300 °C in an Oxford Plasmalab System 100. First, thick coatings were deposited on test structures in order to evaluate the conformality of the PE-CVD thin films, especially its ability to coat the bottom surface of microdisks or the interior surface of sub-100 nm diameter photonic crystal holes. Fig. 5.13 shows SEM cross-section images of thick
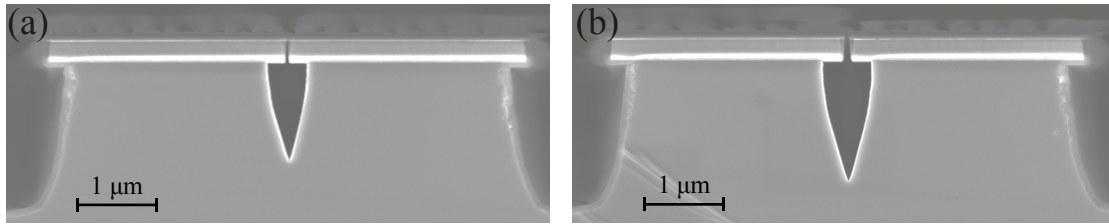
Figure 5.13: SEM images of 100 nm of PE-CVD Si_3N_4 coated on a cleaved test sample. (a) 90 nm epilayer slit width reduced to 60 nm slit by deposition. (b) 170 nm epilayer slit width reduced to 60 nm width by deposition. Note the uniform coating thickness around the outer dimension.

conformal deposition on a cleaved test structure comprised of slits with varying sub-100 nm width. From these images, we conclude that PE-CVD is capable of conformally coating the undersurface of a microdisk cavity but not the interior surface of photonic crystal holes.

Next, 15 nm of PE-CVD SiO_2 was deposited on the same microdisks studied in Section 5.5.1. The optimized RTA treatment had already been performed on the sample prior to deposition. Fig. 5.14 shows the Q factor dispersion at 5 K under 1.6 kW/cm^2 cw HeCd illumination of $\varnothing = 3.0 \, \mu$m microdisks compared to the uncoated reference. No filtering was performed to retain the highest Q values, so Fig. 5.14(a) shows the complete data set from Fig. 5.11. Initially, the maximal Q values from the coating are poorer than the bare surface and similar to the BHF-treated surface. However, annealing the coated sample for 5′ each in ammonia and oxygen at 750 °C reproduced the maximal Q values of the RTA-treated bare surface. Therefore, we conclude that additional scattering losses from the addition of an extra dielectric interface are negligible and that the post-processing RTA treatment reduced surface absorption at the nitride-SiO_2 interface.

5.6 Gas tuning of nanobeam photonic crystals

The clear identification of photoinduced desorption leads to the question of the viability of resonance tuning by gas ad- and desorption. In the following experiment, the nanobeam geometry and the optimized annealed sample from Section 5.5 was used. A single nanobeam was selected for all subsequent measurements at room temperature. Each measurement cycle was carried out in the following manner: first, gas was desorbed from the nanobeam surface by 4.5 kW/cm^2 cw HeCd illumination for 40′ under a vacuum better than 5×10^{-4} mbar. Then, the connection to the vacuum pump was closed and 100 mbar of impurity gas
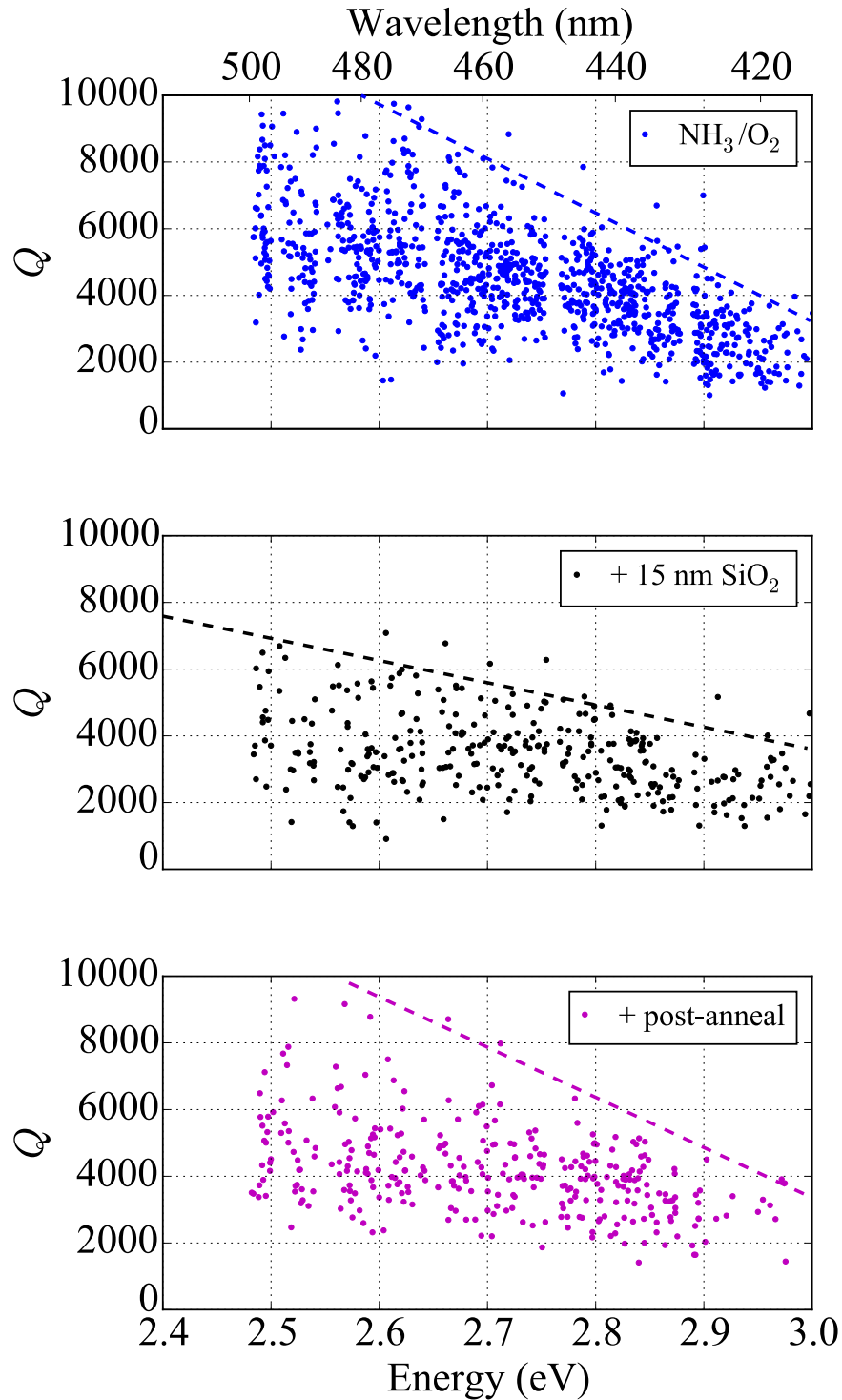
Figure 5.14: Comparison of the same whispering gallery resonances for the (a) optimized RTA treatment, (b) after 15 nm SiO$_2$ deposition by PE-CVD, and (c) after a post-deposition RTA anneal. Measurements were performed at 5 K under 1.6 kW/cm^2 cw optical pumping with the HeCd laser. No filtering of Q values was performed. Dashed lines are guides to the eye.

was introduced.[3] μPL measurements were initially conducted under low intensity HeCd illumination (200 W/cm^2) to see if the modes shifted under low intensity illumination. Then, the intensity was increased back to 4.5 kW/cm^2 and μPL spectra were continuously recorded with 2-4" integration time until the mode no longer shifted. The energies and FWHM of the fundamental and first-order cavity modes were extracted from Lorentzian line shape fits at each point in time and are plotted in Fig. 5.15.
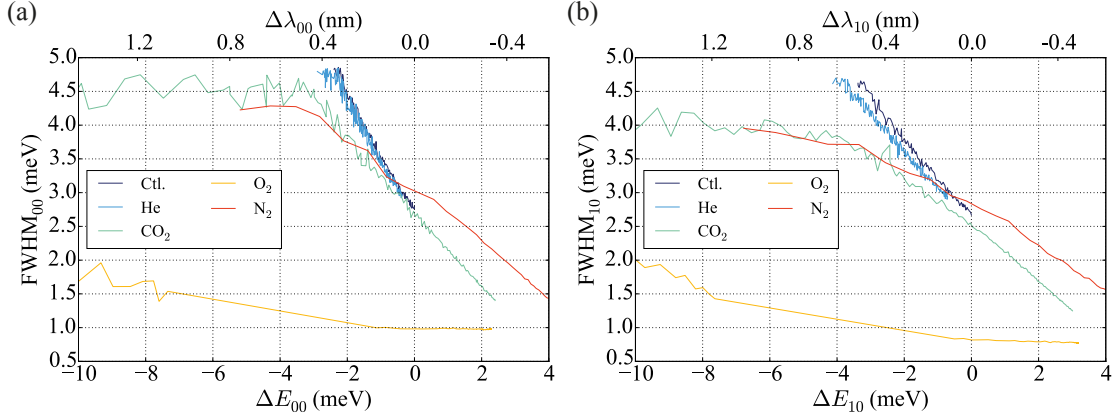
Figure 5.15: Tuning of (a) fundamental and (b) first-order photonic crystal cavity resonances by photoinduced gas adsorption using cw HeCd illumination at 4.5 kW/cm^2. Each gas pressure is 100 mbar.

We see that each gas yields a unique tuning curve. This is attributed to differing optical absorption by chemical-dependent surface state complexes for each gas. A reference measurement was performed because, without the vacuum pump actively purging the chamber, background atmospheric gas could enter the chamber and react with the surface. The leak rate was measured to be 1×10^{-5} mbar/s. We see that the control and helium nearly produce the same results, as expected for a noble gas.

Only O_2 gas was observed to react spontaneously with the surface, meaning that under low intensity or without any illumination, the photonic crystal modes recovered. This observation indicates that photoinduced adsorption occurred for all other gases. Interestingly, the addition of 2% H_2 to N_2 (forming gas) resulted in the disappearance of the photonic crystal modes completely. Illumination of an oxygenated surface in forming gas resulted in the photonic crystal mode broadening and decreasing in amplitude without redshifting. This behavior is attributed to the reducing nature of H_2 as compared to the oxidizing behavior of O_2.

Previous publications of telecom wavelength photonic crystal cavity gas sensors monitored the change in the refractive index of the gas [226, 227]. The maximum relative tuning range for refractive index sensing was $\Delta\lambda/\lambda < 3 \times 10^{-4}$ in a specialized air cavity design [227]. By monitoring the change in the III-nitride surface's optical properties instead of a volume change

---

[3]The pressure response of the vacuum gauge to each gas was compensated [225].

of the refractive index in the gas surrounding the photonic crystal, the relative tuning range increases more than $100\times$ to $\Delta\lambda/\lambda = 4 \times 10^{-2}$. Furthermore, the distinct chemical signature of each gas on the surface opens an additional dimension for chemical sensing in photonic crystals.

The tuning range from oxygen gas adsorption is more than 10 linewidths. Gas tuning offers more range than the piezoelectric bending scheme explored in Section 4.3. To tune a cavity in resonance with a two-level system or a laser line, one could imagine tuning the mode by varying the oxygen pressure and time before cutting the illumination, evacuation, and cooling below 200 K so that oxygen adsorption and desorption stops during subsequent experiments. O_2 adsorption offers the narrowest linewidths over the entire tuning range, but occurs spontaneously. Photoinduced adsorption could be used with other gases for increased control.

5.7 Conclusions

This chapter:

- Provided the conceptual background for whispering gallery resonances in multimode microdisk optical cavities.

- Explained why simulation cannot be used as a predictive tool due to the thick epilayers and absorptive, high refractive index silicon post.

- Showed that experimental spectra were reproducible only for relatively large diameter silicon posts.

- Demonstrated the sensitivity of the optical performance to adsorbed oxygen gas on the microdisk surface.

- Quantified surface state absorption losses exceeding 100 cm^{-1} upon photoinduced oxygen desorption.

- Developed surface passivation techniques to improve optical performance.

- Actively tuned nanobeam photonic crystal resonances by (photoinduced) gas adsorption.

6 Conclusion

6.1 Summary of results

This thesis documents optical nanocavity development for short wavelength III-nitride quantum nanophotonics in LASPE at EPFL. Several tools have been developed that provide the requisite foundation for future solid-state quantum optical experiments in III-nitrides at sub-500 nm wavelengths. For characterization, a dedicated optical laboratory was constructed. To minimize integration times for photon counting experiments, a novel outcoupling scheme for nanobeam photonic crystals was proposed and experimentally verified. On the fabrication side, critical dimension control down to the single nanometer level was demonstrated. A detailed statistical study of nanobeam photonic crystal cavities combined both experiment and simulation to show that surface state absorption limits cavity Q at short wavelengths. The last chapter explored the impact of surface states and their passivation on III-nitride nanophotonic resonator Q. Taken together, these results supply the high performance, stable, reproducible, tunable samples and facilities required for demanding, state-of-the-art nanophotonics experiments in this new materials system.

Because the UV fluorescence microscope implements a back-scattering geometry, photonic engineering can improve upon the fraction of light collected by the microscope objective. Without any photonic engineering, only a fraction $\left((1 - \sqrt{1 - 1/n^2})/2 = 4.5\% \text{ for } n = 2.4\right)$ of the spontaneously emitted radiation of an isotropic emitter embedded in a waveguide is coupled into free space, of which only a fraction is coupled into the microscope objective's light cone. This thesis introduced the concept of an outcoupler based on sub-harmonic (period $2a$) sidewall modulation in a photonic crystal (period a) cavity to controllably couple a fraction of the light inside the photonic crystal cavity into the microscope's light cone objective. Experimentally, the optimized outcoupler was shown to increase the collected far-field emission by nearly a factor of ten over the reference structure without any sidewall modulation. At a fixed number of photon counts, a tenfold increase in signal intensity decreases integration times for second-order intensity autocorelation measurements by a factor of 100.

To reach the strong coupling regime in cavity quantum electrodynamics, Q values must exceed

a threshold value for a given cavity geometry (Eq. 2.9). This thesis demonstrated a maximum nanobeam photonic crystal cavity $Q_{10} = 7,900$ at $\lambda_{10} = 442$ nm and $V_{10} = 0.5 \cdot (\lambda/n)^3$, greatly exceeding the threshold $Q = 4300$ for strong coupling at this wavelength. Moreover, 100% of measured Q_{10} on nominally identical cavities exceeded the strong coupling threshold Q. Therefore, the nanobeam photonic crystal cavities have been developed such that their performance is "good enough" to embed a single photon emitter.

This thesis improved experimental Q values by quantitative studies of the mechanisms contributing to experimental Q. The level of fabrication disorder deduced from algorithmic extraction of critical dimensions (hole size and position) from high magnification SEM images served as input for finite-difference time-domain simulations of disordered cavities. The simulations were able to explain the experimentally observed geometry dependence of Q_{exp} with a single offset Q_{off}. As the offset Q_{off} was lower than the simulated Q_{fab} due to fabrication disorder, we concluded that experimental Q_{exp} are not limited by fabrication disorder at the 1 nm level. Through a series of further simulations and experiments to disentangle the effects of surface roughness from bulk absorption from surface state absorption, surface state absorption constitutes the dominant loss mechanism, between 45 and 75% of the overall losses.

Subsequent efforts were devoted to understanding the role of the surface in III-nitride photonic nanocavities operating in the blue. The microdisk photonic cavity geometry was selected for study of surface effects due to its regularly spaced high Q resonances over the complete bandwidth of interest. III-nitride nanocavities are unstable under intense above band gap illumination in vacuum due to photoinduced oxygen desorption from the III-nitride surfaces at room temperature. Oxygen desorption increases the effective refractive index and optical attenuation by surface states up to 100 cm^{-1} in the microdisk geometry. The effect is non-saturable under vacuum, meaning that the photonic resonances disappear before the effect stops. However, an oxygen atmosphere nearly restores the photonic modes to their original position, providing a stable, reproducible measurement environment under high intensities. Due to nanobeam photonic crystal cavities' larger surface-to-volume ratio, photoinduced oxygen desorption can be used to tune photonic resonances over 10 linewidths (up to 2 nm or 13 meV) at 425 nm or 2.918 eV. This result, in conjunction with the experimental tolerances on the cavity wavelength, could be used to fabricate and tune photonic crystal cavities in resonance with embedded two-level systems with high, reproducible experimental yield and/or for gas sensing applications.

Surface passivation proved vital to nearly doubling the state-of-the-art Q factors of GaN microdisk resonators in the blue spectral range. A substantial amount of time and number of samples were sacrificed during the trials of various surface passivation techniques. Eventually, rapid thermal annealing at 750 °C in NH$_3$ and then O$_2$ provides the optimum improvement in microdisk Q, likely serving to clean and then oxygen passivate the III-nitride surface. The surface treatments can be combined with conformal SiO$_2$ coatings, which could serve in future devices as a protective cladding and heat sink. The annealed and SiO$_2$ coated microdisks

exhibited similar performance to the optimized untreated surface.

6.2 Future outlook

There are many possible future directions for integrated nanophotonics in III-nitrides. This section provides a short list of ideas for subsequent development:

- **Surface passivation:** Photoelectrochemical oxidation of GaN surfaces promises the growth of Ga_2O_3 films on GaN [228–230]. However, maintaining a smooth surface over several crystal orientations without preferentially etching the plentiful number of dislocation pits will require substantial process development. Regrowth of $Al_xGa_{1-x}N$ films on finished structures by MOVPE is also an interesting possibility. The high quality of LASPE's in-house material coupled with the TR-PL streak camera would be ideal for a fundamental study of GaN surface passivation techniques.

- **Squeezed light in nanolasers:** Several studies have already exhaustively explored the unique photon statistics of nanolasers near threshold [27, 29, 33]. However, no experimentalist, has, to the best of the author's knowledge, examined a theoretical proposal for intensity-squeezed light generation in nanolasers [30]. Such a setup would require optical heterodyne measurements between the nanobeam photonic crystal cavity and a suitable laser, necessitating additional equipment investment and construction in the quantum optics laboratory. With the gas tuning, fabrication tolerances, and outcoupler presented in this thesis, LASPE would be in a strong position to carry out such measurements.

- **Electrically injected nanolasers:** Electrically injected nanolasers would be an interesting synthesis of the nanophotonics and tunnel junction development in LASPE [231]. Due to the poor electrical conductivity of the thin epilayers on silicon, such an effort would require a thermal management strategy. Either one could develop nanobeams using higher quality material and photoelectrochemical etching of a sacrificial layer and/or heat sink the nanobeam in a cladding material. Electrically driven nanolasers would not only be interesting for optical communication, but also possibly for bio-nanophotonics. Since GaN is chemically inert and biocompatible, one could penetrate a living cell with such a compact light source [232], or for optogenetics. The GaN surface may be functionalized [233], and the surface sensitivity of III-nitride nanophotonic structures could be exploited for detection of a useful substance in a cell.

- **Optical phased arrays for holographic projection:** A display comprised of optical antennas with individually controllable amplitude and phase could be used for holographic projection when fed by the same single mode laser. Such systems have already been realized at telecommunication wavelengths using active silicon nanophotonics [234] and in the red using passive silicon nitride [235] nanophotonic circuits. III-nitrides would be the ideal material for visible operation. The transposition of nanophotonic

technology from other semiconductors operating in the infrared, such as quantum well absorption [236] and carrier injection modulators [237], could be combined with LASPE's expertise in lattice-matched InAlN/GaN epilayers to create integrated nanophotonic circuits in the visible. Such technology could alternatively be combined with nanolaser development for short distance optical communication.

- **Single photon emission from InGaN/GaN single quantum wells on silicon:** Appendix A shows that the d_{qw} = 3 nm InGaN/GaN quantum well exhibits emission in a second higher energy band ($\sim$ 3.05 eV) with low spatial density ($\sim 1 \times 10^9$ cm^{-2}), narrow linewidth ($\geq$ 135 μeV), and stability up to 85 K. Although this emission currently occurs in a spectral window where the quantum well absorbs strongly, perhaps the sharp line emission or the quantum well's absorption can be shifted to a spectral window where it would be possible to couple the emission to a nanobeam photonic crystal for cavity quantum electrodynamics experiments.

- **Deep level defects for quantum nanophotonics:** For quantum nanophotonic applications, working at such short wavelengths / high photon energies presents challenges for cavity Q due to sub-gap surface state absorption and increased scattering losses. For c-plane GaN, for example, the cut-off energy for optical absorption by surface states is around 1.0 eV [114]. Furthermore, a quantum photonic device at the telecommuncation wavelength λ = 1.5 μm would be more amenable for quantum communication networks. Recently, bright single photon emission at telecom wavelengths at room temperature was discovered in GaN-on-sapphire samples [238]. If this finding can be reproduced and engineered, then perhaps deep level defects in III-nitrides could be deterministically produced at a specific location and energy, such as is the case with silicon ion implantation in the diamond system [239], then the appeal of III-nitrides as a quantum nanophotonic platform would increase tremendously.

A InGaN/GaN Single Quantum Wells on Si (111)

In this thesis, a single InGaN/GaN quantum well is employed as an internal light source, whose spontaneous emission is filtered through photonic crystal modes. Although the properties of the quantum well are not the principal focus of the thesis, its optical absorption complicates measurements of what the "bare" cavity Q would be without the presence of this gain medium. Thus, one cannot fully understand the properties of the photonic crystal cavity while neglecting the internal light source; this appendix devotes space to its more detailed characterization. Here, the optical properties of unprocessed 2 nm and 3 nm thick $In_{0.15}Ga_{0.85}N/GaN$ quantum wells on silicon (111) in both cw and time-resolved experiments are presented as functions of temperature, excitation wavelength, and power density. Special emphasis is placed on carrier localization and nonradiative recombination. The author would like to thank Dr. Gwénolé Jacopin for the TR-PL measurements and Irene Sànchez Arribas for the temperature-dependent PL measurements on the 3 nm thick quantum well sample.

As mentioned in Chapter 1, InGaN/GaN quantum wells depart from simple "toy" models of a particle in a 1D box. First, the spontaneous and piezoelectric polarizations create a $\sim$MV/cm electric field for the typical c-axis growth direction. Second, indium alloy and quantum well width fluctuations create an energy landscape for carriers, resulting in a hybrid quantum dot/quantum well gain medium, whose 0D and 2D emission contributions depend on both the temperature and carrier density [27, 108, 240]. Measurements in this thesis were conducted at temperatures at or below room temperature. Because quantum confinement increases the exciton binding energy by a factor of 2-4 versus that of the bulk material [85], the exciton binding energy of bulk GaN is 26 meV [81], and a significant departure from the bulk GaN value is not expected for low indium contents [161, 241], we expect excitons in the InGaN/GaN quantum wells on silicon to be thermally stable under low density optical pumping. At high density optical pumping at or near the transparency threshold, the Mott transition to an electron-hole plasma will occur [85]. Based on the measurements in this thesis and in publications with collaborators [27], the transparency threshold ($\lambda = 325$ nm) occurs for power densities of ~ 10 W/cm^2 at 4 K and ~ 10 kW/cm^2 at room temperature with nonresonant pumping and for power densities of ~ 10 kW/cm^2 for $\lambda = 405$ nm resonant pumping at 4 K

(Section 4.5.2).

Therefore, we ascribe the 0D component of the emission to localized excitons (subscript "l") and the 2D to free excitons (subscript "fr"). For commercial LEDs, the potential landscape is both a blessing and a curse; carrier localization enhances the likelihood of Auger recombination at high carrier densities, causing an efficiency droop under strong excitation intensity conditions [108]. At low intensities, however, localized excitons exhibit high radiative emission efficiency in a material that, according to prior wisdom from other compound semiconductors, should be too riddled with defects originating from the heteroepitaxy growth to be viable for optoelectronic devices.

The benefit from localized excitons only remains as long as carriers are trapped in local minima of the InGaN/GaN potential landscape. This necessitates two criteria: first, the "hot" injected carriers must become trapped in a local minimum before reaching a nonradiative defect. This condition is fulfilled as long as th localization-limited exciton diffusion length remains much less than the distance between nonradiative defects, which will be shown to be the case for our samples in this Appendix. As evidenced by AFM mappings (Figs. 4.18), the dislocation density for the thin III-nitride epilayers on silicon amounts to $3\text{-}4 \times 10^{10}$ cm^{-2}, which corresponds to an average separation of 50-60 nm between defects. This number should be regarded as a lower bound because AFM detects surface structural defects. Second, the excitons must remain trapped in the localization centers. As will be shown in the next section, the trapping depends on the depth of the confinement potential, the temperature, and the density of localization centers.

A.1   Theoretical model

In the low to moderate excitation regime, the PL emission is ascribed to photogenerated excitons (2D density n_{ph}). n_{ph} is the sum of the localized and free exciton populations, which are described by temperature-dependent 2D densities $n_{\mathrm{l}}(T)$ and $n_{\mathrm{fr}}(T)$, respectively. If we assume that n_{l} and n_{fr} are in thermal equilibrium,[1] then Saha's law describes the ratio between the exciton populations [108]

$$\frac{n_{\mathrm{fr}}(T)}{n_{\mathrm{l}}(T)} = \frac{2M_x k_B T}{\pi \hbar^2 N_{\mathrm{l}}} \exp\left(-\frac{E_{\mathrm{loc}}}{k_B T}\right), \tag{A.1}$$

where N_{l} is the number of available localized states,

$$N_{\mathrm{l}} = \int_E \rho_l(E)\, dE, \tag{A.2}$$

where $\rho_l(E)$ is the localized exciton density of states per unit energy, M_x is the in-plane total exciton mass, and E_{loc} is the localization energy, e.g. the potential depth of localized excitons relative to free excitons.

---

[1]This assumption will be justified *a posteriori*.

Each subpopulation has an overall decay rate (γ_{fr} or γ_{l}) that is the sum of nonradiative (γ_{nr}) and radiative (γ_{r}) decay rates, where

$$\gamma_{\text{fr}}(T) = \gamma_{\text{fr,nr}}(T) + \gamma_{\text{fr,r}}(T). \tag{A.3}$$

For both free and localized excitons, we assume a simple thermal activation process of the nonradiative recombination rate with activation energy $E_{\text{fr,nr}}$,

$$\gamma_{\text{fr,nr}}(T) = \gamma_{\text{fr,nr}}(\infty) \exp\left(-\frac{E_{\text{fr,nr}}}{k_B T}\right). \tag{A.4}$$

Localized excitons' radiative recombination rate is temperature-independent, whereas free excitons' radiative recombination rate decreases with increasing temperature because of the parabolic dispersion relation of exciton energy (Section 2.4.4) and only free excitons in the light cone ($k_\parallel \approx 0$) couple to radiation due to conservation of momentum [240],[2]

$$\gamma_{\text{fr,r}}(T) = \left(\frac{n_1 E}{c}\right)^2 \frac{\Gamma_{0,r}}{6 M_x k_B T}. \tag{A.5}$$

In Eq. A.5, n_1 is the refractive index and $\Gamma_{0,r}$ is the decay rate of excitons at $k_\parallel = 0$. The experimentally observed decay rate ($\gamma_{\text{exp}}(T)$) is the weighted average of the free and localized exciton decay rates,

$$\gamma_{\text{exp}}(T) = \frac{n_{\text{fr}}(T)\gamma_{\text{fr}}(T) + n_{\text{l}}(T)\gamma_{\text{l}}(T)}{n_{\text{fr}}(T) + n_{\text{l}}(T)}. \tag{A.6}$$

The quantum well's internal quantum efficiency can then be defined by dividing the radiative emission by the total emission,

$$\text{IQE} = \frac{n_{\text{fr}}(T)\gamma_{\text{fr,r}}(T) + n_{\text{l}}(T)\gamma_{\text{l,r}}}{n_{\text{fr}}(T)\gamma_{\text{fr}}(T) + n_{\text{l}}(T)\gamma_{\text{l}}}. \tag{A.7}$$

We quantitatively analyze n_{fr} using a model proposed by Xu *et al.* for InAs/GaAs heterostructures [242] and adapted for InGaN layers [243] valid in the low excitation density limit. Now, the density n'_{fr} is defined to be both energy and temperature dependent, and relates to the overall localized carrier density by the formula,

$$n_{\text{fr}} = \int_E n'_{\text{fr}}(E, T) dE. \tag{A.8}$$

---

[2]More generally, $\gamma_{\text{fr,r}}(T) \propto T^{-d/2}$, where d is the dimensionality of the quantum confined system. Therefore, exciton radiative decay rates in bulk, 2D, 1D, and 0D semiconductor systems follow $T^{-3/2}$, T^{-1}, $T^{-1/2}$, and T-independent dependencies, respectively.

The time evolution of $n'_{\text{fr}}(E, T)$ is described by the rate equation,

$$\frac{dn'_1(E, T)}{dt} = R_l(E) - \gamma_{\text{th}} n'_1(E, T) \exp\left(\frac{E - E_{\text{fr}}}{k_B T}\right) + k_r \gamma_{\text{th}} f_c(T) \rho_l(E) - \gamma_l n'_1(E, T), \tag{A.9}$$

where $\rho_l(E)$ is modeled by a Gaussian distribution of states,

$$\rho_l(E) = \frac{N_l}{\sqrt{2\pi\sigma_l^2}} \exp\left(-\frac{(E - E_l)^2}{2\sigma_l^2}\right), \tag{A.10}$$

centered at energy E_l with standard deviation σ_l. In Eq. A.9, the first term represents the optical pump rate. The second term signifies thermal excitation of localized excitons with energy E to free states with energy E_{fr} at an attempt-to-escape rate γ_{th}. The third term models carrier re-capture by localized states with rate constant $k_r \gamma_{\text{th}}$; the function $f_c(T)$ represents the fraction of delocalized carriers recaptured,

$$f_c(T) = \frac{1}{N_l} \int_{E'} n'_1(E', T) \exp\left(\frac{E' - E_{\text{fr}}}{k_B T}\right) dE'. \tag{A.11}$$

In Eq. A.9, the final term captures localized state recombination with total rate γ_l, which we assume to be energy-independent for simplicity.

The model represented by Eqs. A.9-A.11 predicts an "S"-shape of the PL energy with the maximum intensity (E_{PL}) [243, 244]. Under steady-state conditions, $dn'_1(E, T)/dt = 0$, $E_{\text{PL}}(T)$ follows a modified Varshni law, which can be found by setting $dn'_1(E, T)/dE = 0$,

$$E_{\text{PL}}(T) = E_g(T) - x(T) k_B T, \tag{A.12}$$

where $E_g(T)$ is the normal bulk band gap behavior expected from the Varshni model (Eq. 2.14) and $x(T)$ is given by the solution to the transcendental equation,

$$xe^x = \frac{\gamma_{\text{th}}}{\gamma_l}\left[\left(\frac{\sigma_l}{k_B T}\right)^2 - x\right] \exp\left(\frac{E_{\text{loc}}}{k_B T}\right), \tag{A.13}$$

where

$$E_{\text{loc}} = E_l - E_{\text{fr}}. \tag{A.14}$$

Eq. A.13 admits a single solution. In the high temperature regime, $\frac{\gamma_{\text{th}}}{\gamma_l} \exp\left(\frac{E_{\text{loc}}}{k_B T}\right) \gg 1$, Eq. A.12 becomes

$$E_{\text{PL}}(T) \approx E_g(T) - \frac{\sigma_l^2}{k_B T}. \tag{A.15}$$

Hence, in this limit, this model reproduces the temperature dependence expected for emission from localized states in the tail of a Gaussian distribution [245].

Physical interpretation

The "S"-shape dependence of E_{PL} can be explained with the help of the schematic diagram shown in Fig. A.1, which is an anology to thermal annealing in an energy landscape. At 4
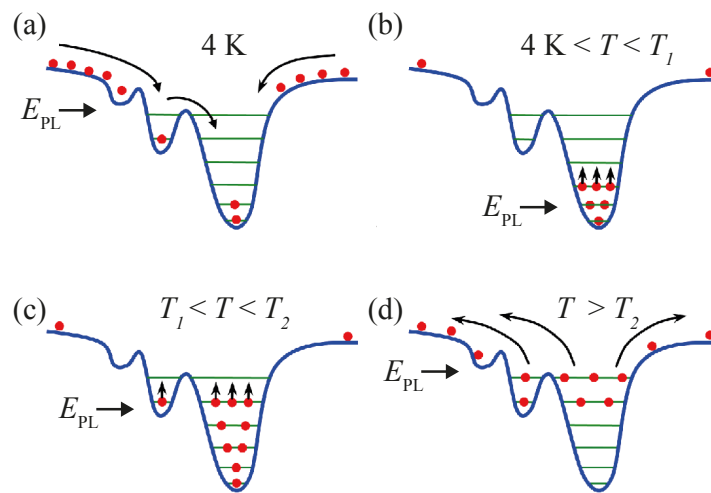
Figure A.1: Schematic explaining the "S"-shape dependence of E_{PL} with temperature. (a) Localized excitons "frozen" at cryogenic temperatures. (b) Localized excitons move to local energy minima up to temperature $T_1 \sim 70$ K before radiative recombination. (c) Fast, thermally activated nonradiative recombination causes localized exciton to recombine before they reach local energy minima between T_1 and $T_2 \sim 160$ K. (d) Above T_2, thermal equilibrium shifts the exciton population in favor of free excitons. Adapted from Wang *et al.* under an open access license [246].

K, excitons remain trapped in whichever potential minima they initially relax into. From cryogenic temperatures up to a sample-dependent temperature T_1 (~ 70 K for the samples considered here), excitons gain enough thermal energy to probe the nearby energy landscape, eventually moving to local energy minima in the spatial vicinity; E_{PL} redshifts. Between T_1 and the delocalization temperature T_2 (160 K for the samples considered here), thermally activated nonradiative recombination quenches excitons before they can reach potential minima; the emission blueshifts and broadens. Above T_2, excitons are fully delocalized into 2D quantum well states, recovering a Varshni-like dependence of E_{PL} with temperature (Eq. A.15) and further broadening the emission.

A.2 Experimental optical properties

Two $In_{0.15}Ga_{0.85}N$/GaN quantum well samples with different thicknesses, $d_{qw} = 2$ nm (A3530) and $d_{qw} = 3$ nm (A2916/A3572), were studied by PL spectroscopy. To improve the collection efficiency in the backscattering geometry, a $\lambda/4n_{SiO2} \approx 80$ nm thick SiO_2 layer was deposited on A2916 by PE-CVD, enabling measurements up to room temperature using nonresonant optical pumping. The sample A3530 remained uncoated, but exhibited stronger PL signal due to its thinner d_{qw}.

Photonic crystal nanobeams processed from the $d_{qw} = 3$ nm quantum well (A2916/A3572) were studied in several publications on nanolasers [13, 27]. Subsequent but nominally identical quantum wells were used in follow-on studies [14, 173]. Specifically, sample A3405 was explored in Sections 4.2, 4.4, and 4.5.4 of this thesis and for the oxygen desorption experiments on microdisks in Chapter 5 (A3572). The PL spectra and their temperature-dependence closely resemble the samples A2916/A3572 studied in this section.

Photonic crystal nanobeams processed from the $d_{qw} = 2$ nm quantum well (A3530) were studied in Sections 4.5.2 and 5.5. Subsequent but nominally identical wafers were used in the microdisk publication [205] and for the doping and passivation experiments on microdisks in Chapter 5 (A3360). Photonic crystals fabricated from a third nominally identical wafer (A3532) were utilized for the study on anisotropic wet etching (Section 4.5.5). The PL spectra and their temperature-dependence closely resemble the sample A3530 examined in this section.

Various experimental apparatus were used. The macro-PL measurement setup, which wasn't introduced in Ch. 3, is introduced here. It consists of a cw HeCd pump laser at $\lambda = 325$ nm (Kimmon Koha), a closed cycle cryostat (Janis), and a Jobin-Yvon iHR 320 spectrometer with Peltier-cooled Synapse CCD. Optical pumping was conducted in an off-axis geometry with a spot size of $\sim 50~\mu m$ and a NA = 0.25 lens was used to collect the PL. The TR-PL setup with the streak camera was already described in Section 3.2.6.

Steady-state photoluminescence

Figure A.2(a) shows the temperature-dependent PL spectra for the 3 nm thick quantum well. $50~W/cm^2$ nonresonant cw optical pumping with a HeCd laser ($\lambda = 325$ nm) and $200~W/cm^2$ resonant pumping with a diode laser ($\lambda = 405$ nm) were employed. The intensity was selected to remain in the low density excitation regime where the model based on Eq. A.9 remains valid; experimentally, this intensity corresponds to the maximum intensity at which no blueshifting of the emission occurs at the base temperature of 11 K. The peak at 2.2 eV is the yellow band defect emission from bulk GaN [81], while the peak at ~ 3.43 eV is the temperature-dependent GaN band edge emission, whose energy is shifted by the large tensile strain. The peak at 2.95 eV (Fig. A.2(b)) is comprised of emission from high-energy InGaN localization centers, and will be discussed in the last section of this Appendix.
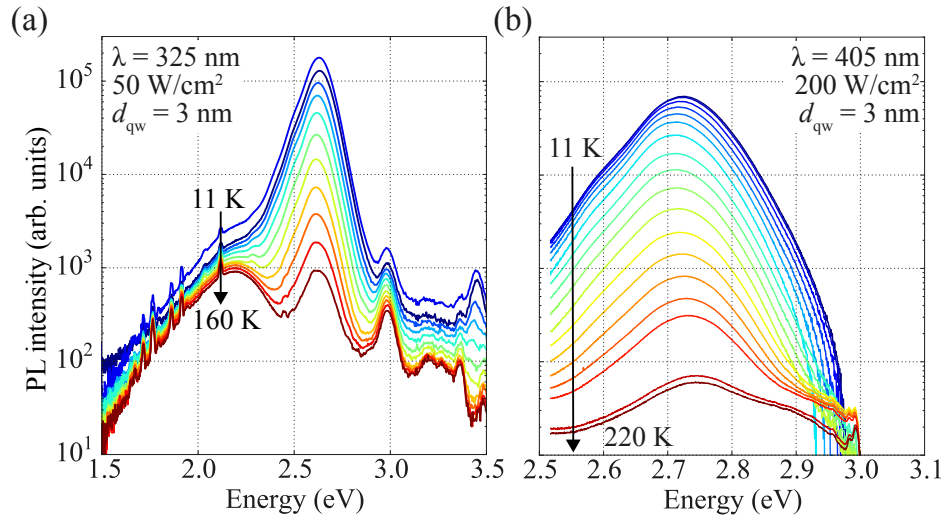
Figure A.2: Temperature-dependent macro-PL of 3 nm thick quantum wells under (a) 50 W/cm^2 cw optical pumping with $\lambda = 325$ nm and (b) 200 W/cm^2 cw optical pumping with $\lambda = 405$ nm. Wafer A2916 was used for non-resonant pumping and A3572 was used for resonant pumping, so the spectra are not strictly comparable.
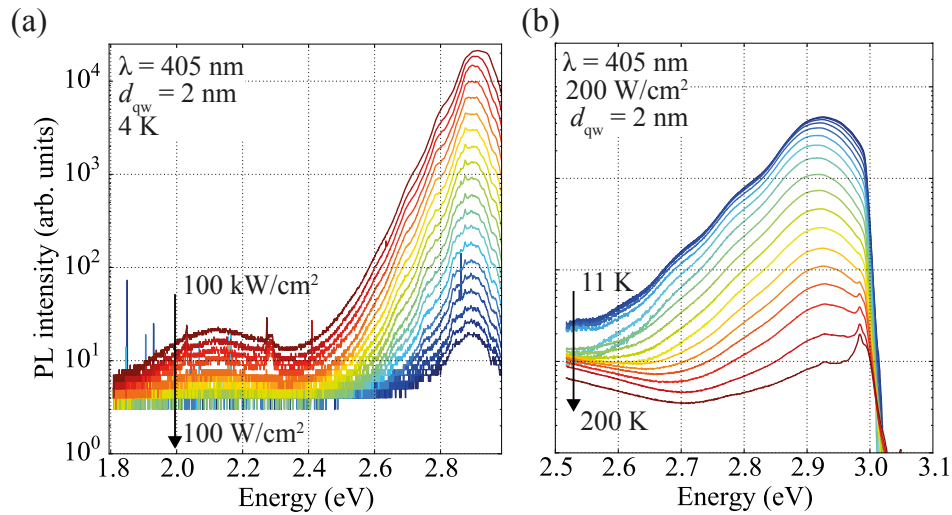
Figure A.3: Temperature-dependent PL of 2 nm thick quantum well under cw resonant pumping with a $\lambda = 405$ nm laser. (a) Power dependence at 4 K measured in μPL. (b) Temperature dependence in macro-PL using 200 W/cm^2 intensity. The shoulder close to 3.0 eV at high temperatures is residual electroluminescence from the pump laser. Wafer A3530 was used for all measurements.

For comparison, Fig. A.3 examines the PL of the $d_{\text{qw}} = 2$ nm quantum well. In order to achieve higher excitation intensities, the power-dependent resonant excitation experiments in Fig. A.3(a) were carried out in the μPL setup. The shoulder on the low energy side of the quantum well μPL is an LO phonon replica. At the highest intensity, a subtle shoulder appears on the high energy side, which may be indicative of the transition to an electron-hole plasma near the transparency threshold [85, 247]. Because the yellow band luminescence originates from the GaN barriers [81], the resonant pumping further increases the ratio of peak quantum well μPL intensity to peak yellow band μPL intensity to 1000. The sharp peaks in the yellow band are cosmic rays, which pass through the CCD during long integration times. Comparing the two quantum well thicknesses, the increase in d_{qw} from 2 to 3 nm shifts E_{PL} from 2.95 to 2.6 eV, as qualitatively expected for a quantum well based on the "toy" model with the quantum confined Stark effect presented in Section 2.4.4.

Keeping the general spectral features of Figs. A.2-A.3 in mind, Fig. A.4 shows the temperature dependence of the integrated PL intensity, which decreases by nearly four and three orders of
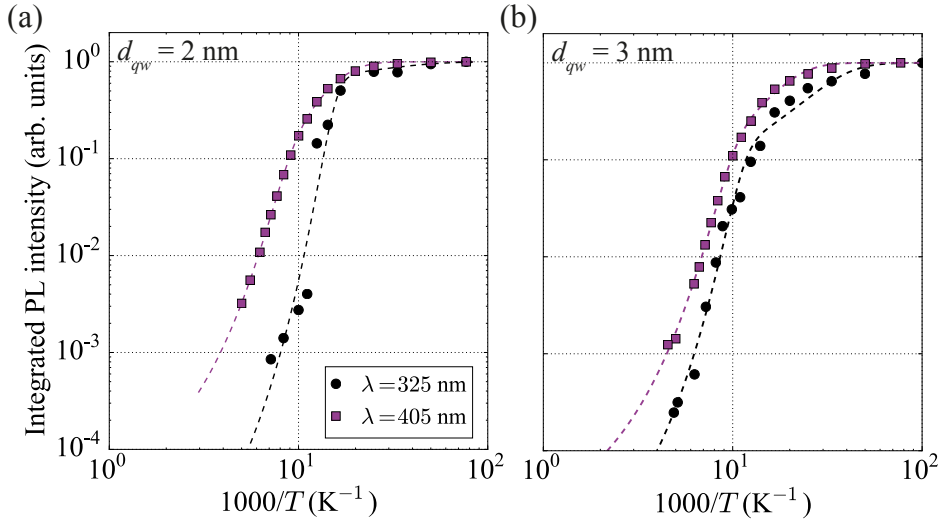
Figure A.4: Temperature-dependent integrated μPL intensity for the (a) 2 nm and (b) 3 nm quantum wells under cw optical pumping. 50 W/cm^2 and 200 W/cm^2 power densities were employed for the nonresonant ($\lambda = 325$ nm) and resonant ($\lambda = 405$ nm) cases, respectively. Dashed lines are fits to a two-component Arrhenius law (Eq. A.16). Fit parameters are given in Table A.1.

magnitude when moving from base to room temperature for nonresonant and resonant pumping, respectively. A two-component Arrhenius law can be fit to the temperature-dependent integrated PL intensity. The fit equation is

$$\frac{I_{\text{PL}}(T)}{I_{\text{PL}}(11 \text{ K})} = \left[C_1 \exp\left(-\frac{E_{a_1}}{k_B T} \right) + C_2 \exp\left(-\frac{E_{a_2}}{k_B T} \right) \right]^{-1}, \tag{A.16}$$

where $I_{\text{PL}}(T)$ is the temperature-dependent PL intensity, C_1 and C_2 are constants, and E_{a_1} and

E_{a_2} are activation energies.

Table A.1 gives a list of the fit parameters for the two quantum wells in the low injection regime. The fits comprise two terms with drastically differing amplitudes and activation energies.

Wafer	d_{qw} (nm)	λ (nm)	C_1	E_{a_1} (meV)	C_2	E_{a_2} (meV)
A3530	2	325	1.1×10^6	75	0.95	9
A3530	2	405	6.1×10^4	94	51	24
A2916	3	325	5.8×10^5	88	18	9
A3572	3	405	8.8×10^4	86	30	17

Table A.1: Fit parameters for a two-component Arrhenius law fit to the temperature-dependent integrated PL intensity (Figs. A.2 & A.3).

Interestingly, C_1 and E_{a_2} differ for near-resonant and nonresonant pumping on the same d_{qw} samples. Because the nonresonant pumping relies upon the transfer of photogenerated electron-hole pairs or excitons from the bulk GaN barriers to the InGaN quantum well, the differing values are ascribed to thermally activated nonradiative recombination occurring in the GaN barriers. In the case of resonant pumping, we attribute C_1 / E_{a_1} to the thermally activated nonradiative recombination of free excitons $E_{\mathrm{fr,nr}} = E_{a_2}$. Since C_2 / E_{a_2} dominate below T_1 in both samples, these values are assigned to thermally activated nonradiative recombination of localized excitons ($E_{\mathrm{l,nr}} = E_{a_2}$).

The dependence of E_{PL} with temperature are extracted from the spectra and plotted in Fig. A.5. Both quantum wells indeed exhibit an "S"-shaped temperature dependence of E_{PL}, with
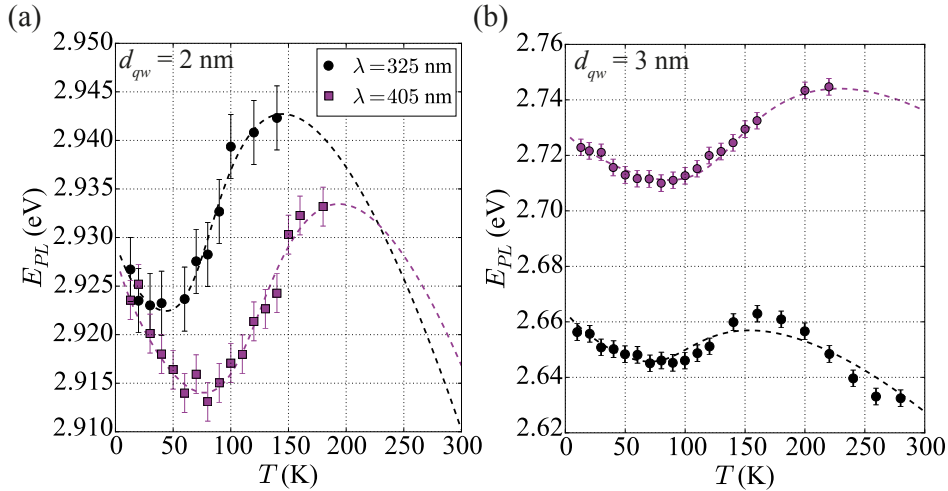
Figure A.5: Temperature dependence of E_{PL} (a) 2 nm and (b) 3 nm quantum well under cw 200 W/cm^2 resonant ($\lambda = 405$ nm) and cw 50 W/cm^2 nonresonant ($\lambda = 325$ nm) optical pumping. Dashed lines are E_{PL} fits. Error bars are defined by the resolution of the large spectral window gratings used in such measurements. Fit parameters are given in Table A.2.

$T_1 = 50$ (80) K and $T_2 = 140$ (150) K for the $d_{qw} = 2$ (3) nm quantum well under nonresonant pumping. Resonant pumping increases the delocalization temperature and localization energy. This is because the resonant pumping excites a different population of localized states than those indirectly excited from the GaN barriers during nonresonant pumping [248].

To further support the idea that a different exciton population is excited, the FWHM for nonresonant pumping is greater than that for resonant pumping (Fig. A.6). For both $d_{qw} =$
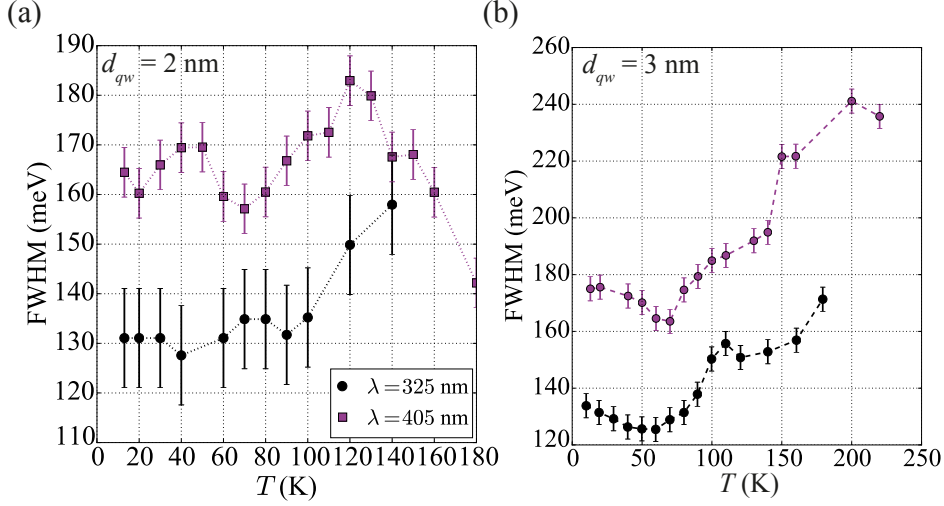
Figure A.6: Temperature dependence of the FWHM (a) 2 nm and (b) 3 nm quantum well under cw 200 W/cm^2 resonant ($\lambda = 405$ nm) and cw 50 W/cm^2 nonresonant ($\lambda = 325$ nm) optical pumping. The last point for resonant pumping on the $d_{qw} = 2$ nm is an artifact. Lines are guides to the eye.

2 and 3 nm, the FWHM reaches a minimum in the vicinity of T_1, in accordance with the schematic presented in Fig. A.1. It broadens as the temperature is increased across T_2 and the exciton population is primarily free excitons.

The localized state emission model (Eqs. A.9-A.15) can be used to fit the experimental dependence of E_{PL}. The fit parameters are given in Table A.2. E_l values are slightly blueshifted

Wafer	d_{qw} (nm)	λ (nm)	E_l (eV)	E_{loc} (meV)	σ_l (meV)	γ_{th}/γ_l
A3530	2	325	2.997	67	21	6.8
A3530	2	405	3.025	96	32	8.4
A2916	3	325	2.718	54	23	30
A3572	3	405	2.865	136	39	9.6

Table A.2: Fit parameters for the E_{PL} temperature dependence under nonresonant pumping following the model of emission from a Gaussian distribution of localized states. The Varshni model parameters ($\alpha_V = 0.84$ meV/K and $\beta_V = 774$ K) are derived from the values given in Table 2.1 using Vegard's law without bowing.

relative to the PL peak intensity. The values of E_l and E_{loc} are in agreement with the literature for InGaN/GaN quantum wells with similar thickness and composition [249, 250]. σ_l is in accord with the 31.5 meV value found by Eliseev *et al.* in the high temperature limit [245]. Furthermore, the ratio of γ_{th} to γ_l justifies the *a priori* assumption that localized and free exciton distributions are in thermal equilibrium. The smaller ratio of $\gamma_{\text{th}}/\gamma_l$ should also be expected for $d_{\text{qw}} = 2$ nm due to faster radiative recombination in this sample. We note that the FWHMs corresponding to σ_l are 49 and 54 meV for non-resonant pumping, which remain much less than the minimum experimental linewidths ~ 125 meV. This indicates that there is an additional source of inhomogeneous broadening in the system [247], such as strain inhomogeneities. This further evidences the poor quality of the single InGaN/GaN quantum well due to the high tensile strain for growth on silicon. Finally, E_{loc} is seen to be deeper for resonant pumping on all samples and σ_l is larger, reflecting the higher delocalization temperature and wider quantum well PL spectra observed under resonant pumping.

Time-resolved photoluminescence

Temperature-dependent TR-PL measurements were conducted on the $d_{\text{qw}} = 3$ nm sample (A2916) using a streak camera. Fig. A.7(a) shows the power dependence of the time-integrated
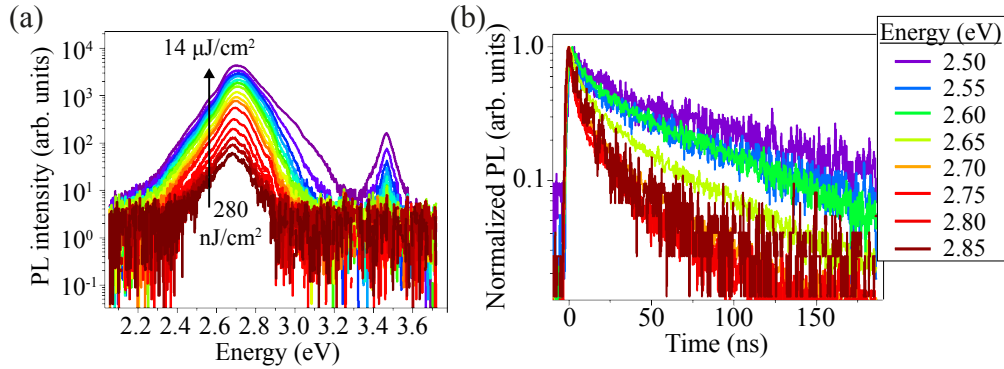
Figure A.7: TR-PL of 3 nm quantum well at 4 K and 80.5 MHz pumping using nonresonant picosecond pulses at $\lambda = 280$ nm. (a) Power dependence. (b) Time traces at 1.5 μJ/cm^2 fluence evidencing the quantum confined Stark effect decreasing the decay rate (increasing the lifetime) of redshifted states. An excitonic picture is valid at such low fluences because the measured lifetime is nearly independent of power up to the highest measured fluence at 4 K.

TR-PL at 4 K. The GaN band edge emission is visible. At high fluences, a high energy shoulder appears possibly indicating a cross over into the high density, electron-hole plasma regime is clearly present. In contrast to Fig. A.2(a), no localized state emission can be observed due to the limited dynamic range of the streak camera.

The decay rate clearly depends on energy due to exciton transfer from high energy to localized states in addition to the quantum confined Stark effect. Redshifted emission exhibits slower decay rates. By normalizing to the intensity at $t = 0$, Fig. A.7(b) shows this effect more clearly.

The highest energy, 2.85 eV, exhibits a lifetime of 18 ns, whereas the lowest energy, 2.50 eV, decays with a lifetime of 105 ns, at the base temperature of 4 K. Although the model discussed in the previous sections does not account for the energy-dependent decay rate, we proceed by integrating the emission over energy at each point in time to arrive at a single decay transient. Although this step obscures many features of the underlying physics, this simplification connects the experimental results to the theoretical model, enabling order-of-magnitude estimates of the lifetimes and density of localization centers, N_l.

Fig. 8 A.8(a) shows the temperature dependence of the average recorded experimental decay time, γ_{exp}^{-1} and the corresponding fit to Eqs. A.6. Parameters, such as the localization energy
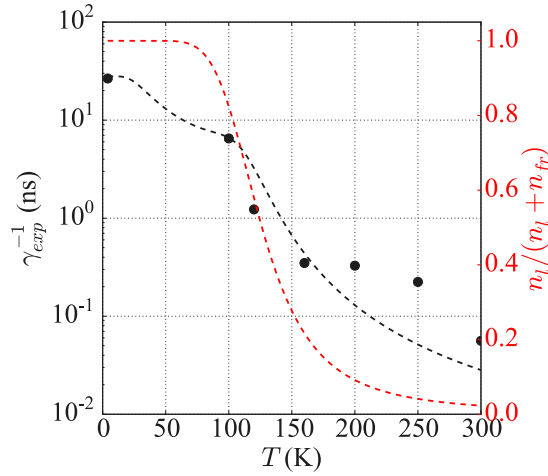
Figure A.8: The 3 nm quantum well's temperature-dependent lifetime using the smallest measureable fluence (1.5 μJ/cm^2) over the entire temperature range. Dashed black curve shows the fit to Eq. A.6 using the self-consistent set of parameters described in the text. Red dashed curve shows the fraction of localized excitons computed by the model.

and activation energies for nonradiative recombination are held constant at the values determined in the previous section ($E_{\text{loc}} = 54$ meV, $E_{\text{l,nr}} = 9$ meV, and $E_{\text{fr,nr}} = 75$ meV). The free fit parameters in the model are N_l along with the various decay rates (Table A.3). Although

N_{l} (cm^{-2})	$\gamma_{\text{l,r}}^{-1}$ (ns)	$\gamma_{\text{l,nr}}^{-1}(\infty)$ (ns)	$\gamma_{\text{fr,r}}^{-1}$(4 K) (ns)	$\gamma_{\text{fr,nr}}^{-1}(\infty)$ (ps)
1×10^{11}	28	3	1	2

Table A.3: Self-consistent fit parameters for the γ_{exp} temperature dependence under nonresonant pumping in Eq. A.6. Other parameters were held constant and were taken from the literature [81], the Arrhenius law fits (Table A.1) and the fit for E_{PL} (Table A.2). See text for details.

there are five free parameters in a nonlinear model, the fit parameters can be deconvoluted based on physical intuition and experimental knowledge of the temperature-dependent lifetime (Fig. A.8(a)) and PL intensity (Fig. A.4(b), near-resonant pumping). First, N_l controls T_2. The radiative lifetime of localized excitons controls the experimental lifetime at 4 K. The

nonradiative lifetime of the localized excitons dominates the ~ 38% relative IQE at ~ 120 K and the ratio of the nonradiative to radiative free exciton lifetimes dictates the IQE at room temperature (~ 0.1%). Note that the IQE is a relative number and does not include losses due to nonradiative recombination in the GaN barriers under nonresonant pumping at low temperatures.

The fit value of $N_l = 1 \times 10^{11}$ cm^{-2} is several times larger than the observed dislocation density (Fig. 4.18), which is consistent with a high quantum well IQE at low temperatures. According to the fit model, the exciton population balance favors free excitons starting a temperature of around 125 K, in line with the observed E_{PL} dependence. A further future development could be to tune the quantum well thickness, alloy composition, and growth conditions to push T_2 to higher temperatures via engineering of E_{loc} and N_l.

The temperature dependence of each of the lifetimes is computed in Fig. A.9(a). Nonradiative
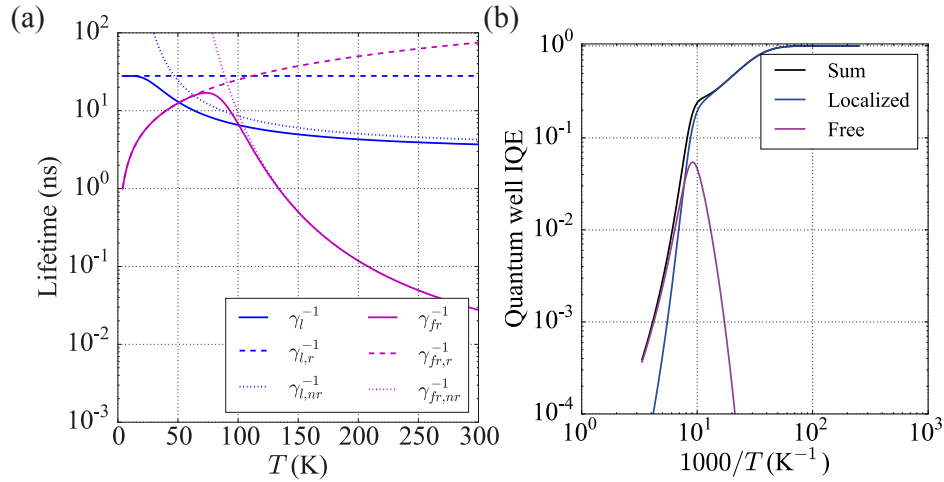
Figure A.9: Computed quantities from fit parameters. (a) Temperature-dependent lifetimes of free and localized excitons separated into radiative and nonradiative contributions resulting from the fit model. (b) Relative quantum well IQE (Eq. A.7) calculated from the fit parameters. The free and localized exciton contributions are shown for each of the two terms in Eq. A.7.

recombination dominates localized exciton lifetime above ~ 80 K and free exciton lifetime above 130 K. Furthermore, free excitons decay faster than localized excitons. Free excitons persist on timescales of hundreds of picoseconds when their emission dominates at temperatures above T_2, whereas localized exciton emission has lifetimes on the order of ~ 8 − 20 ns when their emission dominates at temperatures below T_2.

Fig. A.9(b) shows the individual contributions of localized and exciton radiative emission to the overall IQE. The crossover from emission dominated by localized exciton radiative recombination to free exciton radiative recombination occurs around 100 K, e.g. before the exciton population becomes 50% free excitons at $T_2 = 125$ K. This is consistent with the experimental flattening of the FWHM broadening around this temperature (Fig. A.5(b), red).

A.3   Localized state emission

During measurements of microdisks at cryogenic temperatures, a series of sharp peaks was observed on the high energy side of the $d_{qw} = 3$ nm quantum well (wafer A3572) emission beyond 3.05 eV. The origins of the peaks could not be attributed to photonic resonances for two reasons; first, strong absorption of the quantum well at such energies should strongly broaden and dampen resonances. Second, these peaks were also observed on unprocessed, reference areas of the sample without an air gap.

In order to distinguish between luminescence from GaN deep level defects [156] and InGaN/-GaN quantum well localization centers [199], two additional samples were grown with and without the quantum well. A few faint lines were found around 3.1 eV on the sample without the quantum well, but their emission intensity, spatial concentration, and energy density were more than two orders of magnitude below the second $d_{qw} = 3$ nm sample, whose characteristics reproduced those of the material used in the microdisk sample (A3572). Therefore, the sharp lines are attributed to individual localization centers in the $In_{0.15}Ga_{0.85}N$ quantum well.

First, we can further analyze μPL measurements conducted on the oxygen-passivated microdisk sample (Fig. 5.11(a)) at higher energies to estimate the spectral and spatial energy density of the localization centers. Fig. A.10(a) shows the FWHM dispersion of 81 resonances
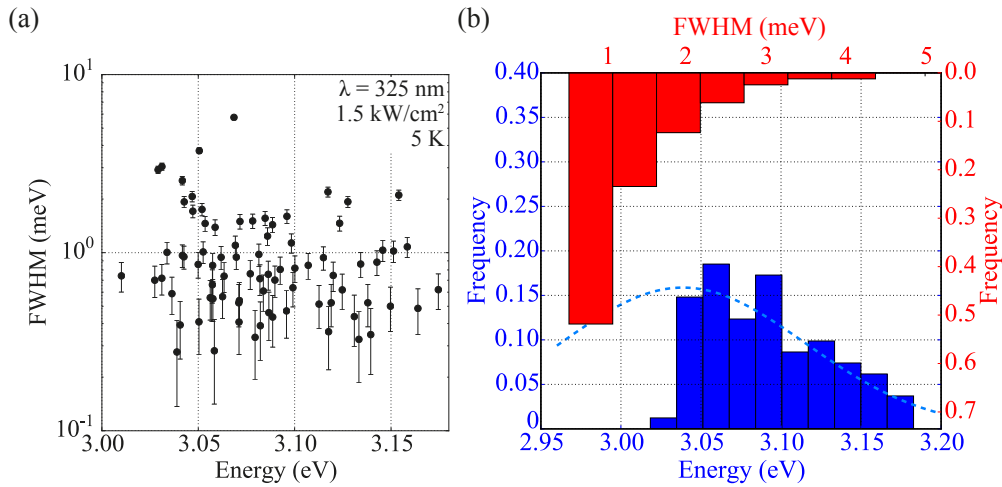
Figure A.10: (a) Scatter plot of FWHM dispersion for $N = 81$ Lorentzian peaks extracted from μPL spectra of 12 nominally identical microdisks. (b) Histogram showing the likelihood of observed energies (blue) and linewidths (red). Light blue dashed line is a fit to a Gaussian distribution centered at 3.04 eV with 180 meV FWHM.

measured and fit by Lorentzian functions over 12 nominally identical $\varnothing = 3$ μm microdisks using 1.5 kW/cm^2 cw $\lambda = 325$ nm optical pumping at 5 K. No clear correlation between energy and FWHM is observed. 59 resonances occured in the 100 meV wide energy window between 3.05 to 3.15 eV. Dividing this by the total microdisk area leads to an estimate of the localization

center spatial and energy density at 3.10 eV,

$$\rho_l(3.10 \text{ eV}, 5 \text{ K}) = 1 \times 10^9 \quad \text{cm}^{-2} \cdot \text{eV}^{-1}. \tag{A.17}$$

Evaluation of Eq. A.10 using the fit parameters determined in the previous section leads to carrier densities of 6×10^9 cm$^{-2}\cdot$eV^{-1} if the experimental quantum well FWHM is used instead of σ_l. Due to the large discrepancy, we conclude that the localized states at 3.10 eV must be of different physical origin than the localized states that make up the quantum well emission at ~ 2.7 eV.

Additional experimental data confirms this supposition. First, the macro-PL spectra at low excitation fluences exhibit a second distinct peak around ~ 3.0 eV that is clearly separate from the quantum well emission (Fig. A.2(a)). The narrow linewidths (< 1 meV) and temperature stability up to 75 K (Fig. A.13, to be discussed subsequently) differs from the previous study of InGaN/GaN quantum well localization center emission, in which few meV linewidths and stable emission up to 20 K was demonstrated in a quantum well with the same thickness and indium concentration [199]. Naïvely, one would expect high energy emission in the quantum well to be *less* stable against temperature because the higher energy localized states should be closer to the continuum. One possible hypothesis that should be investigated in the future is that this emission emerges from V-shaped pits in the rough quantum well, which would tilt the exciton's dipole moment away from the $+c$-axis onto a semipolar crystal plane, reducing the detrimental effects of the quantum confined Stark effect and blueshifting the emission. This would mean that these localization centers could be intermediate to those observed on c-plane InGaN/GaN quantum wells [199] and InGaN/GaN dots grown by making a rough quantum well on nonpolar m-plane GaN surfaces [201, 251].

Fig. A.10(b) bins the peaks extracted from the microdisks into histograms. Emission at lower energies is difficult to fit due to the rising quantum well background emission. The dashed blue line shows a fit to a Gaussian distribution centered at 3.04 eV with 180 meV linewidth. Inversion of Eq. A.10 allows us to solve for the localization center density N_l because the spectral density at 3.10 eV is known (Eq. A.17). We find a localization center spatial density, $N_l = 3 \times 10^8$ cm^{-2}. Note that this should be considered as a lower bound, as the low energy peaks could not be fit due to the rising quantum well background. This density is several orders of magnitude below the localization center density of the quantum well found in the previous section. Interestingly, more than 50% of the emitters exhibit linewidths below 1 meV. This is attributed to faster radiative recombination due to the reduced quantum confined Stark effect for high energy localization centers and potentially an off-axis orientation of the exciton dipole.

With the origin of the emission identified and reproducibility between growths verified, a second chip from A3572 was patterned with 50 nm thick aluminum alignment markers using a standard lift-off electron beam lithography process [252]. These markers facilitated the study of the same localization centers for extended periods of time by allowing mechanical

rescanning to combat sample drift. However, the process should be improved in the future by creating etched mesas instead of alignment markers to both boost the light extraction and drop the quantum well background [201] in addition to passivating the surface in a thick PE-CVD SiO_2 layer to improve the long-term stability.

We conducted spatial mappings near the markers to find positions with sharp localization emission lines. A hyperspectral μPL mapping at base temperature using 55 W/cm^2 $\lambda =$
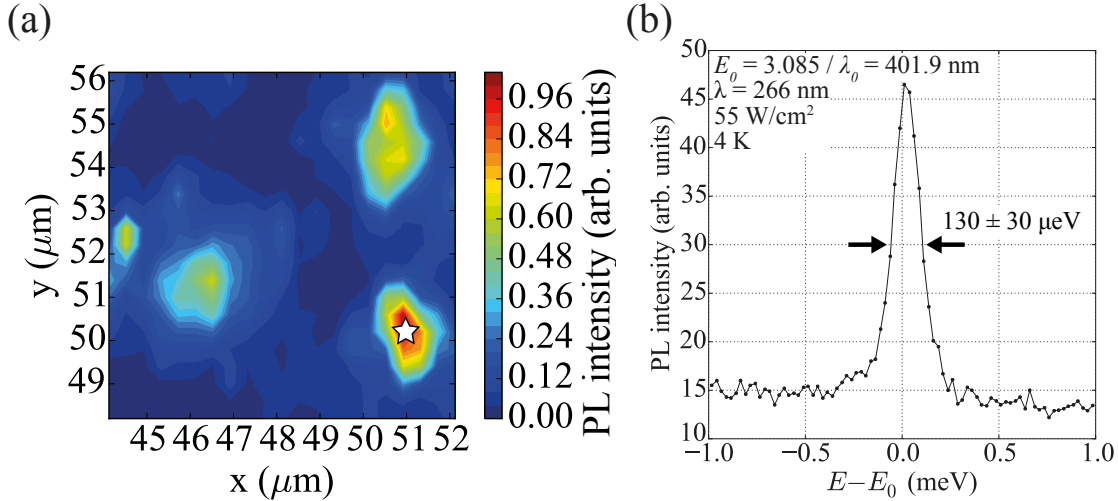
Figure A.11: (a) Energy slice at $E_0 = 3.085$ eV of a hyperspectral map scan using 55 W/cm^2 cw $\lambda = 266$ nm optical pumping at 4 K. The step size was 0.4 μm. The white star indicates the spatial position of a (b) sharp (FWHM $\sim 130\pm30$ μeV) line exhibiting nearly instrument-limited resolution ($\sim 100\pm30$ μeV) recorded using the 1800 lp/mm grating in second order.

266 nm cw optical pumping was performed over a 10×10 μm^2 area in 0.4 μm steps. The energy $E_0 = 3.085$ eV is selected to demonstrate the low spatial localization center density in Fig. A.11(a), where 4 localization centers are found. The objective was then shifted to the point demarcated by the white star. Fig. A.11(b) shows a high resolution spectra recorded using the 1800 lp/mm grating in second order. The measured linewidth of 130 ± 30 μeV is principally limited by the spectral resolution at this energy, 100 μeV. To the best of the author's knowledge, this is the smallest reported linewidth for emission by localization centers in InGaN/GaN c-plane quantum wells. This demonstrates the clear potential of these centers for quantum photonics applications. Futhermore, such narrow linewidths reinforce speculation that emission originates from a small localization center, as InGaN/GaN localization centers are known to be vulnerable to spectral diffusion [200].

After moving to a second spatial location "2," Fig. A.12 shows the power dependence of the sharp lines at base temperature under cw $\lambda = 325$ nm optical pumping. In Fig. A.12(a), the sharp lines at low power densities are due to cosmic rays striking the CCD detector during the few minute integration times. We select two modes separated by 1.2 meV in the vicinity of 3.085 eV for quantitative analysis.

146
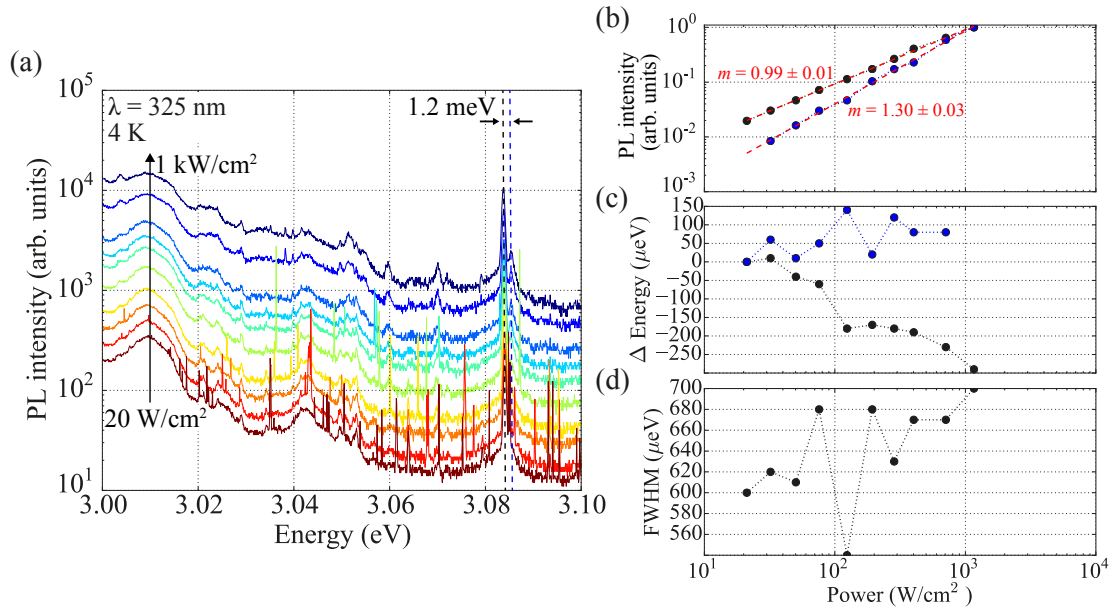
Figure A.12: Power-dependent μPL spectra at 4 K using λ = 325 nm optical pumping on Location 2. (a) Raw spectra. Spurious lines at low power densities are due to cosmic rays. Two lines around 3.085 eV are selected for Lorentzian lineshape fitting. (b) Extracted Lorentzian amplitude as a function of optical pump intensity. Dashed red lines are fits to a power law with exponent m. (c) Extracted peak energy dependence showing increased splitting. (d) Extracted linewidth broadening of the low energy (black) mode.

Fig. A.12(b), (c), and (d) plot the power dependence of the peak intensity, shift, and FWHM, respectively. We see that the energy splitting between the two lines increases and the lower energy line broadens. The lower energy mode (black) exhibits a nearly linear input-output characteristic, whereas the blue line exhibits a superlinear power dependence. Although one could tentatively assign the black and blue modes to exciton and biexciton emission, respectively, power dependent measurements over several spatial positions (not shown) reveal power law exponents ranging from 0.5 to 2.1. It is known that multi-excitonic complexes in InGaN/GaN localization centers can exhibit both binding and anti-binding excitonic behavior [200]. In a given spatial position, the assignment of closely spaced lines to the same localization center requires careful jitter, polarization, and power-dependent measurements [200, 253], which are beyond the scope of the current work.

Figure A.13 explores the temperature dependence of the sharp line at 3.085 eV on Location 2 under 200 W/cm^2 cw $\lambda = 325$ nm optical pumping. At 4 K, the peak at 3.085 eV is most
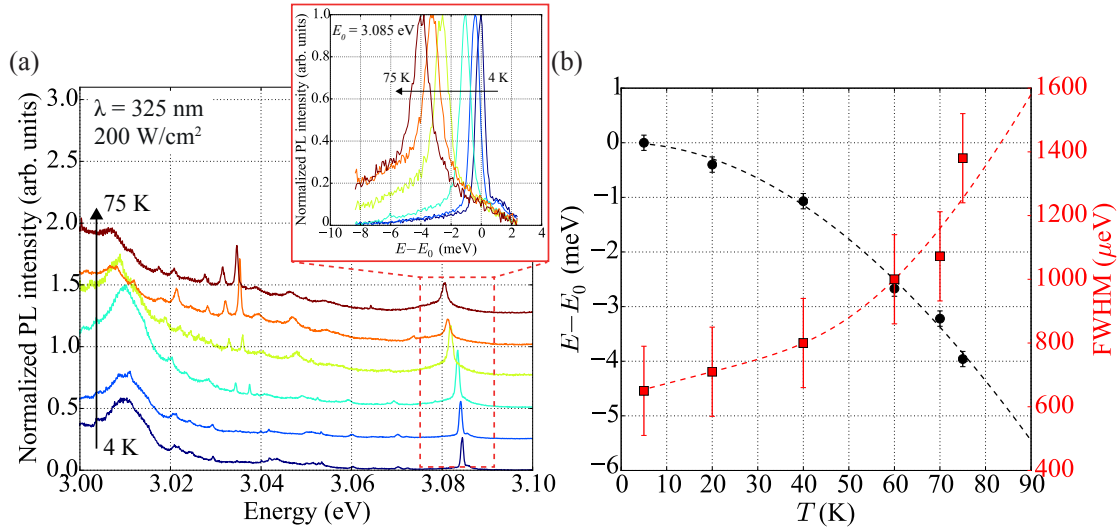
Figure A.13: (a) Temperature-dependent μPL under under 200 W/cm^2 cw $\lambda = 325$ nm optical pumping on Location 2. Spectra are shifted vertically for clarity. The inset shows a magnified version of the spectra in the dashed red box around the peak at $E_0 = 3.085$ eV. (b) Temperature-dependent mode shift (black dots) and broadening (red squares) fit. The black dashed line is a Varshni fit (Eq. 2.14). The red dashed line is a fit to Eq. A.18.

prominent. As temperature increases beyond 30 K, new peaks appear in the vicinity of 3.03 eV. We attribute this to the ability of localized excitons to move about the energy landscape with increasing temperature (Fig. A.1(b)) and to find new potential minima. As expected for thermally activated nonradiative recombination, the intensity relative to the continuum emission at 3.01 eV decreases with temperature. At 80 K (not shown), the peak at 3.085 eV disappears but the peaks at 3.03 remain. We attribute this to thermal excitation of the excitonic complex to the continuum of quantum well states (Fig. A.1(c)).

The inset in Figure A.13(a) zooms in on the region of interest around the sharp line at 3.085 eV.

As temperature increases, the line redshifts and broadens. Besides these obvious features, the lineshape evolves with temperature, exhibiting a high energy shoulder at base temperature and growing a broad pedestal-like base as the sample is heated. The lineshape and its evolution resemble prior work on m-plane InGaN/GaN quantum dots [201, 251].

Lorentzian lineshape fits were performed for the mode at E_0 and the results are plotted in Fig. Figure A.13(b). The redshift follows a clear, parabolic Varshni dependence at low temperatures (Eq. 2.14) with fit $\alpha_V = 0.58$ meV/K. If one inverts Vegard's law to solve for composition, this α_V value would correspond to the alloy $In_{0.68}Ga_{0.34}N$ ($E_g = 1.3$ eV), far from the expected stoichiometry of the quantum well $In_{0.15}Ga_{0.85}N$. Thus, one could speculate that the emission could originate from a tiny, indium rich cluster on a semipolar suface. The redshift with temperature is consistent with previous studies on c-[200] and m-plane [201, 251] InGaN/GaN localization centers.

The extracted linewidths can be fit to a simple model [200],

$$\text{FWHM}(T) = \text{FWHM}(0) + \alpha_l T + \beta_l \exp\left(-\frac{E_{\text{th,l}}}{k_B T}\right), \tag{A.18}$$

where α_l describes broadening by acoustic phonons and the final term represents thermally-activated dephasing into the continuum of InGaN states with rate constant β_l and activation energy $E_{\text{th,l}}$. The fit parameters are $\text{FWHM}(0) = 640$ μeV, $\alpha_l = 3.7$ μeV/K, $\beta_l = 11$ meV, and $E_{\text{th,l}} = 23$ meV. Our fit values are between those found by Seguin *et al.* for a $d_{\text{qw}} = 2$ nm quantum well ($\alpha_l = 1.7$ μeV/K, $\beta_l = 36$ meV, $E_{\text{th,l}} = 31$ meV) [200] and by Wang *et al.* for similar indium content $d_{\text{qw}} = 3$ nm m-plane quantum wells ($\alpha_l = 9$ μeV/K, $E_{\text{th,l}} = 40$ meV) [201]. Using Eq. A.1, we can exploit the extracted localization energy and the delocalization temperature (85 K) to again arrive at an estimate of the localization center density, $N_l = 6 \times 10^9$ cm^{-2}. This value corresponds to an average distance between localization centers of ~ 130 nm, remaining several orders of magnitude below the InGaN/GaN quantum well localization density determined in the previous section.

The polarization dependence of the μPL of Location 2 was measured under 500 W/cm^2 cw $\lambda = 325$ nm optical pumping at 30 K. Note that there may have been a slight positioning offset or surface deposition with the prior measurements, so the spectral shape has changed slightly relative to previous measurements. Fig. A.14(a) shows the results. Arrows indicate the previously studied sharp line at 3.085 eV (black), a faint line at 3.048 eV (blue), and the broad emission at 3.01 eV (red). Fits were conducted for each polarization angle to extract the peak intensity (Fig. A.14(b)) and position (Fig. A.14(c)). The three lines exhibit a high degree of linear polarization (DOLP),

$$\text{DOLP} = \frac{I_{\max} - I_{\min}}{I_{\max} + I_{\min}} = 0.67,$$

with peaks at 40° (3.085 eV), 100° (3.048 eV), and 130° (3.01 eV). The separations by 60° and 30° may indicate that the localization center(s) reflect(s) the underlying symmetry of the wurtzite crystal lattice. The lack of energetic shifts with polarization angle (Fig. A.14(c)) to within the
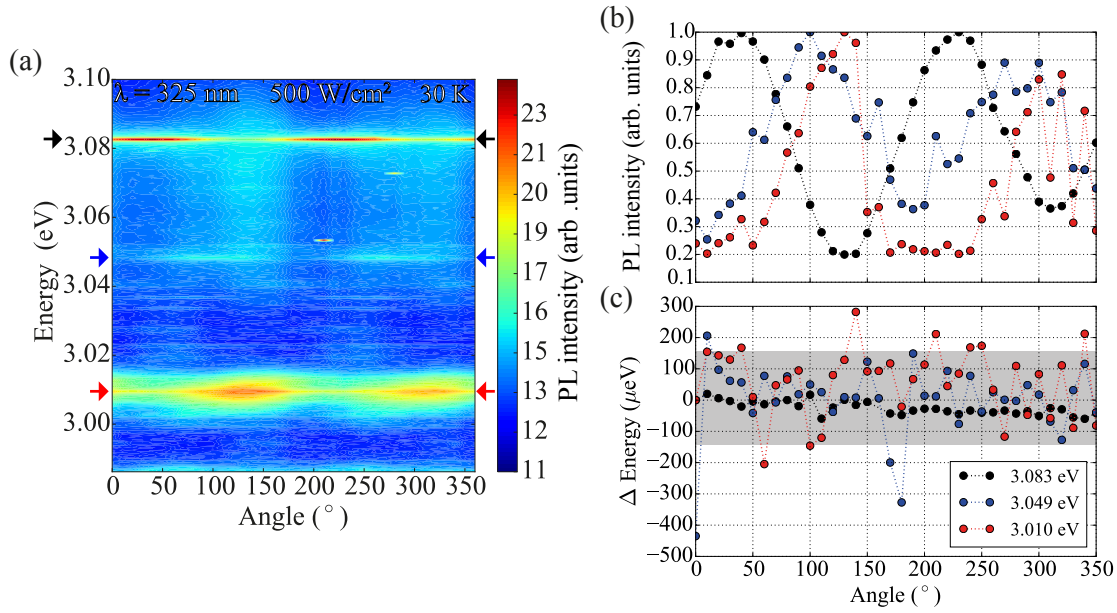
Figure A.14: (a) Polarization dependence of Location 2 under under 500 W/cm^2 cw $\lambda = 325$ nm optical pumping at 30 K measured by rotating the μPL signal using a $\lambda/2$ waveplate before a wire grid polarizer in the detection line. Arrows indicate energies of interest for subsequent fits of (b) peak intensity and (c) peak position.

spectral resolution (gray shaded area) provides evidence for either an extremely small or very large fine structure splitting, e.g. that the localization center is either symmetric or highly antisymmetric.

Summary

This Appendix studied the optical properties of single In$_{0.15}$Ga$_{0.85}$N/GaN quantum well gain media on silicon using PL spectroscopy. The main findings of this Appendix are:

- Under low intensity excitation, quantum well luminescence originates from bosonic excitons, which are localized at low temperatures (< 120 K) or free at higher temperatures.

- Under high intensity excitation, quantum well luminescence is due to a fermionic electron-hole plasma. The transition between excitonic and fermionic behavior occurs when the excitation density in the quantum well approaches the transparency threshold.

- The radiative efficiency of the quantum well is strongly temperature dependent due to thermally activated nonradiative recombination. The relative efficiency at room temperature compared to 4 K is:

  - $\sim 10^{-4}$ for nonresonant pumping of the barriers.
  - $\sim 10^{-3}$ for near-resonant pumping of the quantum well.

- The transparency threshold depends strongly on temperature.

- The transparency threshold is reached for ~ 10 W/cm^2 for nonresonant pumping and ~ 10 kW/cm^2 for near-resonant pumping at 4 K.

- The energy at which maximum quantum well PL intensity occurs exhibits an "S"-shaped temperature dependence due to a shift in thermal equilibrium between localized and free exciton populations in the low density limit.

    - The depth of the confinement potential is between 50 and 120 meV.
    - The depth of the confinment potential depends on the excitation conditions.
    - The spatial density is $\sim 1 \times 10^{11}$ cm^{-2}, which is larger than the observed dislocation density, $3 - 4 \times 10^{10}$ cm^{-2}.
    - The peak spectral density is $\sim 2 \times 10^{13}$ cm^{-2}·eV^{-1}.
    - The crossover from localized (0D-like) to free (2D-like) exciton populations occurs between 120 and 160 K.

- Below the transparency threshold, the lifetime of the quantum well emission at 4 K is around 30 ns and is dominated by radiative recombination of localized excitons.

- Below the transparency threshold, the lifetime of the quantum well emission at room temperature is around 100 ps and is dominated by nonradiative recombination of free excitons.

- A second population of localization centers in the InGaN/GaN quantum wells occurs at energies above the quantum well emission, ~ 3.04 eV.

    - The depth of the confinement potential is ~ 22 meV.
    - The emitter distribution could be a Gaussian centered at 3.04 eV with 180 meV FWHM.
    - The spatial density is estimated to be between 2×10^8 and 6×10^9 cm^{-2}, two to three orders of magnitude lower than first population of quantum well localization centers.
    - The spectral density is $\sim 1 \times 10^9$ cm^{-2}·eV^{-1} at 3.1 eV.
    - Speculative hypotheses about the physical origins of the emission are:
        * Emission emerges from small, indium rich clusters on semipolar surfaces.
        * The centers inherit symmetry from the wurtzite lattice.
    - Linewidths approaching the resolution limits of the measurement equipment have been recorded.
    - Their emission may be useful for single photon emitters pending furture anti-bunching measurements.

B Volume Current Method

The change in the imaginary frequency (and Q_{sr}) due to surface scattering can be calculated using the volume current method [77, 254]. We start with Maxwell's harmonic wave equation for the function describing the photonic crystal cavity's relative permittivity, $\varepsilon(\mathbf{r}')$

$$\nabla \times \left(\nabla \times \mathbf{E}(\mathbf{r}') \right) = \frac{\omega^2}{c^2} \varepsilon(\mathbf{r}') \, \mathbf{E}(\mathbf{r}'). \tag{B.1}$$

Now, we add a small perturbation to the dielectric function due to surface roughness or waviness, $\varepsilon(\mathbf{r}') = \varepsilon^{(0)}(\mathbf{r}') + \varepsilon^{(1)}(\mathbf{r}')$. A perturbative solution to Eq. B.1 is

$$\mathbf{E}(\mathbf{r}') = \mathbf{E}^{(0)}(\mathbf{r}') + \mathbf{E}^{(1)}(\mathbf{r}'), \tag{B.2}$$

where $\mathbf{E}^{(0)}(\mathbf{r}')$ is the solution to Eq. B.1 in the absence of $\varepsilon^{(1)}(\mathbf{r}')$. In this work, $\mathbf{E}^{(0)}(\mathbf{r}')$ is computed by the FDTD method.

Substituting Eq. B.2 into Eq. B.1 and retaining first-order terms results in,

$$\nabla \times \left(\nabla \times \mathbf{E}^{(1)}(\mathbf{r}') \right) = \frac{\omega^2}{c^2} \varepsilon^{(0)}(\mathbf{r}') \, \mathbf{E}^{(1)}(\mathbf{r}') + \frac{\omega^2}{c^2} \varepsilon_r^{(1)}(\mathbf{r}') \, \mathbf{E}^{(0)}(\mathbf{r}'). \tag{B.3}$$

Eq. B.3 resembles a standard Maxwell's equation in the perturbed field, with the last term corresponding to a polarization current source, $\mathbf{J}(\mathbf{r}') = -i\omega\varepsilon_0 \varepsilon^{(1)}(\mathbf{r}')\mathbf{E}^{(0)}(\mathbf{r}')$.

In analogy to Eqs. 4.15 and 4.21, the expression for the polarization current must be corrected when shifting high refractive index contrast boundaries. The parallel component of the electric field and the perpendicular component of the displacement field are used [255],

$$\mathbf{J}^{(1)}(\mathbf{r}') = -i\omega\Delta z \sum_{i=1}^{M} \left\{ \varepsilon_0 \varepsilon^{(1)}(\mathbf{r}', z_i) \, \mathbf{E}_{\parallel}^{(0)}(\mathbf{r}', z_i) - [\varepsilon^{(1)}(\mathbf{r}', z_i)]^{-1} \mathbf{D}_{\perp}^{(0)}(\mathbf{r}', z_i) \right\} \tag{B.4}$$

where the perturbation is assumed to be broken into M slices parallel to the xy plane, each with height Δz.

For a suitable harmonic perturbation, such as the sidewall grating outcoupler (Section 4.4), the zeroth- and first-order far-fields may interfere coherently [77]. Therefore, the zeroth-order far fields must be included. The far fields can be computed from the FDTD-calculated electromagnetic near fields ($\mathbf{E}^{(0)}$, $\mathbf{H}^{(0)}$) in the perturbation plane by defining effective surface electric ($\mathbf{J}_s$) and magnetic ($\mathbf{M}_s$) currents [174].

$$\mathbf{J}_s^{(0)}(\mathbf{r}') = \hat{n} \times \mathbf{H}(\mathbf{r}') \quad = \quad -H_y(\mathbf{r}')\hat{x} + H_x(\mathbf{r}')\hat{y}, \tag{B.5}$$

$$\mathbf{M}_s^{(0)}(\mathbf{r}') = -\hat{n} \times \mathbf{E}(\mathbf{r}') \quad = \quad E_y(\mathbf{r}')\hat{x} - E_x(\mathbf{r}')\hat{y}. \tag{B.6}$$

The overall electric current is then $\mathbf{J}_s(\mathbf{r}') = \mathbf{J}_s^{(0)}(\mathbf{r}') + \mathbf{J}_s^{(1)}(\mathbf{r}')$ and the overall magnetic current is Eq. B.6.

The far-field projected on a sphere of radius $|\mathbf{r}| \gg \lambda$ can be found using a Green's function formalism for the retarded vector potentials $\mathbf{A}(\mathbf{r})$ and $\mathbf{F}(\mathbf{r})$ [174],

$$\mathbf{A}(\mathbf{r}) \quad \approx \quad \frac{\mu_0}{4\pi} \frac{e^{-ik_0|\mathbf{r}|}}{|\mathbf{r}|} \int_V \mathbf{J}_s(\mathbf{r}') e^{ik_0(\hat{\mathbf{r}} \cdot \mathbf{r}')} d^2\mathbf{r}', \tag{B.7}$$

$$\mathbf{F}(\mathbf{r}) \quad \approx \quad \frac{\varepsilon_0}{4\pi} \frac{e^{-ik_0|\mathbf{r}|}}{|\mathbf{r}|} \int_V \mathbf{M}_s(\mathbf{r}') e^{ik_0(\hat{\mathbf{r}} \cdot \mathbf{r}')} d^2\mathbf{r}'. \tag{B.8}$$

Because

$$k_0 \hat{\mathbf{r}} \cdot \mathbf{r}' = \frac{k_0}{|r|}(xx' + yy'),$$

the integrals in Eqs. B.7-B.8 can be viewed as the 2D Fourier transforms of the i'th slice of the surface electric current

$$\tilde{\mathbf{N}}(\theta, \phi) := \mathrm{FT}_2\big[\mathbf{J}_s^{(0)}(\mathbf{r})\big] + \sum_{i=1}^{M} \mathrm{FT}_2\big[\mathbf{J}_{s,i}^{(1)}(\mathbf{r}, z_i')\big], \tag{B.9}$$

and surface magnetic current,

$$\tilde{\mathbf{L}}(\theta, \phi) := \mathrm{FT}_2\big[\mathbf{M}_s^{(0)}(\mathbf{r})\big], \tag{B.10}$$

where $k_x = k_0 x/|\mathbf{r}| = k_0 \sin\theta \cos\phi$ and $k_y = k_0 y/|\mathbf{r}| = k_0 \sin\theta \sin\phi$. Then, the retarded vector potentials are simply [174]

$$\mathbf{A}(\mathbf{r}) \quad \approx \quad \frac{\mu_0}{4\pi} \frac{e^{-ik_0|\mathbf{r}|}}{|\mathbf{r}|} \tilde{\mathbf{N}}(\theta, \phi) \tag{B.11}$$

$$\mathbf{F}(\mathbf{r}) \quad \approx \quad \frac{\varepsilon_0}{4\pi} \frac{e^{-ik_0|\mathbf{r}|}}{|\mathbf{r}|} \tilde{\mathbf{L}}(\theta, \phi). \tag{B.12}$$

After such a derivation, a physical interpretation is instructive. Eqs. B.9-B.12 indicate that scattering losses arise from the components of the Fourier transform lying within the light cone of the product of the initial electric field, $\mathbf{E}^{(0)}(\mathbf{r})$, and the dielectric perturbation, $\varepsilon^{(1)}(\mathbf{r})$. Using the convolution theorem, the physical interpretation could be restated; scattering losses originate from the Fourier components lying within the light cone of the convolution of the Fourier transform of the initial electric field, $\tilde{\mathbf{E}}^{(0)}(\mathbf{k})$, c.f. (Fig. 4.13) with the Fourier transform of the spatial perturbation, $\tilde{\varepsilon}^{(1)}(\mathbf{k})$. This confirms the physical insight into the working principle underlying the grating outcoupler: the photonic crystal cavity mode's electric field profile is peaked at $k_x = \pm\pi/a$. Convolving this with a sinusoidal perturbation with twice the spatial period (peaked at $k_x = \pm\pi/2a$) shifts a "copy" of the photonic crystal cavity peak to $\mathbf{k=0}$, where it can propagate to the far field at normal incidence.

Only the transverse fields radiate power through the half-sphere at position $\mathbf{r}$. However, the vector fields $\tilde{\mathbf{N}}^i$ and $\tilde{\mathbf{L}}^i$ are still in Cartesian coordinates. Their projection into spherical coordinates is

$$\tilde{N}_\theta \quad = \quad (\tilde{N}_x \cos\phi + \tilde{N}_y \sin\phi)\cos\theta - \tilde{N}_z \sin\theta, \tag{B.13}$$
$$\tilde{N}_\phi \quad = \quad -\tilde{N}_x \sin\phi + \tilde{N}_y \cos\phi. \tag{B.14}$$

The power P radiated through a half-sphere enclosing the nanobeam photonic crystal can now be calculated [174],

$$P_{\mathrm{sr}} = \frac{Z_0}{\lambda^2} \int_0^{\pi/2} \int_0^{2\pi} \sin\theta \left(\left| \tilde{N}_\theta + \frac{1}{\eta}\tilde{L}_\phi \right|^2 + \left| \tilde{N}_\phi - \frac{1}{\eta}\tilde{L}_\theta \right|^2 \right) d\phi\, d\theta, \tag{B.15}$$

where Z_0 is the impedance of free space, about 377 Ω. Through inspection of Eqs. B.11-B.12 and Eq. B.15, the scattering losses are expected to scale with the surface roughness/waviness amplitude as Δz for coherent scattering and as $(\Delta z)^2$ for incoherent scattering. In analogy to the simple harmonic oscillator, Q_{sr} can be defined by the amount of energy stored in the resonator U (Eq. 4.21, denominator) times the frequency divided by the energy loss rate,

$$Q_{\mathrm{sr}} = \frac{2\pi c}{\lambda} \frac{U}{P_{\mathrm{sr}}}.$$

Combined with the λ^{-2} scaling of P_{sr}, Q_{sr} is therefore expected to scale as λ^3. Therefore, Q_{sr} is expected to be nearly 40× smaller at $\lambda = 450$ nm compared to telecommunication wavelengths ($\lambda = 1.55$ μm), ceteris paribus.

Due to the normalization of the fields in the FDTD simulation, P_{sr} must be rescaled to yield Q_{sr}. The following normalization,

$$Q_{sr} = \frac{Q_{th}}{g_S} \frac{P_{sr}^{(0)}}{P_{sr}^{(1)}},$$

(B.16)

reproduces the scattering losses calculated by the FDTD method for the sidewall grating outcoupler (Fig. B.1). Here, Q_{th} is the FDTD-calculated Q factor with a smooth surface, g_S
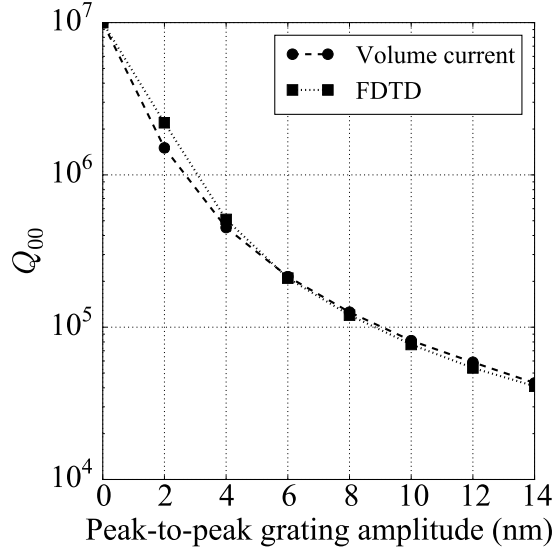
Figure B.1: Comparison of scattering losses for first-principles calculations by FDTD calculations and the volume current method ($\Delta z = 1$ nm) as a function of sidewall grating outcoupler peak-to-peak amplitude.

is the fraction of power lost through the considered surface in the FDTD simulation (around 0.27 for the top surface and fundamental mode), $P_{sr}^{(0)}$ is the (zeroth-order) value of Eq. B.15 computed for the smooth surface, and $P_{sr}^{(1)}$ is the full loss for the rough/wavy surface when adding the first- and zeroth-order fields coherently.

In summary, the relevant physical consequences of scattering by surface perturbations in photonic crystal cavities are:

- $Q_{sr} \propto \lambda^3$, a similar power dependence as for Rayleigh scattering.

- For harmonic surface roughness or waviness, coherent scattering results in Q_{sr} inversely proportional to the surface roughness amplitude.

- For random surface roughness or waviness, incoherent scattering results in Q_{sr} inversely proportional to the surface roughness amplitude squared.

- The far-field profile of a photonic crystal cavity mode is related to the near-field by a two-dimensional Fourier transform.

- Far-field scattering losses originate from the convolution of the 2D Fourier transform of the cavity mode's electric field profile with the 2D Fourier transform of the surface roughness/waviness perturbation.

    - Only spatial frequencies of the convolution falling within the light cone generate scattering losses.

    - For the nanobeam photonic crystal cavity, the surface perturbation must contain sizable components on the spatial frequency interval $[\pi/a - 2\pi/\lambda \leq |k_x| \leq \pi/a + 2\pi/\lambda]$.

C Physical Parameters

This section lists all abbreviations and variables used in this thesis.

Abbreviation	Full descrption
LED	Light-emitting diode
VCSEL	Vertical cavity surface-emitting laser
SPS	Single photon source
OPSL	Optically pumped semiconductor laser
QIP	Quantum information processing
Γ	$\mathbf{k=0}$ point in band structure
$\varnothing$	Diameter
t	Time
μPL	Micro-photoluminescence spectroscopy
μRaman	Micro-Raman spectroscopy
BHF	Buffered hydrofluoric acid
TMAH	Tetramethylammonium hydroxide
HSQ	Hydrogen silsesquioxane
ALD	Atomic layer deposition
(ICP)-RIE	(Inductively coupled plasma) reactive ion etching
AFM	Atomic force microscopy
RMS	Root mean square
SEM	Scanning electron microscopy
TRPL	Time-resolved photoluminescence
FWHM	Full-width at half-maximum
FDTD	Finite-difference time-domain
FEM	Finite element method
$A_1(LO)$	Longitudinal optical phonon mode
E_2^H	Transverse optical phonon mode

Abbreviations used in this work.

Abbreviation	Full descrption
TE	Transverse electric polarization
TM	Transverse magnetic polarization
$\lambda_{00/01}$	Fundamental/first-order photonic crystal cavity mode wavelength
$Q_{00/01}$	Fundamental/first-order photonic crystal cavity mode Q
PSD	Power spectral density
uid	Unintentionally n-doped
n^+	Heavily n-doped
IQE	Internal quantum efficiency
DOLP	Degree of linear polarization

Table C.1: Abbreviations used in this work, continued.

Symbol	Description	Units
λ_d	De Broglie wavelength of a massive particle	m
T	Temperature	K
R_m	Spontaneous emission rate into the mth electromagnetic mode	s^{-1}
n_1	Real part of refractive index	unitless
n_2	Imaginary part of refractive index	unitless
Ψ	Complete single-particle wavefunction	$cm^{-3/2}$
$\mathbf{E}(\mathbf{r},\omega)$	Time-varying electric field, frequency domain	$V \cdot cm^{-1}$
$\tilde{\mathbf{E}}(\mathbf{k},\omega)$	Time-varying electric field, Fourier & frequency domain	$V \cdot cm^{-1}$
$\mathbf{r}$	Position vector	m
ρ_γ	Photonic density of states	$J^{-1} \cdot m^{-3}$
V_0	Electromagnetic mode volume	m^{-3}
Q	Quality factor of resonator	unitless
ω	Angular frequency	$rad \cdot s^{-1}$
β	Spontaneous emission coupling factor	unitless
f_{osc}	Oscillator strength	unitless
F_P	Purcell spontaneous emission enhancement factor	unitless
λ	Electromagnetic field wavelength	nm
u	Internal wurtzite crystal lattice parameter	unitless
a	In-plane wurtzite crystal lattice constant	Å
c	Out-of-plane wurtzite crystal lattice constant	Å
$1/a\frac{\partial a}{\partial T}$	Thermal expansion coefficient	K^{-1}
Δ_{cf}	Valence band crystal field splitting	meV
Δ_{so}	Valence band spin-orbit splitting	meV
E_g	Electronic band gap	eV
α_V	Varshni model parameter	$J \cdot K^{-1}$
β_V	Varshni model parameter	K
ε_r	Relative dielectric permittivity	unitless

Table A.3: Variables and functions used in this work, in order of appearance.

Symbol	Description	Units
α	Optical absorption coefficient	m^{-1}
D	Propagation distance	cm
BW	Bandwidth	s^{-1}
k	Wavevector	m^{-1}
GVD	Group velocity dispersion	$s^2 \cdot m^{-1}$
κ	Thermal conductivity	$W \cdot cm^{-1} \cdot K^{-1}$
C_{ij}	Elastic stiffness coefficient	$N \cdot m^{-2}$
e_{ij}	Piezoelectric coefficient	$C \cdot m^{-2}$
P_{sp}	Spontaneous polarization	$C \cdot m^{-2}$
F_i	Static electric field	$V \cdot m^{-1}$
σ_{ij}	Stress	$N \cdot m^{-2}$
ϵ_{ij}	Strain	unitless
C_0	Reduced elasticity constant for uniaxial strain	unitless
ΔE_c	Conduction band offset	eV
l	Quantum integer	unitless
$\psi_l^e(x,y,z)$	Quantum well electron total wavefunction	$cm^{-1/2}$
$\phi_l^e(x,y,z)$	Quantum well electron envelope	$cm^{-1/2}$
$E_l^e(k_x,k_y)$	Quantum well electron eigenenergy	$cm^{-1/2}$
$\mathbf{D}(\mathbf{r},\omega)$	Time-varying electric displacement field, frequency domain	$C \cdot cm^{-2}$
$\tilde{\mathbf{D}}(\mathbf{k},\omega)$	Time-varying electric displacement field, Fourier & frequency domain	$C \cdot cm^{-2}$
$\mathbf{B}(\mathbf{r},\omega)$	Time-varying magnetic field, frequency domain	T
$\mathbf{H}(\mathbf{r},\omega)$	Time-varying magnetizing field, frequency domain	$A \cdot cm^{-2}$
l_{crit}	Critical dimension of nanostructure	nm
l_{min}	Minimum feature size	nm
NA	Numerical aperture	unitless
$F/\#$	Focal length divided by aperture	unitless
p	Linear momentum	$kg \cdot m \cdot s^{-1}$
KE	Kinetic energy	J
a_λ	Phonon deformation potential 1	cm^{-1}
b_λ	Phonon deformation potential 2	cm^{-1}
c_λ	Phonon deformation potential 3	cm^{-1}
w_R	Gaussian beam waist	nm
z_R	Gaussian beam Rayleigh range	μm
ν_l	Laser linewidth	Hz
τ_0	Temporal resolution	s
f_g	Optical confinement factor	unitless
$g(\lambda)$	Optical gain	cm^{-1}
γ_p	Optical cavity loss rate	s^{-1}
θ_{crit}	Critical angle	radians

Table A.3: Variables and functions used in this work in order of appearance, continued.

Appendix C. Physical Parameters

Symbol	Description	Units
$n_{1,\text{cl}}$	Waveguide cladding refractive index	unitless
$n_{1,\text{co}}$	Waveguide core refractive index	unitless
κ_z	Waveguide mode attenuation constant	cm^{-1}
a_b	Photonic crystal Bragg mirror period	nm
d	Photonic crystal Bragg mirror hole diameter	nm
a_c	Photonic crystal central cavity hole spacing	nm
d_c	Photonic crystal central cavity hole diameter	nm
w	Nanobeam photonic crystal width	nm
Q_{exp}	Experimental Q	unitless
Q_{th}	Theoretical Q	unitless
Q_{abs}	Total absorption loss Q contribution	unitless
Q_{bk}	Bulk absorption loss Q contribution	unitless
Q_{qw}	Quantum well absorption loss Q contribution	unitless
Q_{sa}	Surface state absorption loss Q contribution	unitless
Q_{sr}	Surface roughness/waviness scattering loss Q contribution	unitless
Q_{fab}	Fabrication error induced scattering loss Q contribution	unitless
Tr	Fresnel transmission coefficient	unitless
$\tilde{v}$	Raman mode wavenumber	cm^{-1}
δ_z	Nanobeam vertical mechanical deformation	nm
δ_y	Nanobeam horizontal mechanical deformation	nm
Ω	Simulation volume	cm^3
L_R	Correlation length of surface roughness	nm
$\hat{\lambda}$	Observed estimate of photonic crystal cavity mode wavelength	nm
$\hat{Q}$	Observed estimate of photonic crystal cavity mode Q	unitless
I	Laser power density	W/cm^2
R_{ph}	Optical excitation rate	$\text{cm}^{-2}{\cdot}\text{s}^{-1}$
$\gamma_{\text{exp}}^{-1}(T)$	Experimental photogenerated excitation lifetime	ns
n_{ph}	Photogenerated exciton (charge carrier) density	cm^{-2} (cm^{-3})
$f_{H/V}$	Electromagnetic field overlap integral	unitless
$\gamma(x, y)$	Autocorrelation function of surface roughness	-
$S(k_x, k_y)$	Power spectral density function of surface roughness	-
$\theta(x)$	Heaviside step function	-
$H(x, y)$	Matrix of height values in nanotopography	nm
$I(x, y)$	Matrix of intensity values in image	8-bit binary
I_{th}	Image intensity threshold	8-bit binary

Table A.3: Variables and functions used in this work in order of appearance, continued.

Symbol	Description	Units
$\hat{\sigma}_+$	Observed standard deviation of fundamental and first-order photonic crystal mode average wavelengths	nm
$\hat{\sigma}_-$	Observed standard deviation of fundamental and first-order photonic crystal mode splitting	nm
R	Microdisk radius	μm
ϕ_b	Schottky barrier height	eV
N_d	Extrinsic doping density	cm^{-3}
L_{sc}	Space charge region width	nm
L_{em}	Electromagnetic mode characteristic length scale	nm
$L_{d,h}$	Minority carrier diffusion length of holes	nm
n_{fr}	Free exciton density in quantum well	cm^{-2}
n_{l}	Localized exciton density in quantum well	cm^{-2}
N_l	Density of localization centers in quantum well	cm^{-2}
ρ_l	Spectral density of states in quantum well	cm$^{-2}\cdot$eV^{-1}
γ_{fr} (γ_{l})	Free (localized) exciton total decay rate	s^{-1}
$\gamma_{\text{fr,nr}}$ ($\gamma_{\text{l,nr}}$)	Free (localized) exciton nonradiative decay rate	s^{-1}
$\gamma_{\text{fr,r}}$ ($\gamma_{\text{l,r}}$)	Free (localized) exciton radiative decay rate	s^{-1}
$E_{\text{fr,nr}}$ ($E_{\text{l,nr}}$)	Free (localized) exciton nonradiative decay activation energy	meV
E_{loc}	Localization energy between free and localized excitons	meV
σ_l	Standard deviation of Gaussian distribution of localized states	meV
γ_{th}	Localized state attempt-to-escape rate	s^{-1}
E_{a_1}	Experimental activation energy of nonradiative recombination	meV
E_{a_2}	Experimental activation energy of nonradiative recombination	meV
α_l	Acoustic phonon broadening rate of localized exciton	meV$\cdot$K^{-1}
β_l	Dephasing of localized exciton due to thermal escape	meV
$E_{\text{th,l}}$	Localization energy of a single localization center	meV
$\mathbf{J(r)}$	Effective surface "magnetic current"	A$\cdot$m^{-2}
$\mathbf{M(r)}$	Effective surface "electric current"	C$\cdot$m^{-2}
$\mathbf{A(r)}$	Near-to-far field retarded magnetic vector potential	T
$\mathbf{F(r)}$	Near-to-far field retarded electric vector potential	C$\cdot$m^{-2}
$\tilde{\mathbf{N}}(\theta,\phi)$	2D Fourier transform of surface magnetic current	A
$\tilde{\mathbf{L}}(\theta,\phi)$	2D Fourier transform of surface electric current	C
P_{sr}	Scattered power by surface roughness/waviness	W
g_{S}	Fraction of scattered power lost through top surface	unitless

Table C.2: Variables and functions used in this work. The units given are those typically used for discussion. However, formulas in this thesis are generally in SI units, so any evaluation of the above quantities in a formula is accompanied by the appropriate conversion to SI units.

Bibliography

[1] S. Nakamura. Nobel Lecture: Background story of the invention of efficient blue InGaN light emitting diodes. *Rev. Mod. Phys.*, 87(4):1139–1151, oct 2015.

[2] BP Statistical Review of World Energy 2017. Technical Report 66, British Petroleum P.L.C., 2017.

[3] G. Crosnier, D. Sanchez, S. Bouchoule, P. Monnier, G. Beaudoin, I. Sagnes, R. Raj, and F. Raineri. Hybrid indium phosphide-on-silicon nanolaser diode. *Nature Photon.*, 11(5):297–300, 2017.

[4] N. Gisin and R. Thew. Quantum communication. *Nature Photon.*, 1(3):165–171, 2007.

[5] R. S. Bennink, S. J. Bentley, R. W. Boyd, and J. C. Howell. Quantum and classical coincidence imaging. *Phys. Rev. Lett.*, 92(3):033601, 2004.

[6] D. Gatto Monticone, K. Katamadze, P. Traina, E. Moreva, J. Forneris, I. Ruo-Berchera, P. Olivero, I. P. Degiovanni, G. Brida, and M. Genovese. Beating the Abbe diffraction limit in confocal microscopy via nonclassical photon statistics. *Phys. Rev. Lett.*, 113(14):143602, 2014.

[7] B. Hensen, H. Bernien, A. E. Dréau, A. Reiserer, N. Kalb, M. S. Blok, J. Ruitenberg, R. F. L. Vermeulen, R. N. Schouten, C. Abellán, W. Amaya, V. Pruneri, M. W. Mitchell, M. Markham, D. J. Twitchen, D. Elkouss, S. Wehner, T. H. Taminiau, and R. Hanson. Loophole-free Bell inequality violation using electron spins separated by 1.3 kilometres. *Nature*, 526(7575):682–686, 2015.

[8] M. J. Holmes, K. Choi, S. Kako, M. Arita, and Y. Arakawa. Room-temperature triggered single photon emission from a III-nitride site-controlled nanowire quantum dot. *Nano Lett.*, 14(2):982–986, 2014.

[9] M. Mexis, S. Sergent, T. Guillet, C. Brimont, T. Bretagnon, B. Gil, F. Semond, M. Leroux, D. Néel, S. David, X. Chécoury, and P. Boucaud. High quality factor nitride-based optical cavities: microdisks with embedded GaN/Al(Ga)N quantum dots. *Opt. Lett.*, 36(12):2203, 2011.

Bibliography

[10] S. Sergent, M. Arita, S. Kako, K. Tanabe, S. Iwamoto, and Y. Arakawa. High-Q AlN photonic crystal nanobeam cavities fabricated by layer transfer. *Appl. Phys. Lett.*, 101(10):101106, 2012.

[11] D. Néel, I. Roland, X. Checoury, M. El Kurdi, S. Sauvage, C. Brimont, T. Guillet, B. Gayral, F. Semond, and P. Boucaud. Aluminum nitride photonic crystals and microdiscs for ultra-violet nanophotonics. *Adv. Nat. Sci.: Nanosci. Nanotechnol.*, 5(2):023001, 2014.

[12] N. Niu, A. Woolf, D. Wang, T. Zhu, Q. Quan, R. A. Oliver, and E. L. Hu. Ultra-low threshold gallium nitride photonic crystal nanobeam laser. *Appl. Phys. Lett.*, 106(23):231104, 2015.

[13] N. Vico Triviño, R. Butté, J.-F. Carlin, and N. Grandjean. Continuous wave blue lasing in III-nitride nanobeam cavity on silicon. *Nano Lett.*, 15(2):1259–1263, 2015.

[14] I. Rousseau, I. Sánchez-Arribas, K. Shojiki, J.-F. Carlin, R. Butté, and N. Grandjean. Quantification of scattering loss of III-nitride photonic crystal cavities in the blue spectral range. *Phys. Rev. B*, 95(12):125313, 2017.

[15] F. Tabataba-Vakili, I. Roland, T.-H. Tran, X. Checoury, M. El Kurdi, S. Sauvage, C. Brimont, T. Guillet, S. Rennesson, J.-Y. Duboz, F. Semond, B. Gayral, and P. Boucaud. Q factor limitation at short wavelength (around 300 nm) in III-nitride-on-silicon photonic crystal cavities. *Appl. Phys. Lett.*, 111(13):131103, 2017.

[16] Y. Lai, S. Pirotta, G. Urbinati, D. Gerace, M. Minkov, V. Savona, A. Badolato, and M. Galli. Genetically designed L3 photonic crystal nanocavities with measured quality factor exceeding one million. *Appl. Phys. Lett.*, 104(24):241101, 2014.

[17] B. Guha, F. Marsault, F. Cadiz, L. Morgenroth, V. Ulin, V. Berkovitz, A. Lemaître, C. Gomez, A. Amo, S. Combrié, B. Gérard, G. Leo, and I. Favero. Surface-enhanced gallium arsenide photonic resonator with quality factor of 6×10^6. *Optica*, 4(2):218–221, 2017.

[18] E. Rosencher, B. Vinter, and P. G. Piva. *Optoelectronics*. Cambridge University Press, Cambridge, UK, 2002.

[19] J. D. Joannopoulos, S. G. Johnson, J. N. Winn, and R. D. Meade. *Photonic Crystals: Modeling the Flow of Light*. Princeton University Press, Princeton, NJ, 2nd ed. edition, 2008.

[20] P. Y. Yu and M. Cardona. *Fundamentals of Semiconductors*. Graduate Texts in Physics. Springer, Berlin, DE, 4th edition, 2010.

[21] M. Fox. *Quantum Optics*. Oxford University Press, Oxford, UK, 1st edition, 2006.

[22] E. M. Purcell. Spontaneous emission probabilities at radio frequencies. *Phys. Rev.*, 69:681, 1946.

[23] E. Yablonovitch. Inhibited spontaneous emission in solid-state physics and electronics. *Phys. Rev. Lett.*, 58(20):2059–2062, 1987.

[24] S. John. Strong localization of photons in certain disordered dielectric superlattices. *Phys. Rev. Lett.*, 58(23):2486–2489, 1987.

[25] Nanosys Inc. website, 2018.

[26] QD Vision Company Overview, 2018.

[27] S. T. Jagsch, N. Vico Triviño, F. Lohof, G. Callsen, S. Kalinowski, I. M. Rousseau, R. Barzel, J.-F. Carlin, F. Jahnke, R. Butté, C. Gies, A. Hoffmann, N. Grandjean, and S. Reitzenstein. A quantum optical study of thresholdless lasing features in high-β nitride nanobeam cavities. *Nature Commun.*, 9(1):564, 2018.

[28] P. Rice and H. Carmichael. Photon statistics of a cavity-QED laser: a comment on the laser-phase transition analogy. *Phys. Rev. A*, 50(5):4318–4329, 1994.

[29] D. Elvira, X. Hachair, V. B. Verma, R. Braive, G. Beaudoin, I. Robert-Philip, I. Sagnes, B. Baek, S. W. Nam, E. A. Dauler, I. Abram, M. J. Stevens, and A. Beveratos. Higher-order photon correlations in pulsed photonic crystal nanolasers. *Phys. Rev. A*, 84(6):061802, 2011.

[30] Y. Yamamoto, S. Machida, and G. Björk. Microcavity semiconductor laser with enhanced spontaneous emission. *Phys. Rev. A*, 44(1):657–668, 1991.

[31] G. Björk and Y. Yamamoto. Analysis of semiconductor microcavity lasers using rate equations. *IEEE J. Quantum Electron.*, 27(11):2386–2396, 1991.

[32] L. A. Coldren, S. W. Corzine, and M. L. Mashanovich. *Diode Lasers and Photonic Integrated Circuits.* Wiley Interscience, Hoboken, NJ, 2nd edition, 2012.

[33] S. M. Ulrich, C. Gies, S. Ates, J. Wiersig, S. Reitzenstein, C. Hofmann, A. Löffler, A. Forchel, F. Jahnke, and P. Michler. Photon statistics of semiconductor microcavity lasers. *Phys. Rev. Lett.*, 98(4):043906, 2007.

[34] H. Altug, D. Englund, and J. Vučković. Ultrafast photonic crystal nanocavity laser. *Nature Phys.*, 2(7):484–488, 2006.

[35] R. P. Feynman. Simulating physics with computers. *Int. J. Theor. Phys.*, 21(6-7):467–488, 1982.

[36] S. Haroche. *Exploring the Quantum: Atoms, Cavities, and Photons.* Oxford University Press, Oxford, UK, 1st edition, 2013.

[37] A. Wallraff, D. I. Schuster, A. Blais, L. Frunzio, R.-S. Huang, J. Majer, S. Kumar, S. M. Girvin, and R. J. Schoelkopf. Strong coupling of a single photon to a superconducting qubit using circuit quantum electrodynamics. *Nature*, 431(7005):162–167, 2004.

[38] F. Yan, S. Gustavsson, A. Kamal, J. Birenbaum, A. P. Sears, D. Hover, T. J. Gudmundsen, D. Rosenberg, G. Samach, S. Weber, J. L. Yoder, T. P. Orlando, J. Clarke, A. J. Kerman, and W. D. Oliver. The flux qubit revisited to enhance coherence and reproducibility. *Nature Commun.*, 7:12964, 2016.

[39] A. Blais, R.-S. Huang, A. Wallraff, S. M. Girvin, and R. J. Schoelkopf. Cavity quantum electrodynamics for superconducting electrical circuits: an architecture for quantum computation. *Phys. Rev. A*, 69(6):062320, 2004.

[40] P. Lodahl, S. Mahmoodian, and S. Stobbe. Interfacing single photons and single quantum dots with photonic nanostructures. *Rev. Mod. Phys.*, 87(2):347–400, 2015.

[41] L. M. Duan and H. J. Kimble. Scalable photonic quantum computation through cavity-assisted interactions. *Phys. Rev. Lett.*, 92(12):127902, 2004.

[42] I. Fushman, D. Englund, A. Faraon, N. Stoltz, P. Petroff, and J. Vučković. Controlled phase shifts with a single quantum dot. *Science*, 320(5877):769–772, 2008.

[43] G. Khitrova, H. M. Gibbs, M. Kira, S. W. Koch, and A. Scherer. Vacuum Rabi splitting in semiconductors. *Nature Phys.*, 2(2):81–90, 2006.

[44] A. Reinhard, T. Volz, M. Winger, A. Badolato, K. J. Hennessy, E. L. Hu, and A. Imamoglu. Strongly correlated photons on a chip. *Nature Photon.*, 6(2):93–96, 2012.

[45] T. Bretagnon, P. Lefebvre, P. Valvin, R. Bardoux, T. Guillet, T. Taliercio, B. Gil, N. Grandjean, F. Semond, B. Damilano, A. Dussaigne, and J. Massies. Radiative lifetime of a single electron-hole pair in GaN AlN quantum dots. *Phys. Rev. B*, 73(11):113304, 2006.

[46] D. Englund, D. Fattal, E. Waks, G. Solomon, B. Zhang, T. Nakaoka, Y. Arakawa, Y. Yamamoto, and J. Vučković. Controlling the spontaneous emission rate of single quantum dots in a two-dimensional photonic crystal. *Phys. Rev. Lett.*, 95(1):013904, 2005.

[47] J. Claudon, J. Bleuse, N. S. Malik, M. Bazin, P. Jaffrennou, N. Gregersen, C. Sauvan, Ph. Lalanne, and J.-M. Gérard. A highly efficient single-photon source based on a quantum dot in a photonic nanowire. *Nature Photon.*, 4(3):174–177, 2010.

[48] J.-M. Gérard, B. Sermage, B. Gayral, B. Legrand, E. Costard, and V. Thierry-Mieg. Enhanced spontaneous emission by quantum boxes in a monolithic optical microcavity. *Phys. Rev. Lett.*, 81(5):1110–1113, 1998.

[49] J.-M. Gérard and B. Gayral. Strong Purcell effect for InAs quantum boxes in three-dimensional solid-state microcavities. *J. Light. Technol.*, 17(11):2089–2095, 1999.

[50] N. Somaschi, V. Giesz, L. De Santis, J. C. Loredo, M. P. Almeida, G. Hornecker, S. L. Portalupi, T. Grange, C. Antón, J. Demory, C. Gómez, I. Sagnes, N. D. Lanzillotti-Kimura, A. Lemaître, A. Auffeves, A. G. White, L. Lanco, and P. Senellart. Near-optimal single-photon sources in the solid state. *Nature Photon.*, 10(5):340–345, 2016.

[51] Jonathan P. Goss, R. J. Eyre, and P. R. Briddon. Theoretical models for doping diamond for semiconductor applications. *Phys. Status Solidi B*, 245(9):1679–1700, 2008.

[52] X. Brokmann, E. Giacobino, M. Dahan, and J.-P. Hermier. Highly efficient triggered emission of single photons by colloidal CdSeZnS nanocrystals. *Appl. Phys. Lett.*, 85(5):712–714, 2004.

[53] Q. Zhang, C. Dang, H. Urabe, J. Wang, S. Sun, and A. Nurmikko. Large ordered arrays of single photon sources based on II–VI semiconductor colloidal quantum dot. *Opt. Express*, 16(24):19592, 2008.

[54] M. D. Eisaman, J. Fan, A. Migdall, and S. V. Polyakov. Single-photon sources and detectors. *Rev. Sci. Instrum.*, 82(7):071101, 2011.

[55] S. Masui, T. Miyoshi, T. Yanamoto, and S. Nagahama. Blue and green laser diodes for large laser display. In *2013 Conference on Lasers and Electro-Optics Pacific Rim (CLEO-PR)*, pages SA1–3. Opt. Soc. Am., 2013.

[56] E. Peter, P. Senellart, D. Martrou, A. Lemaître, J. Hours, J.-M. Gérard, and J. Bloch. Exciton-photon strong-coupling regime for a single quantum dot embedded in a microcavity. *Phys. Rev. Lett.*, 95(6):067401, 2005.

[57] K. Srinivasan and O. Painter. Linear and nonlinear optical spectroscopy of a strongly coupled microdisk–quantum dot system. *Nature*, 450(7171):862–865, 2007.

[58] J. P. Reithmaier, G. Sęk, A. Löffler, C. Hofmann, S. Kuhn, S. Reitzenstein, L. V. Keldysh, V. D. Kulakovskii, T. L. Reinecke, and A. Forchel. Strong coupling in a single quantum dot-semiconductor microcavity system. *Nature*, 432(7014):197–200, 2004.

[59] R. Ohta, Y. Ota, M. Nomura, N. Kumagai, S. Ishida, S. Iwamoto, and Y. Arakawa. Strong coupling between a photonic crystal nanobeam cavity and a single quantum dot. *Appl. Phys. Lett.*, 98(17):2009–2012, 2011.

[60] T. Yoshie, A. Scherer, J. Hendrickson, G. Khitrova, H. M. Gibbs, G. Rupper, C. Ell, O. B. Shchekin, and D. G. Deppe. Vacuum Rabi splitting with a single quantum dot in a photonic crystal nanocavity. *Nature*, 432(7014):200–203, 2004.

[61] M. J. Burek, Y. Chu, M. S. Z. Liddy, P. Patel, J. Rochman, S. Meesala, W. Hong, Q. Quan, M. D. Lukin, and Marko Lončar. High quality-factor optical nanocavities in bulk single-crystal diamond. *Nature Commun.*, 5(617):5718, 2014.

[62] Y. Taguchi, Y. Takahashi, Y. Sato, T. Asano, and S. Noda. Statistical studies of photonic heterostructure nanocavities with an average Q factor of three million. *Opt. Express*, 19(12):11916, 2011.

[63] M. Barth, N. Nüsse, J. Stingl, B. Löchel, and O. Benson. Emission properties of high-Q silicon nitride photonic crystal heterostructure cavities. *Appl. Phys. Lett.*, 93(2):021112, 2008.

[64] M. Eichenfield, R. Camacho, J. Chan, K. J. Vahala, and O. Painter. A picogram- and nanometre-scale photonic-crystal optomechanical cavity. *Nature*, 459(7246):550–555, 2009.

[65] M. Khan, T. Babinec, M. W. McCutcheon, P. Deotare, and M. Lončar. Fabrication and characterization of high-quality-factor silicon nitride nanobeam cavities. *Opt. Lett.*, 36(3):421–423, 2011.

[66] M. S. Mohamed, A. Simbula, J.-F. Carlin, M. Minkov, D. Gerace, V. Savona, N. Grandjean, M. Galli, and R. Houdré. Efficient continuous-wave nonlinear frequency conversion in high-Q gallium nitride photonic crystal cavities on silicon. *APL Photon.*, 2(3):031301, 2017.

[67] W. H. P. Pernice, C. Xiong, C. Schuck, and H. X. Tang. High-Q aluminum nitride photonic crystal nanobeam cavities. *Appl. Phys. Lett.*, 100(9):091105, 2012.

[68] N. Vico Triviño, M. Minkov, G. Urbinati, M. Galli, J.-F. Carlin, R. Butté, V. Savona, N. Grandjean, M. Minkov, G. Urbinati, and M. Galli. Gallium nitride L3 photonic crystal cavities with an average quality factor of 16,900 in the near infrared. *Appl. Phys. Lett.*, 105(23):231119, 2014.

[69] C. Jarlov, A. Lyasota, L. Ferrier, P. Gallo, B. Dwir, A. Rudra, and E. Kapon. Exciton dynamics in a site-controlled quantum dot coupled to a photonic crystal cavity. *Appl. Phys. Lett.*, 107(19):191101, 2015.

[70] A. Majumdar, A. Rundquist, M. Bajcsy, and J. Vučković. Cavity quantum electrodynamics with a single quantum dot coupled to a photonic molecule. *Phys. Rev. B*, 86(4):045315, 2012.

[71] S. Wu, S. Buckley, J. R. Schaibley, L. Feng, J. Yan, D. G. Mandrus, F. Hatami, W. Yao, J. Vučković, A. Majumdar, and X. Xu. Monolayer semiconductor nanocavity lasers with ultralow thresholds. *Nature*, 520(7545):69–72, 2015.

[72] B. J. M. Hausmann, B. J. Shields, Q. Quan, Y. Chu, N. P. de Leon, R. Evans, M. J. Burek, A. S. Zibrov, M. Markham, D. J. Twitchen, H. Park, M. D. Lukin, and M. Lončar. Coupling of NV centers to photonic crystal nanobeams in diamond. *Nano Lett.*, 13(12):5791–5796, 2013.

[73] B. O. Bracher and E. L. Hu. Fabrication of high-Q nanobeam photonic crystals in epitaxially grown 4H-SiC. *Nano Lett.*, 15(9):6202–6207, 2015.

[74] J. Y. Lee, X. Lu, and Q. Lin. High-Q silicon carbide photonic-crystal cavities. *Appl. Phys. Lett.*, 106(4):041106, 2015.

[75] S. Yamada, B.-S. Song, T. Asano, and S. Noda. Silicon carbide-based photonic crystal nanocavities for ultra-broadband operation from infrared to visible wavelengths. *Appl. Phys. Lett.*, 99(20):201102, 2011.

[76] M. Borselli, T. J. Johnson, and O. Painter. Measuring the role of surface chemistry in silicon microphotonics. *Appl. Phys. Lett.*, 88(13):131114, 2006.

[77] D. Parrain, C. Baker, G. Wang, B. Guha, E. G. Santos, A. Lemaître, P. Senellart, G. Leo, S. Ducci, and I. Favero. Origin of optical losses in gallium arsenide disk whispering gallery resonators. *Opt. Express*, 23(15):19656–19672, 2015.

[78] T. Asano, Y. Ochi, Y. Takahashi, K. Kishimoto, and S. Noda. Photonic crystal nanocavity with a *Q* factor exceeding eleven million. *Opt. Express*, 25(3):1769, 2017.

[79] D. Schikora, M. Hankeln, D. J. As, K. Lischka, T. Litz, A. Waag, T. Buhrow, and F. Henneberger. Epitaxial growth and optical transitions of cubic GaN films. *Phys. Rev. B*, 54(12):R8381–R8384, 1996.

[80] M. Landmann, E. Rauls, W. G. Schmidt, M. D. Neumann, E. Speiser, and N. Esser. GaN *m*-plane: Atomic structure, surface bands, and optical response. *Phys. Rev. B*, 91(3):035302, 2015.

[81] H. Morkoç. *Handbook of Nitride Semiconductors and Devices.* Wiley-VCH, Weinheim, DE, 2008.

[82] D. Fritsch, H. Schmidt, and M. Grundmann. Band-structure pseudopotential calculation of zinc-blende and wurtzite AlN, GaN, and InN. *Phys. Rev. B*, 67(23):235205, 2003.

[83] M. Suzuki, T. Uenoyama, and A. Yanase. First-principles calculations of effective-mass parameters of AlN and GaN. *Phys. Rev. B*, 52(11):8132–8139, 1995.

[84] N.W. Ashcroft and N.D. Mermin. *Solid-State Physics*, volume 56. Harcourt, Inc., New York, NY, 1st edition, 1976.

[85] G. Rossbach. *High-Density Excitonic Effects in GaN: Mott-Transition and Polariton Lasing.* Ph.D. thesis, EPFL, 2014.

[86] J.-F. Carlin, C. Zellweger, J. Dorsaz, S. Nicolay, G. Christmann, E. Feltin, R. Butté, and N. Grandjean. Progresses in III-nitride distributed Bragg reflectors and microcavities using AlInN/GaN materials. *Phys. Status Solidi B*, 242(11):2326–2344, 2005.

[87] H. Bruus and K. Flensberg. *Introduction to many-body quantum theory in condensed matter physics.* Oxford University Press, Oxford, UK, 2002.

[88] C. Buchheim, M. Röppischer, R. Goldhahn, G. Gobsch, C. Cobet, C. Werner, N. Esser, A. Dadgar, M. Wieneke, J. Bläsing, and A. Krost. Influence of anisotropic strain on excitonic transitions in *a*-plane GaN films. *Microelectron. J.*, 40(2):322–324, 2009.

[89] Y. P. Varshni. Temperature dependence of the energy gap in semiconductors. *Physica*, 34(1):149–154, 1967.

[90] T. S. Moss. A relationship between the refractive index and the infra-red threshold of sensitivity for photoconductors. *Proc. Phys. Soc. B*, 63(3):167–176, 1950.

[91] P. J. L. Hervé and L. K. J. Vandamme. Empirical temperature dependence of the refractive index of semiconductors. *J. Appl. Phys.*, 77:5476–5477, 1995.

[92] H. Haus. *Waves and fields in optoelectronics.* Prentice-Hall, Eaglewood Cliffs, NJ, 1st edition, 1984.

[93] C. Youtsey, I. Adesida, and G. Bulman. Highly anisotropic photoenhanced wet etching of *n*-type GaN. *Appl. Phys. Lett.*, 71(15):2151–2153, 1997.

[94] E. D. Haberer, R. Sharma, A. R. Stonas, S. Nakamura, S. P. DenBaars, and E. L. Hu. Removal of thick (> 100 nm) InGaN layers for optical devices using band-gap-selective photoelectrochemical etching. *Appl. Phys. Lett.*, 85(5):762–764, 2004.

[95] D. Simeonov, E. Feltin, A. Altoukhov, A. Castiglia, J.-F. Carlin, R. Butté, and N. Grandjean. High quality nitride based microdisks obtained via selective wet etching of AlInN sacrificial layers. *Appl. Phys. Lett.*, 92(17):171102, 2008.

[96] T. J. Puchtler, A. Woolf, T. Zhu, D. Gachet, E. L. Hu, and R. A. Oliver. Effect of threading dislocations on the quality factor of InGaN/GaN microdisk cavities. *ACS Photon.*, 2(1):137–143, 2015.

[97] A. Krost and A. Dadgar. GaN-based optoelectronics on silicon substrates. *Mat. Sci. Engin. B*, 93(1-3):77–84, 2002.

[98] E. Feltin. *Hétéro-Épitaxie de Nitrure de Gallium sur Substrat de Silicium (111) et Applications.* Ph.D. thesis, CRHEA/CNRS, 2003.

[99] R. Butté and N. Grandjean. Effects of polarization in optoelectronic quantum structures. In C. Wood, editor, *Polarization Effects in Semiconductors: From Ab Initio Theory to Device Applications*, pages 467–511. Springer, New York, NY, 2008.

[100] R. Bardoux, T. Guillet, P. Lefebvre, T. Taliercio, T. Bretagnon, S. Rousset, B. Gil, and F. Semond. Photoluminescence of single GaN/AlN hexagonal quantum dots on Si(111): Spectral diffusion effects. *Phys. Rev. B*, 74(19):195319, 2006.

[101] D. Simeonov, A. Dussaigne, R. Butté, and N. Grandjean. Complex behavior of biexcitons in GaN quantum dots due to a giant built-in polarization field. *Phys. Rev. B*, 77(7):075306, 2008.

[102] Gerald Hönig, Gordon Callsen, Andrei Schliwa, Stefan Kalinowski, Christian Kindel, Satoshi Kako, Yasuhiko Arakawa, Dieter Bimberg, and Axel Hoffmann. Manifestation of unconventional biexciton states in quantum dots. *Nature Commun.*, 5:5721, 2014.

[103] N. Vico-Triviño. *GaN-Based Photonic Crystal Cavities on Silicon for Visible and Near Infrared Applications.* Ph.D. thesis, EPFL, 2015.

[104] E. Berkowicz, D. Gershoni, G. Bahir, E. Lakin, D. Shilo, E. Zolotoyabko, Amber C. Abare, Steven P. Denbaars, and L. A. Coldren. Measured and calculated radiative lifetime and optical absorption of In$_x$Ga$_{1-x}$N/GaN quantum structures. *Phys. Rev. B*, 61(16):10994–11008, 2000.

[105] J. Iveland, L. Martinelli, J. Peretti, J. S. Speck, and C. Weisbuch. Direct measurement of Auger electrons emitted from a semiconductor light-emitting diode under electrical injection: Identification of the dominant mechanism for efficiency droop. *Phys. Rev. Lett.*, 110(17):177406, 2013.

[106] J.-M. Gérard and C. Weisbuch. Semiconductor structure for optoelectronic components with inclusions, 1990.

[107] C.-K. Li, M. Piccardo, L.-S. Lu, S. Mayboroda, L. Martinelli, J. Peretti, J. S. Speck, C. Weisbuch, M. Filoche, and Y.-R. Wu. Localization landscape theory of disorder in semiconductors. III. Application to carrier transport and recombination in light emitting diodes. *Phys. Rev. B*, 95(14):144206, 2017.

[108] M. Shahmohammadi, W. Liu, G. Rossbach, L. Lahourcade, A. Dussaigne, C. Bougerol, R. Butté, N. Grandjean, B. Deveaud, and G. Jacopin. Enhancement of Auger recombination induced by carrier localization in InGaN/GaN quantum wells. *Phys. Rev. B*, 95(12):125314, 2017.

[109] L. J. Brillson. *Surfaces and Interfaces of Electronic Materials.* Wiley-VCH, Weinheim, DE, 1st edition, 2012.

[110] E. Yablonovitch, C. J. Sandroff, R. Bhat, and T. Gmitter. Nearly ideal electronic properties of sulfide coated GaAs surfaces. *Appl. Phys. Lett.*, 51(6):439–441, 1987.

[111] R. R. Razouk and B. E. Deal. Dependence of Interface State Density on Silicon Thermal Oxidation Process Variables. *J. Electrochem. Soc.*, 126(9):1573, 1979.

[112] Hans Lüth. *Solid Surfaces, Interfaces and Thin Films.* Graduate Texts in Physics. Springer Berlin Heidelberg, Berlin, Heidelberg, 2010.

[113] C. G. Van De Walle and D. Segev. Microscopic origins of surface states on nitride surfaces. *J. Appl. Phys.*, 101(8):081704, 2007.

[114] M. A. Reshchikov, M. Foussekis, and A. A. Baski. Surface photovoltage in undoped n-type GaN. *J. Appl. Phys.*, 107(11):113535, 2010.

[115] M. Foussekis, A. A. Baski, and M. A. Reshchikov. Photoadsorption and photodesorption for GaN. *Appl. Phys. Lett.*, 94(16):162116, 2009.

[116] C. Pfüller, O. Brandt, F. Grosse, T. Flissikowski, C. Chèze, V. Consonni, L. Geelhaar, H. T. Grahn, and H. Riechert. Unpinning the Fermi level of GaN nanowires by ultraviolet radiation. *Phys. Rev. B*, 82(4):045320, 2010.

[117] M. Himmerlich, A. Eisenhardt, S. Shokhovets, S. Krischok, J. Räthel, E. Speiser, M. D. Neumann, A. Navarro-Quezada, and N. Esser. Confirmation of intrinsic electron gap states at nonpolar GaN(1-100) surfaces combining photoelectron and surface optical spectroscopy. *Appl. Phys. Lett.*, 104(17):171602, 2014.

[118] Y. Honda, N. Kameshiro, M. Yamaguchi, and N. Sawaki. Growth of ($1\bar{1}01$) GaN on a 7-degree off-oriented (001)Si substrate by selective MOVPE. *J. Cryst. Growth*, 242(1-2):82–86, 2002.

[119] T. Li. *III–V Compound Semiconductors: Integration with Silicon-Based Microelectronics*. Taylor & Francis, Boca Raton, FL, 1st edition, 2011.

[120] M. Hatzakis. Electron Resists for Microcircuit and Mask Production. *J. Electrochem. Soc.*, 116(7):1033, 1969.

[121] D.R. Herriott, R.J. Collier, D.S. Alles, and J.W. Stafford. EBES: A practical electron lithographic system. *IEEE Trans. Electron. Dev.*, 22(7):385–392, 1975.

[122] N. Saitou. *Handbook of Photomask Manufacturing Technology*. CRC Press, Boca Raton, FL, 1st edition, 2005.

[123] N. Unal, M. D. B. Charlton, Y. Wang, U. Waizmann, T. Reindl, and U. Hofmann. Easy to adapt electron beam proximity effect correction parameter calibration based on visual inspection of a "best dose sensor". *Microelectron. Engin.*, 88(8):2158–2162, 2011.

[124] R. J. Shul, G. B. McClellan, S. A. Casalnuovo, D. J. Rieger, S. J. Pearton, C. Constantine, C. Barratt, R. F. F. Karlicek, C. Tran, and M. Schurman. Inductively coupled plasma etching of GaN. *Appl. Phys. Lett.*, 69(8):1119–1121, 1996.

[125] R. J. Shul, G. B. McClellan, S. J. Pearton, C. R. Abernathy, C. Constantine, and C. Barratt. Comparison of dry etch techniques for GaN. *Electron. Lett.*, 32(15):1408, 1996.

[126] J. Lee, H. Cho, D. C. Hays, C. R. Abernathy, S. J. Pearton, R. J. Shul, G. A. Vawter, and J. Han. Dry etching of GaN and related materials: comparison of techniques. *IEEE J. Sel. Top. Quantum Electron.*, 4(3):557–563, 1998.

[127] ICP-RIE plasma etcher SI 500, 2017.

[128] R. A. Gottscho. Microscopic uniformity in plasma etching. *J. Vac. Sci. Technol. B*, 10(5):2133, 1992.

[129] H. F. Winters and J. W. Coburn. The etching of silicon with XeF_2 vapor. *Appl. Phys. Lett.*, 34(1):70, 1979.

[130] S. W. King, J. P. Barnak, M. D. Bremser, K. M. Tracy, C. Ronning, R. F. Davis, and R. J. Nemanich. Cleaning of AlN and GaN surfaces. *J. Appl. Phys.*, 84(9):5248–5260, 1998.

[131] X. A. Cao, H. Cho, S. J. Pearton, G. T. Dang, A. P. Zhang, F. Ren, R. J. Shul, L. Zhang, R. Hickman, and J. M. Van Hove. Depth and thermal stability of dry etch damage in GaN Schottky diodes. *Appl. Phys. Lett.*, 75(2):232, 1999.

[132] J.-M. Lee, K.-M. Chang, S.-W. Kim, C. Huh, I.-H. Lee, and S.-J. Park. Dry etch damage in n-type GaN and its recovery by treatment with an N_2 plasma. *J. Appl. Phys.*, 87(11):7667, 2000.

[133] J. I. Goldstein, D. E. Newbury, P. Echlin, D. C. Joy, C. E. Lyman, E. Lifshin, L. Sawyer, and J. R. Michael. *Scanning Electron Microscopy and X-ray Microanalysis.* Springer, Boston, MA, 2003.

[134] CMi. SEM Merlin Manual.

[135] M. Shahmohammadi. *Ultrafast Spectroscopy of Wide Bandgap Semiconductor Nanostructures.* Ph.D. thesis, EPFL, 2015.

[136] G. Binnig, C. F. Quate, and Ch. Gerber. Atomic force microscope. *Phys. Rev. Lett.*, 56(9):930–933, 1986.

[137] Q. Zhong, D. Inniss, K. Kjoller, and V. B. Elings. Fractured polymer/silica fiber surface studied by tapping mode atomic force microscopy. *Surf. Sci.*, 290(1-2):L688–L692, 1993.

[138] Bruker Co. PeakForce tapping brochure, 2017.

[139] G. Tompkins and E. A. Irene. *Handbook of Ellipsometry.* Springer, Heidelberg, DE, 1st edition, 2005.

[140] E. Palik, editor. *Handbook of Optical Constants of Solids.* Academic Press, Orlando, FL, 1985.

[141] N. Antoine-Vincent, F. Natali, M. Mihailovic, A. Vasson, J. Leymarie, P. Disseix, D. Byrne, F. Semond, and J. Massies. Determination of the refractive indices of AlN, GaN, and $Al_xGa_{1-x}N$ grown on (111)Si substrates. *J. Appl. Phys.*, 93(9):5222–5226, 2003.

[142] R. Loudon. The Raman effect in crystals. *Adv. Phys.*, 13(52):423–482, 1964.

[143] Renishaw inVia Confocal Microscope, 2018.

[144] J. Gleize. *Dynamique de Réseau de Nanostructures à Base d'Élements III à Grande Bande Interdite: Effets de l'Anisotropie de la Structure Wurtzite.* Ph.D. thesis, Université Paul Sabatier, Toulouse, France, 2001.

[145] H. Harima. Properties of GaN and related compounds studied by means of Raman scattering. *J. Phys.: Cond. Matter*, 14(38):R967–R993, 2002.

[146] J. Gleize, M. A. Renucci, J. Frandon, E. Bellet-Amalric, and B. Daudin. Phonon deformation potentials of wurtzite AlN. *J. Appl. Phys.*, 93(4):2065–2068, 2003.

[147] G. Callsen, J. S. Reparaz, M. R. Wagner, R. Kirste, C. Nenstiel, A. Hoffmann, and M. R. Phillips. Phonon deformation potentials in wurtzite GaN and ZnO determined by uniaxial pressure dependent Raman measurements. *Appl. Phys. Lett.*, 98(6):061906, 2011.

[148] R. J. Briggs and A. K. Ramdas. Piezospectroscopic study of the Raman spectrum of cadmium sulfide. *Phys. Rev. B*, 13(12):5518–5529, 1976.

[149] K. Kumakura, T. Makimoto, N. Kobayashi, T. Hashizume, T. Fukui, and H. Hasegawa. Minority carrier diffusion length in GaN: Dislocation density and doping concentration dependence. *Appl. Phys. Lett.*, 86(5):052105, 2005.

[150] Cobolt 05-01 Series Datasheet, 2017.

[151] E. Hecht. *Optics.* Addison-Wesley, Boston, MA, 4th edition, 2002.

[152] W. S. Li, Z. X. Shen, Z. C. Feng, and S. J. Chua. Temperature dependence of Raman scattering in hexagonal gallium nitride films. *J. Appl. Phys.*, 87(7):3332–3337, 2000.

[153] L. Mandel and E. Wolf. *Optical Coherence and Quantum Optics.* Cambridge University Press, Cambridge, 1995.

[154] W. Becker. *Advanced Time-Correlated Single Photon Counting Applications.* Springer Series in Chemical Physics. Springer, Berlin, DE, 2015.

[155] PMA Series Datasheet, 2017.

[156] M. A. Reshchikov and H. Morkoç. Luminescence properties of defects in GaN. *J. Appl. Phys.*, 97(6):061301, 2005.

[157] K. L. Shaklee and R. F. Leheny. Direct determination of optical gain in semiconductor crystals. *Appl. Phys. Lett.*, 18(11):475–477, 1971.

[158] C. Lange, M. Schwalm, S. Chatterjee, W. W. Rühle, N. C. Gerhardt, S. R. Johnson, J.-B. Wang, and Y.-H. Zhang. The variable stripe-length method revisited: Improved analysis. *Appl. Phys. Lett.*, 91:191107, 2007.

[159] D. Simeonov. *Synthesis and Optical Investigation of Single Polar GaN/AlN Quantum Dots.* Ph.D. thesis, EPFL, 2009.

[160] P. Vukusic and J. R. Sambles. Photonic structures in biology. *Nature*, 424(6950):852–855, 2003.

[161] M. Glauser. *InGaN Alloys and Heterostructures: Impact of Localization Effects on Light-Matter Interaction in Planar Microcavities.* Ph.D. thesis, EPFL, 2014.

[162] J. Kasprzak, M. Richard, S. Kundermann, A. Baas, P. Jeambrun, J. M. J. Keeling, F. M. Marchetti, M. H. Szymańska, R. André, J. L. Staehli, V. Savona, P. B. Littlewood, B. Deveaud, and L. S. Dang. Bose-Einstein condensation of exciton polaritons. *Nature*, 443(7110):409–414, 2006.

[163] J. Klaers, J. Schmitt, F. Vewinger, and M. Weitz. Bose-Einstein condensation of photons in an optical microcavity. *Nature*, 468(7323):545–548, 2010.

[164] A. W. Snyder and J. D. Love. *Optical Waveguide Theory*. Springer US, Boston, MA, 1984.

[165] Lumerical Solutions Inc. MODE Solutions software, 2015.

[166] Ph. Lalanne and J.-P. Hugonin. Bloch-wave engineering for high-Q, small-V microcavities. *IEEE J. Quantum Electron.*, 39(11):1430–1438, 2003.

[167] M. W. McCutcheon and M. Lončar. Design of a silicon nitride photonic crystal nanocavity with a quality factor of one million for coupling to a diamond nanocrystal. *Opt. Express*, 16(23):19136–19145, 2008.

[168] O. Painter, R. K. Lee, A. Scherer, A. Yariv, J. D. O'Brien, P. D. Dapkus, and I. Kim. Two-Dimensional Photonic Band-Gap Defect Mode Laser. *Science*, 284(5421):1819–1821, 1999.

[169] COMSOL Inc. COMSOL Multiphysics software, 2016.

[170] Y.-I. Sohn, M. J. Burek, V. Kara, R. Kearns, and M. Lončar. Dynamic actuation of single-crystal diamond nanobeams. *Appl. Phys. Lett.*, 107(24):243106, 2015.

[171] N.-V.-Q. Tran, S. Combrié, P. Colman, and A. De Rossi. Directive emission from high-Q photonic crystal cavities through band folding. *Phys. Rev. B*, 79(4):041101, 2009.

[172] N.-V.-Q. Tran, S. Combrié, P. Colman, A. De Rossi, and T. Mei. Vertical high emission in photonic crystal nanocavities by band-folding design. *Phys. Rev. B*, 82(7):075120, 2010.

[173] I. Rousseau, I. Sánchez-Arribas, J.-F. Carlin, R. Butté, and N. Grandjean. Far-field coupling in nanobeam photonic crystal cavities. *Appl. Phys. Lett.*, 108:201104, 2016.

[174] J. Vučković, M. Lončar, H. Mabuchi, and A. Scherer. Design of photonic crystal microcavities for cavity QED. *Phys. Rev. E*, 65(1):016608, 2002.

[175] S. Johnson, M. Ibanescu, M. Skorobogatiy, O. Weisberg, J. D. Joannopoulos, and Y. Fink. Perturbation theory for Maxwell's equations with shifting material boundaries. *Phys. Rev. E*, 65(6):066611, 2002.

[176] M. Borselli, T. J. Johnson, and O. Painter. Accurate measurement of scattering and absorption loss in microphotonic devices. *Opt. Lett.*, 32(20):2954, 2007.

[177] Y.-S. Choi, M. T. Rakher, K. Hennessy, S. Strauf, A. Badolato, P. M. Petroff, D. Bouwmeester, and E. L. Hu. Evolution of the onset of coherence in a family of photonic crystal nanolasers. *Appl. Phys. Lett.*, 91(3):031108, 2007.

[178] S. Strauf, K. Hennessy, M. T. Rakher, Y.-S. Choi, A. Badolato, L. C. Andreani, E. L. Hu, P. M. Petroff, and D. Bouwmeester. Self-Tuned Quantum Dot Gain in Photonic Crystal Lasers. *Phys. Rev. Lett.*, 96(12):127404, 2006.

Bibliography

[179] Q. Quan and M. Lončar. Deterministic design of wavelength scale, ultra-high Q photonic crystal nanobeam cavities. *Opt. Express*, 19(19):18529, 2011.

[180] J. F. Muth, J. H. Lee, I. K. Shmagin, R. M. Kolbas, H. C. Casey, B. P. Keller, U. K. Mishra, and S. P. DenBaars. Absorption coefficient, energy gap, exciton binding energy, and recombination lifetime of GaN obtained from transmission measurements. *Appl. Phys. Lett.*, 71(18):2572, 1997.

[181] M. Sugawara, H. Ebe, N. Hatori, M. Ishida, Y. Arakawa, T. Akiyama, K. Otsubo, and Y. Nakata. Theory of optical signal amplification and processing by quantum-dot semiconductor optical amplifiers. *Phys. Rev. B*, 69(23):235332, 2004.

[182] Lumerical Solutions Inc. Complex structures - Surface roughness, 2017.

[183] C. G. Poulton, C. Koos, M. Fujii, A. Pfrang, T. Schimmel, J. Leuthold, and W. Freude. Radiation modes and roughness loss in high index-contrast waveguides. *IEEE J. Sel. Top. Quantum Electron.*, 12(6):1306–1321, 2006.

[184] Itseez. Open source computer vision library. https://github.com/itseez/opencv, 2015.

[185] M. Skorobogatiy, G. Bégin, and A. Talneau. Statistical analysis of geometrical imperfections from the images of 2D photonic crystals. *Opt. Express*, 13(7):2487, 2005.

[186] N. Le Thomas, Z. Diao, H. Zhang, and R. Houdré. Statistical analysis of subnanometer residual disorder in photonic crystal waveguides: Correlation between slow light properties and structural properties. *J. Vac. Sci. Techol. B*, 29(5):051601, 2011.

[187] R. B. D'Agostino and M. A. Stephens, editors. *Goodness-of-fit techniques*. Marcel Dekker, Inc., New York, NY, 1986.

[188] S. L. Portalupi, M. Galli, M. Belotti, L. C. Andreani, T. F. Krauss, and L. O'Faolain. Deliberate versus intrinsic disorder in photonic crystal nanocavities investigated by resonant light scattering. *Phys. Rev. B*, 84(4):045423, 2011.

[189] Y. Yamaguchi, S. Jeon, B.-S. Song, Y. Tanaka, T. Asano, and S. Noda. Analysis of Q-factors of structural imperfections in triangular cross-section nanobeam photonic crystal cavities. *J. Opt. Soc. Am. B*, 32(9):1792–1796, 2015.

[190] M. Minkov, U. P. Dharanipathy, R. Houdré, and V. Savona. Statistics of the disorder-induced losses of high-Q photonic crystal cavities. *Opt. Express*, 21(23):28233, 2013.

[191] H. B. Mann and D. R. Whitney. On a test of whether one of two random variables is stochastically larger than the other. *Ann. Math. Stat.*, 18(1):50–60, 1947.

[192] M. P. Fay and M. A. Proschan. Wilcoxon-Mann-Whitney or t-test? On assumptions for hypothesis tests and multiple interpretations of decision rules. *Stat. Surv.*, 4(0):1–39, 2010.

[193] V. L. Berkovits, I. V. Makarenko, T. A. Minashvili, and V. I. Safarov. Optical transitions on GaAs [110] surface. *Solid State Commun.*, 56(5):449–450, 1985.

[194] M. A. Olmstead and N. M. Amer. Direct measurement of the polarization dependence of Si(111)2×1 surface-state absorption by use of photothermal displacement spectroscopy. *Phys. Rev. Lett.*, 52(13):1148–1151, 1984.

[195] W. Chen, X. Wen, M. Latzel, M. Heilmann, J. Yang, X. Dai, S. Huang, S. Shrestha, R. Patterson, S. Christiansen, and G. Conibeer. Nanoscale characterization of carrier dynamic and surface passivation in InGaN/GaN multiple quantum wells on GaN nanorods. *ACS Appl. Mater. Interfaces*, 8(46):31887–31893, 2016.

[196] H. Sun, M. K. Shakfa, M. Muhammed, B. Janjua, K.-H. Li, R. Lin, T. K. Ng, I. S. Roqan, B. S. Ooi, and X. Li. Surface-passivated AlGaN nanowires for enhanced luminescence of ultraviolet light emitting diodes. *ACS Photon.*, 2017.

[197] F. E. Schubert and D. A. Stocker. Patent: Crystallographic wet chemical etching of III-nitride material, 1998.

[198] T. Palacios, F. Calle, M. Varela, C. Ballesteros, E. Monroy, F. B. Naranjo, M. A. Sánchez-Garcia, E. Calleja, and E. Muñoz. Wet etching of GaN grown by molecular beam epitaxy on Si(111). *Semicond. Sci. Technol.*, 15(10):996–1000, 2000.

[199] H. Schömig, S. Halm, A. Forchel, G. Bacher, J. Off, and F. Scholz. Probing individual localization centers in an InGaN/GaN quantum well. *Phys. Rev. Lett.*, 92(10):106802, 2004.

[200] R. Seguin, S. Rodt, A. Strittmatter, L. Reißmann, T. Bartel, A. Hoffmann, D. Bimberg, E. Hahn, and D. Gerthsen. Multi-excitonic complexes in single InGaN quantum dots. *Appl. Phys. Lett.*, 84(20):4023, 2004.

[201] T. Wang, T. J. Puchtler, T. Zhu, J. C. Jarman, L. P. Nuttall, R. A. Oliver, and R. A. Taylor. Polarisation-controlled single photon emission at high temperatures from InGaN quantum dots. *Nanoscale*, 9(27):9421–9427, 2017.

[202] S. L. McCall, A. F. J. Levi, R. E. Slusher, S. J. Pearton, and R. A. Logan. Whispering-gallery mode microdisk lasers. *Appl. Phys. Lett.*, 60(3):289–291, 1992.

[203] A. C. Tamboli, E. D. Haberer, R. Sharma, K. H. Lee, S. Nakamura, and E. L. Hu. Room-temperature continuous-wave lasing in GaN/InGaN microdisks. *Nature Photon.*, 1(1):61–64, 2007.

[204] B. E. Little and S. T. Chu. Estimating surface-roughness loss and output coupling in microdisk resonators. *Opt. Lett.*, 21(17):1390–1393, 1996.

[205] I. Rousseau, G. Callsen, G. Jacopin, J.-F. Carlin, R. Butté, and N. Grandjean. Optical absorption and passivation of surface states in III-nitride photonic devices. *J. Appl. Phys.*, 123(11):113103, 2018.

Bibliography

[206] R. E. Slusher, A. F. J. Levi, U. Mohideen, S. L. McCall, S. J. Pearton, and R. A. Logan. Threshold characteristics of semiconductor microdisk lasers. *Appl. Phys. Lett.*, 63(10):1310, 1993.

[207] E. Rozas-Jiménez, A. Cros, S. Murcia-Mascarós, Z. Fang, and B. Daudin. Phonon-plasmon coupling in Si doped GaN nanowires. *Mat. Sci. Semicon. Proc.*, 55:63–66, 2016.

[208] L. Liu and J. H. Edgar. Substrates for gallium nitride epitaxy. *Mater. Sci. Eng. R-Rep.*, 37(3):61–128, 2002.

[209] E. K. Sichel and J. I. Pankove. Thermal conductivity of GaN, 25-360 K. *J. Phys. Chem. Solids*, 38(3):330, 1977.

[210] G. A. Slack. Nonmetallic crystals with high thermal conductivity. *J. Phys. Chem. Solids*, 34(2):321–335, 1973.

[211] V. I. Koshchenko, Y. K. Grinberg, and A. Demidenko. Thermodynamic properties of AlN (5-2700 K), GaP (5-1500 K) and BP (5-800 K). *Inorg. Mater.*, 20(11):1550–1553, 1984.

[212] V. M. Bermudez and J. P. Long. Chemisorption of H_2O on GaN(0001). *Surf. Sci.*, 450(1-2):98–105, 2000.

[213] J. Long and V. Bermudez. Band bending and photoemission-induced surface photovoltages on clean *n*- and *p*-GaN (0001) surfaces. *Phys. Rev. B.*, 66(12):121308, 2002.

[214] Wei Ou. Personal Communication.

[215] V. Portz, M. Schnedler, H. Eisele, R. E. Dunin-Borkowski, and Ph. Ebert. Electron affinity and surface states of GaN *m*-plane facets: Implication for electronic self-passivation. *Phys. Rev. B*, 97(11):115433, 2018.

[216] S. M. Sze and K. K. Ng. *Semiconductor Devices: Physics and Technology.* Wiley Interscience, Hoboken, NJ, 3rd edition, 2007.

[217] A. Winnerl, R. N. Pereira, and M. Stutzmann. Photo-induced changes of the surface band bending in GaN: Influence of growth technique, doping and polarity. *J. Appl. Phys.*, 121(20):205307, 2017.

[218] L. L. Smith, S. W. King, R. J. Nemanich, and R. F. Davis. Cleaning of GaN surfaces. *J. Electron. Mat.*, 25(5):805–810, 1996.

[219] V. M. Bermudez. Study of oxygen chemisorption on the GaN(0001)-(1×1) surface. *J. Appl. Phys.*, 80(2):1190–1200, 1996.

[220] V. M. Bermudez. Investigation of the initial chemisorption and reaction of fluorine (XeF_2) with the GaN(0001)-(1 × 1) surface. *Appl. Surf. Sci.*, 119(1-2):147–159, 1997.

[221] A. Woolf, T. Puchtler, I. Aharonovich, T. Zhu, N. Niu, D. Wang, R. Oliver, and E. L. Hu. Distinctive signature of indium gallium nitride quantum dot lasing in microdisk cavities. *Proc. Natl. Acad. Sci. U.S.A.*, 111(39):14042–14046, 2014.

[222] N. A. K. Kaufmann, A. Dussaigne, D. Martin, P. Valvin, T. Guillet, B. Gil, F. Ivaldi, S. Kret, and N. Grandjean. Thermal annealing of molecular beam epitaxy-grown InGaN/GaN single quantum well. *Semicond. Sci. Technol.*, 27(10):105023, 2012.

[223] R. Calarco, M. Marso, T. Richter, A. I. Aykanat, R. Meijers, A. van der Hart, T. Stoica, and H. Lüth. Size-dependent photoconductivity in MBE-grown GaN nanowires. *Nano Lett.*, 5(5):981–984, 2005.

[224] V. Miikkulainen, M. Leskelä, M. Ritala, and R. L. Puurunen. Crystallinity of inorganic films grown by atomic layer deposition: Overview and general trends. *J. Appl. Phys.*, 113(2):021301, 2013.

[225] R. Grinham and A. Chew. Gas Correction Factors for Vacuum Pressure Gauges. *Vakuum in Forschung und Praxis*, 29(2):25–30, 2017.

[226] T. Sünner, T. Stichel, S.-H. Kwon, T. W. Schlereth, S. Höfling, M. Kamp, and A. Forchel. Photonic crystal cavity based gas sensor. *Appl. Phys. Lett.*, 92(26):261112, 2008.

[227] J. Jágerská, H. Zhang, Z. Diao, N. Le Thomas, and R. Houdré. Refractive index sensing with an air-slot photonic crystal nanocavity. *Opt. Lett.*, 35(15):2523, 2010.

[228] H. Cho, S. M. Donovan, C. R. Abernathy, S. J. Pearton, F. Ren, J. Han, and R. J. Shul. Photoelectrochemical etching of $In_xGa_{1-x}N$. *MRS Internet J. of Nitride Semiconductor Research*, 4(S1):691–696, 1999.

[229] T. Rotter, D. Mistele, J. Stemmer, F. Fedler, J. Aderhold, J. Graul, V. Schwegler, C. Kirchner, M. Kamp, and M. Heuken. Photoinduced oxide film formation on n-type GaN surfaces using alkaline solutions. *Appl. Phys. Lett.*, 76(26):3923–3925, 2000.

[230] N. Niu, T.-S. Liu, I. Aharonovich, K. J. Russell, A. Woolf, T. C. Sadler, H. A. R. El-Ella, M. J. Kappers, R. A. Oliver, and E. L. Hu. A full free spectral range tuning of p-i-n doped gallium nitride microdisk cavity. *Appl. Phys. Lett.*, 101(16):161105, 2012.

[231] M. Malinverni. *Optimization of NH_3-MBE Grown p-Doped (Al)GaN Layers and their Implementation in Long Wavelength Laser Diodes and Tunnel Junctions.* Ph.D. thesis, EPFL, 2015.

[232] G. Shambat, S.-R. Kothapalli, J. Provine, T. Sarmiento, J. Harris, S. S. Gambhir, and J. Vučković. Single-cell photonic nanocavity probes. *Nano Lett.*, 13(11):4999–5005, 2013.

[233] B. Baur, G. Steinhoff, J. Hernando, O. Purrucker, M. Tanaka, B. Nickel, M. Stutzmann, and M. Eickhoff. Chemical functionalization of GaN and AlN surfaces. *Appl. Phys. Lett.*, 87(26):263901, 2005.

Bibliography

[234] J. Sun, E. Timurdogan, A. Yaacobi, E. S. Hosseini, and M. R. Watts. Large-scale nanophotonic phased array. *Nature*, 493:195–199, 2013.

[235] C. V. Poulton, M. J. Byrd, M. Raval, Z. Su, N. Li, E. Timurdogan, D. Coolbaugh, D. Vermeulen, and M. R. Watts. Large-scale silicon nitride nanophotonic phased arrays at infrared and visible wavelengths. *Opt. Lett.*, 42(1):21, 2017.

[236] D. A. B. Miller, D. S. Chemla, T. C. Damen, A. C. Gossard, W. Wiegmann, T. H. Wood, and C. A. Burrus. Electric field dependence of optical absorption near the band gap of quantum-well structures. *Phys. Rev. B*, 32(2):1043–1060, 1985.

[237] G. T. Reed, G. Mashanovich, F. Y. Gardes, and D. J. Thomson. Silicon optical modulators. *Nature Photon.*, 4(8):518–526, 2010.

[238] Y. Zhou, Z. Wang, A. Rasmita, S. Kim, A. Berhane, Z. Bodrog, G. Adamo, A. Gali, I. Aharonovich, and W. Gao. Room temperature solid-state quantum emitters in the telecom range. *Science Adv.*, 4:eaar3580, 2018.

[239] A. Sipahigil, R. E. Evans, D. D. Sukachev, M. J. Burek, J. Borregaard, M. K. Bhaskar, C. T. Nguyen, J. L. Pacheco, H. A. Atikian, C. Meuwly, R. M. Camacho, F. Jelezko, E. Bielejec, H. Park, M. Lončar, and M. D. Lukin. An integrated diamond nanophotonics platform for quantum-optical networks. *Science*, 354(6314):847–850, 2016.

[240] P. Corfdir, J. Levrat, A. Dussaigne, P. Lefebvre, H. Teisseyre, I. Grzegory, T. Suski, J.-D. Ganière, N. Grandjean, and B. Deveaud-Plédran. Intrinsic dynamics of weakly and strongly confined excitons in nonpolar nitride-based heterostructures. *Phys. Rev. B*, 83(24):245326, 2011.

[241] S. Chichibu, T. Azuhata, T. Sota, and S. Nakamura. Luminescences from localized states in InGaN epilayers. *Appl. Phys. Lett.*, 70(21):2822, 1997.

[242] Z. Y. Xu, Z. D. Lu, Z. L. Yuan, X. P. Yang, B. Z. Zheng, J. Z. Xu, W. K. Ge, Y. Wang, J Wang, and L. L. Chang. Thermal activation and thermal transfer of localized excitons in InAs self-organized quantum dots. *Superlattices and Microstructures*, 23(2):381–387, 1998.

[243] Q. Li, S. J. Xu, W. C. Cheng, M. H. Xie, S. Y. Tong, C. M. Che, and H. Yang. Thermal redistribution of localized excitons and its effect on the luminescence band in InGaN ternary alloys. *Appl. Phys. Lett.*, 79(12):1810, 2001.

[244] Y.-H. Cho, G. H. Gainer, A. J. Fischer, J. J. Song, S. Keller, U. K. Mishra, and S. P. DenBaars. S-shaped temperature-dependent emission shift and carrier dynamics in InGaN/GaN multiple quantum wells. *Appl. Phys. Lett.*, 73(10):1370, 1998.

[245] P. G. Eliseev, P. Perlin, J. Lee, and M. Osiński. "Blue" temperature-induced shift and band-tail emission in InGaN-based light sources. *Appl. Phys. Lett.*, 71(5):569, 1997.

[246] H. Wang, Z. Ji, S. Qu, G. Wang, Y. Jiang, B. Liu, X. Xu, and H. Mino. Influence of excitation power and temperature on photoluminescence in InGaN/GaN multiple quantum wells. *Opt. Express*, 20(4):3932–3940, 2012.

[247] M. Glauser, C. Mounir, G. Rossbach, E. Feltin, J.-F. Carlin, R. Butté, and N. Grandjean. In-GaN/GaN quantum wells for polariton laser diodes: Role of inhomogeneous broadening. *J. Appl. Phys.*, 115(23):233511, 2014.

[248] W. E. Blenkhorn, S. Schulz, D. S. P. Tanner, R. A. Oliver, M. J. Kappers, C. J. Humphreys, and P. Dawson. Resonant photoluminescence studies of carrier localisation in *c*-plane InGaN/GaN quantum well structures. *J. Phys. Condens. Matter*, 30(17):175303, 2018.

[249] H. C. Yang, T. Y. Lin, and Y. F. Chen. Persistent photoconductivity in InGaN/GaN multi-quantum wells. *Appl. Phys. Lett.*, 78(3):338, 2001.

[250] D. Watson-Parris, M. J. Godfrey, P. Dawson, R. A. Oliver, M. J. Galtrey, M. J. Kappers, and C. J. Humphreys. Carrier localization mechanisms in $In_xGa_{1-x}N$/GaN quantum wells. *Phys. Rev. B*, 83(11):115321, 2011.

[251] T. J. Puchtler, T. Wang, C. X. Ren, F. Tang, R. A. Oliver, R. A. Taylor, and T. Zhu. Ultra-fast, Polarized, Single-Photon Emission from *m*-Plane InGaN Quantum Dots on GaN Nanowires. *Nano Lett.*, 16(12):7779–7785, 2016.

[252] CMi. Electrons, resists, and substrates.

[253] B. Patton, W. Langbein, and U. Woggon. Trion, biexciton, and exciton dynamics in single self-assembled CdSe quantum dots. *Phys. Rev. B*, 68(12):125316, 2003.

[254] S. G. Johnson, M. L. Povinelli, M. Soljačić, A. Karalis, S. Jacobs, and J. D. Joannopoulos. Roughness losses and volume-current methods in photonic-crystal waveguides. *Appl. Phys. B*, 81(2-3):283–293, 2005.

[255] J. E. Heebner, T. C. Bond, and J. S. Kallman. Generalized formulation for performance degradations due to bending and edge scattering loss in microdisk resonators. *Opt. Express*, 15(8):4452, 2007.

Ian Rousseau

✉ ian.rousseau@gmail.com

Skills

Languages	English (native), German (certified fluent/C2), French (certified advanced B2/C1).
Experimental Optics	Microphotoluminescence and Raman spectroscopy, spectroscopic ellipsometry, confocal microscopy, time-correlated single photon counting, basic ultrafast optics, time-domain terahertz spectroscopy, micro-optical imaging systems, spatial light modulators, white light interferometry.
Fabrication	Photolithography, electron beam lithography, reactive ion etching, scanning electron microscopy, focused ion beam milling, nanoimprint lithography, atomic force microscopy, optical profilometry, thermal evaporation, RF sputtering, basic mill and lathe.
Programming	Python, MATLAB, Java, Scheme, LaTeX, C++, Bash, Mathematica.
Software	Optics: FDTD (Lumerical & MEEP), FEM (COMSOL & Lumerical), Zemax. CAD: SolidWorks. Microcontrollers: Atmel AVR & Arduino. Instrumentation: LabView.

Professional Experience

6.2015 – 6.2018	**Ph.D. Student**, *Advanced Semiconductors for Photoncis and Electronics Laboratory*, EPFL, Lausanne, CH.
	Cleanroom fabrication and optical characterization of gallium nitrde photonic nanocavities on silicon. Built a UV quantum optics laboratory.
1.2014 – 5.2015	**Optical Engineer**, *Creative Microsystems*, Waitsfield, VT, USA.
	Simulated waveguide coupling using eigenmode expansion; designed, built, and characterized micro-optics for multi-aperture cameras and heads-up displays; constructed laser diffraction particle sizer; built computer-generated holography demo using spatial light modulator.
2.2012 – 12.2013	**Research Assistant**, *Laboratory for Nanoelectronics*, ETH-Zurich, Zurich, CH.
	Simulated polymer photonic crystal nanoresonators using FDTD method; nanoimprinted photonic nanostructures into polymers.
1.2011 – 2.2012	**Masters Student**, *Ultrafast Phenomena in Correlated Systems Group*, University of Constance, Constance, DE.
	Measured non-equilibrium time dynamics of superconducting niobium nitride with ultrafast terahertz pump-probe spectroscopy.

Education

6.2015 – 6.2018	**Ph.D. Physics**, *École polytechnique fédérale de Lausanne (EPFL)*, Lausanne, CH.
	Thesis: *III-nitride semiconductor photonic nanocavities on silicon.*
9.2010 – 2.2012	**M.Sc. Physics**, *University of Constance*, Constance, DE, Average grade: 1.0/1.0.
	Thesis: *Near-resonant pump-probe spectroscopy of superconducting NbN*
9.2006 – 6.2010	**B.S. Physics**, *Massachusetts Institute of Technology (MIT)*, Cambridge, MA, USA, GPA: 4.74/5.00.

Honors

3.2010	**Fulbright Research Scholar**, *German-American Fulbright Commission*, Berlin, DE.
	Awarded year-long research fellowship in Konstanz, Germany.
6.2006	**Presidential Scholar**, *Presidential Scholars Commission*, Washington DC.
	Selected as one of 120 US high school students to be honored for academics by the US President.

<table>
<tr><td>6.2005</td><td>**Research Science Institute**, *Center for Excellence in Education*, Washington DC.
Chosen as one of 60 US high school students to attend intensive summer research program at MIT.</td></tr>
<tr><td>7.2016</td><td>**Best student poster**, *Photonic and Electromagnetic Crystal Structures XII*, York, UK.
Awarded cash prize for best student poster.</td></tr>
<tr><td>4.2016</td><td>**Best student talk**, *SPIE Photonics Europe Conference*, Brussels, BE.
Awarded year-long SPIE membership for best student talk in photonic crystals session.</td></tr>
<tr><td>1.2012</td><td>**VEUK Preis**, *University of Constance*, Constance, DE.
Recognized as top foreign student in physics by the alumni association.</td></tr>
</table>

Selected Publications

I. Rousseau and P. Sohi. Vacuum gauge based on III-nitride semiconductor surfaces (Patent Application). PCT/IB2018/053177 2018.

I. Rousseau, G. Callsen, G. Jacopin, J.-F. Carlin, R. Butté, and N. Grandjean. Optical absorption and oxygen passivation of surface states in III-nitride photonic devices. *J. Appl. Phys.*, 123(11):113103, 2018.

S. T. Jagsch, N. Vico Triviño, F. Lohof, G. Callsen, S. Kalinowski, I. Rousseau, R. Barzel, J.-F. Carlin, F. Jahnke, R. Butté, C. Gies, A. Hoffmann, N. Grandjean, and S. Reitzenstein. A quantum optical study of thresholdless lasing features in high-β nitride nanobeam cavities. *Nature Commun.*, 9(1):564, 2018.

I. Rousseau, I. Sánchez-Arribas, K. Shojiki, J.-F. Carlin, R. Butté, and N. Grandjean. Quantification of scattering loss of III-nitride photonic crystal cavities in the blue spectral range. *Phys. Rev. B*, 95(12):125313, 2017.

M. Beck, M. Klammer, I. Rousseau, M. Obergfell, P. Leiderer, M. Helm, V. V. Kabanov, I. Diamant, A. Rabinowicz, Y. Dagan, and J. Demsar. Energy dependence of the electron-boson coupling strength in the electron-doped cuprate superconductor $Pr_{1.85}Ce_{0.15}CuO_{4-\delta}$. *Phys. Rev B*, 95(8):085106, 2017.

I. Rousseau, I. Sánchez-Arribas, J.-F. Carlin, R. Butté, and N. Grandjean. Far-field coupling in nanobeam photonic crystal cavities. *Appl. Phys. Lett.*, 108:201104, 2016.

W.P. Parker, M.A. Strauss, I. Rousseau, and E.P. Gallo. Integrated MicroOptic Imager, Processor, and Display (Patent Application), US20160370588A1 2013.

I. Rousseau and V. Wood. Nanophotonic luminescent solar concentrators. *Appl. Phys. Lett.*, 103(13):131113, 2013.

M. Beck, I. Rousseau, M. Klammer, P. Leiderer, M. Mittendorff, S. Winnerl, M. Helm, G. N. Gol'tsman, and J. Demsar. Transient increase of the energy gap of superconducting NbN thin films excited by resonant narrow-band terahertz pulses. *Phys. Rev. Lett.*, 110(26):267003, 2013.

V. Wood, M. Panzer, D. Bozyigit, Y. Shirasaki, I. Rousseau, S. Geyer, M. Bawendi, and V. Bulović. Electroluminescence from nanoscale materials via field-driven ionization. *Nano Lett.*, 11(7):2927–2932, 2011.

P. Pochet, L. Genovese, D. Caliste, I. Rousseau, S. Goedecker, and T. Deutsch. First-principles prediction of stable SiC cage structures and their synthesis pathways. *Phys. Rev. B*, 82(3):035431, 2010.

A. Arango, I. Rousseau, and V. Bulović. Photovoltaic devices (patent). *US Patent Office*, US2011/007923A1 2009.